Turbulent convection in Rayleigh-Bénard cells with modified boundary conditions

Andres Castillo-Castellanos

Université Pierre et Marie Curie

École Doctorale Sciences Mécaniques, Acoustique, Électronique & Robotique

Institut Jean le Rond ∂'Alembert (∂'Alembert UMR7190) / Laboratoire d'Informatique pour la Mécanique et les Sciences de l'Ingénieur (LIMSI UPR3251)

Turbulent convection in Rayleigh-Bénard cells with modified boundary conditions

Par Andrés Alonso CASTILLO-CASTELLANOS

Thèse de doctorat de Mécanique des Fluides

Dirigée par Maurice Rossi & Anne Sergent

Soutenance effectuée le 13 septembre 2017

Devant un jury composé de :

Mme.	Francesca Chillà	ENS Lyon	Rapporteuse
M.	Mahendra K. Verma	IIT Kanpur	Rapporteur
M.	Denis Funfschilling	ICube	Examinateur
M.	Stephane Popinet	Institut ∂'Alembert	Examinateur
Mme	Bérengère Podvin	LIMSI	Examinatrice
Mme	Anne Sergent	LIMSI	Co-directrice de Thèse
M.	Maurice Rossi	Institut ∂'Alembert	Directeur de Thèse

**Convection turbulente dans les cellules de Rayleigh-Bénard
avec des conditions limites modifiées**

Résumé :

Le présent document est consacré à l'étude des écoulements à grande échelle dans la convection turbulente de Rayleigh-Bénard, et de l'influence exercée par différents facteurs sur leur structure et leur évolution temporelle. Ce travail se compose de trois parties.

Dans la première partie, nous étudions la structure et l'évolution temporelle des écoulements à grande échelle à l'intérieur d'une cellule carré (2D) de type Rayleigh-Bénard. La caractérisation proposée mélange une approche statistique avec une approche physique en s'appuyant sur l'évolution du moment cinétique angulaire ainsi que sur l'évolution des énergies cinétiques et potentiel disponibles, pour mettre en évidence les mécanismes physiques sous-jacents. Nous essayons par la suite de relier ces mécanismes aux structures pérsirtentes observées et à leur évolution temporelle.

Dans la deuxième partie, nous nous concentrons sur les changements dans la circulation à grande échelle résultant de l'imposition d'une condition de surface libre dans une cellule carré (2D) de type Rayleigh-Bénard, ainsi brisant la symétrie haut/bas. Cette configuration présente une température moyenne plus faible, un flux de chaleur amélioré et des fluctuations accrues par rapport au cas classique.

Dans la dernière partie, nous nous concentrons sur les changements dans la circulation à grande échelle, cette fois résultant de l'imposition d'un fort degré de confinement latéral dans une cellular rectangulaire mince (3D) de type Rayleigh-Bénard. Cette configuration présente la formation des grandes structures cohérentes dans la direction verticale, connues sous le nom des canaux turbulents, au lieu d'une circulation à l'échelle du système. Le confinement présente également une forte influence sur différentes quantités globales, tels que les numéros de Nusselt et Reynolds. Afin d'aider à l'exploration du régime sévèrement confiné, nous développons et validons un modèle de dimensionnalité réduit avec corrections inertielles. En utilisant ce modèle, nous sommes en mesure d'explorer l'espace des paramètres et effectuer des observations dans la limite d'un fort confinement.

Mots clés: Turbulence, Chaleur - Convection, Convection de Rayleigh-Bénard

**Turbulent convection in Rayleigh-Bénard cells
with modified boundary conditions**

Abstract:

The present document is dedicated to the study of the large-scale flow patterns in turbulent Rayleigh-Bénard convection, and of the influence exerted by different factors on the flow structures and on their temporal evolution. This work is composed of three parts.

In the first part, we study the structure and the temporal evolution of the large-scale flow inside a square (2D) Rayleigh-Bénard cell. The proposed characterization combines a statistical analysis with a physical approach relying on the angular momentum as well as the kinetic and potential energies to highlight the underlying physical mechanisms. We subsequently attempt to tie these mechanisms together to each of the distinctive flow patterns observed and to their temporal evolution.

In the second part, we focus on the changes in the large-scale flow resulting from imposing a stress-free surface on a square (2D) Rayleigh-Bénard cell, thus breaking the top/bottom symmetry. This configuration exhibits a lower bulk temperature, enhanced heat-flux and increased fluctuations with respect to the classical case.

In the last part, we focus on the changes in the large-scale flow resulting from imposing a strong degree of lateral confinement on a slim rectangular (3D) Rayleigh-Bénard cell. This configuration exhibits the formation of large coherent structures in the vertical direction, or *turbulent channels*, instead of a system-wide circulation. Confinement also exhibits a strong influence on several global quantities such as the *Nusselt* and *Reynolds* numbers. In order to assist in the exploration of the severely confined regime, we develop and validate a reduced dimensionality model with inertial corrections. Using this model, we are able to explore the parameter space and provide further insight in the limit of strong confinement.

Keywords : Turbulent convection, convection in cavities, Bénard convection

Contents

List of Notations

Roman Symbols

k	Thermal conductivity
e_{int}	Internal energy per unit of mass
e_{k}	Kinetic energy per unit of mass
e_{p}	Potential energy per unit of mass
p	Thermodynamic pressure
p*	Driven pressure
q	Heat flux density vector field
g	Gravity vector
u	Velocity vector field
d	Depth of the cavity
y_r	Reference height
C_{p}	Specific heat at constant pressure
C_{v}	Specific heat at constant volume
E_{a}	Available potential energy
E_{b}	Background potential energy
E_{k}	Global kinetic energy
E_{p}	Total potential energy
E_θ	Global temperature fluctuations
L_{2D}	Global angular impulse
Nu	*Nusselt* number
Pr	*Prandtl* number
Ra	*Rayleigh* number
Re	*Reynolds* number
S_{ij}	Strain rate tensor
T	Temperature
H	Height of the cavity
K	Darcy permeability coefficient
W	Width of the cavity
M	External torque

Greek Symbols

α_k	k-th POD modal coefficient
δ_{p}	Kinetic boundary layer thickness at top/bottom plates
δ_θ	Thermal boundary layer thickness at top/bottom plates
δ_{w}	Kinetic boundary layer thickness at side-walls
ϵ_θ	Thermal-energy dissipation rate
ϵ	Kinetic-energy dissipation rate
κ	Thermal diffusivity coefficient
λ_k	k-th Eigenvalue
μ	Dynamic viscosity
ν	Kinematic viscosity
$\phi_k^{(\theta)}$	POD mode of the temperature
$\phi_k^{(u)}$	POD mode of the velocity u
$\phi_k^{(v)}$	POD mode of the velocity v
ρ	Mass density
θ	Reduced temperature field
ϕ	Viscous dissipation
$\boldsymbol{\omega}$	Vorticity vector field
ε	Half aspect ratio in z, *i.e.* $\varepsilon = d/(2H)$
Γ_{x}	Aspect ratio in x, *i.e.* $\Gamma_{\text{x}} = W/H$
Γ_{z}	Aspect ratio in z, *i.e.* $\Gamma_{\text{z}} = d/H$
Π	Pressure potential
Φ_{b1}	Energy transfer rate due to external forces
Φ_{b2}	Energy transfer rate due to external forces
Φ_{b3}	Energy transfer rate due to external forces
Φ_{y}	Energy transfer rate due to buoyancy flux
Φ_{i}	Energy transfer rate due to conduction
Φ_{d}	Energy transfer rate due to mixing
Φ_τ	Energy transfer rate due to external shear
δ_{ij}	*Kronecker* delta
τ_{ij}	Stress tensor
ε_{kji}	*Levi-Civita* tensor

Subscripts

ref	Property evaluated at the reference state $(T_{\text{ref}}, p_{\text{ref}})$
x	Component in the x-direction
y	Component in the y-direction
z	Component in the z-direction

Operators

$\frac{D}{Dt}a$	Material derivative *i.e.* $\partial_t a + \partial_j(u_j a)$
$\overline{a}$	Temporal average
a'	Temporal fluctuation field, *i.e.* $a' = a - \overline{a}$
$\langle a \rangle$	Spatial average
$\{a\}$	Spatial fluctuation, *i.e.* $\{a\} = a - \langle a \rangle$

Part I

General Introduction

Chapter 1

Introduction

The term natural convection indicates the motion of fluid due to density variations. Thermal convection, in which density variations are induced by local temperature differences, is present inside stars and planets, in the atmosphere and the ocean, but also in engineering and in day to day life. The universal nature of thermal convection and its relevance to different fields is reflected by the abundance of publications on the subject.

1.1 Context

Consider an object such as a hot air balloon (or "Montgolfiere") placidly hovering in mid-air as displayed on figure 1.1a. The balloon has a density such that, there is a balance between the weight of the balloon and the buoyancy force, i.e. the force exerted by the displaced fluid. If we dispose of some heat source aboard, the air contained inside the balloon will increase its temperature, decreasing its density with respect to surrounding air and driving the hot air balloon upwards until a new equilibrium is reached. In this sense, it is the density variation due to local temperature differences that drives motion. This represents the basic principle of thermal convection.

Examples of thermally-driven flows are abundant in nature. The grainy appearance of the solar surface (see figure 1.1b) is generated by convection currents inside the Sun - hot, bright rising 'granules' of order 1 Mm surrounded by cooler, darker intergranular lanes (Leighton, 1963). Convection of the Earth mantle drives the generation of plate tectonics, volcanism, earthquakes and mountain building (Bercovici, 2003). The general circulation of the atmosphere is composed of thermal cells created by uneven heating of the Earth's surface by solar radiation coupled with rotation. At "smaller-scales", the sea-breeze, and major weather events (hurricanes, flash-floods, electrical storms, and tornadoes) are also driven by thermal convection (B. Stevens, 2005). In the ocean, the thermohaline circulation is powered by the effect of thermohaline forcing (thermo- referring to temperature and haline- to the concentration of salt) and turbulent mixing (winds and tides) (Rahmstorf, 2003). Engineering applications for thermal convection are equally abundant. It is found nearly everywhere, from heat exchangers, industrial cooling equipment, and natural ventilation systems like solar chimneys, to domestic appliances and consumer electronic devices and even in our day to day life.
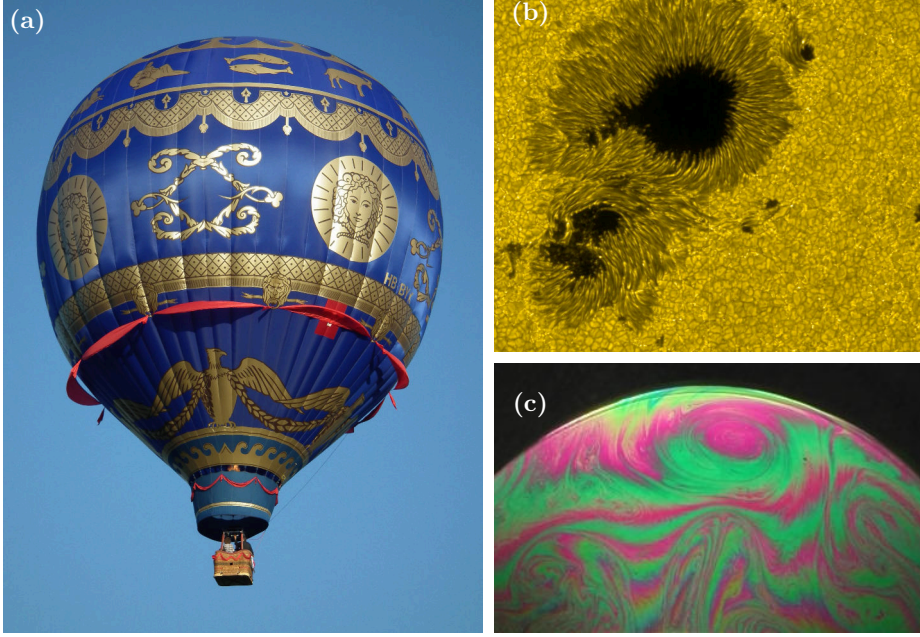
Figure 1.1: (a) A picture of a "Montgolfiere" (Wikimedia commons, 2011). (b) Granular structure of the photosphere (NASA / JAXA, 2015). (c) Convection in a "soap" bubble (Seychelles et al., 2008).

Most of these examples involve thermal convection in complex geometries or combined with other physical processes, such as magnetic forcing, radiative transfer, phase changes, chemical reactions or biological processes. The study of such complex systems requires the use of large material resources which may not be necessarily available at the time. Because of this, most fundamental studies are centered on simplified systems such as thermal convection between two horizontal plates, convection between concentric spheres (Egbers et al., 2003; Travnikov et al., 2003), convection in 'soap' films (see figure 1.1c, Adami, 2014; Seychelles et al., 2008), and a differentially heated cavity (De Vahl Davis, 1983; Le Quéré and Behnia, 1998).

For this work, we focus on the Rayleigh-Bénard convection which involves a horizontal fluid layer of height H, which is heated uniformly from below and cooled uniformly from above in the presence of gravity. By convention the gravity force $\mathbf{g} = \{0, -g, 0\}$ is opposed to the unit vector in the y-direction.

$$T = T_{\text{bot}} \qquad\qquad\qquad \text{at } y = 0 \qquad\qquad (1.1a)$$

$$T = T_{\text{top}} = T_{\text{bot}} - \Delta T \qquad\qquad \text{at } y = H \qquad\qquad (1.1b)$$

Ideally the fluid layer extends over an infinite plane, but in practice, one must also consider the fluid container, usually a cylinder or a square box. The latter type is defined by a width W (see figure 1.2a) and for the 3-D case, a depth d. In the following, we assume side-walls to be adiabatic.

Additionally, we assume the boundaries to be rigid no-slip boundaries, except for one case

4
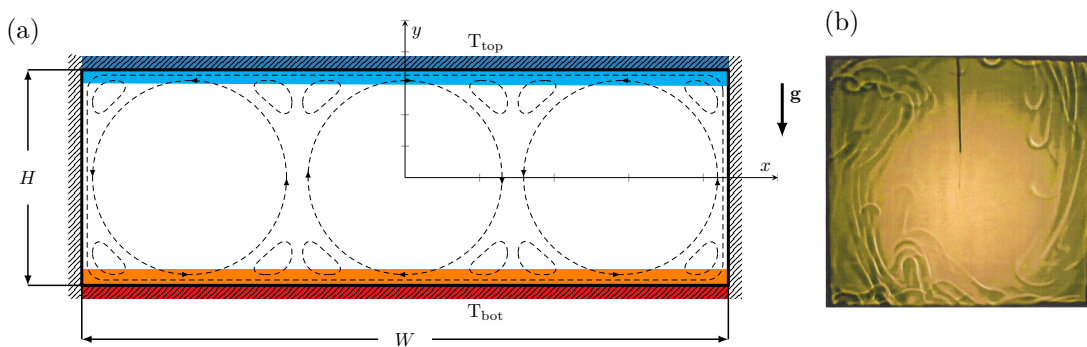
Figure 1.2: (a) Schematic representation of the Rayleigh-Bénard problem and (b) a shadowgraph of rising and falling plumes in a clockwise circulation (Shang et al., 2003).

where the top boundary is assumed to be a free surface.

$$\mathbf{u} = 0 \qquad \text{on rigid boundaries (no-slip condition)} \qquad (1.2a)$$

$$v = \partial_y u = \partial_y w = 0 \qquad \text{on a free surface (stress-free condition)} \qquad (1.2b)$$

Above a critical temperature difference $\Delta \mathrm{T}_c$, the buoyancy force overcomes the viscous damping force driving the warm fluid upwards (resp. cold fluid downwards) thus creating a convective current. At the onset of convection flow appears as steady two-dimensional or three-dimensional rolls. For temperature differences larger than $\Delta \mathrm{T}_c$, the flow exhibits a systematic transition to turbulence via periodic and chaotic solutions. For this work, we are concerned with the (weakly-)turbulent convection regime.

In order to introduce some of the distinctive features of turbulent Rayleigh-Bénard convection, let us consider the schematic representation displayed in figure 1.2. A *kinetic boundary layer* develops in the vicinity of the plates and side-walls, where viscous effects are dominant and most of the frictional drag is concentrated. Similarly, a *thermal boundary layer* develops in proximity to the top and bottom plates where most of the temperature gradient is concentrated. The fluid contained outside of the viscous and thermal boundary layers is referred to as the *bulk*.

One important feature of turbulent Rayleigh-Bénard convection is the spontaneous development of spatially ordered *coherent structures*. Thermal *plumes* are mushroom-like coherent structures that detach from the boundary layers (see figure 1.2b) and are responsible for the transport of most of the heat across the domain (hot *plumes* rise from the bottom boundary layer, cold *plumes* fall from the top boundary layer.) The interaction between *plumes* and walls is responsible for the formation of a large-scale circulation (LSC), also called '*the wind of turbulence*' (Niemela et al., 2001). The LSC in turn deforms the *plumes* and deflects their trajectory creating a complex dynamics (for instance, the roll-like structure on figure 1.2b). The characterization of the spatial structure and the long-term evolution of the LSC, and their sensitivity to different parameters has become a major research subject in recent years.

1.2 Key system parameters and response

Rayleigh-Bénard convection is characterized by competing physical mechanisms: heat conduction, momentum dissipation, and the buoyancy force. For each mechanism we may define a characteristic velocity scale

$$U_{\text{cond}} = \frac{\kappa}{H} \qquad\qquad U_{\text{visc}} = \frac{\nu}{H} \qquad\qquad U_{\text{buoy}} = \sqrt{\frac{|\Delta\rho|}{\rho} gH} \qquad (1.3)$$

where H is the characteristic length of the system, κ (resp. ν) the thermal (resp. momentum) diffusivity coefficient. The buoyancy velocity scale U_{buoy} is that of a fluid parcel, lighter than its surroundings with a density difference $\Delta\rho = -\rho\beta\Delta\text{T}$, with $\beta = -\frac{1}{\rho}\left(\frac{d\rho}{d\text{T}}\right)_p$ being the volumetric thermal expansion coefficient.

The characteristic velocities may be combined to form a non-dimensional parameter known as the *Rayleigh* number

$$\text{Ra} \equiv \frac{\text{Buoyancy}}{\text{Diffusivity}} = \frac{U_{\text{buoy}}^2}{U_{\text{cond}}\, U_{\text{visc}}} = \frac{\beta\Delta\text{T}gH^3}{\kappa\nu} \qquad (1.4)$$

which quantifies the competition of buoyancy forces compared to thermal and viscous diffusion. The *Rayleigh* number is a control parameter, much like the *Reynolds* number which depends on the fluid and on the flow regime. Typical values of Ra range from Ra $\sim 10^3 - 10^4$ near the onset of convective motion, up to Ra $\sim 10^{24} - 10^{27}$ (!) for deep oceanic convection (Chillà and Schumacher, 2012). In contrast, direct numerical simulations are currently limited to Ra $\sim 10^{12} - 10^{13}$ in simple geometries (R. Stevens, Lohse, et al., 2011; Verzicco et al., 2015).

A second important parameter is the *Prandtl* number, which measures the relative importance of momentum (viscous) diffusivity to heat conduction by molecular dissipation.

$$\text{Pr} \equiv \frac{\text{Viscous diffusivity}}{\text{Thermal diffusivity}} = \frac{U_{\text{visc}}}{U_{\text{cond}}} = \frac{\nu}{\kappa} \qquad (1.5)$$

The *Prandtl* number depends only of the fluid properties. Typical values of Pr are around $0.7 - 1.0$ for air and other gases, from $1.0 - 10.0$ for water, and around 10^{23} for the mantle of the Earth.

The geometry of the container is represented by one or more dimensionless aspect ratios. For a rectangular container we define the longitudinal and transversal aspect ratios

$$\Gamma_{\text{x}} \equiv \frac{W}{H} \qquad\qquad\qquad \Gamma_{\text{z}} \equiv \frac{d}{H} \qquad (1.6)$$

where W is the width and d is the depth of the container.

The central elements of the Rayleigh-Bénard problem are summarized by (Ahlers, Grossmann, et al., 2009) as follows: for a given fluid in a closed container heated from below and cooled from above, how effective is the transfer of heat and momentum, and which are the main features of the flow inside the container. In this sense, one of the main responses of the system are the *Nusselt* and *Reynolds* numbers. The *Nusselt* number represents the
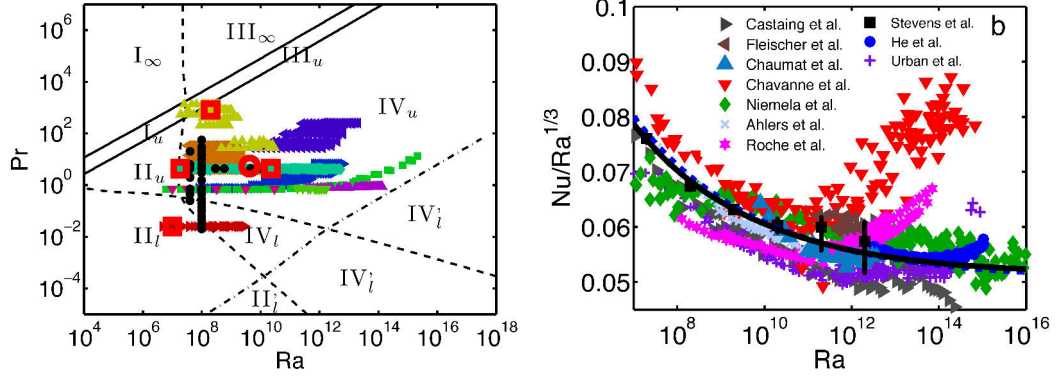
Figure 1.3: Left: Phase diagram in Ra-Pr plane indicating the different turbulent regimes of the Grossmann-Lohse scaling theory in a cylindrical cell of aspect ratio $\Gamma = 1$, Right: Comparison between simulations, experiments, and the prediction of the Grossmann-Lohse theory (R. Stevens, Poel, et al., 2013).

ratio between the overall heat transfer with respect to the heat transfer by conduction

$$\mathrm{Nu} \equiv \frac{\langle \overline{v\mathrm{T}} \rangle_{\mathrm{xz}} - \kappa \partial_y \langle \overline{\mathrm{T}} \rangle_{\mathrm{xz}}}{\kappa \Delta \mathrm{T}/H} \tag{1.7}$$

where v is the vertical velocity and $\langle \overline{\cdot} \rangle_{\mathrm{xz}}$ indicates the average over time and over a plane xz at constant y. We also define a *Reynolds* number based on the height H and a characteristic velocity U

$$\mathrm{Re} \equiv \frac{UH}{\nu} \tag{1.8}$$

where U may be a characteristic velocity of the large-scale circulation, or a root mean squared velocity.

1.3   Scaling theories for the Nusselt number

It is easy to understand why so many theoretical, numerical, and experimental studies have focused over the years on explaining the evolution of the system responses, Nu and Re, in terms of the input parameters: Ra, Pr, and the aspect ratios. Most of the earlier theories predict general scaling laws

$$\mathrm{Nu} \sim \mathrm{Ra}^{\beta_{\mathrm{Nu}}} \mathrm{Pr}^{\gamma_{\mathrm{Nu}}} \qquad\qquad \mathrm{Re} \sim \mathrm{Ra}^{\beta_{\mathrm{Re}}} \mathrm{Pr}^{\gamma_{\mathrm{Re}}} \tag{1.9}$$

where examples include the $\beta_{\mathrm{Nu}} = \frac{1}{3}$ regime by (Malkus, 1954) which assumes the heat-flux to be independent of the height of the cavity, and the hard turbulence regime with $\beta_{\mathrm{Nu}} = \frac{2}{7}$ and $\beta_{\mathrm{Re}} = \frac{1}{2}$ by (Castaing et al., 1989). The latter theory assumes the existence of a mixing zone where plumes are detached from the boundary layers and accelerate to match the velocities of the central region. A model unifying the different scaling regimes was developed by (Grossmann and Lohse, 2000) based on the exact relations between the Nusselt number and the viscous and thermal dissipation rates (Shraiman and Siggia, 1990). The main idea is to decompose the viscous and thermal dissipation rates into contributions from the bulk flow and from the boundary layers, then use dimensional analysis to estimate

7
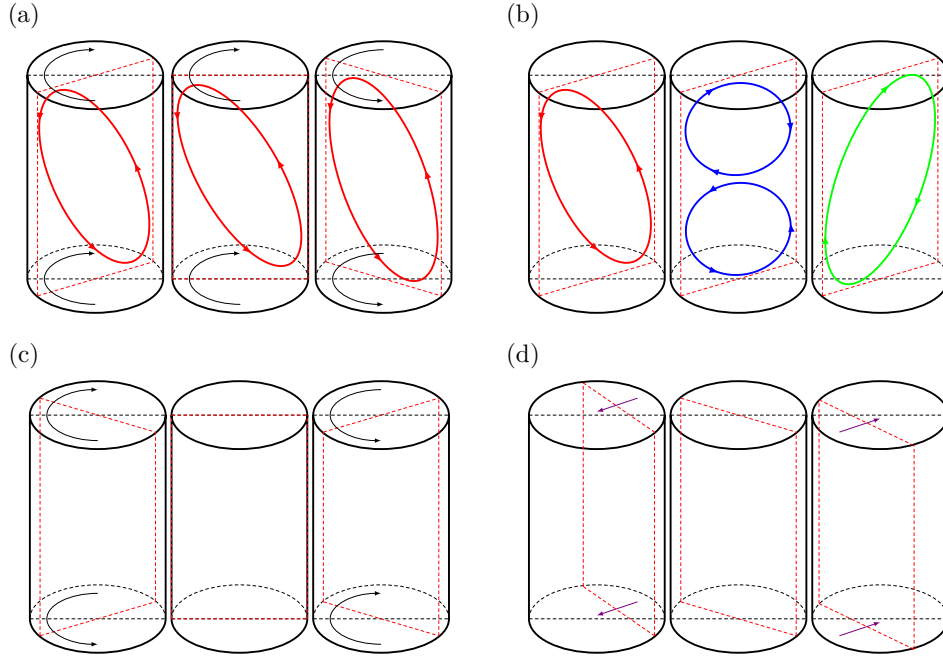
Figure 1.4: Long-term evolution of the LSC inside a cylinder: (a) Azimuthal meandering of the LSC plane (Funfschilling and Ahlers, 2004); (b) Reversal of the LSC inside a cylindrical cell (Xi and Xia, 2008); (c) Torsional oscillations of the LSC plane (Funfschilling, Brown, et al., 2008); and (d) off-center oscillations of the LSC plane (Zhou et al., 2009).

these separate contributions in terms of Ra and Pr. This theory identifies different scaling regimes and makes use of crossover functions to combine scalings in a way which would not be possible with simpler power laws, see figure 1.3. A detailed discussion of the historical aspects of the scaling theories can be found in (Ahlers, Grossmann, et al., 2009).

1.4   Re-orientations of the large-scale circulation

Despite its apparent simplicity, the Rayleigh-Bénard convection exhibits some incredibly rich and complex dynamics of the large-scale flow. Generally, the 'wind' breaks one or more of the natural symmetries of the system. For a cylindrical cell, the 'wind' takes the form of roll-like structures. Over time, the 'wind' may go through a series of transformations and re-orientations which help restore the (statistical) symmetry of the system. The first type of re-orientation is known as the *azimuthal meandering* is displayed on figure 1.4a. The plane of the roll-like structure exhibits spontaneous and erratic reorientations through azimuthal displacements. A complete rotation of the entire structure may be observed without major changes in the flow speed (Funfschilling and Ahlers, 2004). The second type of re-orientation is through a *cessation* of the roll-like structure, before restarting in a different direction, see figure 1.4b. Both kinds of reversals are often superposed to other events, such as *torsional oscillations* of the LSC plane displayed in figure 1.4c (Funfschilling, Brown, et al., 2008) and off-center oscillations of the LSC plane displayed in figure 1.4d (Zhou et al., 2009). The precise nature of these transformations is not fully understood.

One approach commonly used in the study of *cessation-led* reversals, is to constrain the

(a)   (b)
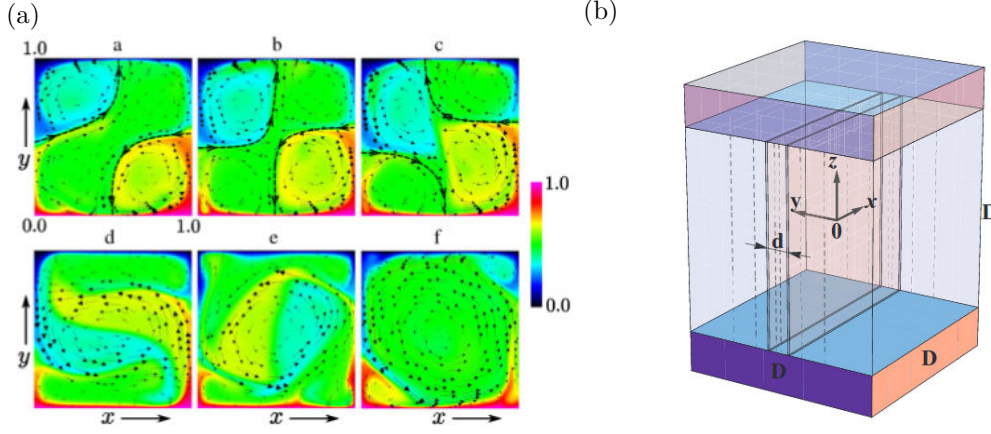
Figure 1.5: Configurations used in the study of flow reversals: (a) numerical studies on a pure 2-D geometry (image from Chandra and Verma, 2011), and (b) experimental and numerical studies on a slim rectangular geometry (image from Vasiliev and Frick, 2011).

large scale circulation to a plane by restricting the fluid domain to a pure 2-D geometry (Sugiyama, Ni, et al., 2010; Chandra and Verma, 2011; Podvin and Sergent, 2015) or to a slim rectangular geometry of small aspect ratio in the transversal direction (Vasiliev and Frick, 2011; Ni et al., 2015), see figure 1.5. Sugiyama, Ni, et al., 2010 identified a region in the $(\mathrm{Ra}, \mathrm{Pr})$ space in which reversals of the large-scale flow are observed numerically in a (2-D) square and experimentally inside a rectangular geometry with $\Gamma_x = 1$ and $\Gamma_z = 0.3$. In such configurations, the flow is composed of a large diagonal roll and two counter-rotating corner-rolls. Flow reversals has been observed experimentally by Ni et al., 2015 for $0.84 \leq \Gamma_x \leq 1.10$ and $0.33 \leq \Gamma_z \leq 0.25$, and by Vasiliev and Frick, 2011 for $\Gamma_x = 1$ and $0.06 \leq \Gamma_z \leq 0.2$ for different values of Ra and Pr. However, given some of the differences between pure 2-D and (quasi-)2-D turbulent convection, it is not entirely clear if the reversals observed in each case correspond to the same phenomenon. A more complete characterization of the reversal dynamics is required to help addressing this question.

1.5   Motivation and objectives

The present document is dedicated to the study of the large-scale flow patterns in turbulent Rayleigh-Bénard convection, and of the influence exerted by different factors on the flow structures and on their temporal evolution. The proposed characterization combines a statistical analysis with a physical approach relying on the angular momentum as well as the kinetic and potential energies to highlight the underlying physical mechanisms. We subsequently attempt to tie these mechanisms together to each of the distinctive flow patterns observed and to their evolution. Investigating the nature of these coherent structures may be useful in modeling and controlling turbulent flows, as well as to improve our understanding of the large-scale dynamics.

The contents of this work are organized as follows. Part I (chapters §2 to §3) is focused on the numerical computation and outlines the methodology used in the characterization of large-scale flow patterns in turbulent convection. Part II (chapters §4 and §5) is dedicated to the study of spontaneous re-organization of the large-scale flow inside square (2-D)

cells. Part III (chapter §6) deals with the effects on the large-scale flow of imposing a free surface on a square cell. The last part of this work (chapters §7 and §8) deals with the influence of lateral confinement on a slim rectangular geometry.

Chapter 2

Governing equations and statistical characterization tools

In the first part of this chapter we define the classic statement of the Rayleigh-Bénard problem in the framework of the Boussinesq approximation. Additionally, we detail the two main configurations studied throughout this work: a square (2-D) geometry with a rigid or a stress-free surface, and a slim rectangular (3-D) geometry. In the second part we introduce some quantities useful in the subsequent analyses. Sections §2.2 and §2.3 deal with different global quantities used to characterize the flow from energetic and hydrodynamic viewpoints. Sections §2.4 to §2.6 focused on the spatial structure of the flow and the separation of large- and small-scale flow patterns.

2.1 Problem description

2.1.1 Governing equations

For thermal convection it is necessary to write governing equations for the temperature, velocity and pressure fields, couple with equations of state. In buoyancy driven flows, if the density field does not deviate too much from an average value, the Boussinesq approximation is used to obtain a simpler set of governing equations, called the Oberbeck-Boussinesq equations or Boussinesq equations.

Navier-Stokes equations for compressible fluids

The starting point are the compressible Navier-Stokes equations in the following form

$$\partial_t \rho + \partial_j(\rho u_j) = 0 \qquad (2.1)$$

$$\partial_t(\rho u_i) + \partial_j(\rho u_j u_i) = \rho g_i + \partial_j \tau_{ij} \qquad (2.2)$$

with ρ being the density, and τ_{ij} the stress tensor. For a Newtonian fluid the stress tensor τ_{ij} is modeled as

$$\tau_{ij} = -\mathrm{p}\delta_{ij} + 2\mu \left(\mathrm{S}_{ij} - \frac{1}{3}\partial_k u_k \delta_{ij} \right) \tag{2.3}$$

with p being the thermodynamic pressure, μ the dynamic viscosity, δ_{ij} the Kronecker delta and S_{ij} the rate of strain tensor

$$\mathrm{S}_{ij} \equiv \frac{1}{2}(\partial_j u_i + \partial_i u_j) \tag{2.4}$$

Equations for mechanical energy in compressible fluids

If we multiply equation (2.2) by **u** one obtains an expression for the kinetic energy,

$$\frac{\mathrm{D}}{\mathrm{Dt}}(\rho \mathrm{e_k}) = \rho u_i g_i + \mathrm{p}\partial_i u_i + \partial_j(u_i \tau_{ij}) - \phi \tag{2.5}$$

where $\frac{\mathrm{D}}{\mathrm{Dt}}$ indicates the material derivative, $\mathrm{e_k} \equiv \frac{1}{2}u_i u_i$ the specific, i.e. per unit mass, kinetic energy, and ϕ the rate of viscous dissipation

$$\phi \equiv 2\mu(\mathrm{S}_{ij} - \frac{1}{3}\partial_k u_k \delta_{ij})(\mathrm{S}_{ij} - \frac{1}{3}\partial_k u_k \delta_{ij}) \tag{2.6}$$

The change in specific potential energy $\mathrm{e_p} \equiv g_i x_i$, reads as

$$\frac{\mathrm{D}}{\mathrm{Dt}}(\rho \mathrm{e_p}) = -\rho u_i g_i \tag{2.7}$$

Combining the above expression with (2.5) yields the following expression for the total mechanical energy

$$\frac{\mathrm{D}}{\mathrm{Dt}}(\rho(\mathrm{e_k} + \mathrm{e_p})) = \mathrm{p}\partial_i u_i + \partial_j(u_i \tau_{ij}) - \phi \tag{2.8}$$

Equation for internal energy in compressible fluids

Now consider $\mathrm{e_{int}}$ as the specific internal energy. Using the first law of thermodynamics on the material volume Ω gives

$$\frac{\mathrm{D}}{\mathrm{Dt}} \int_\Omega \rho(\mathrm{e_{int}} + \mathrm{e_k} + \mathrm{e_p})\mathrm{d}\Omega = \oint_{\partial\Omega} (\tau_{ij}u_i n_j - \mathrm{q}_i n_i)\mathrm{dS} \tag{2.9}$$

where q is the heat-flux, dS the surface element and **n** the outward normal unit vector. The above implies

$$\frac{\mathrm{D}}{\mathrm{Dt}} [\rho(\mathrm{e_{int}} + \mathrm{e_k} + \mathrm{e_p})] = \partial_j(u_i \tau_{ij}) - \partial_i \mathrm{q}_i \tag{2.10}$$

Taking the difference between equations (2.8) and (2.10) yields an equation for the internal energy e_{int}

$$\frac{D}{Dt}(\rho e_{int}) = \phi - \partial_i q_i - p \partial_i u_i \tag{2.11}$$

Equation (2.11) is implicitly coupled with (2.1) and (2.2) through a phenomenological equation for the heat-flux, the equation of state $e_{int} = e_{int}(T, p)$ and the fluid properties $\rho = \rho(T, p)$, $\mu = \mu(T, p)$, and so on.

2.1.2   The Oberbeck-Boussinesq approximation

Under the Boussinesq approximation, variations of density are neglected everywhere except in the buoyancy term. Additionally, we assume the density to depend linearly on the temperature only,

$$\rho(T) = \rho_{ref} \left(1 - \beta[T - T_{ref}]\right) \tag{2.12}$$

where β is the coefficient of thermal expansion at the reference state (T_{ref}, p_{ref}). In our case, the reference temperature is taken as $T_{ref} = (T_{bot} + T_{top})/2$. All the properties of the fluid are considered as constants and are evaluated at this reference state.

This hypothesis is valid for most fluids if we consider that: *a)* the compressibility effects are negligible, *b)* the vertical scale is small enough so that density variations due to the hydrostatic pressure variations are negligible, and *c)* temperature variations in the flow are small. For most liquid configurations these conditions are generally satisfied, whereas for gases the following conditions must be verified

$$\frac{g\beta H}{r}\left[1 + \beta\left(T - T_{ref}\right)\right] \ll 1 \tag{2.13a}$$

$$\beta\left(T - T_{ref}\right) \ll 1 \tag{2.13b}$$

where r is the specific gas constant measured in SI units, i.e. $[\text{J kg}^{-1} \text{ K}^{-1}]$ (see for instance Tritton, 2012; Hinch et al., 2012).

The internal energy equation is simplified under the Boussinesq approximation. (Getling, 1998; Kundu and Cohen, 2012). In that approximation, we suppose the heat flux follows Fourier law $q_i = -k\partial_i T$, the heating due to viscous dissipation of energy is negligible $\frac{\phi}{\rho C_v} \approx 0$, and the internal energy follows the Ideal gas's law $e_{int} = C_v T$, one obtains a partial differential equation for T

$$\frac{D}{Dt}T = \frac{1}{\rho C_v}\left[\partial_j(k\partial_j T) - p(\partial_i u_i)\right] \tag{2.14}$$

with C_v being the specific heat at constant volume, and k being the thermal conductivity. The volume expansion term $-p(\partial_i u_i)$ may be written as

$$-p(\partial_i u_i) = -\rho(C_p - C_v)\frac{D}{Dt}T \tag{2.15}$$

with C_p being the specific heat at constant pressure. This leads to the following expression

for the temperature field

$$\frac{D}{Dt}T = \partial_j(\kappa\partial_j T) \tag{2.16}$$

where the thermal diffusivity κ is defined as $\kappa = \frac{k}{\rho C_p}$.

We introduce $p^*(\mathbf{x},t)$ as the difference between the thermodynamic pressure and the hydrostatic pressure, commonly referred as driven pressure,

$$-\partial_i p^* = -\partial_i p + g_i \rho_{\text{ref}} \tag{2.17}$$

to obtain the Oberbeck-Boussinesq equations

$$\boxed{\begin{aligned} \partial_i u_i &= 0 \\ \partial_t u_i + \partial_j(u_j u_i) &= -\frac{1}{\rho_{\text{ref}}}\partial_i p^* + \nu_{\text{ref}}\partial_j\partial_j u_i - \beta(T - T_{\text{ref}})g_i \\ \partial_t T + \partial_j(u_j T) &= \kappa_{\text{ref}}\partial_j\partial_j T \end{aligned}} \tag{2.18}$$

where $\nu_{\text{ref}} = \mu_{\text{ref}}/\rho_{\text{ref}}$ is the kinematic viscosity of the fluid. Since fluid properties are always evaluated at the reference state, in the following we drop the subscript everywhere except for the reference temperature T_{ref}.

2.1.3   Dimensionless parameters

Fluid flow problems without electro-magnetic forcing or chemical reactions involve only mechanical and thermal variables, can be expressed in terms of four basic quantities: a length, a time, a mass and a temperature. We define the characteristic mass $[M]$, length $[L]$, temperature $[\Theta]$, and velocity $[U]$ scales as follows. The relevant length scale corresponds to the height of the fluid layer H, while the temperature scale is fixed by the temperature difference ΔT between the top and bottom plates. A characteristic velocity scale is obtained from dimensional analysis by a balance between the friction and buoyancy forces (Bejan, 2013, Sec. 4.3., Scale analysis) which corresponds to the free-fall velocity U_{buoy} divided by $Pr^{0.5}$

$$[M] = \rho H^3, \qquad [L] = H, \qquad [\Theta] = \Delta T, \qquad [U] = \frac{\kappa}{H}\sqrt{\frac{g\beta\Delta T H^3}{\kappa\nu}} \tag{2.19}$$

We proceed to define a set of non-dimensional variables

$$\tilde{\mathbf{x}} = \frac{\mathbf{x}}{[L]} \qquad \tilde{\mathbf{u}} = \frac{\mathbf{u}}{[U]} \qquad \tilde{t} = \frac{t}{[L]/[U]} \qquad \tilde{p} = \frac{p^*}{\rho[U]^2} \tag{2.20}$$

and a reduced temperature θ

$$\theta = \frac{T - T_{\text{ref}}}{[\Theta]} \tag{2.21}$$

From this point on, quantities are written in dimensionless form only and tildes (˜) are omitted.

14
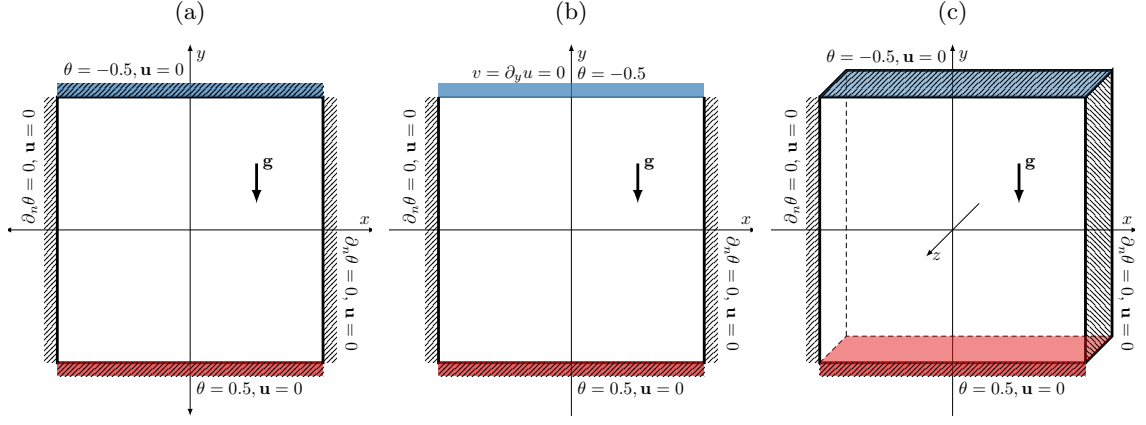
Figure 2.1: Configurations considered for this work: (a) a 2-D square with top and bottom no-slip conditions; (b) a 2-D square with top stress-free surface and bottom no-slip condition; and (c) a slim rectangular geometry of aspect ratio $\Gamma_x = 1$ and $\Gamma_z < 1$.

The Oberbeck-Boussinesq equations may be written in dimensionless form as

$$
\begin{aligned}
\partial_i u_i &= 0 \\
\partial_t u_i + \partial_j(u_j u_i) &= -\partial_i \mathrm{p} + \mathrm{Pr}\mathrm{Ra}^{-0.5}\partial_j\partial_j u_i + \mathrm{Pr}\theta\delta_{\mathrm{i2}} \\
\partial_t \theta + \partial_j(u_j\theta) &= \mathrm{Ra}^{-0.5}\partial_j\partial_j\theta
\end{aligned} \tag{2.22}
$$

In addition, we impose the thermal boundary conditions

$$\theta = -1/2 \qquad\qquad \text{at the top plate } (y = 1/2) \tag{2.23a}$$

$$\theta = 1/2 \qquad\qquad \text{at the bottom plate } (y = -1/2) \tag{2.23b}$$

$$\partial_n \theta = 0 \qquad\qquad \text{on the sidewalls} \tag{2.23c}$$

and the mechanical boundary conditions

$$\mathbf{u} = 0 \qquad\qquad \text{on rigid boundaries (no-slip condition)} \tag{2.24a}$$

$$v = \partial_y u = \partial_y w = 0 \qquad\qquad \text{on a free surface (stress-free condition)} \tag{2.24b}$$

and the geometry of the domain. Three main configurations are considered in this work. Chapters §4 to §5 are dedicated to the study of square (2-D) cell with rigid boundaries (figure 2.1a), chapter §6 deals with square (2-D) cells with top stress-free surface and bottom no-slip condition (figure 2.1b)

$$\mathbf{x} \in \left[-\frac{1}{2}, \frac{1}{2}\right] \times \left[-\frac{1}{2}, \frac{1}{2}\right] \qquad\qquad \text{with } \mathbf{x} \in \mathbb{R}^2$$

whereas chapters §7 and §8 deal with a slim rectangular (3-D) geometry with rigid adiabatic walls under various degrees of lateral confinement, with Γ_z being the aspect ratio in the transversal direction (figure 2.1c).

$$\mathbf{x} \in \left[-\frac{1}{2}, \frac{1}{2}\right] \times \left[-\frac{1}{2}, \frac{1}{2}\right] \times \left[-\frac{\Gamma_z}{2}, \frac{\Gamma_z}{2}\right] \qquad \text{with } \mathbf{x} \in \mathbb{R}^3$$

2.2 Analysis of global quantities related to the mechanical energy, the temperature variance, and Nusselt number

2.2.1 Definition of statistical quantities

In this section, we detail some of quantities used in the description of energy exchanges in convective turbulence. It is convenient to introduce the following notation convention regarding temporal and spatial averages, and other meaningful quantities.

Temporal fluctuations

Consider $\phi(\mathbf{x}, t)$ to be a given field which may be decomposed as follows

$$\phi'(\mathbf{x}, t) \equiv \phi(\mathbf{x}, t) - \overline{\phi}(\mathbf{x}) \qquad \overline{\phi}(\mathbf{x}) \equiv \frac{\int_{t_o}^{t_f} \phi(\mathbf{x}, t) \, \mathrm{dt}}{(t_f - t_o)} \qquad (2.25)$$

where $\overline{\phi}(\mathbf{x})$ is the mean field or time-averaged field evaluated in the interval $[t_o, t_f]$ and $\phi'(\mathbf{x}, t)$ is the fluctuating field. One introduces as well the variance Var ϕ, the standard deviation $\sigma(\phi)$, and the skewness coefficient Skew(ϕ) as

$$\text{Var } \phi(\mathbf{x}) \equiv \overline{\phi'\phi'} \qquad \sigma(\phi)(\mathbf{x}) \equiv (\overline{\phi'\phi'})^{1/2} \qquad \text{Skew}(\phi)(\mathbf{x}) \equiv \frac{\overline{\phi'\phi'\phi'}}{(\text{Var } \phi)^{3/2}} \qquad (2.26)$$

Spatial fluctuations

A similar decomposition may be performed in space rather than in time. For instance $\langle\phi\rangle_{\text{xyz}}$ is the average over a volume V, $\langle\phi\rangle_{\text{xz}}$ the average value over a plane A_{xz}, and $\langle\phi\rangle_{\text{x}}$ the average value over a line L_x in the x-direction. This introduces the following spatial decomposition

$$\{\phi\}_{\text{xyz}}(\mathbf{x}, t) \equiv \phi(\mathbf{x}, t) - \langle\phi\rangle_{\text{xyz}}(t) \qquad \langle\phi\rangle_{\text{xyz}}(t) \equiv \frac{\iiint \phi(x, y, z, t) \, \mathrm{dxdydz}}{V} \qquad (2.27\text{a})$$

$$\{\phi\}_{\text{xz}}(\mathbf{x}, t) \equiv \phi(\mathbf{x}, t) - \langle\phi\rangle_{\text{xz}}(y, t) \qquad \langle\phi\rangle_{\text{xz}}(y, t) \equiv \frac{\iint \phi(x, y, z, t) \, \mathrm{dxdz}}{A_{xz}} \qquad (2.27\text{b})$$

$$\{\phi\}_{\text{x}}(\mathbf{x}, t) \equiv \phi(\mathbf{x}, t) - \langle\phi\rangle_{\text{x}}(y, z, t) \qquad \langle\phi\rangle_{\text{x}}(y, z, t) \equiv \frac{\int \phi(x, y, z, t) \, \mathrm{dx}}{L_x} \qquad (2.27\text{c})$$

For any such spatial averages, we define a spatial variance $\langle\phi\rangle^{\text{Var}}$ and root mean square $\langle\phi\rangle^{\text{rms}}$. For instance $\langle\phi\rangle_{\text{yz}}^{\text{Var}}$ and $\langle\phi\rangle_{\text{yz}}^{\text{rms}}(x, t)$ corresponds to the spatial variance and the root mean squared value evaluated over y and z-directions.

$$\langle\phi\rangle_{\text{yz}}^{\text{Var}}(x, t) \equiv \langle\{\phi\}_{\text{yz}}\{\phi\}_{\text{yz}}\rangle_{\text{yz}} \qquad \langle\phi\rangle_{\text{yz}}^{\text{rms}}(x, t) \equiv \left(\langle\phi\rangle_{\text{yz}}^{\text{Var}}\right)^{1/2} \qquad (2.28)$$

Note that, any of these definitions can be trivially extended to other directions.

Spatio-temporal fluctuations

Additionally, we may use a spatial and temporal average, i.e. $\langle\overline{\phi}\rangle$ and introduce the spatio-temporal root mean square $\langle\phi\rangle^{\overline{\mathrm{rms}}}$

$$\langle\phi\rangle^{\overline{\mathrm{rms}}} \equiv \sqrt{\overline{\langle(\phi - \langle\overline{\phi}\rangle)^2\rangle}} = \sqrt{\overline{\langle\phi\phi\rangle} - \langle\overline{\phi}\rangle\langle\overline{\phi}\rangle} \tag{2.29}$$

where the following property of the averaging operator $\overline{\langle\langle\overline{\phi}\rangle\phi\rangle} = \langle\overline{\phi}\rangle\langle\overline{\phi}\rangle$, is implied. Again this is valid to any spatial average, the direction of which is indicated by the subscript.

2.2.2 Instantaneous Nusselt numbers

One of the main responses of the system under convection is the Nusselt number which quantifies the dimensionless heat-flux across the fluid layer

$$\mathrm{Nu_y}(y,t) \equiv \mathrm{Ra}^{0.5}\langle v\theta\rangle_{\mathrm{xz}} - \langle\partial_y\theta\rangle_{\mathrm{xz}} \tag{2.30}$$

We define the instantaneous Nusselt numbers evaluated at the bottom and top plates, $\mathrm{Nu_{bot}}$ and $\mathrm{Nu_{top}}$, and a volume-averaged Nusselt number $\mathrm{Nu_{vol}}$ as

$$\mathrm{Nu_{bot}}(t) \equiv \mathrm{Nu_y}(y = -0.5, t) \tag{2.31a}$$
$$\mathrm{Nu_{top}}(t) \equiv \mathrm{Nu_y}(y = 0.5, t) \tag{2.31b}$$
$$\mathrm{Nu_{vol}}(t) \equiv \langle\mathrm{Nu_y}\rangle_y \tag{2.31c}$$

Other global quantities are useful to characterize at each time the instantaneous state of the system and can be shown to have a direct relation to the Nusselt number.

2.2.3 Mechanical energy: global kinetic and total potential energies

Consider the instantaneous global kinetic and total potential energies

$$\mathrm{E_k}(t) \equiv \frac{1}{2}\langle u_i u_i\rangle_{\mathrm{xyz}}$$
$$\mathrm{E_p}(t) \equiv -\mathrm{Pr}\langle y\theta\rangle_{\mathrm{xyz}}$$

This latter quantifies the amount of energy that is required to bring all fluid parcels against gravity from their position at time t to the reference level $y = 0$. However, one can introduce a more pertinent instantaneous quantity, namely the *available potential energy* (see for instance Winters et al., 1995; Sutherland, 2010) and the notion of a *background* state of minimal potential energy.

2.2.4 Available and background potential energies

Given a state at time t, the background state associated refers to the temperature field obtained by rearranging inside the fluid domain, the fluid particles in order to decrease as much as possible the global potential energy $\mathrm{E_p}(t)$. It is easy to understand that
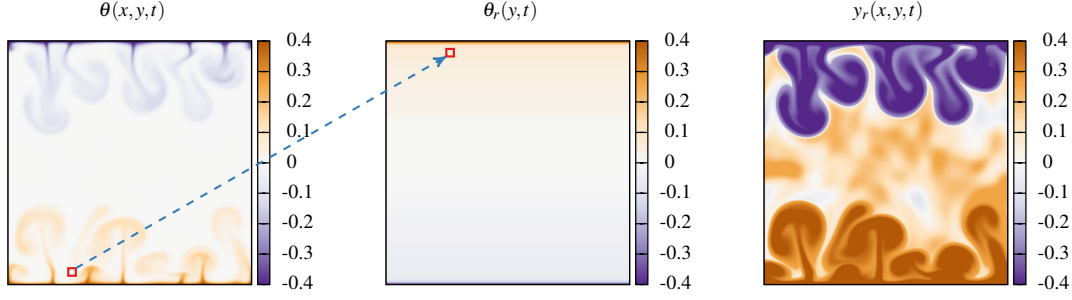
Figure 2.2: Temperature field $\theta(x, y, t)$, corresponding temperature field $\theta_r(y, t)$ at the reference state and height $y_r(x, y, t)$ for a square RB cell. Reference state is obtained by rearranging the fluid into a stable stratified configuration, see text.

the background state has no horizontal dependency and that its density decreases (i.e. temperature increases) monotonically with height. For a given time t, a fluid particle located in (x, y, z) is rearranged into the background state at $y_r(x, y, z, t)$. It is safe to assume that if the temperature field is continuous and differentiable, there exist a corresponding field $y_r(\mathbf{x}, t)$ that is also continuous and differentiable. Since rearranging occurs through virtual adiabatic processes, temperature distribution of the background state is identical to the one of the instantaneous state.

Using the above remarks, it is straightforward to get the temperature distribution $\theta_r(y, t)$ of the background state from the statistical distribution of temperature at time t. If we consider $\mathrm{P}_\theta(\widetilde{\theta})$ as the probability density function for the instantaneous temperature field and $\widetilde{\theta} \in [\theta_{\min}, \theta_{\max}]$, then $y_r(\theta)$ is evaluated as the cumulative density function.

$$y_r(\theta) - y_{\mathrm{bot}} = \int_{\theta_{\min}}^{\theta} \mathrm{P}_\theta(\widetilde{\theta}) \, \mathrm{d}\widetilde{\theta} \tag{2.32}$$

Its inverse function corresponds to the temperature distribution of the background state denoted by $\theta_r(y_r)$. The quantity $y_r(x, y, z, t)$ is obtained using the identity $\theta_r(y_r, t) = \theta(x, y, z, t)$ (see Tseng and Ferziger, (2001)). The reference height field $y_r(\mathbf{x}, t)$ illustrates the spatial dependence of the temperature field (figure 2.2).

The background potential energy $\mathrm{E_b}$ is defined as the potential energy of the background reference state

$$\mathrm{E_b}(t) \equiv -\mathrm{Pr}\langle y_r \theta \rangle_{\mathrm{xyz}}$$

while the change in potential energy between the instantaneous state $\mathrm{E_p}$ and its background companion $\mathrm{E_b}$ is defined as the available potential energy $\mathrm{E_a}$

$$\mathrm{E_a}(t) \equiv \mathrm{E_p}(t) - \mathrm{E_b}(t) = -\mathrm{Pr}\langle (y - y_r)\theta \rangle_{\mathrm{xyz}}$$

which represents the part of the potential energy which can be effectively transformed into motion (Lorenz, 1955; Winters et al., 1995).

2.2.5 Energy pathways or energy conversion rates

The energy exchange process may be better grasped by considering the evolution of the mechanical energy and the available potential energy through the following exact relations (see Winters et al., (1995) and Hughes et al., (2013)).

Conversion rates for the global kinetic energy

If we multiply by $\mathbf{u}$ the momentum equation and average over the fluid volume V, we obtain the following relation for the conversion rate of E_k

$$
\frac{\mathrm{d}}{\mathrm{d}t}E_k = \mathrm{PrRa}^{-0.5}\left[\underbrace{\mathrm{Ra}^{0.5}\langle\theta u_y\rangle_{\mathrm{xyz}}}_{\Phi_y} - \underbrace{2\,\langle S_{ij}S_{ij}\rangle_{\mathrm{xyz}}}_{\epsilon} + \underbrace{V^{-1}\oint u_i\partial_n u_i\,\mathrm{dS}}_{\Phi_\tau}\right] \tag{2.33}
$$

where the first bulk term corresponds to the convective vertical heat-flux Φ_y, the second bulk term corresponds to the energy conversion rate due to viscous dissipation ϵ, while the last term is a boundary term that quantifies the input of mechanical energy due to external forcing Φ_τ. If one considers the mechanical boundary conditions, from (2.33) it is straightforward to show that $\Phi_\tau = 0$ for both no-slip and stress-free boundary conditions. The viscous dissipation ϵ, is written in this general form to allow for the use of a stress-free condition in §8, expressed in terms of the velocity gradient and the vorticity field $\omega_k = \varepsilon_{kji}\partial_j u_i$ (ε_{kji} being the Levi-Civita symbol),

$$
\begin{aligned}
\epsilon(t) \equiv 2\,\langle S_{ij}S_{ij}\rangle_{\mathrm{xyz}} &= 2\,\langle\partial_j u_i\partial_j u_i\rangle_{\mathrm{xyz}} - \langle\omega_k\omega_k\rangle_{\mathrm{xyz}} \\
&= \langle\partial_j u_i\partial_j u_i\rangle_{\mathrm{xyz}} - \langle\partial_j u_i\partial_i u_j\rangle_{\mathrm{xyz}} \\
&= \langle\partial_j u_i\partial_j u_i\rangle_{\mathrm{xyz}} - V^{-1}\oint u_i\partial_i u_n\,\mathrm{dS}
\end{aligned} \tag{2.34}
$$

From (2.34) it is possible to show for no-slip boundary conditions

$$
\epsilon(t) = \langle\partial_j u_i\partial_j u_i\rangle_{\mathrm{xyz}} \tag{2.35}
$$

From equation (2.31c) it is easily found that $\mathrm{Nu}_{\mathrm{vol}} = (\Phi_y + 1)$. In this way, it is possible to write $\frac{\mathrm{d}}{\mathrm{d}t}E_k$ in terms of the instantaneous volume Nusselt number $\mathrm{Nu}_{\mathrm{vol}}$ as

$$
\frac{\mathrm{d}}{\mathrm{d}t}E_k = \mathrm{PrRa}^{-0.5}\left(\mathrm{Nu}_{\mathrm{vol}} - (\epsilon + 1)\right) \tag{2.36}
$$

Conversion rates for the total potential energy

If we multiply by y the temperature equation and average over the fluid volume, we obtain the following relation for the conversion rate of E_p

$$
\frac{\mathrm{d}}{\mathrm{d}t}E_p = -\mathrm{PrRa}^{-0.5}\left[\underbrace{\mathrm{Ra}^{0.5}\langle\theta u_y\rangle_{\mathrm{xyz}} - \langle\partial_y\theta\rangle_{\mathrm{xyz}}}_{\mathrm{Nu}_{\mathrm{vol}}=\Phi_y+1} + \underbrace{V^{-1}\oint y\partial_n\theta\,\mathrm{dS}}_{-\Phi_{b1}}\right] \tag{2.37}
$$

which contains the volume averaged Nusselt Nu_{vol}, and a boundary term Φ_{b1} which quantifies the energy conversion rate from external sources to E_{p}. For the present geometry and considering adiabatic side-walls, from equation (2.30) one easily verifies that $\Phi_{\text{b1}} = \frac{1}{2}(\text{Nu}_{\text{bot}} + \text{Nu}_{\text{top}})$ and obtain a relation between Nu_{bot}, Nu_{top}, and Nu_{vol}

$$\frac{\text{d}}{\text{dt}}\text{E}_{\text{p}} = \text{PrRa}^{-0.5}\left[-\text{Nu}_{\text{vol}} + \frac{1}{2}(\text{Nu}_{\text{bot}} + \text{Nu}_{\text{top}})\right] \tag{2.38}$$

Conversion rates for the background potential energy

If we multiply by y_r the temperature equation and average over the fluid volume, we obtain the following relation for the conversion rate of E_{b}

$$\frac{\text{d}}{\text{dt}}\text{E}_{\text{b}} = -\text{Pr}\langle y_r \partial_t \theta \rangle_{\text{xyz}} - \text{Pr}\langle \theta \partial_t y_r \rangle_{\text{xyz}} \tag{2.39}$$

Where the second term in the right hand side vanishes when integrated over the fluid domain (see corresponding demonstration on the appendix D.1). Introducing the dynamical equation for the temperature (2.22) leaves

$$\frac{\text{d}}{\text{dt}}\text{E}_{\text{b}} = \text{Pr}\langle y_r \partial_j (u_j \theta) \rangle_{\text{xyz}} - \text{PrRa}^{-0.5}\langle y_r \partial_j \partial_j \theta \rangle_{\text{xyz}} \tag{2.40}$$

Based on the spatial dependence of y_r on $\theta(\mathbf{x}, t)$, Winters et al., 1995 defines an auxiliary function Ψ such that $\partial_j \Psi = y_r \partial_j \theta$. Introducing this expression and making use of Green's first identity on the second term in equation (2.40) gives

$$\frac{\text{d}}{\text{dt}}\text{E}_{\text{b}} = V^{-1}\text{Pr}\oint_S u_n \Psi \, \text{dS} + \text{PrRa}^{-0.5}\langle \partial_j y_r \partial_j \theta - \partial_j (y_r \partial_j \theta) \rangle_{\text{xyz}} \tag{2.41}$$

For a closed system, i.e. $u_n = 0$ on all boundaries, leaves the following expression

$$\frac{\text{d}}{\text{dt}}\text{E}_{\text{b}} = \text{PrRa}^{-0.5}\left[\underbrace{\langle \partial_j y_r \partial_j \theta \rangle_{\text{xyz}}}_{\Phi_{\text{d}}} - \underbrace{V^{-1}\oint (y_r \partial_n \theta) \, \text{dS}}_{\Phi_{\text{b2}}}\right] \tag{2.42}$$

where the bulk term Φ_{d} quantifies the energy conversion rate due to diapycnal mixing and Φ_{b2} measures the conversion rate from external sources to E_{b}. Since iso-thermal conditions are imposed on the top and bottom walls, $y_r(x, -0.5, z, t) = 0.5$ and $y_r(x, 0.5, z, t) = -0.5$, and due to the adiabaticity of side-walls, one obtains that $\Phi_{\text{b1}} = \Phi_{\text{b2}} = \frac{1}{2}(\text{Nu}_{\text{bot}} + \text{Nu}_{\text{top}})$.

The diapycnal mixing can also be written as

$$\Phi_{\text{d}} \equiv \langle \frac{\partial y_r}{\partial \theta} \partial_j \theta \partial_j \theta \rangle_{\text{xyz}} \tag{2.43}$$

Since by definition $\frac{\partial y_r}{\partial \theta} > 0$, the mixing term Φ_{d} is bound to be positive.

Conversion rates for the available potential energy

Finally, by substracting equation (2.38) by equation (2.42) one gets

$$\frac{\mathrm{d}}{\mathrm{d}t}\mathrm{E_a} = \mathrm{PrRa}^{-0.5}(\Phi_{\mathrm{b1}} + \Phi_{\mathrm{b2}} - \mathrm{Nu_{vol}} - \Phi_{\mathrm{d}}) \qquad (2.44)$$

Since iso-thermal conditions are imposed on the top and bottom walls, one may prefer to write $\frac{\mathrm{d}}{\mathrm{d}t}\mathrm{E_a}$ as function of the instantaneous Nusselt numbers instead.

$$\frac{\mathrm{d}}{\mathrm{d}t}\mathrm{E_a} = \mathrm{PrRa}^{-0.5}(\mathrm{Nu_{top}} + \mathrm{Nu_{top}} - \mathrm{Nu_{vol}} - \Phi_{\mathrm{d}}) \qquad (2.45)$$

2.2.6 Global Temperature fluctuations

Consider the dimensionless form of the global temperature fluctuations around the reduced temperature $\theta = 0$,

$$\mathrm{E_\theta}(t) \equiv \frac{1}{2}\langle\theta^2\rangle_{\mathrm{xyz}} \qquad (2.46)$$

The temperature fluctuation $\mathrm{E_\theta}$ is not an energy *per se*. However, we have decided to show it here since we follow the same process and resulting terms are alike to those obtained for the potential energy.

If we multiply the temperature equation by θ and integrate over the fluid volume, the rate of change $\frac{\mathrm{d}}{\mathrm{d}t}\mathrm{E_\theta}$ is shown to verify the following relation,

$$\frac{\mathrm{d}}{\mathrm{d}t}\mathrm{E_\theta} = -\mathrm{Ra}^{-0.5}\left[\underbrace{\langle\partial_j\theta\partial_j\theta\rangle_{\mathrm{xyz}}}_{\epsilon_\theta} - \underbrace{V^{-1}\oint \theta\partial_n\theta \,\mathrm{dS}}_{\Phi_{\mathrm{b3}}}\right] \qquad (2.47)$$

where the bulk term $\epsilon_\theta > 0$ corresponds to the global thermal dissipation rate and a boundary term Φ_{b3} provides the conversion rate from external sources to $\mathrm{E_\theta}$. Since iso-thermal conditions are imposed on the top and bottom walls, $\theta(x, 0.5, z, t) = -0.5$ and $\theta(x, -0.5, z, t) = 0.5$, and due to the adiabaticity of side-walls, it becomes clear that $\Phi_{\mathrm{b1}} = \Phi_{\mathrm{b2}} = \Phi_{\mathrm{b3}} = \frac{1}{2}(\mathrm{Nu_{bot}} + \mathrm{Nu_{top}})$.

2.2.7 Exact relations to the Nusselt number

We evaluate the time-averaged Nusselt numbers from equation (2.30) and (2.31c)

$$\overline{\mathrm{Nu}_{\mathrm{y}}}(y) = \mathrm{Ra}^{0.5}\langle\overline{v\theta}\rangle_{\mathrm{xz}} - \langle\overline{\partial_y\theta}\rangle_{\mathrm{xz}} \qquad (2.48)$$

$$\overline{\mathrm{Nu}_{\mathrm{vol}}} = \mathrm{Ra}^{0.5}\langle\overline{v\theta}\rangle_{\mathrm{xyz}} - \langle\overline{\partial_y\theta}\rangle_{\mathrm{xyz}} \qquad (2.49)$$

For a system with adiabatic side-walls, $\overline{\mathrm{Nu}_{\mathrm{y}}}$ has no dependence on the vertical direction y. As such one expects $\overline{\mathrm{Nu}} = \overline{\mathrm{Nu}_{\mathrm{vol}}} = \overline{\mathrm{Nu}_{\mathrm{bot}}} = \overline{\mathrm{Nu}_{\mathrm{top}}}$.

Since temperature and velocity remain bounded, the time-averaged values of conversion rates for E_k, E_p, E_b, and E_a must be zero (Hughes et al., 2013). This is also true for the rate of change for E_θ. Averaging equations 2.36, 2.42, and 2.47, one has

$$\text{from } \overline{\frac{\mathrm{d}}{\mathrm{dt}}E_k} = 0 : \qquad \overline{\mathrm{Nu}} = \overline{\mathrm{Nu}_\epsilon} \qquad \text{where} \qquad \overline{\mathrm{Nu}_\epsilon} \equiv (\bar{\epsilon} + 1) \qquad (2.50)$$

$$\text{from } \overline{\frac{\mathrm{d}}{\mathrm{dt}}E_b} = 0 : \qquad \overline{\mathrm{Nu}} = \overline{\mathrm{Nu}_d} \qquad \text{where} \qquad \overline{\mathrm{Nu}_d} \equiv \overline{\Phi_d} \qquad (2.51)$$

$$\text{from } \overline{\frac{\mathrm{d}}{\mathrm{dt}}E_\theta} = 0 : \qquad \overline{\mathrm{Nu}} = \overline{\mathrm{Nu}_\theta} \qquad \text{where} \qquad \overline{\mathrm{Nu}_\theta} \equiv \overline{\epsilon_\theta} \qquad (2.52)$$

All these quantities should be equal as shown by Shraiman and Siggia, 1990 and Hughes et al., 2013. These relations are valid for all of the configurations considered in this work.

2.3 Analysis of global quantities related to vorticity in 2-D

For the study of two-dimensional flows, the flow structure is characterized in term of different global functions of the vorticity. For a **two-dimensional** configuration $\mathbf{x} \in \mathbb{R}^2$, vorticity has only one component perpendicular to the plane (xy), $\boldsymbol{\omega} = \omega \mathbf{e}_z$. The first global quantity is the mean vorticity

$$C \equiv \langle \omega \rangle_{\mathrm{xy}} \qquad (2.53)$$

which is always zero for no-slip boundary conditions, but is non vanishing for the free-surface.

A second quantity is the global angular impulse L_{2D}

$$L_{2D} \equiv -\frac{1}{2} \langle |\mathbf{x}|^2 \omega \rangle_{\mathrm{xy}} \qquad (2.54)$$

This quantity provides a measure of the organized motion around the center of a cavity. The flow dynamics and the time evolution of L_{2D}, may be better understood through some exact relations developed in the study of self-organization in 2-D turbulent flows (Molenaar et al., 2004; Van Heijst et al., 2006). The rate-of-change for L_{2D} may be written as follows

$$\frac{\mathrm{d}}{\mathrm{dt}}L_{2D} = \mathrm{PrRa}^{-0.5}I + \frac{1}{\Gamma_{\mathrm{x}}}II + \mathrm{PrM} \qquad (2.55a)$$

with I, II, and M given as

$$I = \oint \left(r_n \omega - \frac{1}{2} r_k r_k \partial_n \omega \right) \mathrm{ds} - 2C \qquad (2.55b)$$

$$II = \oint \frac{1}{2}(u_i u_i)(n_x y - n_y x) \, \mathrm{ds} \qquad (2.55c)$$

$$M = -\frac{1}{2} \langle r_k r_k \partial_x \theta \rangle_{\mathrm{vol}} \qquad (2.55d)$$

with ds being an infinitesimal element of the boundary and the loop integral is **counter-clockwise**. The derivation process of (2.55a) is presented on the appendix E. Observe, that imposing **no-slip** boundary conditions gives in return the same expressions from

Molenaar et al., 2004. The bulk term M (boundary term resp. II) corresponds to the contributions from the external thermal (resp. mechanical) forcing to L_{2D}, and can be seen as a form of external torque. However, it is difficult to provide an interpretation for I, other than being a viscous response of the system to the external torque.

2.4 Analysis of spatial structure of the flow: thermal and kinetic boundary layers

The thermal and kinetic boundary layers have a primordial role on the efficiency of heat transport and on different statistical properties. Near the top and bottom plates we define thermal (resp. kinetic) boundary layers of thickness δ_θ (resp. δ_p). A kinetic boundary layer of thickness δ_w may be also defined along the side-walls. In this section we present different estimates of the boundary layer thicknesses.

2.4.1 Thickness of the thermal boundary layers

i.) Based on the Nusselt number. We suppose that the temperature gradient is concentrated at the top and bottom boundary layers of constant thickness δ_θ, and the center region, called the bulk of almost constant temperature $\frac{1}{2}(\theta_{top} + \theta_{bot})$. As a consequence

$$\delta_\theta \approx 1/(2\overline{\mathrm{Nu}}) \tag{2.56}$$

provides an estimate of the boundary layer thickness by supposing a top-bottom symmetry.

ii.) Based on the root mean squared temperature profile. One alternative considers the fluctuations of the temperature field to characterize the average thickness of the thermal boundary layer. A local thickness may be derived from the temperature temporal fluctuations $\sigma(\theta(\mathbf{x}, t))$, as done for instance in (Wang, J. and Xia, K.-Q., 2003). Another estimate of the average thickness is obtained from the distance of the closest peak in the spatio-temporal fluctuations $\langle\theta\rangle_{xz}^{\overline{\mathrm{rms}}}$ to the top and bottom plates, as done for instance in (Kerr, 1996; S. Wagner, and Shishkina, 2013). *We use the latter estimate except when specified otherwise.*

iii.) Based on the thermal dissipation profile. The use of thermal dissipation layer based on the spatial distribution of the thermal dissipation rate has been proposed (Petschel, Stellmach, et al., 2013). The boundary layer thickness is estimated by the closest distance from the top and bottom plates to the vertical position where $\langle\overline{(\partial_j\theta)(\partial_j\theta)}\rangle_{xz}(y) = \overline{\mathrm{Nu}}$.

2.4.2 Thickness of the kinetic boundary layers at bottom and top plates

i.) Based on the root mean squared horizontal velocity profile. One alternative considers the spatio-temporal fluctuations of the horizontal velocity component to characterize the kinetic boundary layer at the plates, for instance see (Kerr, 1996). The

average thickness is estimated from the closest distance from the top and bottom plates to the peak in $\langle u \rangle_{\mathrm{xz}}^{\overline{\mathrm{rms}}}$. However, this definition supposes to the presence of a rigid boundary surface. *In the following, we use this estimate except when specified otherwise.*

ii.) Based on the viscous dissipation profile. The spatial distribution of the viscous dissipation rate has been proposed (Petschel, Stellmach, et al., 2013) as an alternative to the fluctuation profiles. In this case, the boundary layer thickness is estimated by the closest distance from the top and bottom plates to the vertical position where $\langle \overline{\partial_j u_i \partial_j u_i} \rangle_{\mathrm{xz}}(y) = \overline{\mathrm{Nu}} - 1$.

In the 3-D cases, we prefer to use a slightly different definition: instead of the transversal average, we use a definition based on the median plane $z = 0$, i.e. the thickness is based on the closest distance between the position where $\langle \overline{\partial_j u_i \partial_j u_i} \rangle_{\mathrm{x}}(z = 0) = (\overline{\mathrm{Nu}} - 1)$ to the top and bottom plates. The median plane $z = 0$ is chosen in order to avoid as much as possible the influence of the side-walls.

In the 2-D cases, in chapters §4 to §6 we use $\langle \overline{\partial_j u_i \partial_j u_i} \rangle_{\mathrm{x}}(y) = \overline{\mathrm{Nu}} - 1$.

2.5 Analysis of spatial structure of the flow: Half-range Fourier decomposition

A simplified representation of the large-scale flow by projecting into Fourier modes has been used extensively in configurations such as 2-D cells (Chandra and Verma, 2011) and cylindrical cells (Xi and Xia, 2008). Ideally, the basis for such projection should verify the boundary conditions and respect the natural symmetries of the targeted system. Furthermore, selecting the relevant modes requires a great deal of knowledge of system. For simplicity, let us consider a square (2-D) cell with isothermal top and bottom walls. If we consider the cell to be centered around $(x = 0, y = 0)$, the following symmetries are identified (Podvin and Sergent, 2015):

i. A reflexion symmetry with respect to the vertical axis, $\mathbb{S}_{\mathrm{x}}$

$$\begin{bmatrix} u \\ v \\ \theta \end{bmatrix}(x, y) \rightarrow \begin{bmatrix} -u \\ v \\ \theta \end{bmatrix}(-x, y) \tag{2.57}$$

ii. A reflexion symmetry with respect to the horizontal axis, $\mathbb{S}_{\mathrm{y}}$

$$\begin{bmatrix} u \\ v \\ \theta \end{bmatrix}(x, y) \rightarrow \begin{bmatrix} u \\ -v \\ -\theta \end{bmatrix}(x, -y) \tag{2.58}$$

iii. A rotation of origin of the cell center, $\mathrm{R}_\pi = \mathbb{S}_{\mathrm{x}} \odot \mathbb{S}_{\mathrm{y}}$

In order to observe the spatial dependence of the temperature and velocity field, (Das et al., 2000) proposed fields to be projected into modes describing rolls. This decomposition
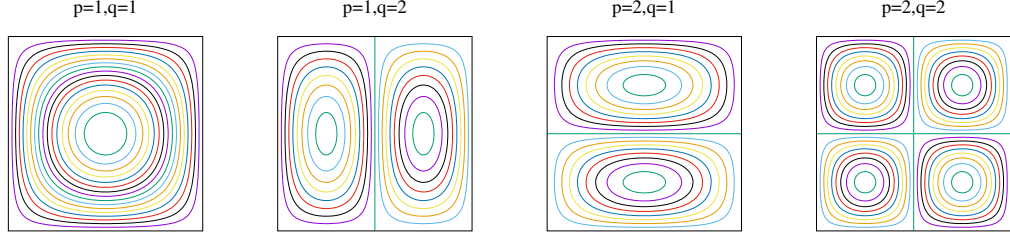
Figure 2.3: Schematic representation of the first modal forms in the plane xy presented by (Das et al., 2000).

was initially proposed in the context of stress-free isothermal boundaries and periodic side-walls. This projection has been used extensively by (Chandra and Verma, 2011; Chandra and Verma, 2013) in the study reversals in a 2-D Rayleigh-Bénard cell. The primitive fields are expressed as a half-Fourier series in the plane (x, y)

$$u(x, y, t) = \sum_{p,q \geq 1} \widetilde{u}_{pq}(t) \sin(p\pi x) \cos(q\pi y) \tag{2.59a}$$

$$v(x, y, t) = \sum_{p,q \geq 1} \widetilde{v}_{pq}(t) \cos(p\pi x) \sin(q\pi y) \tag{2.59b}$$

$$\Theta(x, y, t) = \sum_{p,q \geq 1} \widetilde{\Theta}_{pq}(t) \cos(p\pi x) \sin(q\pi y) \tag{2.59c}$$

where $\Theta(x, y, t) \equiv \theta(x, y, t) + y$ is the (dimensionless) temperature deviation from the conduction state such that $\Theta = 0$ on the top and bottom plates. The series coefficients are obtained using the discrete sine and discrete cosine transform as required. A schematic representation of the first couple modes in both directions is shown in figure 2.3. While this decomposition verifies the symmetries of the system, but does not satisfy the no-slip boundary conditions.

Chandra and Verma, 2011; Chandra and Verma, 2013 sought to explore the relation between selected Fourier modes inside a regime of consecutive reversals for $\mathrm{Pr} = 1$ by exploring the natural symmetries of 2-D Rayleigh-Bénard cells. Each Fourier mode belongs to one of four possible groups: even-even (E), odd-odd (O), even-odd (M_{eo}), and odd-even (M_{oe}). The quadratic non-linear interaction between two such modes results on a mode with a particular symmetry. More precisely, they respect the following rules:

$\otimes$	O	E	M_{eo}	M_{oe}
O	E	O	M_{oe}	M_{eo}
E		E	M_{eo}	M_{oe}
M_{eo}			E	O
M_{oe}				E

Table 2.1: Symmetric matrix summarizing the quadratic non-linear interaction between even-even (E), odd-odd (O), even-odd (M_{eo}), and odd-even (M_{oe}) modes.

For instance $O \otimes O = E$ means that non-linear interaction between two odd modes results in an even mode.

Because of the above, the following symmetry operators

$$
\begin{aligned}
i) && E \to E, && O \to -O, && M_{eo} \to M_{eo}, && M_{oe} \to -M_{oe} \\
ii) && E \to E, && O \to -O, && M_{eo} \to -M_{eo}, && M_{oe} \to M_{oe} \\
iii) && E \to E, && O \to O, && M_{eo} \to -M_{eo}, && M_{oe} \to -M_{oe}
\end{aligned}
$$

leave the Boussinesq equations in the Fourier space invariant (Chandra and Verma, 2013; Verma et al., 2015). As a result, if a set of modes $\{E, O, M_{eo}, M_{oe}\}$ is a solution of the Boussinesq equations, then $\{E, -O, M_{eo}, -M_{oe}\}$, $\{E, -O, -M_{eo}, M_{oe}\}$, and $\{E, O, -M_{eo}, -M_{oe}\}$ are also a solution of these equations. Additional symmetry operators may be defined by considering fluctuating modes with zero mean (Verma et al., 2015).

In this sense, if we have a configuration that exhibits a flow reversal. Then, the flow structure observed after the reversal, is similar to the one obtained if one applies these symmetry operators to the structure observed before the reversal. This line of reasoning becomes particularly useful to identify the modes that play an active role during the re-organization and reorientations of the large-scale flows.

2.6 Analysis of spatial structure of the flow: Proper orthogonal decomposition (POD)

The proper orthogonal decomposition (POD) is a procedure for extracting an optimal basis of decomposition from a data set $\psi(\mathbf{x}, t)$ (see for instance Berkooz et al., 1993; Podvin, 2001; Holmes et al., 2012). A given field $\psi(\mathbf{x}, t)$ is expanded in a set of orthonormal functions ϕ_k which satisfy the boundary conditions. We define a coherent structure by a function ϕ that maximizes the energy content

$$
\overline{\langle \phi | \psi \rangle^2} / \langle \phi | \phi \rangle \tag{2.60}
$$

where the operator $\langle \cdot | \cdot \rangle$ corresponds to the complex inner product operator, defined in $\mathbb{R}^2$ (resp. $\mathbb{R}^3$) as $\langle a | b \rangle = \int (a^* b) \mathrm{dxdy}$ (resp. $\langle a | b \rangle = \int (a^* b) \mathrm{dxdydz}$) where a^* indicates the complex conjugate of a. It is shown, that this implies that ϕ is an eigenfunction of the symmetric two-point correlation tensor $\mathbf{R}(\mathbf{x}, \mathbf{y}) = \overline{\psi(\mathbf{x}, t) \psi(\mathbf{y}, t)}$

$$
\int \mathbf{R}(\mathbf{x}, \mathbf{y}) \phi(\mathbf{y}) \mathrm{d}\mathbf{y} = \lambda \phi(\mathbf{x}) \tag{2.61}
$$

The Hilbert-Schmidt theory implies there exists not one, but a denumerable infinity of solutions, or empirical eigenfunctions ϕ_k, which compose an orthonormal basis, i.e. $\langle \phi_j | \phi_k \rangle = \delta_{jk}$.

The modal decomposition of $\psi(\mathbf{x}, t)$ into the empirical base functions ϕ_k reads as

$$
\psi(\mathbf{x}, t) = \sum_{k=1}^{\infty} \alpha_k(t) \phi_k(\mathbf{x}) \tag{2.62}
$$

26

where the corresponding modal coefficients α_k

$$\alpha_k(t) = \langle \psi(\mathbf{x}, t) | \phi_k(\mathbf{x}) \rangle \tag{2.63}$$

are uncorrelated to each other

$$\overline{\alpha_j^* \alpha_k} = \delta_{jk} \lambda_k \tag{2.64}$$

The eigenvalue λ_k can be seen as the mean energy of the system projected on the ϕ_k-axis in the function space.

$$\lambda_k = \overline{|\langle \psi | \phi_k \rangle|^2} \tag{2.65}$$

This implies that the energy of the flow is such that

$$\langle \psi(\mathbf{x}, t) | \psi(\mathbf{x}, t) \rangle = \sum_{k=1}^{\infty} \alpha_k \alpha_k \qquad \overline{\langle \psi(\mathbf{x}, t) | \psi(\mathbf{x}, t) \rangle} = \sum_{k=1}^{\infty} \lambda_k \tag{2.66}$$

2.6.1 The snapshot method

If we consider a discretized domain of size N_x by N_y in 2D (resp. N_x by N_y by N_z in 3D), the discretized correlation tensor $R_{ij}(\mathbf{x}, \mathbf{x}')$ is of size $4N_x N_y$ for measurements in 2D (resp. $9N_x N_y N_z$ for measurements in 3D). Because of this large size, it is often not possible to obtain a direct solution of equation (2.61). An alternative may be found in the snapshot method proposed by Sirovich, 1987. This method relies on the ergodicity hypothesis to approximate the correlation tensor as follows

$$\mathbf{R}(\mathbf{x}, \mathbf{y}) = \sum_{m=1}^{M} \psi(\mathbf{x}, t_m) \psi(\mathbf{y}, t_m) \quad \text{with} \quad t_m = m\Delta t \tag{2.67}$$

for large M. The time Δt between snapshots is assumed to be sufficiently large for snapshots to be uncorrelated. Introducing hypothesis (2.67) into equation (2.61) results in a degenerate integral equation and solutions can be expressed as a linear combination of the fields $\psi(\mathbf{x}, t_m)$.

$$\phi_k(\mathbf{x}) = \sum_{m=1}^{M} \alpha_{km} \psi(\mathbf{x}, t_m) \tag{2.68}$$

where the coefficients α_{km} verify the following equation

$$K_{mn} \alpha_{kn} = \lambda_k \alpha_{km} \tag{2.69}$$

with the matrix K_{mn} defined as

$$K_{mn} = \frac{1}{M} \langle \psi(\mathbf{x}, t_m) | \psi(\mathbf{x}, t_n) \rangle \tag{2.70}$$

leaving one eigenvalue problem of size M^2 instead of $4N_x N_y$ in 2D (resp. $9N_x N_y N_z$ in 3D).

2.6.2 Different formulations of the POD for convective flows

For thermal convection, different alternative formulations of the POD can be defined. Velocity and temperature fields may be treated separately or jointly. And one may apply the POD to the complete or the fluctuating fields. Consider the following options for two-dimensional problems

$$
\psi(\mathbf{x}, t) = \begin{cases} \theta & \text{(A) Temperature formulation} \\ (u, v) & \text{(B) Velocity formulation} \\ (au, av, b\theta) & \text{(C) Joint Temperature-Velocity formulation} \end{cases} \tag{2.71}
$$

All of which are admissible. The latter is formulated with the intent of capturing the velocity/temperature coupling and commonly is used in natural convection, see for instance (Podvin and Le Quéré, 2001; Bailon-Cuba et al., 2010; Podvin and Sergent, 2015). Since both fields represent different physical quantities, for the joint-formulation we require to introduce arbitrary scale factors a and b. In our case, we use $a = b = 1$. Given the difficulty to obtain proper time-averaged fields that respect the natural symmetries of the system, we perform the POD on the complete fields.

For each case, we assemble a matrix K_{mn}

$$
K_{mn} = \begin{cases} \frac{1}{M} \int \theta_m \theta_n \mathrm{d}\mathbf{x} & \text{for formulation (A)} \\ \frac{1}{M} \int (u_m u_n + v_m v_n) \mathrm{d}\mathbf{x} & \text{for formulation (B)} \\ \frac{1}{M} \int (u_m u_n + v_m v_n + \theta_m \theta_n) \mathrm{d}\mathbf{x} & \text{for formulation (C)} \end{cases} \tag{2.72}
$$

and solve an eigenvalue problem (2.69) providing λ_k and α_{km}. One may then proceed to assemble our orthonormal functions $\phi_k(\mathbf{x})$ for each formulations. For the formulation (C), the POD analysis provides both temperature and velocity fields.

$$
(\phi_k^{(u)}, \phi_k^{(v)}, \phi_k^{(\theta)})(\mathbf{x}) = \sum_{m=1}^{M} \alpha_k(t_m)\, \psi(\mathbf{x}, t_m) \qquad \text{for formulation (C)} \tag{2.73}
$$

For formulation (A), only modes corresponding to the temperature field are obtained, i.e. $\phi_k^{(\theta)}(\mathbf{x}) = \sum_{m=1}^{M} \alpha_k(t_m)\, \theta(\mathbf{x}, t_m)$. Thereafter, the educed POD modes for the velocity field may be computed to ensure the same modal coefficient (Borée, 2003)

$$
(\phi_k^{(u)}, \phi_k^{(v)})(\mathbf{x}) = \sum_{m=1}^{M} \alpha_k(t_m)\, \mathbf{u}(\mathbf{x}, t_m) \qquad \text{for formulation (A)} \tag{2.74}
$$

For the velocity formulation (B), one obtains first $(\phi_k^{(u)}, \phi_k^{(v)}) = \sum_{m=1}^{M} \alpha_k(t_m)\, \mathbf{u}(\mathbf{x}, t_m)$, and then the educed temperature field,

$$
\phi_k^{(\theta)}(\mathbf{x}) = \sum_{m=1}^{M} \alpha_k(t_m)\, \theta(\mathbf{x}, t_m) \qquad \text{for formulation (B)} \tag{2.75}
$$

to ensure the same modal coefficient. In formulations (A) and (B), it is important to observe that orthogonality is not preserved for the educed modes.

In the following chapters, we perform the POD analysis on a relatively large dataset using an implementation of the snapshot method written in modern FORTRAN, based on an existing and freely available F77 routine (Pierce, 2003).

Chapter 3

Direct numerical simulations (DNS) of the Boussinesq equations

In this chapter, we present the numerical methodology used for the investigation of natural convection. In the first part, we provide a minimal description of the numerical method and the most distinctive features of the two numerical codes we used. In the second part, we present details of the validation process of both codes. The first test case corresponds to a differentially heated cavity (Tric et al., 2000) and allows to validate the incompressible flow solver with the buoyancy effect using no-slip conditions, adiabatic and iso-thermal boundary conditions. The second test case corresponds to a rectangular (3-D) Rayleigh-Bénard cell (S. Wagner, and Shishkina, 2013). It is mostly focused on reproducing the onset of unsteady motion as function of the aspect ratio inside a rectangular cell. We conclude with a series of performance tests, demonstrating that the Basilisk code can be run efficiently and without modification in distributed memory parallel machines.

3.1   Presentation of the numerical codes: Fusion and Basilisk

The first computing code Fusion is written in modern Fortran and was developed over the past two decades within the LIMSI. This code is specific to natural convection and solves the 3D Navier-Stokes equations under the Boussinesq approximation on Cartesian grids using a second-order accuracy scheme. The code was modified to support shared-memory parallelism through OpenMP directives. The second computing code uses an extension of the C programming language known as Basilisk C. A number of pre-defined solver blocks can be put together to solve partial differential equations on adaptive Cartesian meshes. At the time of this writing, Basilisk C supports both the shared-memory (OpenMP) and the distributed-memory (MPI) parallelism models.

By the time we began this work, Basilisk was in early development at the Institut ∂'Alembert with the intention to become the successor of Gerris (Popinet, 2003). Results from Basilisk were cross-validated against Fusion during every stage of the development process to ensure the integrity of the numerical simulations. Additional work included developing a series of post-processing tools and a parallel I/O implementation of the XDMF format (Clarke and Namburu, 2002; Clarke and Mark, 2007; XDMF Standard, 2016) which is

designed to store and organize large amounts of data, briefly introduced in at the end of this chapter.

3.1.1   Code FUSION

FUSION is a finite volume code written in FORTRAN tailored for natural convection problems under the Boussinesq approximation. Numerical solutions are obtained using a finite volume method with second-order accuracy in space and in time. The Boussinesq equations are discretized in space using a central difference approximation on a staggered grid and in time using the second-order backward Euler method. To ensure the numerical stability, the viscous terms are considered implicitly, whereas the convective terms are evaluated explicitly and approximated using an second-order Adams-Bashforth scheme. Due to the incompressibility condition and the pressure gradient involved, the velocity-pressure coupling is more complex. We use a *rotational incremental-pressure correction* scheme (see for instance Chorin, 1969; Guermond et al., 2006). In this scheme, the pressure term is treated explicitly to obtain a provisional velocity field $\mathbf{u}^*$ which may not be divergence-free. We introduce a pressure potential Π

$$\partial_i^2 \Pi = \frac{3}{2\Delta t}\partial_i u_i^* \qquad \text{with } \partial_n \Pi = 0 \text{ on the boundaries}$$

from which a correction to velocity and pressure fields may be evaluated.

The discretized equations have the following form

$$\partial_i u_i^{n+1} = 0$$

$$\frac{(3u_i^* - 4u_i^n + u_i^{n-1})}{2\Delta t} + \partial_j(2u_j^n u_i^n - u_j^{n-1} u_i^{n-1}) = -\partial_i p^n + \mathrm{PrRa}^{-0.5}\partial_j^2 u_i^* + \mathrm{Pr}\theta^{n+1}\delta_{i2}$$

$$\frac{(3\theta^{n+1} - 4\theta^n + \theta^{n-1})}{2\Delta t} + \partial_j(2u_j^n\theta^n - u_j^{n-1}\theta^{n-1}) = \mathrm{Ra}^{-0.5}\partial_j^2\theta^{n+1}$$

In this way, the problem is reduced to the solution of one 3D Helmholtz-Poisson problem for each primitive variable (u,v,w, and θ) and one Poisson problem for the pressure correction term Π.

For each of the 3-D Helmholtz-Poisson problems we use the Douglas-Rachford *Alternating Direction Implicit* (ADI) method to separate the operators into one-dimensional components and split the scheme into one sub-step for each coordinate. Consider the following model equation of the form

$$\left(1 - D\partial_j^2\right)\phi^{n+1} = Q \tag{3.2}$$

Here ϕ represents the primitive variables $\phi = \{\mathbf{u}, \theta\}$, D the corresponding diffusion coefficients $D = \{\frac{2\Delta t}{3}\mathrm{PrRa}^{-0.5}, \frac{2\Delta t}{3}\mathrm{Ra}^{-0.5}\}$, and Q the corresponding source terms. The main component the ADI method is the factorization of the right-hand side of our model equation as the product of one-dimensional operators in the following form (Ferziger and Perić, 2002).

$$\begin{aligned}\left(1 - D\partial_j^2\right)\phi^{n+1} &= \left(1 - D\partial_x^2\right)\left(1 - D\partial_y^2\right)\left(1 - D\partial_z^2\right)\phi^{n+1} \\ &\quad - D^2(\partial_x^2\partial_y^2 + \partial_x^2\partial_z^2 + \partial_y^2\partial_z^2)\phi^{n+1} + D^3\partial_x^2\partial_y^2\partial_z^2\phi^{n+1}\end{aligned} \tag{3.3}$$

By dropping $\mathcal{O}(\Delta t^2)$, i.e. D^2 and D^3 terms, we obtain the following simplified expression

$$\left(1 - D\partial_x^2\right)\left(1 - D\partial_y^2\right)\left(1 - D\partial_z^2\right)\phi^{n+1} = Q$$

Using a multi-step approach leaves a 1-D Helmholtz problem for each ADI sub-step

$$
\begin{aligned}
(1 - D\partial_x^2)\phi^{n+\frac{1}{3}} &= Q & \text{w/ BC on } \mathbf{e}_x \\
(1 - D\partial_y^2)\phi^{n+\frac{2}{3}} &= \phi^{n+\frac{1}{3}} & \text{w/ BC on } \mathbf{e}_y \\
(1 - D\partial_z^2)\phi^{n+1} &= \phi^{n+\frac{2}{3}} & \text{w/ BC on } \mathbf{e}_z
\end{aligned}
$$

We use an staggered grid arrangement (Harlow and Welch, 1965) with a central differentiation scheme (CDS) and linear interpolation for an overall second-order precision. For this arrangement one defines different type of grids. A cell centered grid for the scalar quantities, such as the temperature, pressure and density fields, and one additional grid for each velocity component. In this way, each ADI sub-step takes the form of a tridiagonal system that can be solved directly using the Thomas algorithm. The bidiagonalization algorithm is used for the Poisson problem, sometimes referred to as a fast Poisson solver (Golub et al., 1998; Strang, 2007; Shishkina, Shishkin, et al., 2009). The time step is fixed to ensure that CFL=0.5 is verified

$$\left(\frac{u}{\Delta x} + \frac{v}{\Delta y} + \frac{w}{\Delta z}\right)\Delta t \le \text{CFL} \tag{3.4}$$

where Δx, Δy, and Δy correspond to the dimensions of the control volume along the x, y, and z directions, respectively. A detailed explanation of the numerical method used in FUSION is given in the annex A.

3.1.2 Code BASILISK

Basilisk is an ensemble of solver-blocks written using an extension to the C programming language, called Basilisk C, useful to write discretization schemes in Cartesian grids (Stéphane Popinet, 2016). Instead of writing an entirely new code, existing blocks of code were combined to solve Boussinesq equations. The formulation of the Boussinesq equations uses the fractional-step method using a staggered in time discretization of the velocity and the scalar fields (see Popinet, 2003; Popinet, 2009): one supposes the velocity field to be known at time n and the scalar fields (pressure, temperature, density) to be known at time $n-1/2$, and one computes velocity at time $n+1$ and scalars at time $n+1/2$.

We use a *pressure correction* scheme (see for instance Chorin, 1969; Guermond et al., 2006) for the velocity-pressure coupling. In this scheme, the pressure term is treated explicitly to obtain a provisional velocity field $\mathbf{u}^*$ which may not be divergence-free. A correction term is obtained by projecting the provisional velocity into a divergence-free space, similar

to Fusion. The discretized equations would have the following form

$$\partial_i u_i^{n+1} = 0 \tag{3.5a}$$

$$\frac{u_i^* - u_i^n}{\Delta t} + \partial_j(u_j u_i)^{n+\frac{1}{2}} = \text{PrRa}^{-0.5}\frac{\partial_j(\partial_j u_i^* + \partial_j u_i^n)}{2} - \text{Pr}\theta^{n+\frac{1}{2}}\delta_{i2} \tag{3.5b}$$

$$u_i^{n+1} = u_i^* - \Delta t\left(\partial_i p^{n+\frac{1}{2}}\right) \tag{3.5c}$$

$$\frac{\theta^{n+\frac{1}{2}} - \theta^{n-\frac{1}{2}}}{\Delta t} + \partial_j(u_j\theta)^n = \partial_j(\text{Ra}^{-0.5}\partial_j\theta)^{n+\frac{1}{2}} \tag{3.5d}$$

Space is discretized using a Cartesian (multi-level or tree-based) grid where the variables are located at the center of each control volume (a square in 2-D, a cube in 3-D) and at the center of each control surface.

The velocity advection term $\partial_j(u_j u_i)^{n+\frac{1}{2}}$ and the temperature advection term $\partial_j(u_j\theta)^n$ are estimated by means of the Bell–Colella–Glaz second-order unsplit upwind scheme (Bell et al., 1989; Popinet, 2003). In this way, the problem is reduced to the solution of a 3D Helmholtz-Poisson problem for each primitive variable (u^*, v^*, w^*, θ) and a Poisson problem for the pressure correction terms. Both the Helmholtz-Poisson and Poisson problems are solved using an efficient multilevel Poisson solver described in (Popinet, 2003). Basilisk uses a variable time-step to ensure the CFL condition (3.4) is verified. Observe that (3.4) is a necessary condition, but does not automatically ensures the stability of the numerical method. Additional restrictions on the time-step may be required. Additional details on the numerical method used in Basilisk are given in the annex B.

3.1.3 Implementation of a parallel Input/Output (I/O) model

I would like to present some of the work done for retrieving and storing the large amount of data generated from direct numerical simulations. This work was motivated by a healthy need to store and organize large sets of data which greatly facilitates the post-processing and by a growing trend to implement standard data formats in scientific computing. To this end, we implemented the *eXtensible Data Model and Format* (see Clarke and Namburu, 2002; Clarke and Mark, 2007) for outputs produced in both Fusion and Basilisk. It is worth noting that other formats, like netCDF, are also widely used. Each one has its own set of strengths and weaknesses. We choose to use the XDMF format since the libraries required are usually available in large computing centers. The XDMF format has a low entry barrier and supports the use of hierarchical structures inside the data files. Additional features include support for a large number of objects, file compression, a parallel I/O implementation through the MPI-IO or MPI POSIX drivers. A software library that provides a high-level API with interfaces to both C and Fortran, can be usually found already installed in a large number of computing centers.

The amount of I/O operations in large scale simulations may consume an important part of the execution time. One of the most common approaches consists in sending data to a single MPI task, which is responsible of writing data into the disk. This approach is not scalable. Another option consist in writing one file per MPI task, but this implies handling large numbers of files. Our implementation of parallel I/O uses PHDF5 (Parallel HDF5) and is divided in three parts. First, the MPI tasks collectively create/open a single parallel

(a) Differentially heated cavity
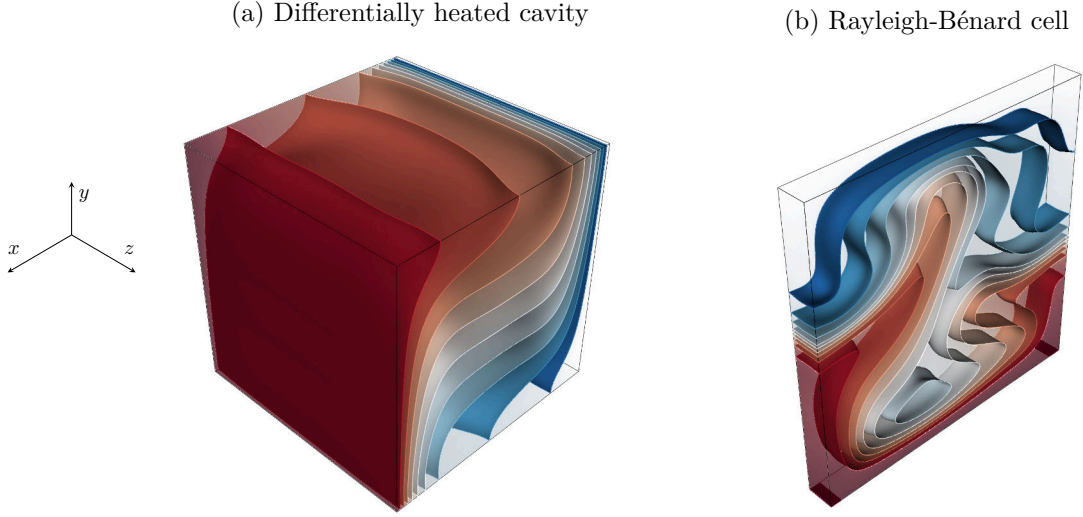
(b) Rayleigh-Bénard

Figure 3.1: Iso-contours of the temperature field corresponding to each of the test cases selected. (a) Differentially heated cavity for Ra $= 10^5$ and Pr $= 0.71$ to be compared against (Tric et al., 2000). (b) Rectangular Rayleigh-Bénard cell with aspect ratio $\Gamma_z = 1/10$ for Ra $= 10^6$ and Pr $= 0.786$ to be compared against (S. Wagner, and Shishkina, 2013).

HDF5 file and create/open groups, sub-groups and so on. Second, each MPI task is set to write a part or a *chunk* of the data into each dataset independently. Once each task has finished writing into the file, the MPI tasks collectively close the datasets, before closing the file. This strategy has been implemented on the Ada and Turing parallel computing clusters (IDRIS, 2016a; IDRIS, 2016b).

3.2 Validation of the numerical codes: case studies

In order to validate the two numerical codes we compare their results against benchmark results for two different configurations within the Boussinesq approximation.

3.2.1 Case study 1: Differentially heated cavity

The first test case is a classical problem and has become a very popular to compare the different numerical algorithms available for incompressible flows. For this test case, commonly known as a differentially heated cavity, we will study both 2-D and 3-D cavities. The fluid domain is a 2-D square (resp. 3-D square box) cavity of size 1, centered around $(0, 0)$ (resp. $(0, 0, 0)$), see figure 3.1a. We consider no-slip boundary conditions in all borders, imposed temperature in the left and right walls, $\theta(\pm 0.5, y) = \pm 0.5$ in 2-D (resp. $\theta(\pm 0.5, y, z) = \pm 0.5$ in 3-D). Adiabatic boundary conditions are imposed on all other boundaries.

The fluid is initially at rest and a linear temperature gradient is imposed in the horizontal direction. We start the simulation on a very coarse regular Cartesian grid and run until a steady-state condition is met, i.e. the maximum change in the x-velocity component over two consecutive time steps is lower than 10^{-8}. This final state is then used as an initial
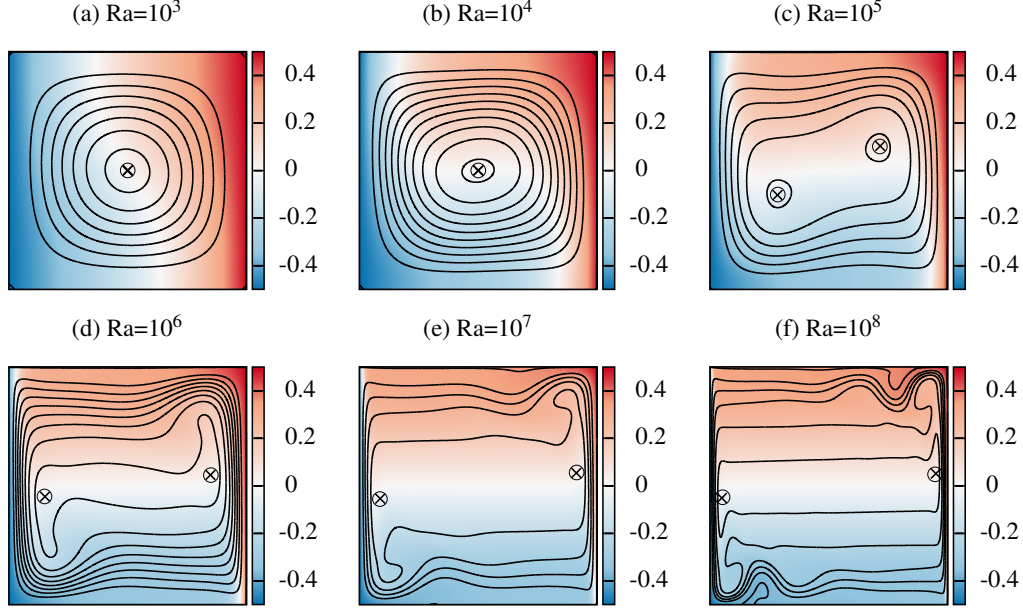
Figure 3.2: 2-D Cavity: Streamlines superposed to $\theta(\mathbf{x}, t)$ obtained using Basilisk for $\mathrm{Pr} = 0.71$ at the steady-state. Position of $\psi_{\max}$ is indicated using a $\times$ symbol and compared to the position given in the reference results (Le Quéré, 1991), displayed here as $\circ$.

condition for a finer grid size and it is run until a new steady-state is obtained. This process is repeated until convergence is reached.

The benchmark solutions used for the validation of the two-dimensional differentially heated square cavity are (De Vahl Davis, 1983; Le Quéré, 1991; Tric et al., 2000), while solutions for the three-dimensional cavity are taken from (Tric et al., 2000).

Differentially heated 2-D square cavity

Numerical results used for validation inside a square cavity can be of several kinds: different global quantities, profiles measured along a vertical or horizontal line, or local measurements. Figure 3.2 displays ψ iso-lines superposed to the temperature field $\theta(\mathbf{x}, t)$ evaluated at the steady state. These results are in agreement with figure 4 ($\mathrm{Ra} = 10^7$) and figure 6 ($\mathrm{Ra} = 10^8$) from (Le Quéré, 1991). In addition, one may compare the peak value of the stream-function $\psi_{\max}$ and its position. The placement of $\psi_{\max}$ is indicated in figure 3.2. We measure the relative error of $\psi_{\max}$

$$e^{\psi_{\max}} = \frac{\psi_{\max}^{(N)} - \psi_{\max,\mathrm{ref}}}{\psi_{\max,\mathrm{ref}}} \times 100 \tag{3.6}$$

The evolution of $e^{\psi_{\max}}$ as function of the grid spacing is displayed on figure 3.3a for $\mathrm{Ra} = 10^7$ and $\mathrm{Ra} = 10^8$. Results converge towards reference values from (Le Quéré, 1991) as we increase the grid resolution. In addition, we compare a global quantity, such as Nu. More precisely, the relative error of Nu

$$e^{\mathrm{Nu}} = \frac{\mathrm{Nu}^{(N)} - \mathrm{Nu}_{\mathrm{ref}}}{\mathrm{Nu}_{\mathrm{ref}}} \times 100 \tag{3.7}$$

(a) Convergence of ψ_{max} (b) Convergence of Nu
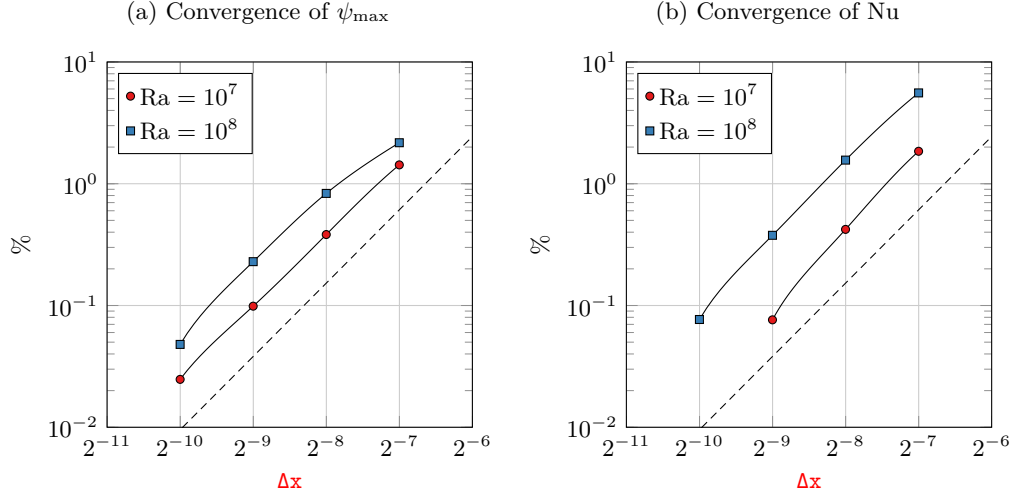
Figure 3.3: 2-D Cavity: Convergence of ψ_{max} and Nu obtained using Basilisk compared with respect to (Le Quéré, 1991) as a function of grid spacing. Dashed line correspond to ideal slope for second order scheme.

is computed as function of the grid spacing for $\mathrm{Ra} = 10^7$ and $\mathrm{Ra} = 10^8$ (see figure 3.3b). Again, results are consistent with a global second order accuracy.

Other quantities used in benchmark results include the components of velocity field evaluated along a vertical or horizontal centerline (figures 3.4a,d and 3.4b,e), or the local heat-flux evaluated in one of the iso-thermal walls (figure 3.4c,f). Figure 3.4 displays the numerical results obtained using Basilisk (figures 3.4a to 3.4c) and Fusion (figures 3.4d to 3.4f), and as well as the benchmark results from (Tric et al., 2000). Both codes are in good agreement with previous studies and with each other.

(a) $v(x,0)$ (b) $u(0,y)$ (c) $q_{\mathrm{x}}(-0.5,y)$

(d) $v(x,0)$ (e) $u(0,y)$ (f) $q_{\mathrm{x}}(-0.5,y)$
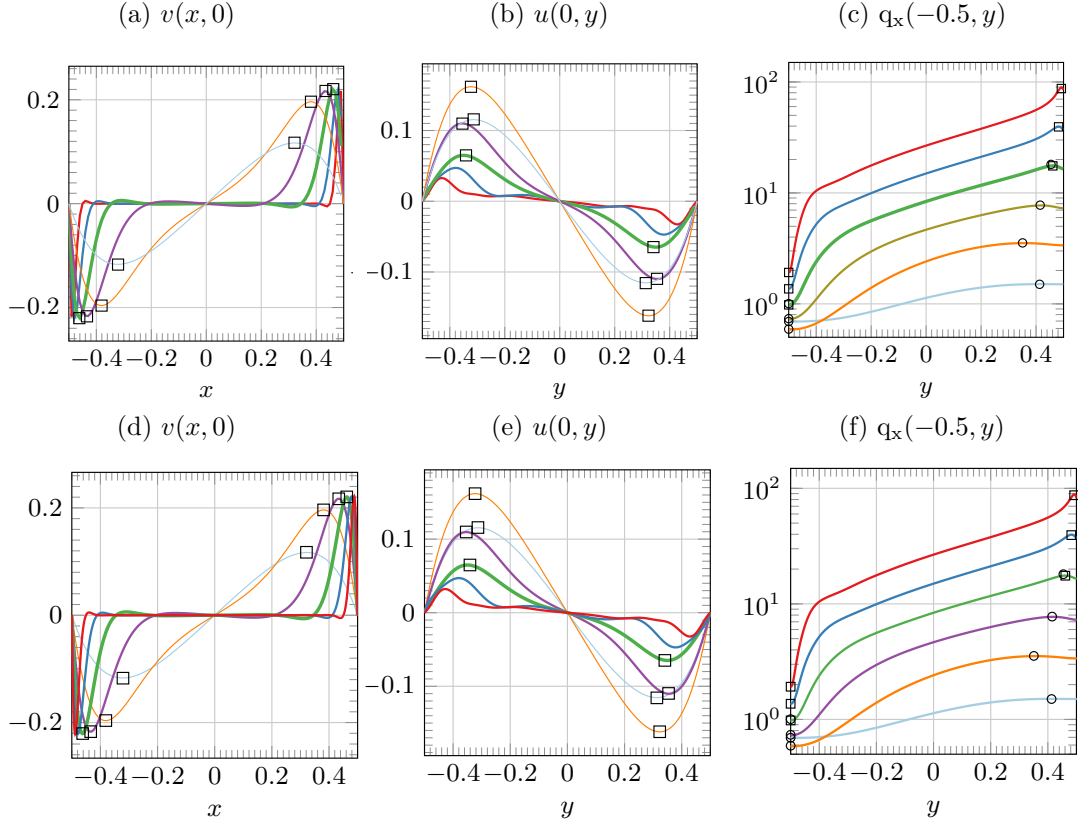
Figure 3.4: 2-D Cavity: Profiles measured at the steady state for Pr = 0.71. Lines correspond to different Ra: Ra = 10^3 ——, Ra = 10^4 ——, Ra = 10^5 ——, Ra = 10^6 ——, Ra = 10^7 ——, Ra = 10^8 ——. Marks correspond to results from (Tric et al., 2000). Figures (a,b,c) correspond to results from Basilisk. Figures (d,e,f) correspond to results from Fusion.

(a) Relative error of $\mathrm{Nu_{3D}}$ (%) (b) Relative error of $\mathrm{Nu_{mp}}$ (%)
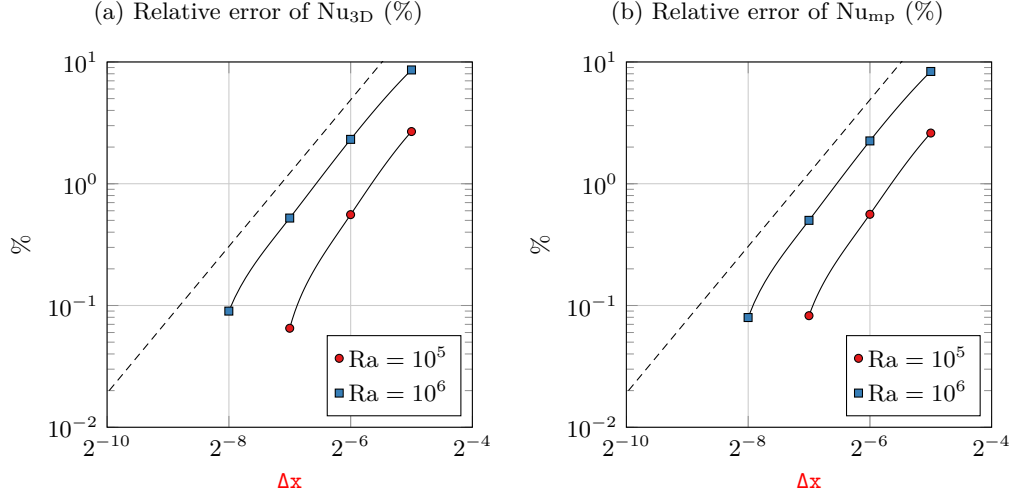
Figure 3.5: 3D Cavity (Basilisk): Convergence of $\mathrm{Nu_{3D}}$ and $\mathrm{Nu_{mp}}$ compared with respect to (Tric et al., 2000) as a function of the grid spacing. Dashed line correspond to ideal slope for a second order scheme.

Differentially heated 3-D cubic cavity

3D calculations with Fusion and Basilisk have been performed for four values $\mathrm{Ra} < 10^6$ using different grids up to 512^3, see table 3.1c. All converge into a steady-state flow, see for instance figure 3.1a. To test the convergence of Basilisk we use the following Nusselt numbers

$$\mathrm{Nu}(z) \equiv \int_{-0.5}^{0.5} \mathrm{q_x}(-0.5, y, z)\mathrm{dy} \tag{3.8}$$

$$\mathrm{Nu_{3D}} \equiv \int_{-0.5}^{0.5} \mathrm{Nu}(z)\mathrm{dz} \tag{3.9}$$

$$\mathrm{Nu_{mp}} \equiv \mathrm{Nu}(z) \qquad\qquad \text{with } z = 0 \tag{3.10}$$

Values of $\mathrm{Nu_{3D}}$ and $\mathrm{Nu_{mp}}$ display a monotonic convergence towards the reference values consistent with a second order method (figure 3.5). We are also interested in comparing the departure from bi-dimensionality of the steady-state for the different codes. More precisely, we evaluate the relative difference between these terms $(\mathrm{Nu_{2D}} - \mathrm{Nu_{3D}})/\mathrm{Nu_{2D}}$, $(\mathrm{Nu_{2D}} - \mathrm{Nu_{mp}})/\mathrm{Nu_{2D}}$, and $(\mathrm{Nu_{3D}} - \mathrm{Nu_{mp}})/\mathrm{Nu_{3D}}$ (figure 3.6), where $\mathrm{Nu_{2D}}$ is the Nusselt number obtained for a 2D square cavity. In addition to the convergence of $\mathrm{Nu_{3D}}$ and $\mathrm{Nu_{mp}}$, one may also consider the evolution of $\mathrm{Nu}(z)$ displayed on figure 3.7a. Another possibility consists in following the maximum amplitude of the velocity components measured over the vertical and horizontal centerlines: $\max{(u(0, y, 0))}$ and $\max{(w(x, 0, 0))}$. Let us consider the vertical (resp. horizontal) velocity profiles measured over the horizontal (resp. vertical) centerlines (figures 3.7b and 3.7c). This is confirmed in table 3.2, where the values of $\max{(u(x, y, z))}$, $\max{(v(x, y, z))}$, $\max{(w(x, y, z))}$ are found.

Results from both codes are in good agreement with benchmark results and with each other. In most cases, results obtained from Basilisk were found to be more accurate than Fusion for an equivalent number of grid points.

39
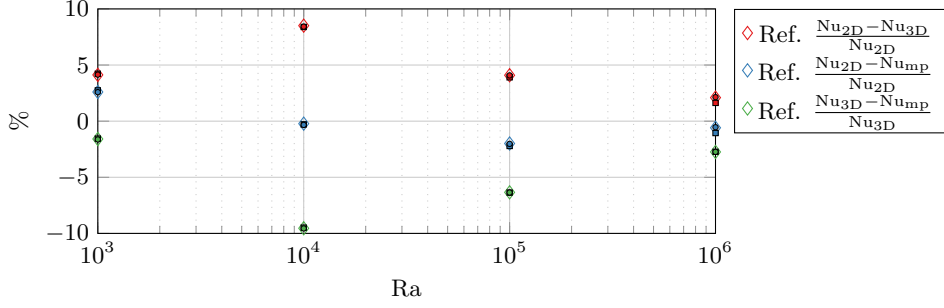
Figure 3.6: Relative heat transfer rates as a function of Ra for Pr = 0.71. Reference results from (Tric et al., 2000) shown in ◇ marks, results from Fusion shown in □ marks and results from Basilisk in ● marks. Nu_{3D} and Nu_{mp} as defined in equation (3.8), while Nu_{2D} corresponds to the Nusselt number obtained for the 2D differentially heated cavity.

(a) $Nu(z)$ (b) $w(x, 0, 0)$ (c) $u(0, y, 0)$
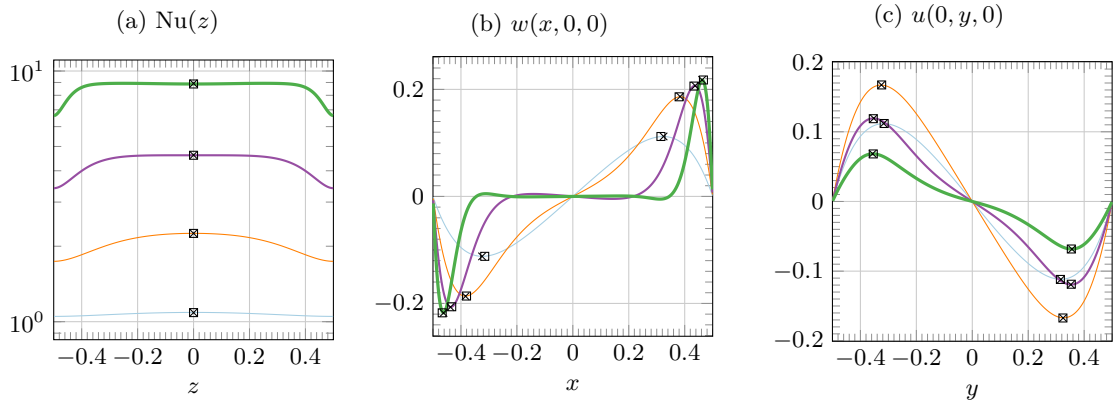
Figure 3.7: Profiles measured at the steady state for Pr = 0.71. Solid lines indicates results obtained using Basilisk, × marks indicate results obtained using Fusion and □ marks correspond to reference results from (Tric et al., 2000).
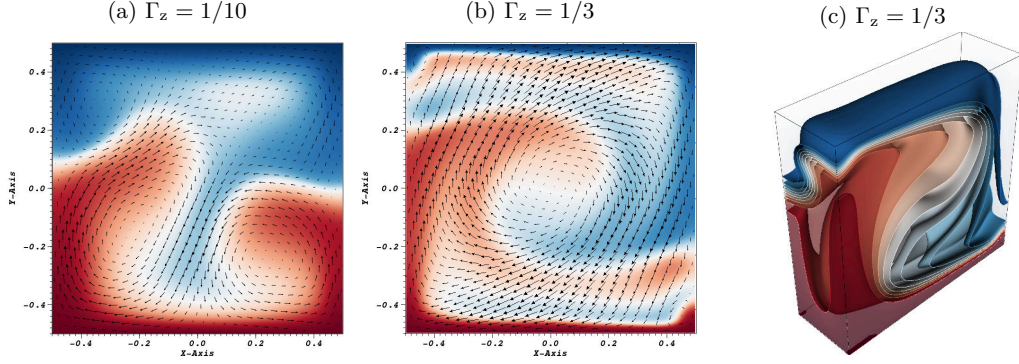
Figure 3.8: Flow structure for ($\text{Ra} = 10^6, \text{Pr} = 0.786$) with $\Gamma_z = 1/10$ and $\Gamma_z = 1/3$ using <u>Basilik</u>. Figures (a,b) display a slice at the vertical mid-plane of the instantaneous temperature field with velocity vectors. Figure (c) displays iso-thermal contours.

3.2.2 Case study 2: Rectangular Rayleigh-Bénard cells

The second test-case focuses on a rectangular Rayleigh-Bénard cell near the onset of convection[1]. The fluid domain is a box with equal height and width, while the depth is defined by the aspect ratio $\Gamma_z = d/H$ and ranges from $1/10$ to $1/3$, see figure 3.1b. We consider no-slip boundary conditions in all borders, adiabatic conditions on the side-walls and imposed temperature on the top and bottom walls $\theta(x, \pm 0.5, z) = \mp 0.5$.

The fluid is initially at rest and a linear temperature gradient is imposed in the vertical direction. To avoid waiting for the transient to end, we speed up the process as follows: we start the simulation on a very coarse regular Cartesian grid and run until statistical convergence is met (in practice, this corresponds to several hundred convective time units). The final state is then used as an initial condition for a finer grid size and it is run again with the same criteria. This process is repeated until convergence is reached, see table 3.2.

In the following, we focus only on comparing results produced using <u>Basilik</u> and benchmark results. The same test case was performed using <u>Fusion</u>, but is not presented for simplicity since there are no notable differences between the results. The benchmark solutions used for the validation are results obtained using a fourth order accurate finite volume method by (S. Wagner, and Shishkina, 2013) inside rectangular Rayleigh-Bénard cells for for ($\text{Ra} = 10^6, \text{Pr} = 0.786$) and three different aspect ratios: $\Gamma_z = 1/10$, $\Gamma_z = 1/4$, and $\Gamma_z = 1/3$. For these values of (Ra, Pr) the influence of the aspect ratio on the flow dynamics and on the Nusselt was found to be quite strong: a steady state solution is observed for $\Gamma_z = 1/4$, whereas $\Gamma_z = 1/10$ and $\Gamma_z = 1/3$, result in a unsteady flow: for $\Gamma_z = 1/10$ one obtains a type of oscillatory solution, whereas for $\Gamma_z = 1/3$ the solution is oscillatory and periodic (S. Wagner, and Shishkina, 2013).

Figures 3.8a and 3.8b display a slice taken at the vertical mid-plane of the instantaneous temperature field with the velocity vector field for $\Gamma_z = 1/10$ and $\Gamma_z = 1/3$ corresponding to unsteady-state solutions. For $\Gamma_z = 1/10$, a (quasi-)two-dimensional flow is observed. This configuration is characterized by the presence of large thermal plumes along the side-walls, and compares well with figure 11a in (S. Wagner, and Shishkina, 2013). For $\Gamma_z = 1/3$, one observes a single-roll similar to figure 11b in (S. Wagner, and Shishkina,

---

[1] We will revisit this configuration in the turbulent flow regime in chapters §7 and §8
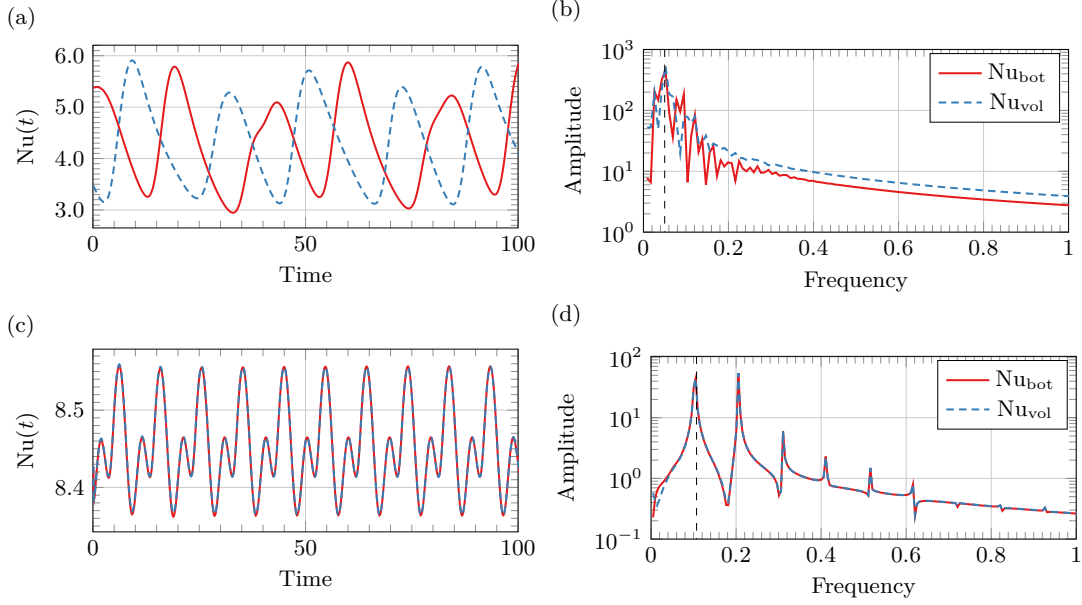
Figure 3.9: Rayleigh-Bénard convection using <u>Basilisk</u> for (Ra $= 10^6$, Pr $= 0.786$) and different aspect ratios. Top row corresponds to $\Gamma_z = 1/10$, bottom row to $\Gamma_z = 1/3$. Figures (a,c) display a time series for $\mathrm{Nu_{bot}}$ and $\mathrm{Nu_{top}}$, while (b,d) display the corresponding time-frequency spectra.

2013). In addition, a 3-D plot (figure 3.8c) illustrates the roll axis is located in the horizontal plane but twisted from the z axis. This is also consistent with (S. Wagner, and Shishkina, 2013).

A time series is displayed along with the time-frequency spectra of $\mathrm{Nu_{top}}$ and $\mathrm{Nu_{bot}}$ in figures 3.9a to 3.9d. On the one hand, for $\Gamma_z = 1/10$, the values of $\mathrm{Nu_{top}}$ and $\mathrm{Nu_{bot}}$ oscillate out-of-phase with each other but display the same dominant frequency $f = 0.1026 \pm 0.004$ compared to $f = 0.107$ reported by (S. Wagner, and Shishkina, 2013), see figure 3.9b. On the other hand, for $\Gamma_z = 1/3$ the values of $\mathrm{Nu_{top}}$ and $\mathrm{Nu_{bot}}$ oscillate in-phase with a single characteristic frequency $f = 0.0482 \pm 0.004$ compared to $f = 0.0500$ reported by (S. Wagner, and Shishkina, 2013), see figures 3.9c and 3.9d.

An alternative validation of <u>Basilisk</u> consists in verifying numerically the exact time-dependent relations between the rate-of-change of the kinetic energy $\frac{\mathrm{d}}{\mathrm{dt}}E_k$, of the potential energy $\frac{\mathrm{d}}{\mathrm{dt}}E_p$, of the available potential energy $\frac{\mathrm{d}}{\mathrm{dt}}E_a$, and the corresponding energy transfer rates (see §2)

$$
\begin{aligned}
\mathrm{Ra}^{0.5}\mathrm{Pr}^{-1}\tfrac{\mathrm{d}}{\mathrm{dt}}E_k &= \mathrm{Nu_{vol}} - (\epsilon + 1) \\
\mathrm{Ra}^{0.5}\mathrm{Pr}^{-1}\tfrac{\mathrm{d}}{\mathrm{dt}}E_p &= \tfrac{1}{2}(\mathrm{Nu_{bot}} + \mathrm{Nu_{bot}}) - \mathrm{Nu_{vol}} \\
\mathrm{Ra}^{0.5}\mathrm{Pr}^{-1}\tfrac{\mathrm{d}}{\mathrm{dt}}E_a &= \mathrm{Nu_{bot}} + \mathrm{Nu_{bot}} - \mathrm{Nu_{vol}} - \Phi_d \\
\mathrm{Ra}^{0.5}\tfrac{\mathrm{d}}{\mathrm{dt}}E_\theta &= \tfrac{1}{2}(\mathrm{Nu_{bot}} + \mathrm{Nu_{bot}}) - \epsilon_\theta
\end{aligned}
\tag{3.11}
$$

The left hand sides of equations 3.11 is approximated using a second-order finite differences approximation, see figure 3.10 for $\Gamma_z = 1/10$ and $\Gamma_z = 1/3$. Evaluating the time derivatives introduces an error function of the sampling frequency. The corresponding right hand side is evaluated using the instantaneous Nusselt numbers and the energy transfer rates and matches the left hand side satisfactorily. This agreement is useful to evaluate the adequacy of the spatial resolution. This check is similar to one proposed by R. Stevens, Verzicco,
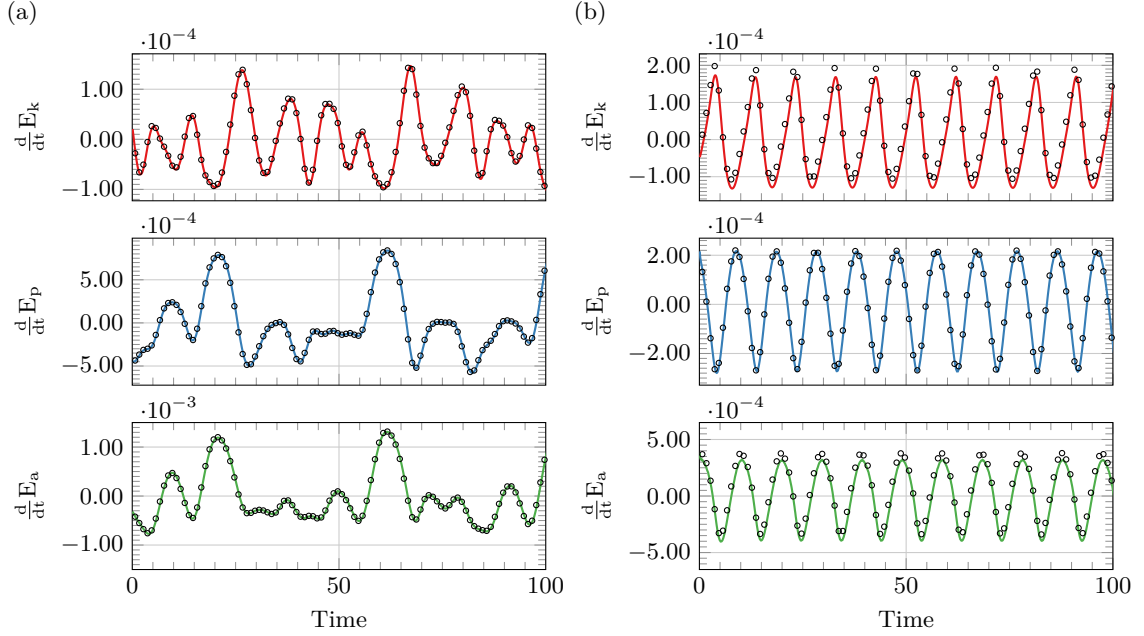
Figure 3.10: Rayleigh-Bénard convection using <u>Basilisk</u> for $(\mathrm{Ra} = 10^6, \mathrm{Pr} = 0.786)$ and two different aspect ratios: (a) $\Gamma_z = 1/10$, and (b) $\Gamma_z = 1/3$. From top to bottom: Time derivatives $\frac{d}{dt}E_k$, $\frac{d}{dt}E_p$, and $\frac{d}{dt}E_a$. Left hand sides of equations (3.11) are evaluated using finite differences (continuous lines), whereas the right hand sides are displayed in $\circ$ marks.

et al., 2010 but is based on instantaneous global quantities, not on the time-averaged ones.

We conclude the validation of both numerical codes. Both codes are consistent with a global second order method and the reference literature. In the following, we discuss a more practical aspect of the numerical simulations, regarding the time and computing resources required to perform direct numerical simulations at $\mathrm{Ra} \sim 10^7 - 10^9$. In the following we focus on the code Basilisk which is better suited for large parallel computations.

3.3 Parallel performance of the numerical codes

There are two important reasons for using a parallel computer : to have access to more memory or to obtain higher performance (Eijkhout, 2011). While the available memory is the sum of the individual memory of the machines, the performance gains or speed-up in a parallel execution are more difficult to measure due to the additional overhead (redundant, idle, and extra computation and time spent in communications). Two metrics are used to quantify the performance of the code: a *strong* scaling and a *weak* scaling. On the one hand, the *strong* scaling is defined by the evolution of the restitution time as function of the number of processors for a fixed overall problem size. Ideally, the restitution time should decrease as a linear function of the number of processors. However, distributing a sequential problem over many threads may give a distorted picture since each processor may end up with very little data. On the other hand, the *weak* scaling is defined by the evolution of the restitution time as a function of the number of processors for a fixed size per processor. Ideally, if the number of grid points and the number of processors increase proportionally, the restitution time should remain constant.
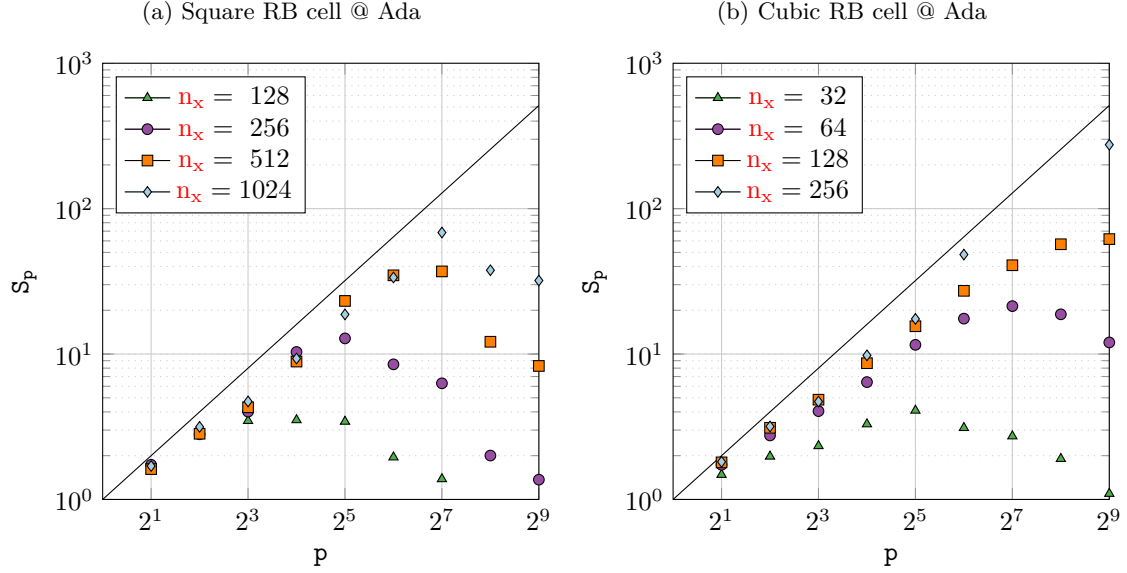
Figure 3.11: Strong scaling: Speed-up factor S_p as a function of the number of processors p for a constant grid size. Measurements correspond to a 2D (resp. 3D) RB cell for a grid of size $n_x n_y$ with $n_y = n_x$ on the left panel (resp. $n_x n_y n_z$ with $n_y = n_z = n_x$ on the right panel). Ideally, both curves should increase linearly.

Weak scaling tests were carried on two computing clusters: Ada (IDRIS, 2016a) Turing (IDRIS, 2016b), while strong scaling test were only performed on Ada. Ada has 332 compute nodes, each of four 8-cores cadenced at 2.7 GHz (Intel Sandy Bridge E5-4650 processors). Its theoretical peak processing power is 233 TFLOPS. Each node has 128 GB of memory and nodes are interconnected by a high-speed InfiniBand network. In practice, the resources are accessible for up to 2,048 execution cores. Turing (IDRIS, 2016b) has 6 racks, each containing 1,024 compute nodes of 16-core processors cadenced at 1.6GHz (IMB Power BQC 16C). Its theoretical peak processing power is 1,258 TFLOPS. In practice, resources are accessible for up to 65,536 execution cores.

The test simulation used corresponds to a 2-D square (or 3-D cubic) Rayleigh-Bénard cell from the unstable conductive state with a random perturbation. Each simulation lasts 5 convective time units, i.e. hundreds of time steps. The cpu time per time step is then obtained by averaging over the number of time steps.

Strong scaling

For the strong scaling, the two configurations, 2-D and 3-D were tested: a square Rayleigh-Bénard cell from 128^2 up to 1024^2 grid points and a cubic Rayleigh-Bénard cell from 32^2 up to 256^2 grid points. Both configurations were chosen based on the type of simulations to be performed in this thesis. We define a speed-up factor S_p, which compares the restitution time on a single processor $u.t_{mono}$ and on a parallel machine with p processors $u.t(p)$ and a parallel efficiency E as

$$S_p = \frac{u.t_{mono}}{u.t(p)} \qquad\qquad E = \frac{S_p}{p} \qquad\qquad (3.12)$$

44

(a) Cubic RB cell @ Ada (b) Cubic RB cell @ Turing
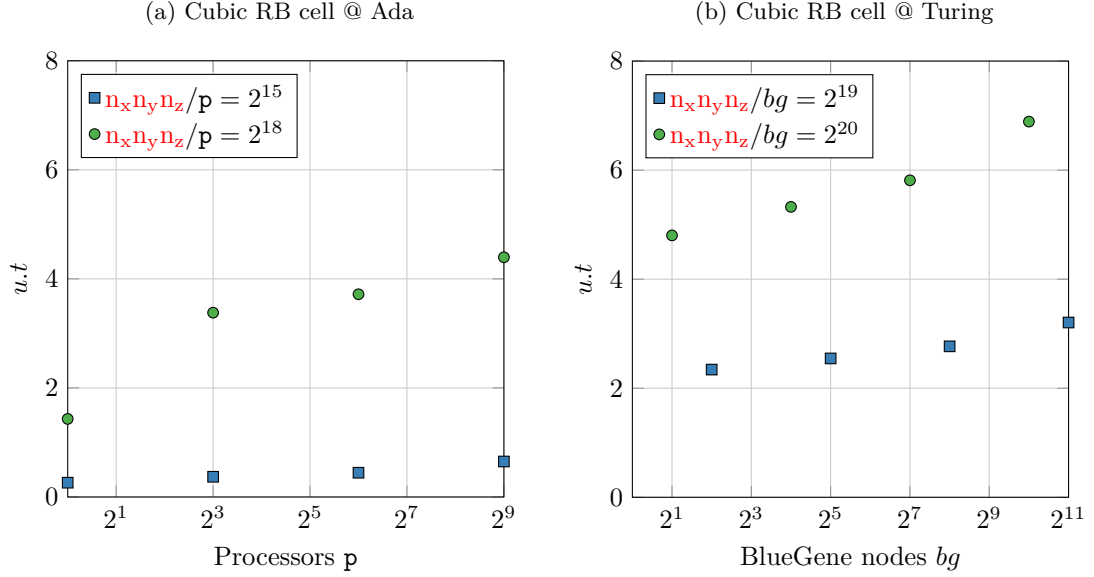
Figure 3.12: Weak scaling: (a) restitution time for a single time-step as function of the number of processors for two values of $(n_x n_y n_z/p)$; (b) restitution time for a single time-step as function of the number BlueGene compute nodes bg for two values of $(n_x n_y n_z/bg)$. Ideally, both curves should remain constant.

This approach works as long as the available memory on a single processor is large enough to solve the reference problem. The optimal value of S_p is bounded by the value of p. The speed-up factor for 2D simulations peaks at $S_p = 70$ for 128 MPI processes, i.e. $E = 0.54$ for a 1024^2 mesh, whereas for a 3D simulation one obtains a peak value $S_p = 278$, i.e. $E = 0.54$ for a 256^3 mesh when using 512 MPI processes, see figure 3.11.

Weak scaling

For the weak scaling, only the cubic Rayleigh-Bénard cells were tested. However, measurements were performed on both computing clusters, Ada and Turing. In Ada we tested different domain sizes up to 512^3 grid points and using from 1 up to 512 cores. The architecture of Turing allowed to test domain sizes up to 1024^3 grid points and using from 1 up to 2,048 BlueGene compute nodes (or alternatively from 64 up to 32,768 cores). A good overall weak scaling is achieved in both machines as seen on figure 3.12.

Additional metrics, such as the user time per time-step per grid point, $u.t/n_x n_y n_z$ are also commonly used for estimating the compute and restitution times for a given simulation - values range from 10^{-5} s/step/point for sequential execution up to $4 \cdot 10^{-8}$ s/step/point for parallel runs on Ada (512^3 points and 512 processors) and up to $3 \cdot 10^{-9}$ s/step/point for parallel runs on Turing (1024^3 points and 2,048 nodes).

These results are used to define the range of Ra values that can be explored through direct numerical simulations with the available resources and how to use efficiently said resources. The numerical simulations presented in the following chapters were performed using the HPC resources of LIMSI and GENCI-IDRIS under generous allocations made by GENCI.

Complementary material: Simulation parameters and numerical convergence

(a) Differentially-heated square cavity (2D)

	Ra	Pr	Grid	α	min Δx	max Δx
De Vahl Davis, 1983	$10^3 - 10^4$	0.71	40	-		0.025
	$10^5 - 10^6$	0.71	80	-		0.0125
Le Quéré, 1991	10^6	0.71	$N = 73$	-	$9.5 \cdot 10^{-4}$	$2.1 \cdot 10^{-2}$
	10^7	0.71	$N = 81$	-	$4.6 \cdot 10^{-4}$	$1.9 \cdot 10^{-2}$
Tric et al., 2000	$10^3 - 10^7$	0.71	$N = 51$	-	$3.8 \cdot 10^{-4}$	$3.1 \cdot 10^{-2}$
Fusion	$10^3 - 10^8$	0.71	128^2	-		$7.9 \cdot 10^{-3}$
			256^2	-		$3.9 \cdot 10^{-3}$
			512^2	-		$2 \cdot 10^{-3}$
	10^8		768^2	-		$1.3 \cdot 10^{-3}$
Basilisk	$10^3 - 10^8$	0.71	128^2	-		$7.8 \cdot 10^{-3}$
			256^2	-		$3.9 \cdot 10^{-3}$
			512^2	-		$2 \cdot 10^{-3}$
			1024^2	-		$9.8 \cdot 10^{-4}$

(b) Differentially-heated cubic cavity (3D)

	Ra	Pr	Grid	α	min Δx	max Δx
Tric et al., 2000	$10^3 - 10^6$	0.71	$N = 81$	-	$2.31 \cdot 10^{-3}$	$3.92 \cdot 10^{-2}$
Fusion (OpenMP)	$10^3 - 10^6$	0.71	64^3	1.5	$1.1 \cdot 10^{-2}$	$1.9 \cdot 10^{-2}$
			128^3	1.5	$5.5 \cdot 10^{-3}$	$9.3 \cdot 10^{-3}$
			192^3	1.5	$3.7 \cdot 10^{-3}$	$6.2 \cdot 10^{-3}$
			256^3	1.5	$2.7 \cdot 10^{-3}$	$4.6 \cdot 10^{-3}$
Basilisk (MPI)	$10^3 - 10^6$	0.71	32^3	-		$3.1 \cdot 10^{-2}$
			64^3	-		$1.6 \cdot 10^{-2}$
			128^3	-		$7.8 \cdot 10^{-3}$
			256^3	-		$3.9 \cdot 10^{-3}$
			512^3	-		$2 \cdot 10^{-3}$

(c) Rayleigh-Bénard cells (3D) for Pr = 0.786

	Ra	Γ_z	Grid	γ	min Δx	max Δx
Wagner and Shishkina, 2013	10^5	1/10–1/3	$64^2 \times 32$	-	-	-
	10^6	1/10–1/3	$96^2 \times 32$	-	-	-
Fusion (OpenMP)	10^5–10^6	1/10–1/3	$64^2 \times 32$	1.5	$1.1 \cdot 10^{-2}$	$1.9 \cdot 10^{-2}$
			$128^2 \times 64$	1.5	$5.5 \cdot 10^{-3}$	$9.3 \cdot 10^{-3}$
			$192^2 \times 96$	1.5	$3.7 \cdot 10^{-3}$	$6.2 \cdot 10^{-3}$
Basilisk (MPI)	10^5–10^6	1/10	$160^2 \times 16$	-		$6.3 \cdot 10^{-3}$
			$320^2 \times 32$	-		$3.1 \cdot 10^{-3}$
			$640^2 \times 64$	-		$1.6 \cdot 10^{-3}$
		1/4	$64^2 \times 16$	-		$1.6 \cdot 10^{-2}$
			$128^2 \times 32$	-		$7.8 \cdot 10^{-3}$
			$256^2 \times 64$	-		$3.9 \cdot 10^{-3}$
			$512^2 \times 128$	-		$2 \cdot 10^{-3}$
		1/3	$48^2 \times 16$	-		$2.1 \cdot 10^{-2}$
			$96^2 \times 32$	-		$1 \cdot 10^{-2}$
			$192^2 \times 64$	-		$5.2 \cdot 10^{-3}$
			$288^2 \times 96$	-		$3.5 \cdot 10^{-3}$

Table 3.1: Simulation parameters used for the different test cases. Here N indicates the number of spectra elements used in the benchmark results. The parameter γ corresponds to the stretching coefficient along the vertical direction, see appendix A.

(a) *Fusion*

Ra	Grid	$\mathrm{Nu_{3D}}$	$\mathrm{Nu_{mp}}$	$\max(u)$	$\max(v)$	$\max(w)$
$1 \cdot 10^3$	64	1.071	1.088	$1.123 \cdot 10^{-1}$	$1.121 \cdot 10^{-1}$	$5.444 \cdot 10^{-3}$
$1 \cdot 10^3$	128	1.071	1.087	$1.121 \cdot 10^{-1}$	$1.121 \cdot 10^{-1}$	$5.434 \cdot 10^{-3}$
$1 \cdot 10^3$	192	1.071	1.087	$1.121 \cdot 10^{-1}$	$1.121 \cdot 10^{-1}$	$5.432 \cdot 10^{-3}$
$1 \cdot 10^3$	256	1.071	1.087	$1.120 \cdot 10^{-1}$	$1.121 \cdot 10^{-1}$	$5.432 \cdot 10^{-3}$
$1 \cdot 10^3$	Ref.	1.070	1.087	$1.120 \cdot 10^{-1}$	$1.121 \cdot 10^{-1}$	$5.471 \cdot 10^{-3}$
$1 \cdot 10^4$	64	2.069	2.266	$1.678 \cdot 10^{-1}$	$1.901 \cdot 10^{-1}$	$2.171 \cdot 10^{-2}$
$1 \cdot 10^4$	128	2.058	2.254	$1.675 \cdot 10^{-1}$	$1.900 \cdot 10^{-1}$	$2.160 \cdot 10^{-2}$
$1 \cdot 10^4$	192	2.056	2.251	$1.675 \cdot 10^{-1}$	$1.901 \cdot 10^{-1}$	$2.159 \cdot 10^{-2}$
$1 \cdot 10^4$	256	2.056	2.250	$1.675 \cdot 10^{-1}$	$1.901 \cdot 10^{-1}$	$2.157 \cdot 10^{-2}$
$1 \cdot 10^4$	Ref.	2.054	2.250	$1.672 \cdot 10^{-1}$	$1.898 \cdot 10^{-1}$	$2.156 \cdot 10^{-2}$
$1 \cdot 10^5$	64	4.440	4.724	$1.398 \cdot 10^{-1}$	$2.246 \cdot 10^{-1}$	$3.100 \cdot 10^{-2}$
$1 \cdot 10^5$	128	4.364	4.642	$1.394 \cdot 10^{-1}$	$2.247 \cdot 10^{-1}$	$3.080 \cdot 10^{-2}$
$1 \cdot 10^5$	192	4.349	4.626	$1.392 \cdot 10^{-1}$	$2.248 \cdot 10^{-1}$	$3.075 \cdot 10^{-2}$
$1 \cdot 10^5$	256	4.344	4.620	$1.391 \cdot 10^{-1}$	$2.248 \cdot 10^{-1}$	$3.073 \cdot 10^{-2}$
$1 \cdot 10^5$	Ref.	4.337	4.612	$1.388 \cdot 10^{-1}$	$2.247 \cdot 10^{-1}$	$3.064 \cdot 10^{-2}$
$1 \cdot 10^6$	64	9.193	9.439	$1.285 \cdot 10^{-1}$	$2.386 \cdot 10^{-1}$	$2.645 \cdot 10^{-2}$
$1 \cdot 10^6$	128	8.808	9.048	$1.279 \cdot 10^{-1}$	$2.372 \cdot 10^{-1}$	$2.593 \cdot 10^{-2}$
$1 \cdot 10^6$	192	8.719	8.956	$1.276 \cdot 10^{-1}$	$2.371 \cdot 10^{-1}$	$2.576 \cdot 10^{-2}$
$1 \cdot 10^6$	256	8.685	8.922	$1.274 \cdot 10^{-1}$	$2.368 \cdot 10^{-1}$	$2.569 \cdot 10^{-2}$
$1 \cdot 10^6$	Ref.	8.640	8.877	$1.270 \cdot 10^{-1}$	$2.367 \cdot 10^{-1}$	$2.556 \cdot 10^{-2}$

(b) *Basilisk*

Ra	Grid	$\mathrm{Nu_{3D}}$	$\mathrm{Nu_{mp}}$	$\max(u)$	$\max(v)$	$\max(w)$
$1 \cdot 10^3$	32	1.077	1.096	$1.112 \cdot 10^{-1}$	$1.113 \cdot 10^{-1}$	$5.757 \cdot 10^{-3}$
$1 \cdot 10^3$	64	1.074	1.092	$1.116 \cdot 10^{-1}$	$1.116 \cdot 10^{-1}$	$5.637 \cdot 10^{-3}$
$1 \cdot 10^3$	128	1.072	1.090	$1.118 \cdot 10^{-1}$	$1.118 \cdot 10^{-1}$	$5.552 \cdot 10^{-3}$
$1 \cdot 10^3$	256	1.072	1.089	$1.118 \cdot 10^{-1}$	$1.119 \cdot 10^{-1}$	$5.506 \cdot 10^{-3}$
$1 \cdot 10^3$	512	1.071	1.089	$1.119 \cdot 10^{-1}$	$1.119 \cdot 10^{-1}$	$5.482 \cdot 10^{-3}$
$1 \cdot 10^3$	Ref.	1.070	1.087	$1.120 \cdot 10^{-1}$	$1.121 \cdot 10^{-1}$	$5.471 \cdot 10^{-3}$
$1 \cdot 10^4$	32	2.070	2.266	$1.679 \cdot 10^{-1}$	$1.887 \cdot 10^{-1}$	$2.105 \cdot 10^{-2}$
$1 \cdot 10^4$	64	2.058	2.254	$1.674 \cdot 10^{-1}$	$1.893 \cdot 10^{-1}$	$2.134 \cdot 10^{-2}$
$1 \cdot 10^4$	128	2.055	2.251	$1.673 \cdot 10^{-1}$	$1.895 \cdot 10^{-1}$	$2.147 \cdot 10^{-2}$
$1 \cdot 10^4$	256	2.055	2.251	$1.673 \cdot 10^{-1}$	$1.897 \cdot 10^{-1}$	$2.153 \cdot 10^{-2}$
$1 \cdot 10^4$	512	2.055	2.251	$1.672 \cdot 10^{-1}$	$1.898 \cdot 10^{-1}$	$2.155 \cdot 10^{-2}$
$1 \cdot 10^4$	Ref.	2.054	2.250	$1.672 \cdot 10^{-1}$	$1.898 \cdot 10^{-1}$	$2.156 \cdot 10^{-2}$
$1 \cdot 10^5$	32	4.453	4.732	$1.427 \cdot 10^{-1}$	$2.207 \cdot 10^{-1}$	$3.015 \cdot 10^{-2}$
$1 \cdot 10^5$	64	4.361	4.638	$1.404 \cdot 10^{-1}$	$2.240 \cdot 10^{-1}$	$3.043 \cdot 10^{-2}$
$1 \cdot 10^5$	128	4.340	4.616	$1.396 \cdot 10^{-1}$	$2.242 \cdot 10^{-1}$	$3.058 \cdot 10^{-2}$
$1 \cdot 10^5$	256	4.336	4.612	$1.392 \cdot 10^{-1}$	$2.246 \cdot 10^{-1}$	$3.061 \cdot 10^{-2}$
$1 \cdot 10^5$	512	4.336	4.612	$1.390 \cdot 10^{-1}$	$2.247 \cdot 10^{-1}$	$3.065 \cdot 10^{-2}$
$1 \cdot 10^5$	Ref.	4.337	4.612	$1.388 \cdot 10^{-1}$	$2.247 \cdot 10^{-1}$	$3.064 \cdot 10^{-2}$
$1 \cdot 10^6$	32	9.383	9.619	$1.331 \cdot 10^{-1}$	$2.287 \cdot 10^{-1}$	$2.635 \cdot 10^{-2}$
$1 \cdot 10^6$	64	8.840	9.076	$1.301 \cdot 10^{-1}$	$2.370 \cdot 10^{-1}$	$2.561 \cdot 10^{-2}$
$1 \cdot 10^6$	128	8.685	8.921	$1.285 \cdot 10^{-1}$	$2.355 \cdot 10^{-1}$	$2.563 \cdot 10^{-2}$
$1 \cdot 10^6$	256	8.648	8.884	$1.277 \cdot 10^{-1}$	$2.364 \cdot 10^{-1}$	$2.561 \cdot 10^{-2}$
$1 \cdot 10^6$	512	8.640	8.877	$1.274 \cdot 10^{-1}$	$2.366 \cdot 10^{-1}$	$2.559 \cdot 10^{-2}$
$1 \cdot 10^6$	Ref.	8.640	8.877	$1.270 \cdot 10^{-1}$	$2.367 \cdot 10^{-1}$	$2.556 \cdot 10^{-2}$

Table 3.2: Numerical convergence of characteristic values for $\mathrm{Pr} = 0.71$ obtained using (a) Fusion and (b) Basilisk. Nusselt numbers $\mathrm{Nu_{3D}}$ and $\mathrm{Nu_{mp}}$ defined in equation (3.8), and maximum velocity components: $\max\left(u(x,y,z)\right)$, $\max\left(v(x,y,z)\right)$, $\max\left(w(x,y,z)\right)$.

Part II

Large-scale flow dynamics inside a square Rayleigh-Bénard cell

Chapter 4

Reversal cycle in square Rayleigh-Bénard cells in turbulent regime

In the next two chapters we are interested in characterizing the large-scale flow dynamics inside two-dimensional (2-D) square Rayleigh-Bénard cells in the (weakly-) turbulent regime. For the range of Rayleigh numbers and Prandtl numbers considered, two types of flow regimes are observed intermittently: a regime consisting of consecutive flow reversals, when the large-scale circulation (LSC) switches sign; and a regime consisting of an extended cessation of the LSC.

In the present chapter, a statistical characterization of the regime of consecutive flow reversals is portrayed in terms of different global quantities. This work led to the preparation of an article (Castillo-Castellanos et al., 2016), which is reproduced verbatim in this chapter. The presence of a generic reversal cycle is evidenced by means of a time re-scaling procedure. This cycle is composed of three successive phases: acceleration, accumulation and release including a rebound event. Reversals are then viewed in terms of available potential energy and global kinetic energy, and their corresponding energy transfer rates. A decomposition of the rate-of-change of the global angular impulse reveals a delicate balance between thermal and viscous forces. Based on this analysis, we identify two points of interest signaling a transition of flow regime before the flow reversal takes place during the accumulation phase.

In chapter 5 we continue the analysis of the reversal regime by performing a proper orthogonal decomposition (POD) analysis (Podvin and Sergent, 2015; Podvin and Sergent, 2017) combined to the statistical approach to the modal coefficients.

4.1   Paper: Reversal cycle in square Rayleigh-Bénard cells

Reversal cycle in square Rayleigh–Bénard cells in turbulent regime

Andres Castillo Castellanos[1,2], Anne Sergent[2,3]† and Maurice Rossi[1,4]

[1]Sorbonne Universités, UPMC Univ Paris 06, UMR 7190, Institut Jean Le Rond d'Alembert, F-75005, Paris, France

[2]LIMSI, CNRS, Université Paris-Saclay, F-91405 Orsay, France

[3]Sorbonne Universités, UPMC Univ Paris 06, UFR d'Ingénierie, F-75005, Paris, France

[4]CNRS, UMR 7190, Institut Jean Le Rond d'Alembert, F-75005, Paris, France

We consider long-term data from direct numerical simulations of turbulent Rayleigh–Bénard convection inside 2D square cells. For the range of *Rayleigh* numbers $\mathrm{Ra} = 10^7 - 10^8$ and *Prandtl* numbers $\mathrm{Pr} = 3.0 - 4.3$, two types of flow regimes are observed: a regime consisting of *consecutive reversals*, when the global rotation switches signs; and a regime consisting of an *extended cessation*, when global rotation is absent. A filtering method discriminates these two regimes and allows to identify two characteristic time-scales for the former regime. A time re-scaling is then used to tune our records to a common duration thus putting into evidence a generic reversal cycle. This cycle is composed of three successive phases: *acceleration*, *accumulation*, and *release* including a *rebound* event. We complement this view in terms of global angular impulse, available mechanical energy, global kinetic energy, and their corresponding transfer rates. For a particular realisation of a reversal, each phase is described in terms of the flow patterns (large diagonal roll, counter-rotating corner-flows and thermal plumes) and tied to the corresponding energy processes. We conclude by performing linear as well as nonlinear stability studies to account for the triggering mechanism of the release.

1. Introduction

Decaying or stochastically forced two-dimensional turbulence in the presence of rigid boundaries is characterised by self-organised coherent structures. For a square domain (Clercx *et al.* 1998; Molenaar *et al.* 2004), a spontaneous spin-up is observed which leads to the formation of a single vortex structure. This structure can persist for very long periods of time, before suddenly breaking and re-organising itself, in some cases with a reversed rotation sense. A similar process occurs in the geomagnetic field under the form of polarity switches (Wicht *et al.* 2009; Valet *et al.* 2012). In turbulent Rayleigh-Bénard (RB) convection experiments, this phenomenon is also observed: a large scale circulation (LSC), commonly referred to as the *wind*, changes sign intermittently. Several models have been proposed to describe this process in RB convection through either stochastic differential equations (Sreenivasan *et al.* 2002; Benzi 2005; Brown & Ahlers 2007; Podvin & Sergent 2015) or phenomenological and physically motivated assumptions (Araujo *et al.* 2005; Resagk *et al.* 2006; Brown & Ahlers 2007).

The LSC structure, its global properties and the transition between dominant flow structures are found to be dependent on the cavity shape (Grossmann & Lohse 2003; Xi & Xia 2008b; van der Poel *et al.* 2011). Inside cylindrical cells, a change of sign of the

LSC occurs either by a *rotation-led* reversal through an azimuthal rotation of the near-vertical circulation plane known as *azimuthal meandering*, or by a *cessation-led* reversal through the breakdown of the existing LSC before re-organising in a different spatial direction (see, for instance Niemela *et al.* (2001); Sreenivasan *et al.* (2002); Brown & Ahlers (2007); Funfschilling *et al.* (2008); Xi & Xia (2008*a*,*b*)). One approach to separate rotation-led from cessation-led reversal events consists in restricting the experimental study to a square box of small aspect ratio in the transversal direction (Xia *et al.* 2003; Sugiyama *et al.* 2010; Wagner & Shishkina 2013; Ni *et al.* 2015). Another viewpoint uses two-dimensional direct numerical simulations (Sugiyama *et al.* 2010; Petschel *et al.* 2011; Chandra & Verma 2011; Verma *et al.* 2015; Podvin & Sergent 2015) since rotation-led reversals are not possible in such a configuration. However, it is not entirely clear whether 2D reversals and cessation-led reversals correspond to the same phenomenon. Sugiyama *et al.* (2010) have identified a region in the (Ra, Pr) space in which reversal events are observed experimentally inside quasi-two-dimensional cells as well as numerically in two-dimensional simulations. For this range of (Ra, Pr), the flow inside a square cell is mainly composed of a large diagonal roll and two counter-rotating corner-rolls. (Chandra & Verma 2013; Sugiyama *et al.* 2010) pointed out the feeding of corner-rolls by plumes detached from horizontal boundary layers. Both papers proposed that the growth of corner-rolls ended by a sudden LSC transition.

The presence of such coherent structures has been investigated by computing the first *Fourier* modes (Chandra & Verma 2011; Verma *et al.* 2015), or by obtaining these modes from a *proper orthogonal decomposition* (Bailon-Cuba *et al.* 2010; Podvin & Sergent 2015). Coherent structures are actually associated with a sum of various such modes: a large-scale monopole, a quadrupole and a vertically or horizontally stacked dipole. A study of the transition sequences between these first Fourier modes indicated the presence of a reversal path (Petschel *et al.* 2011). To analyse such a process, one could adopt the perspective used in geomagnetic fields combining a careful selection of reversal records as well as a time rescaling (Valet *et al.* 2012; Lhuillier *et al.* 2013). In geomagnetism, this method led to the definition of three successive phases: a precursory event, a polarity switch and a rebound.

Another viewpoint is based on energetical considerations. For instance available potential energy is key to understand how mechanical energy is transported, stored, and dissipated in RB convection (Winters *et al.* 1995; Hughes *et al.* 2013). This approach could make more precise the idea of an *avalanche* mechanism (mentioned in Sreenivasan *et al.* (2002)), due to a localised accumulation of energy, which increases local gradients until a certain threshold is reached and energy is expelled as a single burst.

In the present paper, we propose for RB convection, a formulation similar to the one proposed in geomagnetism (Valet *et al.* (2012)): the main objective is to establish the existence of a generic reversal cycle and to identify in this cycle three phases (release, accumulation, and acceleration). This analysis combines a statistical analysis with a physical approach relying on the angular momentum as well as kinetic and potential energy to highlight the underlying physical mechanisms. In addition, we identify flow patterns corresponding to each phase of the generic cycle by using a conditional averaging. A threshold state in generic reversal cycles is identified from which the release is inevitable.

The paper is organised as follows. Section 2 introduces the model equations and global quantities: global angular impulse, available mechanical energy and corresponding conversion rates. A brief description of the numerical method and the spatial resolution is presented in section 3. In section 4, a filtering method is proposed that identifies two regimes, and then allows to perform a statistical study of reversals. The dynamics of a

generic reversal mechanism is described as composed by three phases in section 5. These results are then analysed in terms of coherent flow structures, physical mechanisms in section 6 for particular realisations. In section 7, a stability analysis is applied on the generic cycle. Section 8 contains a brief comparison of the present analysis with previous works. Finally, some prospective works are mentioned in conclusion.

2. Model equations and analysis tools

Consider a fluid contained in a square cell, cooled at the top with constant temperature T_{top} and heated at the bottom with constant temperature $T_{bot} > T_{top}$. The flow equations are based on the *Boussinesq* approximation. The flow regime is defined as a function of the *Rayleigh* and *Prandtl* numbers,

$$\mathrm{Ra} \equiv \frac{gH^3 \beta \left(T_{bot} - T_{top}\right)}{\kappa \nu}, \qquad \mathrm{Pr} \equiv \frac{\nu}{\kappa} \qquad (2.1)$$

where g denotes gravity, H the cell height and β, κ, ν are respectively volumetric thermal expansion, thermal diffusivity and kinematic viscosity coefficients. The values of $(\mathrm{Ra}, \mathrm{Pr})$ used for direct numerical simulations (DNS) correspond to a weakly turbulent flow regime where reversals have been reported (Sugiyama *et al.* 2010). As far as notations are concerned, x (resp. u) and y (resp. v) stand for the horizontal and vertical directions (resp. velocities). Coordinate vector $\vec{x} = (x, y)$ is equal to $(0, 0)$ at the cavity centre. One introduces the reduced temperature $\theta(\vec{x}, t) \equiv (T - T_0)/(T_{bot} - T_{top})$, with $T_0 \equiv (T_{bot} + T_{top})/2$ as well as the only vorticity component $\omega(\vec{x}, t) \equiv \partial_x v - \partial_y u$. For a field $a(\vec{x}, t)$, the fields $\overline{a}(\vec{x})$ and $\sigma(a)(\vec{x})$ denote the time average and standard deviation computed using the full long-term time series. In addition, quantity $\langle a \rangle_{vol}(t)$ stands for the volume average of $a(\vec{x}, t)$.

Based on the cell height H as characteristic length scale and $\frac{\kappa}{H}\mathrm{Ra}^{0.5}$ as velocity scale, the dimensionless velocity $\vec{u} = (u, v)$ and reduced temperature θ satisfy the dimensionless system of equations

$$\begin{cases} \boldsymbol{\nabla} \cdot \vec{u} &= 0, \\ \partial_t \vec{u} + \boldsymbol{\nabla} \cdot [\vec{u} \otimes \vec{u}] &= -\boldsymbol{\nabla} p + \mathrm{Pr}\mathrm{Ra}^{-0.5}\boldsymbol{\nabla}^2\vec{u} + \mathrm{Pr}\theta\vec{e}_y, \\ \partial_t \theta + \boldsymbol{\nabla} \cdot [\vec{u}\theta] &= \mathrm{Ra}^{-0.5}\boldsymbol{\nabla}^2\theta \end{cases} \qquad (2.2)$$

No-slip condition for the velocity field is ensured on walls. On top (resp. bottom) walls, one imposes $\theta = -0.5$ (resp. $\theta = 0.5$) while adiabaticity $\partial_x \theta = 0$ is satisfied on side-walls. From now on, quantities are written in dimensionless form only.

2.1. *Global angular impulse*

The global angular momentum

$$\mathrm{L_{2D}}(t) \equiv -\frac{1}{2} \int \vec{x}^2 \omega(\vec{x}, t) \mathrm{d}x \mathrm{d}y \qquad (2.3)$$

serves as a measure of organised rotation (see for instance Molenaar *et al.* (2004)). Figure 1 shows a time series of the normalised angular momentum $\mathrm{L_{2D}}/|\overline{\mathrm{L_{2D}}}|$. Two different regimes are observed. Blue areas correspond to periods of time where $\mathrm{L_{2D}}$ changes sign spontaneously over time: positive (resp. negative) peaks in $\mathrm{L_{2D}}$ alternate that are associated to a dominant counter-clockwise (resp. clockwise) central vortex. The blue areas consisting of a sequence of consecutive transitions is hereafter called the *consecutive reversal* (CR) regime. Outside this regime, the LSC is no longer well-defined
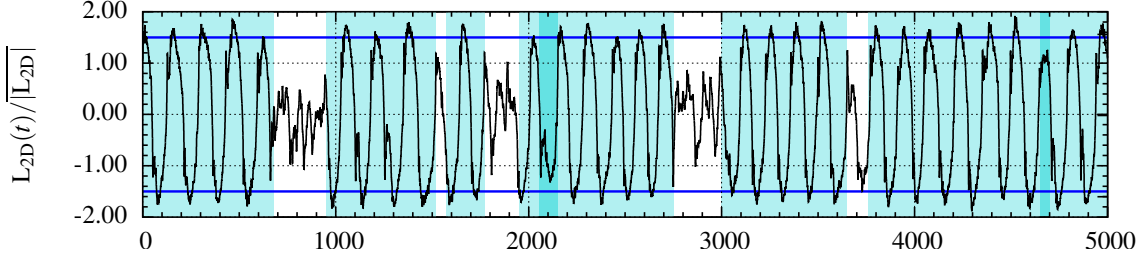
FIGURE 1. Time evolution of $L_{2D}(t)/\overline{|L_{2D}|}$ shown for $(Ra = 5 \cdot 10^7, Pr = 3)$. Light blue areas correspond to a consecutive reversal (CR) regime, while blank areas correspond to an extended cessation (EC) regime. Some events (darker blue areas) may not be clearly assigned to CR régime, see text. The two continuous lines correspond to the thresholds used by the filtering procedure. Value of the normalized standard deviation: $\sigma(|L_{2D}|)/\overline{|L_{2D}|} = 0.499$.

and one observes an extended cessation. Such complementary region is denoted here as the *extended cessation* (EC) regime.

In order to differentiate in a precise manner the CR regime from the EC regime, a filtering algorithm has been devised which is modeled after (Lhuillier *et al.* 2013; Podvin & Sergent 2015). We identify the set of consecutive times r_i at which L_{2D} changes sign. The time interval $[r_i, r_{i+1}]$ is considered to be inside the CR regime if, during this interval, the value of $|L_{2D}|$ reaches at least once the threshold value $\overline{|L_{2D}|} + \sigma(|L_{2D}|)$ (light blue area in figure 1). A time interval where such threshold is not reached can be of two kinds corresponding to the darker blue areas or the white areas in figure 1. The first kind is sandwiched between two CR intervals and corresponds to a "rogue" reversal, which likely belongs to the CR regime but has been filtered out by our criterion (the criteria for the selection of events in the CR regime is rather stringent as seen from the "rogue" events displayed in figure 1). The second type, displayed in white, corresponds to an extended cessation.

For any interval $[r_i, r_{i+1}]$, its duration $\tau_{1,i} \equiv r_{i+1} - r_i$ is also computed. When both intervals $[r_{i-1}, r_i]$ and $[r_i, r_{i+1}]$ are inside a CR regime, the duration $\tau_{d,i}$ of the jump occurring around time r_i between a clockwise and counter-clockwise central vortex or vice versa can be evaluated. It is computed by identifying the times located just before and just after time r_i such that $|L_{2D}|$ reaches the threshold value $\overline{|L_{2D}|} - \sigma(|L_{2D}|)$. $\tau_{d,i}$ is simply the time lapse between these two events.

The change of the global angular momentum L_{2D} may be better understood considering the relation directly obtained from the governing equations (2.2),

$$\frac{dL_{2D}}{dt} = M + I_a - I_b \quad \begin{cases} M(t) \equiv \frac{1}{2}Pr \int \vec{x}^2 \ \partial_x\theta \ dxdy \\ I_a(t) \equiv \ PrRa^{-0.5} \oint [\vec{x} \cdot \vec{n}] \ \omega \ dl \\ I_b(t) \equiv \frac{1}{2}PrRa^{-0.5} \oint \vec{x}^2 \ \vec{n} \cdot \boldsymbol{\nabla}\omega \ dl \end{cases} \quad (2.4)$$

where $\vec{n}$ stands for the outwards unit normal vector to the domain boundary and dl for a contour line differential element. Note that it is assumed that line integrals are performed in a counterclockwise direction. The angular momentum thus evolves because of a bulk forcing term $M(t)$ known as the input torque (Molenaar *et al.* 2004) and two boundary integrals terms $I_a(t)$ and $I_b(t)$. $I_b(t)$ is close but not identical to the integrated vorticity flux over the domain boundary. For a square cavity, the boundary term $I_a(t)$ simplifies to $I_a = \frac{1}{2}PrRa^{-0.5} \oint \omega dl$. Vorticity on the boundary is related to the friction exerted by the fluid on the walls. This integral $I_a(t)$ is thus quantifying friction along the boundary.
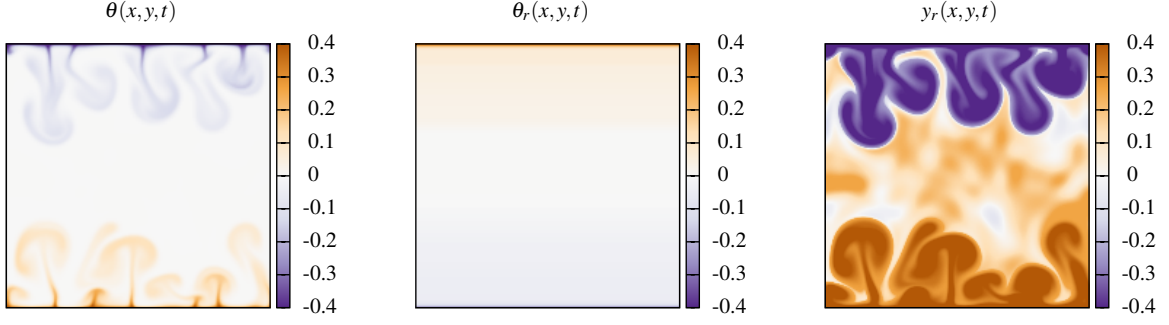
FIGURE 2. Temperature field $\theta(x, y, t)$ at a given instant t (left), the corresponding *background* state $\theta_r(y, t)$ (center) and height $y_r(x, y, t)$ (right) for a square RB cell.

2.2. *Mechanical energy balance*

Other global quantities are useful to characterise at each time the instantaneous state of the system: the global kinetic energy $E_{kin}(t) \equiv \frac{1}{2} \int \vec{u}^2 dx dy$ and the global potential energy $E_{pot}(t) \equiv -\text{Pr} \int y\theta \, dx dy$. This latter quantifies the energy amount required to bring all fluid particles against gravity from their position at time t to the reference level $y = 0$. However, one can introduce a more pertinent instantaneous quantity namely the *available potential energy* (Sutherland 2010), which is defined here below. For a given time t, the fluid is characterized by an instantaneous temperature field $\theta(x, y, t)$ with a lower (resp. upper) bound at θ_{min}(resp. θ_{max}). Let us consider a one-to-one mapping $(x_r(x, y), y_r(x, y))$ from the square onto the square. This may be interpreted as a reordering of fluid particles inside the square cell. Rearranging modifies the temperature field leading to a new field $\theta_r(x, y, t)$ but this process is an adiabatic one i.e. $\theta_r(x_r, y_r, t) = \theta(x, y, t)$. As a consequence, the probability distribution function (PDF) of temperature in the rearranged state is identical to the PDF in the instantaneous state. The potential energy of the rearranged state can be measured. Among the set of such mappings, there exists a subset which corresponds to the lowest potential energy. It is easy to understand that all mappings belonging to this subset have identical rearranged temperature field $\theta_r(y, t)$ with no x dependency and increasing (i.e. density decreasing) monotonically with height (figure 2). This field characterizes the *background* state. Although $y_r(x, y, t)$ is not a simple function of (x, y), the above remark implies that y_r is a one-to one function of θ for a mapping in this subset. In practice (see Tseng & Ferziger (2001)), the field $\theta_r(y, t)$ is computed by the following procedure. First, the PDF of the instantaneous temperature at time t which is denoted by $P(\theta)$, is directly evaluated numerically within the interval $[\theta_{min}, \theta_{max}]$ since $\theta(x, y, t)$ is known on the whole square box. Second, the conservation of temperature PDF with rearrangement imposes that $y_r(\theta)$ be evaluated as a cumulative density function

$$y_r(\theta) - y_{bot} = y_r(\theta) - y_r(\theta_{min}) = \int_{\theta_{min}}^{\theta} P(\theta) \, d\theta. \quad (2.5)$$

This relation depends *a priori* on the domain geometry. For a square box of unit size, however, the proportionality is factor is reduced to unity. Third, function $\theta_r(y, t)$ is then obtained by a simple inversion of $y_r(\theta, t)$.

The *background* state is characterized by the lowest potential energy that can be reached by an adiabatic process starting from the instantaneous temperature field $\theta(x, y, t)$. This quantity called the *background potential energy* is equal to $E_{bpot} \equiv -\text{Pr} \int y_r(x, y, t)\theta(x, y, t) \, dx dy$. By a simple change of variable and using

adiabaticity $\theta_r(x_r, y_r, t) = \theta(x, y, t)$, one gets

$$\mathrm{E_{bpot}} = -\mathrm{Pr} \int y_r \theta_r(y_r) \, \mathrm{d}x_r \mathrm{d}y_r = -\mathrm{Pr} \int y_r \theta_r(y_r) \mathrm{d}y_r.$$

The difference $\mathrm{E_{apot}}(t) \equiv \mathrm{E_{pot}}(t) - \mathrm{E_{bpot}}(t) > 0$ in potential energy between the instantaneous state and its background companion is called the *available potential energy* and represents the potential energy which could be effectively transformed from the instantaneous field $\theta(x, y, t)$ into motion (Lorenz 1955; Winters *et al.* 1995).

In analogy with $\mathrm{L_{2D}}$, the process may be better grasped by considering the evolution of the energies $\mathrm{E_{kin}}$, $\mathrm{E_{pot}}$, $\mathrm{E_{apot}}$, through some exact relations (see Winters *et al.* (1995); Hughes *et al.* (2013)). For the kinetic energy $\mathrm{E_{kin}}$, the following relation holds (e_{ij} denotes the symmetric velocity gradient tensor)

$$\frac{\mathrm{dE_{kin}}}{\mathrm{dt}} = \mathrm{PrRa}^{-0.5}[\varPhi_y - \epsilon], \quad \begin{cases} \varPhi_y \equiv \mathrm{Ra}^{0.5}\langle v\theta \rangle_{\mathrm{vol}} \\ \epsilon \equiv \langle \boldsymbol{\nabla}\vec{u} : \boldsymbol{\nabla}\vec{u} \rangle_{\mathrm{vol}} = 2\langle e_{ij}e_{ij} \rangle_{\mathrm{vol}} \end{cases} \tag{2.6}$$

The first bulk term $\varPhi_y(t)$ is a convective heat flux. More precisely let us introduce the volume-averaged Nusselt number $\mathrm{Nu_{vol}} \equiv \mathrm{Ra}^{0.5}\langle v\theta \rangle_{\mathrm{vol}} - \langle \partial_y\theta \rangle_{\mathrm{vol}}$. It is easily found that, for RB cells, $\varPhi_y(t) = \mathrm{Nu_{vol}}(t) - 1$. The second bulk term $\epsilon(t) > 0$ stands for the viscous dissipation rate. Finally one may write

$$\frac{\mathrm{dE_{kin}}}{\mathrm{dt}} = \mathrm{PrRa}^{-0.5}[\mathrm{Nu_{vol}} - (\epsilon + 1)] \tag{2.7}$$

The potential energy $\mathrm{E_{pot}}$ verifies instead the relation

$$\frac{\mathrm{dE_{pot}}}{\mathrm{dt}} = \mathrm{PrRa}^{-0.5}[-\mathrm{Nu_{vol}} + \varPhi_{b1}] \tag{2.8}$$

which contains the bulk term $\mathrm{Nu_{vol}}$ and a boundary term

$$\varPhi_{b1}(t) \equiv -\oint y[\vec{n} \cdot \boldsymbol{\nabla}\theta] \, \mathrm{d}l \tag{2.9}$$

quantifying the conversion rate to $\mathrm{E_{pot}}$ from external sources. More precisely, let us introduce the Nusselt number $\mathrm{Nu_{top}}(t) \equiv -\int \partial_y\theta \mathrm{d}x$ evaluated at the top $y = 0.5$ as well as the Nusselt number $\mathrm{Nu_{bot}}(t) \equiv -\int \partial_y\theta \mathrm{d}x$ evaluated at the bottom plates $y = -0.5$. For the present square cell, one easily verifies that $\varPhi_{b1} = \frac{1}{2}(\mathrm{Nu_{top}} + \mathrm{Nu_{bot}})$ and consequently

$$\frac{\mathrm{dE_{pot}}}{\mathrm{dt}} = \mathrm{PrRa}^{-0.5}[-\mathrm{Nu_{vol}} + \frac{1}{2}(\mathrm{Nu_{top}} + \mathrm{Nu_{bot}})] \tag{2.10}$$

Finally, the evolution equation for the available potential energy $\mathrm{E_{bpot}}$ reads as

$$\frac{\mathrm{dE_{bpot}}}{\mathrm{dt}} = \mathrm{PrRa}^{-0.5}[\varPhi_d - \varPhi_{b2}], \quad \begin{cases} \varPhi_d \equiv \langle \frac{\partial y_r}{\partial\theta}\boldsymbol{\nabla}\theta \cdot \boldsymbol{\nabla}\theta \rangle_{\mathrm{vol}} = \langle \boldsymbol{\nabla}y_r \cdot \boldsymbol{\nabla}\theta \rangle_{\mathrm{vol}} \\ \varPhi_{b2} \equiv \oint y_r[\vec{n} \cdot \boldsymbol{\nabla}\theta] \, \mathrm{d}l \end{cases} \tag{2.11}$$

where the bulk term $\varPhi_d(t)$ quantifies the energy conversion rate due to diapycnal mixing. Since by definition $\frac{\partial y_r}{\partial\theta} > 0$, $\varPhi_d(t)$ is bound to be positive. The boundary term $\varPhi_{b2}$ provides the conversion rate from external sources. For the present RB cells, since $y_r(x, 1/2, t) = -1/2$ and $y_r(x, -1/2, t) = 1/2$ and because adiabaticity of side walls it is clear that $\varPhi_{b2}(t) = \varPhi_{b1}(t)$. Finally by substracting equation 2.8 by equation 2.11, one gets

$$\frac{\mathrm{dE_{apot}}}{\mathrm{dt}} = \mathrm{PrRa}^{-0.5}[\mathrm{Nu_{bot}} + \mathrm{Nu_{top}} - \mathrm{Nu_{vol}} - \varPhi_d] \tag{2.12}$$

Pr	Ra	Time	Events	$\overline{\mathrm{Nu}}$	%Diff
3.0	10^7	9,600	48	12.5	0.30
	$3 \cdot 10^7$	9,600	77	17.6	0.53
	$5 \cdot 10^7$	9,600	83	20.7	0.69
	10^8	12,000	83	25.6	1.44
4.3	$3 \cdot 10^7$	19,000	22	18.4	0.24
	$5 \cdot 10^7$	29,000	161	21.0	0.70
	10^8	19,000	156	25.9	1.38

TABLE 1. For various Prandtl and Rayleigh numbers, the table provides the simulation length in convective time units, the number of reversal events, the average Nusselt number and maximum relative difference between $\overline{\mathrm{Nu}}_{\mathrm{vol}}$, $\overline{\mathrm{Nu}}_{\mathrm{top}}$, $\overline{\mathrm{Nu}}_{\mathrm{bot}}$, $\overline{\mathrm{Nu}}_{\theta}$, and $\overline{\mathrm{Nu}}_{\epsilon}$.

3. Numerical method

Simulations are carried out using a finite volume code using a semi-implicit scheme based on Bell-Colella-Glaz advection scheme (Bell *et al.* 1989), and a pressure-correction scheme for the velocity-pressure coupling, with a global second order precision. Numerical implementation is done using `BASILISK C`, details of which can be found in Popinet (2016). Simulations listed in table 1 have been performed on a uniform Cartesian grid with 512 points in each direction, with a variable time-step that verifies the condition CFL< 0.5. In the most unfavorable case $(\mathrm{Ra} = 10^8, \mathrm{Pr} = 4.3)$ the thermal boundary layers contain 10 points along the vertical direction.

Spatial resolution is verified evaluating numerical convergence of time-averaged Nusselt numbers obtained by different methods (Stevens *et al.* 2010). Note that to perform the averaging, statistical sampling is obtained at regular intervals. We compare $\overline{\mathrm{Nu}}_{\mathrm{vol}}$, $\overline{\mathrm{Nu}}_{\mathrm{top}}$ and $\overline{\mathrm{Nu}}_{\mathrm{bot}}$ to the Nusselt numbers obtained from the thermal and viscous dissipations

$$\overline{\mathrm{Nu}}_{\theta} \equiv \langle \overline{\boldsymbol{\nabla}\theta \cdot \boldsymbol{\nabla}\theta} \rangle_{\mathrm{vol}}, \qquad \overline{\mathrm{Nu}}_{\epsilon} \equiv \overline{\epsilon} + 1 \qquad (3.1)$$

All these quantities should be equal (Shraiman & Siggia 1990). The value of $\overline{\mathrm{Nu}}$ shown in table 1 is the average value of $\overline{\mathrm{Nu}}_{\mathrm{vol}}, \overline{\mathrm{Nu}}_{\mathrm{top}}, \overline{\mathrm{Nu}}_{\mathrm{bot}}, \overline{\mathrm{Nu}}_{\theta}, \overline{\mathrm{Nu}}_{\epsilon}$ while the maximum relative difference between any of them is shown as %Diff. These values converge within 2% of $\overline{\mathrm{Nu}}$ for all $(\mathrm{Ra}, \mathrm{Pr})$ presented. We have also verified that our numerical results are well-converged in a completely different way. This check has been performed by comparing results of the probability density functions (PDF) of the time interval τ_1 obtained by our code against benchmark results. This computation requires to get long term simulations and was done for $(\mathrm{Ra} = 5 \cdot 10^7, \mathrm{Pr} = 4.3)$ since such parameter values had already been computed by a spectral code (Podvin & Sergent 2015). The data for this check are postponed at the end of section 4.

4. Temporal analysis and statistical characterisation

In the present work, we focus on turbulent RB systems for which flow reversals are observed. For $\mathrm{Pr} = 3.0$, this dynamics is associated with the interval $\mathrm{Ra} \in [5 \cdot 10^6, 3 \cdot 10^8]$. For $\mathrm{Pr} = 4.3$, it corresponds to the interval $\mathrm{Ra} \in [3 \cdot 10^7, 4 \cdot 10^8]$ (Sugiyama *et al.* 2010). Note that, these boundaries are not clearly established. For instance, some transitions were found for very long runs at $(\mathrm{Pr} = 4.3, \mathrm{Ra} = 10^7)$ (not presented here) but it is difficult to assert whether or not the few cycles observed correspond to an established statistical steady state or to a transient behaviour. In the following, we consider only

Pr	Ra	p_{cr}	p_{rr}	p_{ec}	Pr	Ra	p_{cr}	p_{rr}	p_{ec}
3.0	10^7	85%	1%	14%	4.3	-	-	-	-
	$3 \cdot 10^7$	73%	3%	24%		$3 \cdot 10^7$	95%	1%	4%
	$5 \cdot 10^7$	77%	3%	20%		$5 \cdot 10^7$	83%	1%	16%
	10^8	96%	4%	0%		10^8	89%	2%	9%

TABLE 2. Probabilities as a function of Ra and Pr. p_{cr} (resp. p_{ec}) denotes the probability that the system be inside the CR (resp. EC) regime. p_{rr} denotes the probability of a "rogue" reversal..

values inside the aforementioned range for which the number of events is large enough (see table 1): simulations are performed from 9,600 to 29,000 convective time units (see table 1), which gives from 50 to 160 events (except for Pr $= 4.3$ and Ra $= 3 \cdot 10^7$ which is situated close to the boundary region where the reversal dynamics is established).

For a given couple (Ra, Pr), one computes the percentage of time or equivalently the probability that the system be in one of the three states: p_{cr} in the CR regime, p_{ec} in the EC regime and p_{rr} inside a "rogue" reversal. The probability p_{rr} of rogue events is always of a few percents (see table 2). For both Pr $= 3.0$ and Pr $= 4.3$, in the interval where the CR regime is observed, p_{cr} first decreases and then increases with increasing Ra (see table 2).

The PDFs of τ_1 and τ_d are measured based on the full simulation length and shown on figure 3 (resp. figure 4) for Pr $= 4.3$ (resp. Pr $= 3$). Using the filtering method of section 2.1, we separated the PDF of τ_1 into three contributions: one for intervals inside the CR regime (color blue), one for intervals from the EC regime (color red) and one corresponding to rogue events (color purple). This PDF shows that the distribution of τ_1 is not peaked inside the CR regime: intervals may have different durations. This is also valid for the EC regime. For Pr $= 4.3$, a similar probability distribution of τ_1 is observed for both values of Ra (figure 3) and a characteristic time-scale $\tau_c \approx 60$ exists which separates EC from CR regimes. For Pr $= 3.0$, a change in the PDFs of τ_1 and τ_d is observed as we increase the values of Ra (figure 4). For the lowest Ra displayed, a characteristic time τ_c cannot be clearly defined. For the highest Ra displayed Ra $= 10^8$, the EC regime completely disappears. For intermediate Ra, reversal events become evenly distributed over a narrow band of τ_1 (see figure 4 center and right) and a clear separation of time-scales between the EC and CR regimes is observed at $\tau_c \approx 50$ which is at least one order of magnitude larger than the large eddy turn-over time, $\tau_E \equiv 4\pi/\overline{|\omega_c|}$ (ω_c denoting vorticity measured at the cavity center). The PDF of the inter-switch intervals observed for cylindrical convection cell experiments is an exponential distribution (Sreenivasan et al. (2002)). It is not seen here (figures 3 and 4) illustrating the fact that rotation-led reversals are not present here contrary to cylindrical cells.

From the PDF of transition durations τ_d for CR regime only (see figures 3 and 4 bottom), the peak value tends to increase as Ra is increased for both Pr $= 3.0$ and Pr $= 4.3$. Concerning the numerical check, the average value $\overline{\tau_1}|_{cr}$ during the CR regime and the average duration $\overline{\tau_d}$ of transition were both found to be in good agreement with published results for (Ra $= 5 \cdot 10^7$, Pr $= 4.3$): $\overline{\tau_1}|_{cr} = 146$ and $\overline{\tau_d} = 11.5$ convective time units (Podvin & Sergent 2015).

5. Dynamics of the generic reversal

We have shown above that reversals cycles have different durations $\tau_{1,i}$. A simple time-rescaling, however, can be used to identify features common to all reversal cyles.
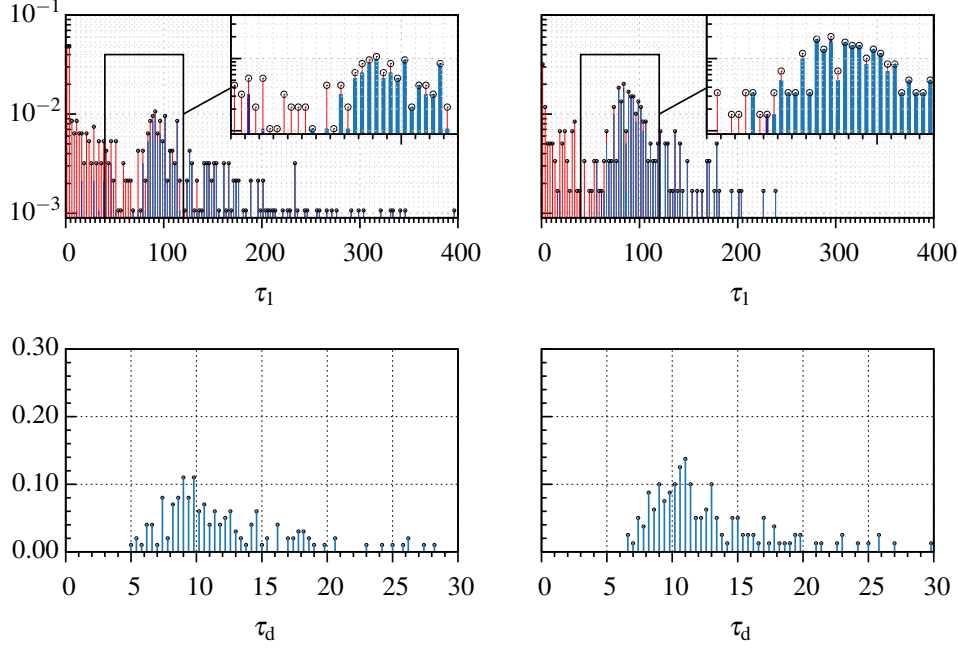
FIGURE 3. Probability density function (PDF) of τ_1 (top) and τ_d (bottom) for Pr = 4.3, (left figure) Ra = $5 \cdot 10^7$, (right figure) Ra = 10^8. The PDF value is represented by ∘ marks. For τ_1 it is the sum of three conditional PDFs: one in (———) corresponding to the CR regime, a smaller one in (———) corresponding to "rogue reversals", and an additional part in (———) corresponding to the EC regime.
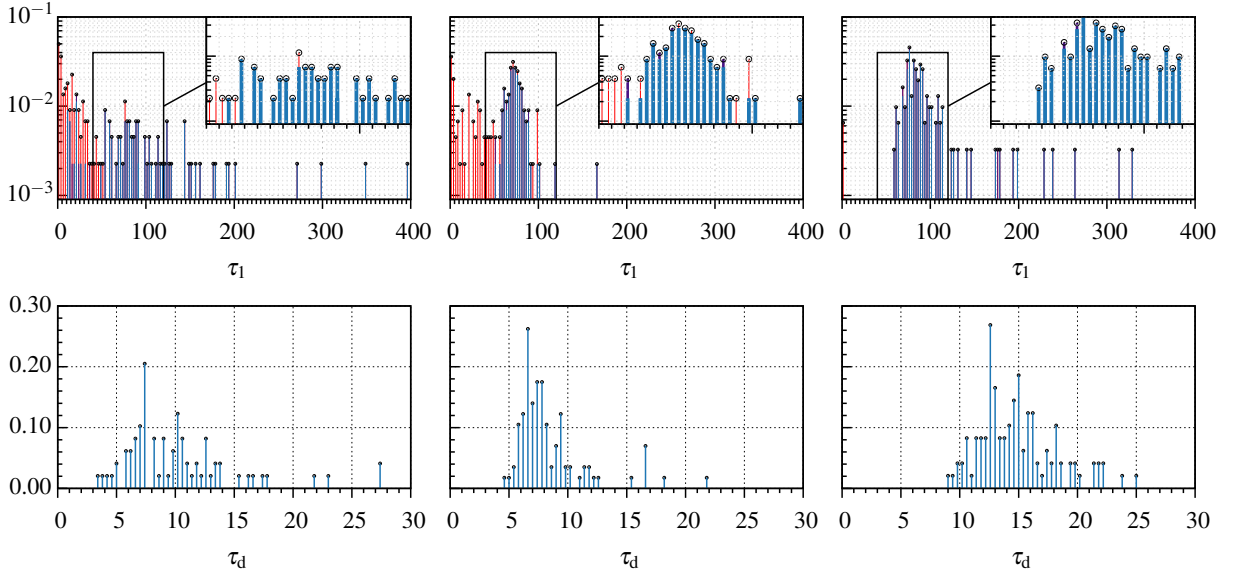
FIGURE 4. Probability density function (PDF) for τ_1 (top) and τ_d (bottom) for Pr = 3.0 and Ra = 10^7 (left), Ra = $5 \cdot 10^7$ (centre) and Ra = 10^8 (right). Layout is similar to figure 4.

5.1. *Averaging procedure and generic reversal as function of* (Ra, Pr)

In order to identify similarities between different intervals in the CR regime, the following procedure is proposed to treat time-series of global quantities such as L_{2D}, E_{kin}, and E_{apot}. Once the intervals $[r_i, r_{i+1}]$ inside the CR regime are properly identified, all these intervals with $L_{2D} > 0$ (resp. $L_{2D} < 0$) are stacked together so that they have a common origin at r_i (resp. r_{i+1}). If the time axis of each interval is re-scaled by $\overline{\tau_1}$, one obtains figure 5 left. If the time axis of each interval is rescaled by its particular duration $\tau_{1,i}$, these curves display a consistent dynamical pattern (see figure 5 centre).
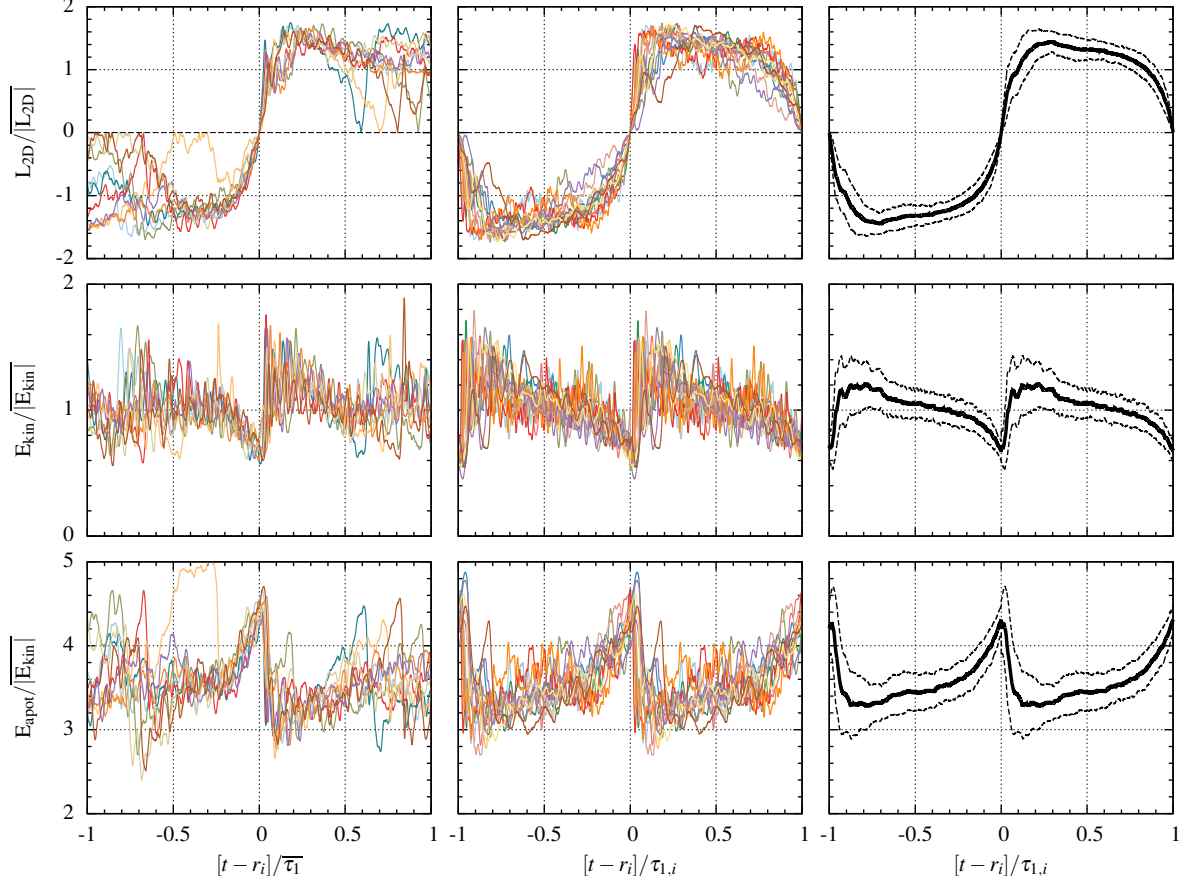
FIGURE 5. From top to bottom: Normalised global angular impulse $L_{2D}/\overline{|L_{2D}|}$, normalised kinetic energy $E_{kin}/\overline{|E_{kin}|}$, and normalised available potential energy $E_{apot}/\overline{|E_{kin}|}$ for $(Ra = 5 \cdot 10^7, Pr = 4.3)$. Left panel: Each reversal cycle is centred and its time is rescaled by $\overline{\tau}_1$ (only 10 reversals are displayed and each colour is a different reversal); Centre panel: Each reversal cycle is centred and its time is rescaled by $\tau_{1,i}$; Right panel: Average value of rescaled curves obtained from the complete time-series (thick lines) and curves corresponding to one standard deviation (dashed lines).

Note that, while figure 5 displays only 10 reversals to avoid cluttered graphs, these events displayed are considered as representative of the entire set. Obviously, all of the events inside the CR regime are taken into account in our procedure but "rogue reversal" events are not. This procedure is similar to one used in the study of statistical properties of magnetic switches in the geodynamo problem (Valet *et al.* 2012; Lhuillier *et al.* 2013). For a sufficiently large number of recorded events, the average over these rescaled curves is expected to remove the noisy dynamics and to represent a *generic reversal cycle* (figure 5 right). This averaging technique, once applied to E_{kin} and E_{apot}, recovers the evolution of mechanical energies during the generic reversal cycle.

   Figure 6 shows the $L_{2D}/\overline{|L_{2D}|}$ curves for generic reversal cycle at $Pr = 3.0$: as we increase Ra, the reversal cycle becomes more regular and the band representing the standard deviation narrows. The same averaging procedure can be applied to instantaneous temperature and velocity fields in order to obtain the evolution of a conditionally averaged temperature $\theta^o(x, y, t)$ and velocity $\vec{u}^o(x, y, t)$ fields during the reversal cycle (e.g. figure 7 for $(Ra = 5 \cdot 10^7, Pr = 3.0)$). Despite fluctuations between various realisations, dominant and persistent structures appear at specific times of the generic cycle.
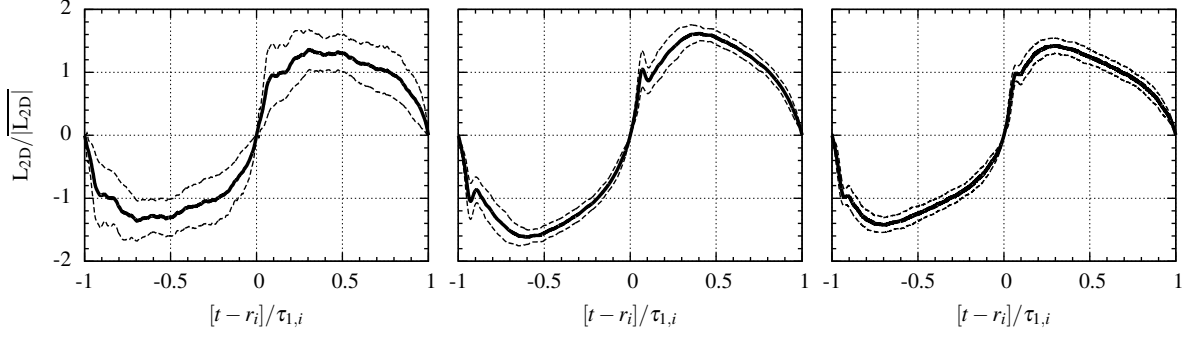
FIGURE 6. Curves corresponding to reversals for Pr = 3.0 as obtained using the procedure described in figure 5. The average $L_{2D}/\overline{|L_{2D}|}$ is shown in thick lines and one standard deviation in dashed lines. From left to right: a) Ra = 10^7, b) Ra = $5 \cdot 10^7$, and c) Ra = 10^8.
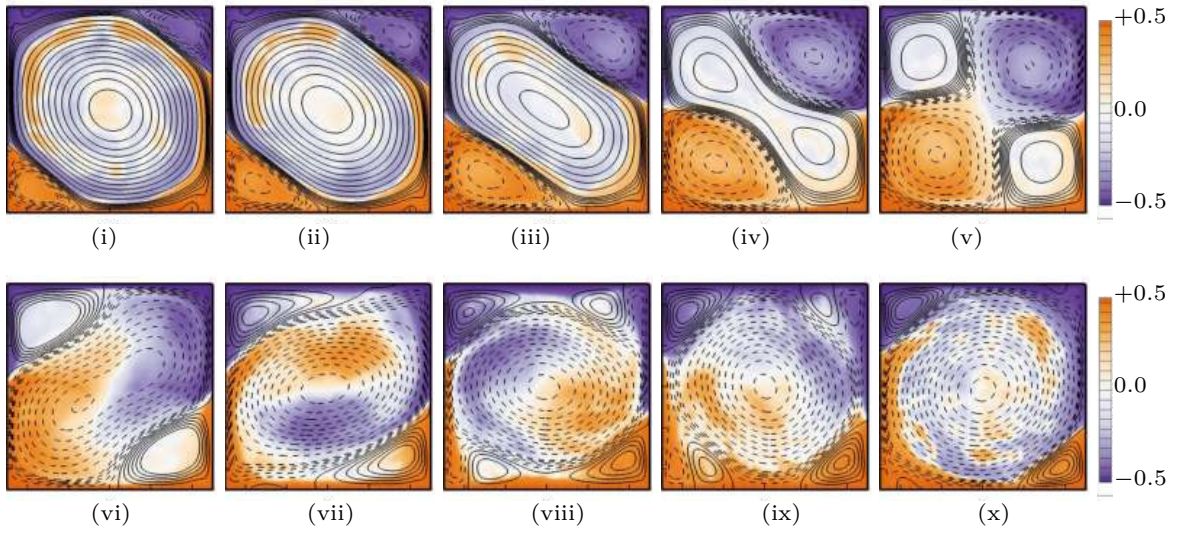
FIGURE 7. Conditionally averaged fields $\vec{u}^o(x,y,t)$ and $y_r(\theta^o(x,y,t))$ at different instants during the generic reversal cycle for (Ra = $5 \cdot 10^7$, Pr = 3.0). Fields are obtained as the ensemble average over 83 particular reversal cycles. Streamlines of the velocity field $\vec{u}^o$ are superposed over the color map of field $y_r(\theta^o)$. Solid and dashed streamlines indicate the two senses of rotation.

5.2. *Phases of reversal cycle*

In the phase space $(L_{2D}/\overline{|L_{2D}|}, E_{kin}/\overline{|E_{kin}|}, E_{apot}/\overline{|E_{kin}|})$, let us consider the generic reversal cycle (figure 8). Consecutive instants (a)-(b)-(c)-(d)-(e) pinpoints particular dynamical times: $L_{2D} = 0$ at instant (a); E_{kin} reaches a local maximum at instant (b), E_{kin} reaches a local minimum at instant (c); E_{apot} reaches its minimum at instant (d); $|L_{2D}|$ reaches its maximum at instant (e). Points (a')-(b')-(c')-(d')-(e') are similar but correspond to an opposite rotation sign. Based on these instants, three successive phases are identified for the generic reversal cycle. They are called *accumulation*, *release* and *acceleration*.

The *accumulation* phase is located between points (e') and (a). It is characterised by a steady accumulation of E_{apot} and a progressive decay of $|L_{2D}|$ and E_{kin}. This phase ends when E_{apot} reaches a maximum and E_{kin} a minimum (figure 8). In terms of generic velocity field $\vec{u}^o(x,y,t)$, a central vortex is present during this phase (see figures 7 i to iii) until the global rotation switches signs at point (a) i.e. $L_{2D} = 0$ (figure 7 iv).

The *release* phase located between points (a) and (d), is defined by a sudden exchange from E_{apot} to E_{kin}. It can be split in three sub-steps. The first step from point (a) to point (b) contains a rapid increase of E_{kin} to a maximum value and a rapid decrease of
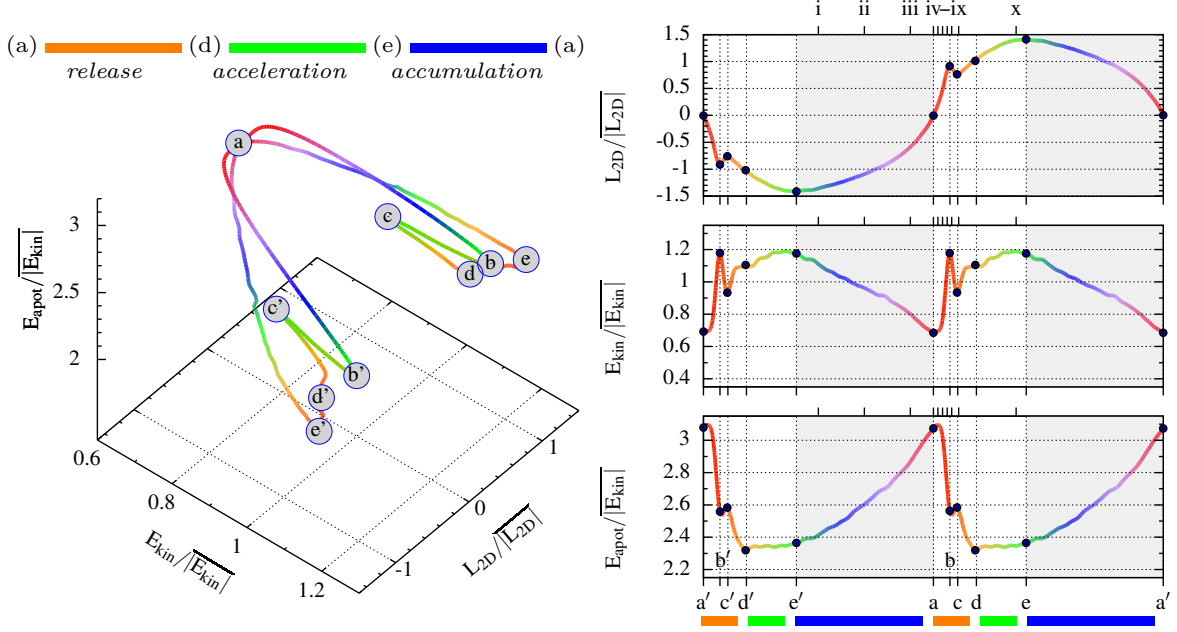
FIGURE 8. Generic reversal cycle for $(\mathrm{Ra} = 5 \cdot 10^7, \mathrm{Pr} = 3.0)$. Left panel: system trajectory in phase space $(\mathrm{L_{2D}}/\overline{|\mathrm{L_{2D}}|}, \mathrm{E_{kin}}/\overline{|\mathrm{E_{kin}}|}, \mathrm{E_{apot}}/\overline{|\mathrm{E_{kin}}|})$; Right panel from top to bottom: average curves for $\mathrm{L_{2D}}/\overline{|\mathrm{L_{2D}}|}$, $\mathrm{E_{kin}}/\overline{|\mathrm{E_{kin}}|}$ and $\mathrm{E_{apot}}/\overline{|\mathrm{E_{kin}}|}$. Marks (i-x) and (a-e) indicate particular instants (see text for explanations). The accumulation phase is shaded and indicated by a blue colour bar. The release (resp. acceleration) phase is indicated by an orange (resp. green) colour bar. The same colour code is used in the phase space trajectory position.
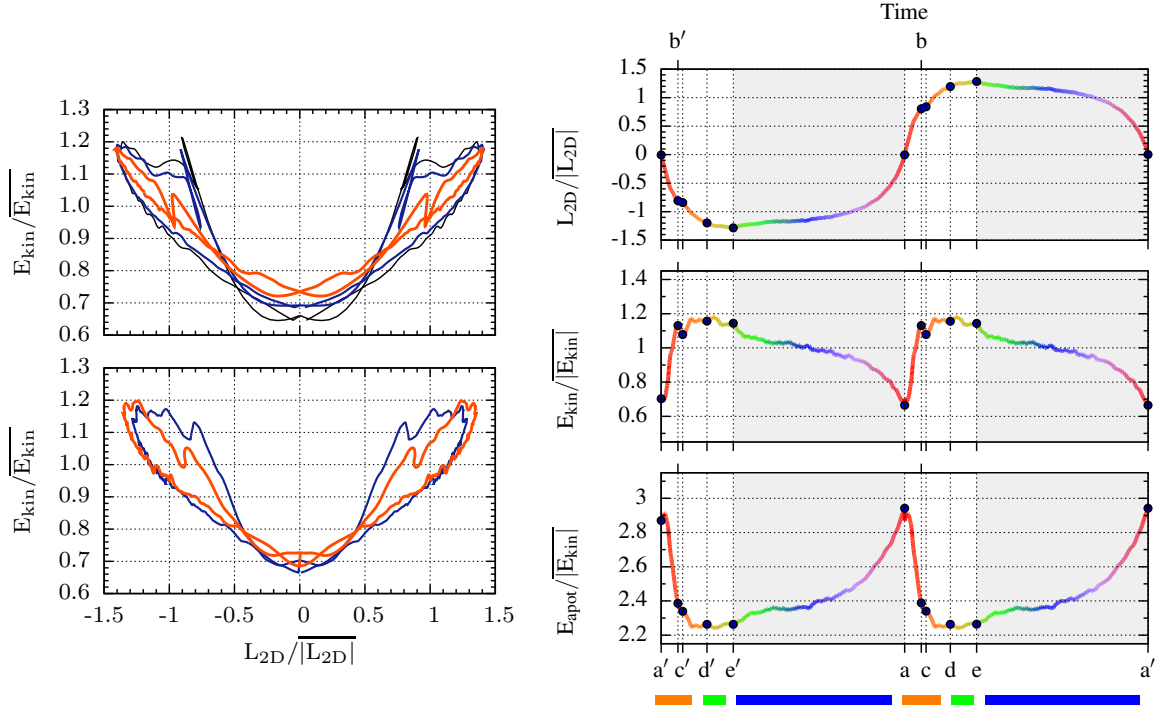
FIGURE 9. Left panel: generic reversal curves in the plane $(\mathrm{L_{2D}}/\overline{|\mathrm{L_{2D}}|}, \mathrm{E_{kin}}/\overline{|\mathrm{E_{kin}}|})$. Each curve corresponds to a different Ra: $\mathrm{Ra} = 3 \cdot 10^7$ (———), $\mathrm{Ra} = 5 \cdot 10^7$ (———), and $\mathrm{Ra} = 10^8$ (———). Top figure correspond to Pr = 3.0 and bottom one to Pr = 4.3. Right panel: average curves during one cycle for $\mathrm{L_{2D}}/\overline{|\mathrm{L_{2D}}|}$, $\mathrm{E_{kin}}/\overline{|\mathrm{E_{kin}}|}$ and $\mathrm{E_{apot}}/\overline{|\mathrm{E_{kin}}|}$ for $(\mathrm{Ra} = 5 \cdot 10^7, \mathrm{Pr} = 4.3)$. Figures are displayed as in figure 8 .

E_{apot}. It corresponds to figures 7 v to vii. A second step follows from points (b) to (c) in which E_{kin} suddenly decreases and E_{apot} remains almost constant. This is associated with figures 7 viii to ix. After these two steps referred to as a *rebound*, a new increase of E_{kin} is observed from points (c) to (d) concomitantly with a decrease of E_{apot} until it reaches its minimum value.

Finally, the *acceleration* phase is located between points (d) and (e) and is characterised by an increase of $|L_{2D}|$ and E_{kin} to peak values, whereas E_{apot} remains almost constant. During this period, the flow reorganises gradually into a single dominant vortex (figure 7x).

For the (Ra, Pr) considered inside the CR regime, we are able to recover a generic reversal cycle expressed in terms of the available mechanical energy (figure 9). Similarities between these curves for different (Ra, Pr) suggest an equivalent underlying mechanism behind flow reversals, even if the intensity of the rebound decreases with Pr. For $(Ra = 5 \cdot 10^7, Pr = 3.0)$, the accumulation phase lasts longer (60%), while the release and acceleration phases have shorter and similar durations (respectively 18% and 22% of the reversal cycle). For the range of Ra considered these proportions are similar: for instance, the accumulation, release, and acceleration are observed to last 75%, 13%, and 12% of the reversal cycle for $(Ra = 10^8, Pr = 3.0)$.

6. Dynamics of a particular reversal

From now on, we focus on a single value of (Ra, Pr) $(Ra = 5 \cdot 10^7, Pr = 3.0)$ in order to explore the nature of the reversal dynamics. To look at the small-scales effects, the analysis below considers particular realisations of reversal cycles rather than conditionally averaged fields.

For each particular reversal cycle, we define similarly to the generic curve, consecutive instants (a_p)-(b_p)-(c_p)-(d_p)-(e_p) which pinpoints the dynamical times: $L_{2D} = 0$ at instant (a_p); E_{kin} reaches a local maximum at instant (b_p), E_{kin} reaches a local minimum at instant (c_p); E_{apot} reaches its minimum at instant (d_p); $|L_{2D}|$ reaches its maximum at instant (e_p).

6.1. *Time evolution of the available mechanical energy and flow structures*

The spatial distribution of *mechanical energy* can be linked to flow structures observed during different phases of a reversal cycle. At the beginning of the *accumulation* phase (point (e_p')), a large diagonal vortex with small counter-rotating corner-flows is observed (top figure 10). On the one hand, it corresponds to a state of maximum kinetic energy condensed inside the central vortex (bottom figure 10). On the other hand, the integrand $Pr \int (y_r - y)$ of E_{apot} is mostly distributed inside the corner-flows or along thin thermal boundary layers (top figure 11). The field $\nabla y_r \cdot \nabla \theta$ is used to highlight the contour of thermal plumes (bottom figure 11). This field is related to the spatial distribution of Φ_d (see equation 2.11). Small-scale thermal plumes are observed to be detached from the thermal boundary layers. They are then swept by the central vortex. Plumes are channelled into the corner-flows, directly or after having been advected along the side-walls. The progressive growth of corner-flows is illustrated on figures 10 and 11. This is consistent with previous observations by (Sugiyama *et al.* 2010) that tied the time evolution of the corner-flows height. The steady increase in E_{apot} coincides with a deceleration of the central vortex and to a build-up of thermal energy inside the corner-flows. Indeed, let us compute the contributions to E_{apot} due to the region of thermal boundary layers (BL) and the bulk. The hot and cold BL are taken to have a constant
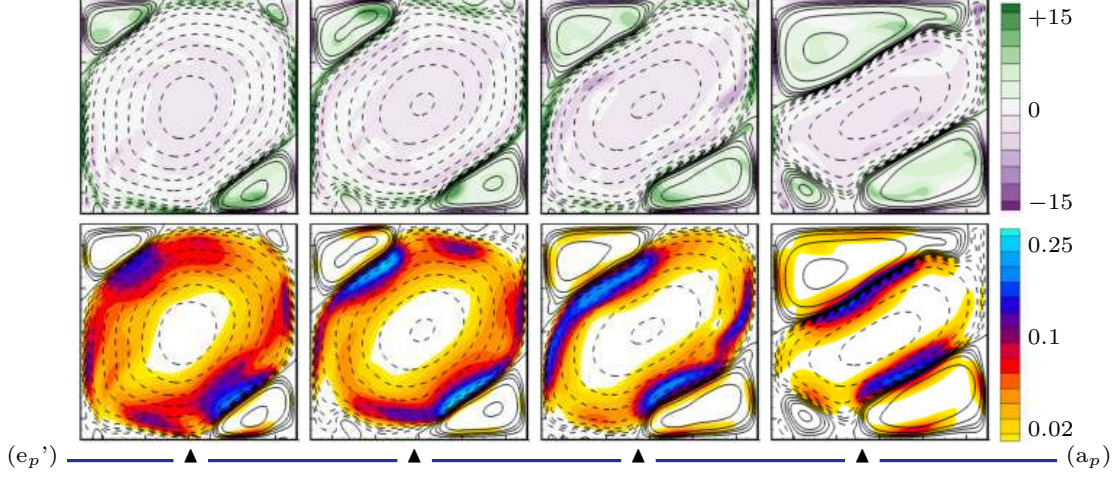
FIGURE 10. Instantaneous fields for a particular reversal cycle during the *accumulation* phase at regular time intervals at $(\mathrm{Ra} = 5 \cdot 10^7, \mathrm{Pr} = 3.0)$. The first snapshot follows point (e_p') the last precedes point (a_p). Streamlines are superposed either to vorticity ω (top figures), or to kinetic energy $\frac{1}{2}u_i u_i$ (bottom figures).
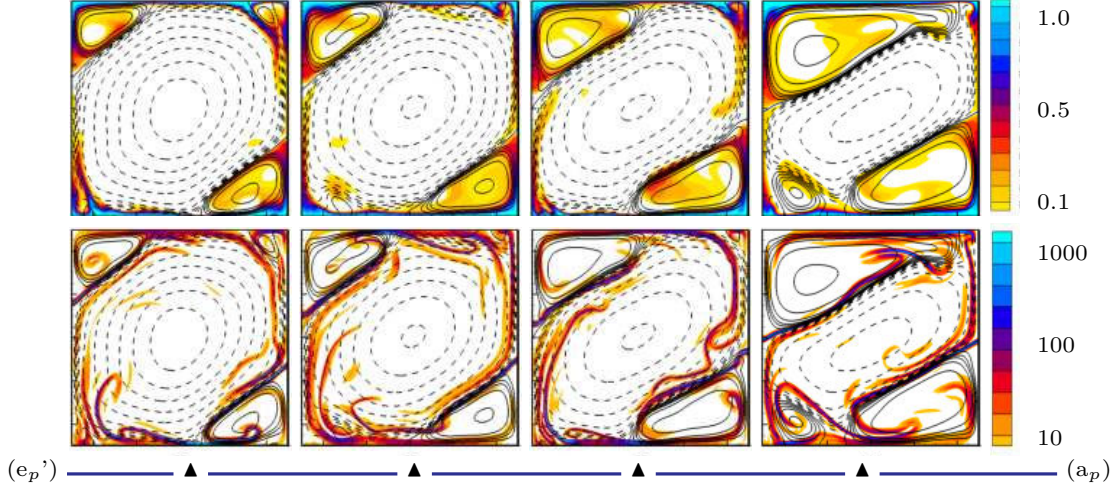
FIGURE 11. Instantaneous fields for a particular reversal cycle during the *accumulation* phase. They are identical to those of figure 10 but streamlines are superposed either to the field $\mathrm{Pr}(y_r - y)\theta$ (top figures) or to the field $\nabla y_r \cdot \nabla \theta$ (bottom figures). Snapshots correspond to the same instants as in figure 10.
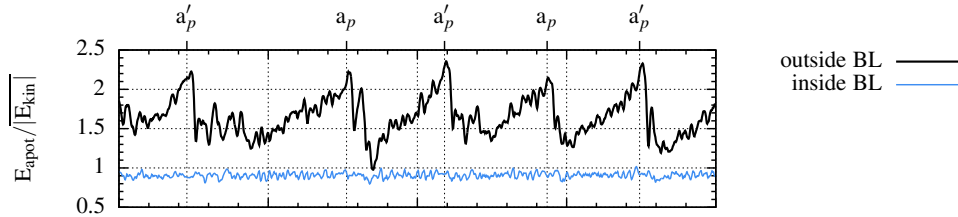
FIGURE 12. Evolution of $\mathrm{E}_{\mathrm{apot}}$ contained within the thermal boundary layers (———) and outside (———) at $(\mathrm{Ra} = 5 \cdot 10^7, \mathrm{Pr} = 3.0)$.

thickness $\delta_\theta^{-1} = 2\overline{\mathrm{Nu}}$. Contributions inside both BL (figure 12) amount to 30-40% of $\overline{\mathrm{E}_{\mathrm{apot}}}$ and are fairly constant in time: standard deviation is less than 1%. On the contrary, contributions to $\mathrm{E}_{\mathrm{apot}}$ from outside BL are directly influenced by the reversal cycle: a steady increase is observed during the *accumulation phase* until the *release* phase (figure 12) . This suggests that the energy exchange observed during the *release* takes place only inside the bulk, while the boundary layers seem to be largely unaffected by the reversals.
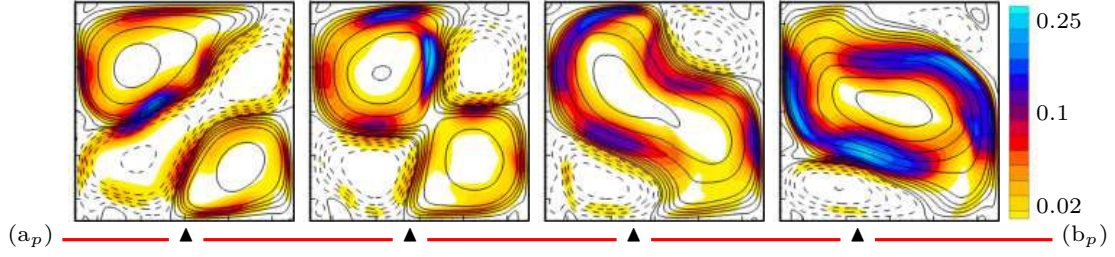
FIGURE 13. Instantaneous fields for a particular reversal cycle during the *early release* phase (point (a_p)-(b_p)) at regular time intervals ($\mathrm{Ra} = 5 \cdot 10^7, \mathrm{Pr} = 3.0$). Streamlines are superposed to the field $\frac{1}{2}u_i u_i$. First snapshot follows point (a_p), last precedes point (b_p).
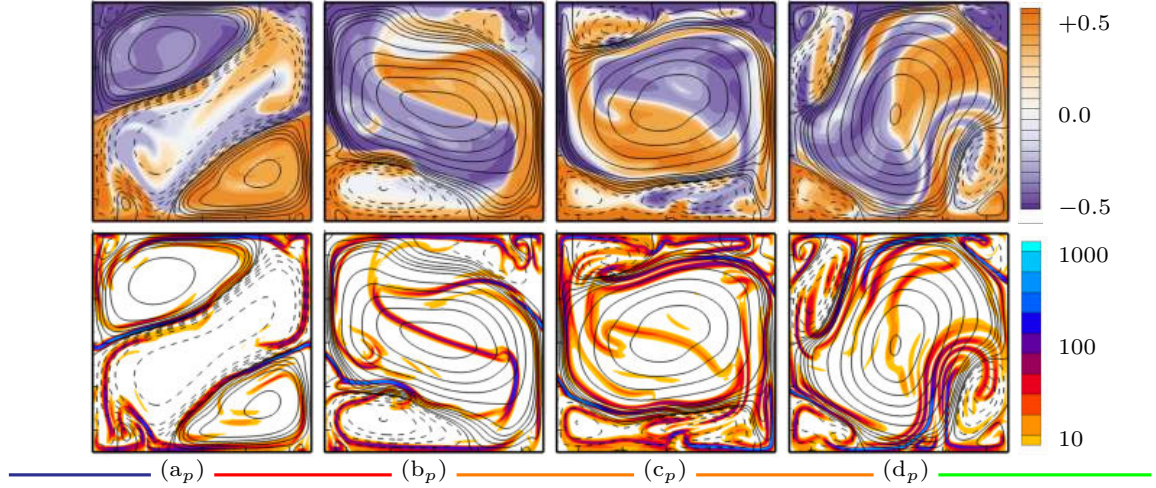
FIGURE 14. Instantaneous fields for a particular reversal cycle during the *release* phase at ($\mathrm{Ra} = 5 \cdot 10^7, \mathrm{Pr} = 3.0$). Snapshots correspond to points (a_p) to (d_p). Streamlines are superposed to either the field $y_r(x, z, t)$ (top figures), or to field $\nabla y_r \cdot \nabla \theta$ (bottom figures).

During the first part of the *rebound* (points (a_p) to (b_p)), the opposing corner-flows have become large and strong enough to deform and finally split the central vortex (figure 13): opposing corner-flows then connect and form a single vortex (with opposite rotation with respect to the previous LSC). This allows the thermal energy stored inside corners to be rapidly released and transformed into kinetic energy. By the end of this exchange, the amount of thermal energy $\mathrm{E_{apot}}$ stored outside the thermal boundary layers will be halved (figure 12). The complete *rebound* period (point (a_p)-(c_p)) can be better illustrated by highlighting the role of the thermal plumes and boundary layers. To do so, one uses $y_r(x, y, t)$ which is a bijective function of temperature, and function $\nabla y_r \cdot \nabla \theta$ in figure 14. Once the vortex reconnection has taken place, the blobs of hot (resp. cold) fluid which are now inside the main central vortex, are allowed to travel upwards (resp. downwards) directly into the bulk. This results in the exchange of potential energy (contained inside small scale structures) into kinetic energy (contained inside the central vortex). The newly formed circulation proceeds to rotate and is able to advect thermal blobs against the action of buoyancy forces (as seen between points (b_p) and (c_p) figure 14). Simultaneously as the thermals are released into the bulk, the surface separating hot and cold fluid increases which reinforces the mixing process (bottom figures 14).

The *acceleration* phase is illustrated on figure 15. Self-organisation of the LSC takes place, during which the kinetic energy and the angular impulse arrive to peak values. During that phase, the bulk contains less and less plumes: temperature becomes nearly homogeneous. By the end of this phase the flow settles to a large diagonal roll with small corner-flows.

FIGURE 15. Instantaneous fields for a particular reversal cycle taken at regular intervals during the *acceleration* phase at $(\mathrm{Ra} = 5 \cdot 10^7, \mathrm{Pr} = 3.0)$. The first snapshot follows point (d_p); the last corresponds to point (e_p). Streamlines are superposed either to vorticity ω (top figures), or to $\nabla y_r \cdot \nabla \theta$ (bottom figures).
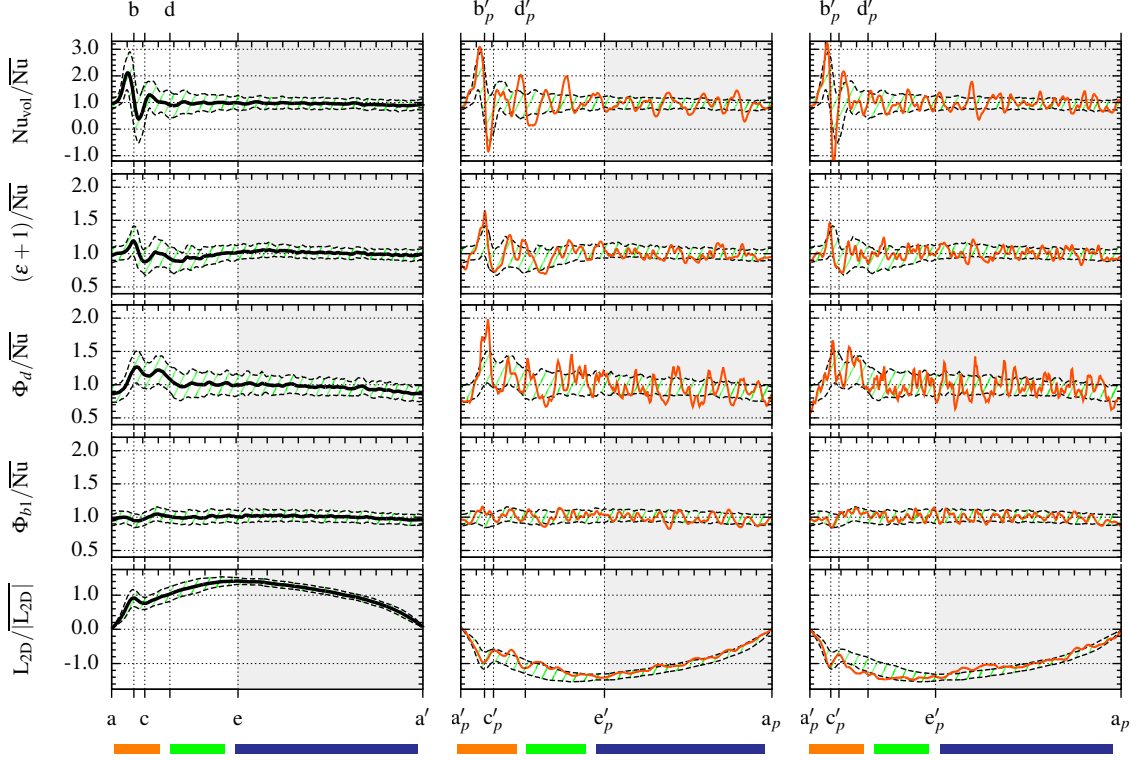
FIGURE 16. Time evolution of the energy transfer rates. From top to bottom: normalised $\mathrm{Nu}_{\mathrm{vol}}/\overline{\mathrm{Nu}}$, $(\epsilon + 1)/\overline{\mathrm{Nu}}$, $\Phi_d/\overline{\mathrm{Nu}}$, , $\Phi_{b1}/\overline{\mathrm{Nu}}$ for $(\mathrm{Ra} = 5 \cdot 10^7, \mathrm{Pr} = 3.0)$. Figure for $\mathrm{L_{2D}}/|\overline{\mathrm{L_{2D}}}|$ is given as a reference curve. The left figure corresponds the generic reversal: the curve in —— corresponds to the average, while the hatched region represent one standard deviation from this average. The center and right figures correspond to particular reversals displayed in —— alongside the standard deviation.

6.2. *Mechanical energy transfer rates*

Figure 16 displays the evolution of energy transfer rates (given in equations 2.6 to 2.12) for a generic reversal cycle as well as for two particular reversal cycles. More precisely, the bulk terms $\mathrm{Nu}_{\mathrm{vol}} = \Phi_y + 1$, $\epsilon + 1$, Φ_d, and boundary term $\Phi_{b1} = \frac{1}{2}(\mathrm{Nu}_{\mathrm{top}} + \mathrm{Nu}_{\mathrm{bot}})$ normalised by $\overline{\mathrm{Nu}}$ are presented. First, note that, while the time-averaged quantities $\bar{\epsilon}+1$,
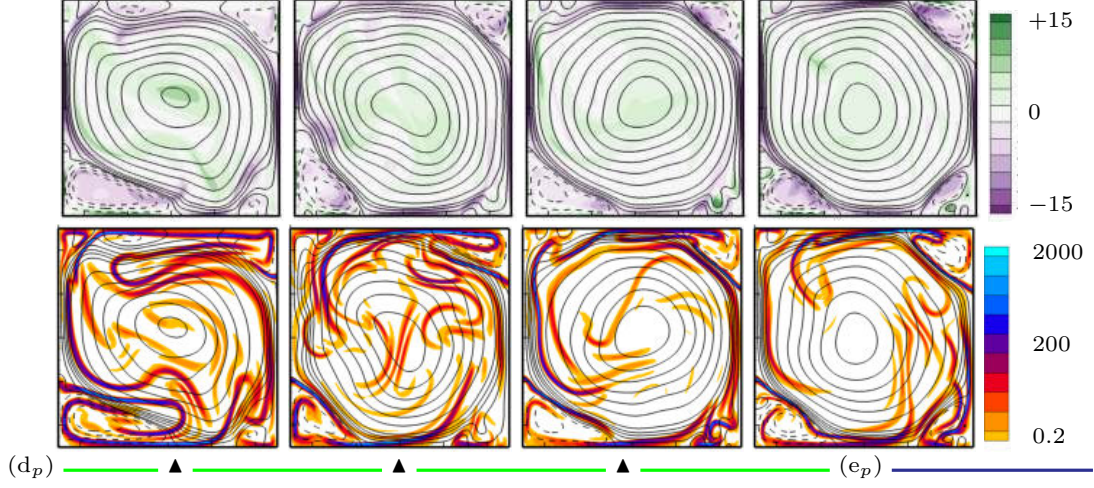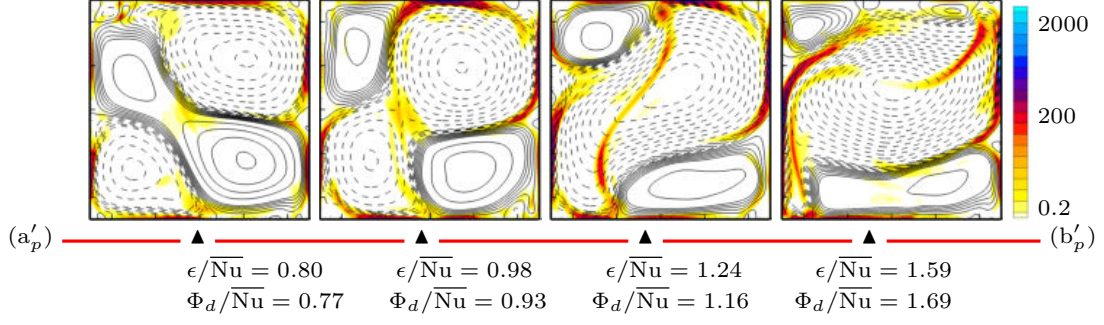
FIGURE 17. Instantaneous fields for a particular reversal cycle taken at regular intervals during the *early release* phase at $(\mathrm{Ra} = 5 \cdot 10^7, \mathrm{Pr} = 3.0)$. The first (resp. last) snapshot follows point (a'_p) (resp. precedes point (b'_p)). Streamlines are superposed to field $2e_{ij}e_{ij}$ the value of which is given by the colour. Corresponding values of ϵ and Φ_d below each snapshot.

$\overline{\Phi_d}$ and $\overline{\Phi_{b1}}$ converge to $\overline{\mathrm{Nu}}$, each corresponding term has a specific behaviour during the different phases of the reversal cycle. Let us describe each instantaneous transfer rates in turn.

The vertical heat flux $\mathrm{Nu}_{\mathrm{vol}}$ which measures the conversion from $\mathrm{E}_{\mathrm{apot}}$ to $\mathrm{E}_{\mathrm{kin}}$ (see equations 2.7 and 2.8), is by far the term that is found the most fluctuating, notably during the *release*. During the first part of the *rebound* i.e. the interval between points (a_p) and (b_p) (resp. (a) and (b)) for the particular reversal (resp. for the generic curve), $\mathrm{Nu}_{\mathrm{vol}}$ reaches peak values which are several times larger than $\overline{\mathrm{Nu}}$. This is related to the release of thermal energy $\mathrm{E}_{\mathrm{apot}}$ (figure 8) and plumes (figure 14). Between points (b) and (c), the generic $\mathrm{Nu}_{\mathrm{vol}}$ abruptly decreases. In terms of a particular realisation, this is due to the rotation of the bulk acting against buoyancy forces (points (b_p) and (c_p) in figure 14) and may result in a negative heat transfer as seen in figure 16 for the particular reversal cycle. This is consistent with results from (Chandra & Verma 2013). During the acceleration and accumulation phases, $\mathrm{Nu}_{\mathrm{vol}}$ fluctuates less and slightly decreases.

In addition to $\mathrm{Nu}_{\mathrm{vol}}$, the viscous dissipation rate ϵ governs the evolution of $\mathrm{E}_{\mathrm{kin}}$ (see equation 2.7). Viscous dissipation increases briefly during the re-organisation periods: once during the *release* phase around point (b), and again during the rotation of the central vortex between points (c) and (d). A gradual increase in ϵ is observed during the *acceleration* phase, between points (d) and (e), followed by a progressive decay during the *accumulation* phase. For a particular reversal cycle, contributions to the viscous dissipation rate ϵ are located (see figure 17) primarily along the vertical side-walls and along the horizontal plates where ascending (resp. descending) plumes collide.

In addition to $\mathrm{Nu}_{\mathrm{vol}}$, $\mathrm{E}_{\mathrm{apot}}$ is governed by the mixing term Φ_d (see equation 2.12). As seen in fields $\nabla y_r \cdot \nabla \theta$ on figures 14 and 15, contributions to Φ_d are distributed along thin filaments which trace the contour of thermal plumes. Φ_d is thus affected by small scales and fluctuates during all the process.

However, fluctuations are slightly larger during the second part of the *release* phase (points (b_p) to (d_p)). An increase on such mixing fronts during the rotation of the bulk leads to the corresponding increase of Φ_d. Note that during the *accumulation* phase, the generic curve for Φ_d slightly decreases. Finally, the forcing boundary term Φ_{b1} does not fluctuate much on the whole cycle.

To summarize, the dominant mechanisms during the release phase are first the energy conversion $\mathrm{Nu}_{\mathrm{vol}}$ followed by the mixing Φ_d during the rebound. The acceleration phase is characterized by the increase of the viscous dissipation ϵ. A constant decay of both dissipation ϵ and mixing Φ_d processes is conversely observed during the accumulation phase.
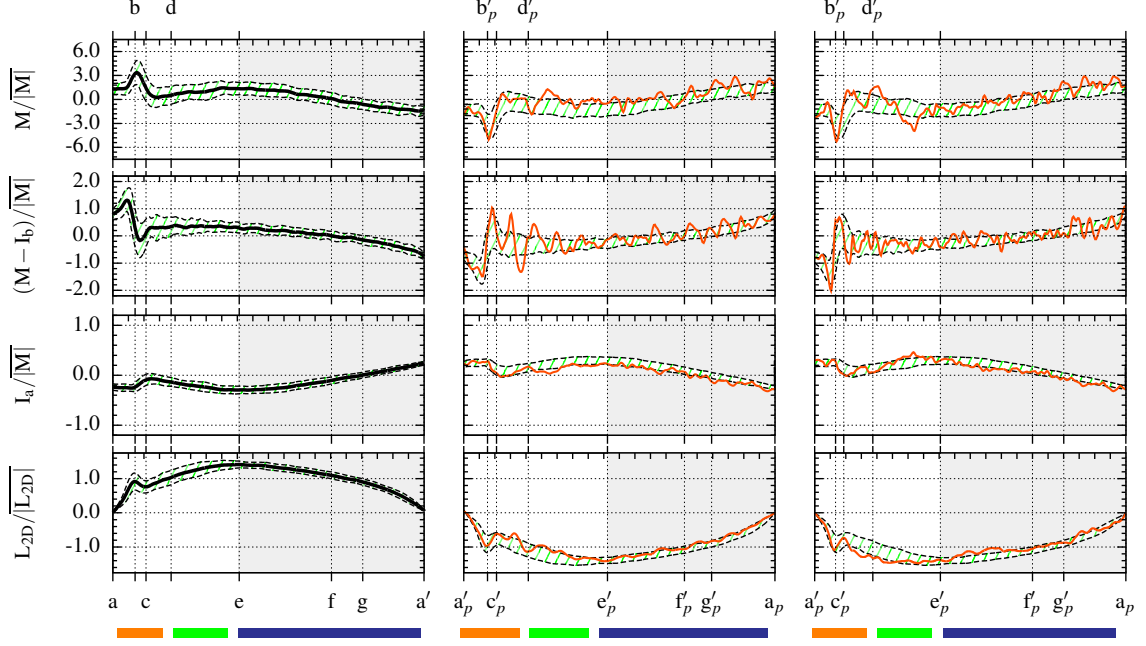
FIGURE 18. Time evolution of the angular impulse transfer rates for $(\mathrm{Ra} = 5 \cdot 10^7, \mathrm{Pr} = 3.0)$. From top to bottom: Evolution of $\mathrm{M}/\overline{|\mathrm{M}|}$, $(\mathrm{M} - \mathrm{I_b})/\overline{|\mathrm{M}|}$, and $\mathrm{I_a}/\overline{|\mathrm{M}|}$. Figure for $\mathrm{L_{2D}}/\overline{|\mathrm{L_{2D}}|}$ is given as a reference curve. The left figure corresponds to the generic reversal: the average curve is displayed in ——— and the hatched region represents one standard deviation from this average. The center and right figures depict two particular reversal cycles.
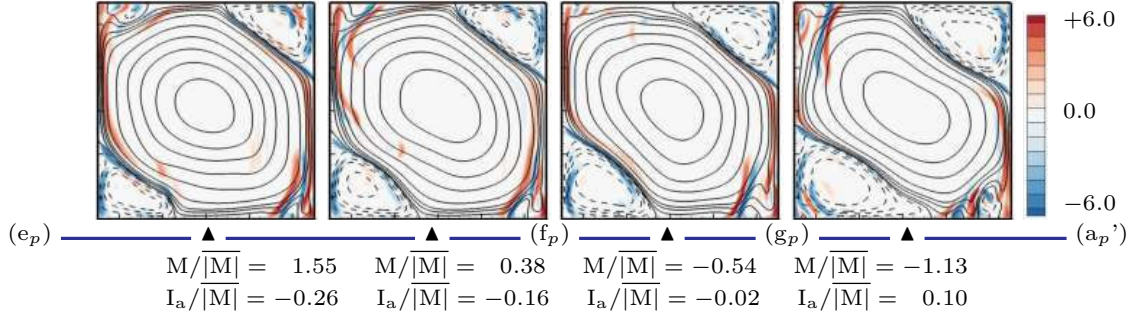
FIGURE 19. Instantaneous fields for a particular reversal cycle taken at regular intervals during the *accumulation* phase at $(\mathrm{Ra} = 5 \cdot 10^7, \mathrm{Pr} = 3.0)$. The first (resp. last) snapshot follows point (e_p) (resp. precedes point (a_p')). Streamlines are superposed to field $0.5(\vec{x} \cdot \vec{x})\partial_x\theta$ (the value is provided by the color code). Corresponding values of M and $\mathrm{I_a}$ are given below each snapshot.

6.3. *Angular momentum transfer rates*

Since the evolution of $\mathrm{L_{2D}}$ is characteristic of flow reversals, it is of interest to examine the angular impulse transfer rates M, $(\mathrm{M} - \mathrm{I_b})$ and $\mathrm{I_a}$ of equation 2.4 (figure 18). In addition to points (a) to (e), we introduce points (f) and (g). These points are located inside the accumulation phase and coincide for point (f) with a change of sign for M and for point (g) with a change of sign for $\mathrm{I_a}$.

Time evolution of the input torque M has a maximum value during the rebound, followed by a local minimum near point (d), a slight increase during the acceleration phase and a monotonic decrease during the accumulation phase. The bulk term $\mathrm{M}(t)$ and the boundary term $\mathrm{I_b}(t)$ are well-correlated and have similar orders of magnitude. This is why only the $\mathrm{M}(t) - \mathrm{I_b}(t)$ evolution is plotted.

Before point (e), the difference $\mathrm{M}(t) - \mathrm{I_b}(t)$ is larger than $\mathrm{I_a}(t)$, from (e) to (f) it is the opposite ($\frac{\mathrm{dL_{2D}}}{\mathrm{dt}}$ changes sign). One may discriminate three time periods: from (a)

to (f), I_a opposes L_{2D} (i.e. the central vortex), contrary to the torque M or $(M − I_b)$; from (f) to (g), I_a opposes L_{2D} similarly to M or $(M − I_b)$; and finally, from (g) to (a), I_a contributes to L_{2D} which is opposed by M or $(M − I_b)$. During the accumulation phase, the integrand $0.5\text{Pr}[\vec{x} \cdot \vec{x}]\partial_x\theta$ of the input torque M(t) is spatially distributed as follows (figure 19): it is negligible inside the bulk, and concentrated in two regions, i.e. along vertical side-walls associated with the central vortex and inside corners-flows. In these two regions they are overall of opposite sign. At point (f), M(t) changes sign: the corner-flows become dominant in the integrand of M(t) and the overall torque is then opposing the central vortex (figure 18). Similarly, during the accumulation phase, the integrand of I_a that is vorticity, is distributed in two sectors along the boundaries: one along the boundaries of the central vortex, and another of opposite sign along the top and bottom corners (figure 10). From point (g), I_a has changed sign: this is related to the dominant contribution of the corner-rolls.

As a consequence, it is noteworthy that the input torque M(t) changes sign at point (f) long before the reversal time (point (a)). The interval from point (f) to point (g) can be seen as a transition period from a central vortex-dominated to a corner-rolls-dominated flow.

7. Mechanism of transitions

7.1. *Linear stability approach*

The significance of instant (g) where I_a changes sign, is tentatively explained by two complementary approaches. In a first approach, one considers the following hypothesis: the change occurring in the *accumulation* phase near point (g), is due to a modification of the dynamics governing fluctuations around large scale structures. The large scale structures identified by fields $\theta^o(x, y, t)$ and $\vec{u}^o(x, y, t)$ are here obtained by an ensemble average over many realisations (see section 5.1). A linear stability analysis is thus defined. The base state at time t_o is given by fields $\theta^o(x, y, t_o)$ and $\vec{u}^o(x, y, t_o)$ frozen at this particular time. The evolution of infinitesimal fluctuations $\theta'(x, y, t)$ and $\vec{u}'(x, y, t)$ is studied around this frozen base state. The linear stability analysis is performed by direct numerical simulations of the linearised Boussinesq equations,

$$\begin{cases} \boldsymbol{\nabla} \cdot \vec{u}' &= 0 \\ \partial_t\vec{u}' + \boldsymbol{\nabla} \cdot [\vec{u}' \otimes \vec{u}^o + \vec{u}^o \otimes \vec{u}'] &= -\boldsymbol{\nabla}p' + \text{PrRa}^{-0.5}\boldsymbol{\nabla}^2\vec{u}' + \text{Pr}\theta'\vec{e}_y \\ \partial_t\theta' + \boldsymbol{\nabla} \cdot [\vec{u}'\theta^o + \vec{u}^o\theta'] &= \text{Ra}^{-0.5}\boldsymbol{\nabla}^2\theta' \end{cases} \quad (7.1)$$

Each linearized simulation starts with random disturbances of velocity and temperature fields and is computed for several hundred time units. The perturbation kinetic energy $\langle u_i' u_i' \rangle_{\text{vol}}$ or the square of the fluctuation temperature $\langle \theta'\theta' \rangle_{\text{vol}}$ are monitored in time. In figure 20, each curve is related to a different base state t_o. Positive values of growth rate σ are obtained in all cases.

For t_o before transition point (g), the values of σ are quite small ($\sim 10^{-3} − 10^{-2}$) and the most amplified mode corresponds to a trace of the base state itself (see figure bottom left 20). This is possibly related to a slow variation in time of the large scale flow. In contrast, once point (g) is reached, the growth rate σ increases by a factor of 20, while a different most amplified mode appears. This amplified mode is reminiscent of the flow features observed in the bottom right corner of figure 10.

7.2. *Non-linear approach with adiabatic boundary conditions*

We have identified through a linear stability analysis a critical generic state around point (g). Let us now seek to relate this state to the "avalanche" mechanism: a mechanism
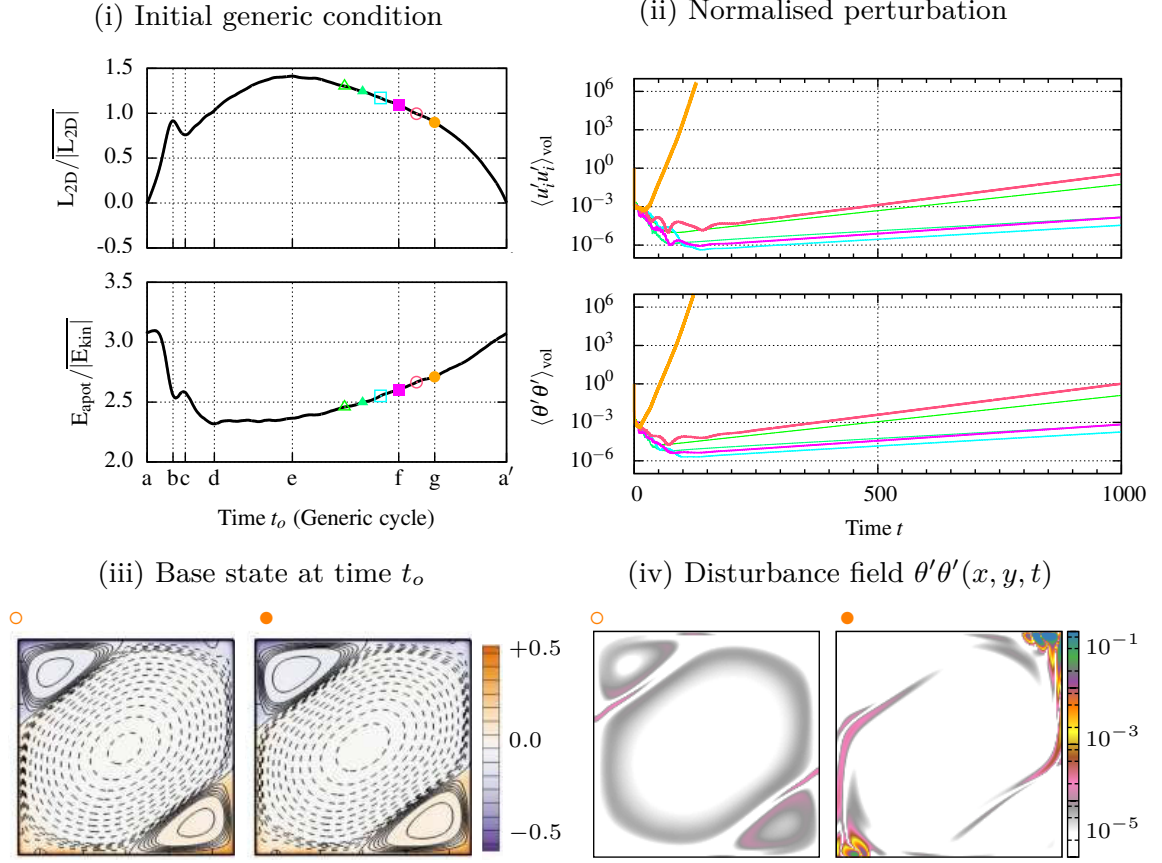
FIGURE 20. Linear stability analysis of the generic fields for $(\text{Ra} = 5\cdot10^7, \text{Pr} = 3.0)$. (i) Placement of the different values of t_o with respect to the generic L_{2D} and E_{apot} curves. (ii) Evolution of the energy of the normalised velocity and temperature perturbations for different base states (or equivalently t_o). Growth rate σ measured for different values of t_o: $\triangle$ $\sigma = 0.009$, $\blacktriangle$ $\sigma = 0.005$, $\square$ $\sigma = 0.005$, $\blacksquare$ $\sigma = 0.006$, $\circ$ $\sigma = 0.011$, $\bullet$ $\sigma = 0.250$; (iii) Streamlines corresponding to field $\vec{u}^o(x,y,t_o)$ superposed to base state $\theta^o(x,y,t_o)$ shown for two values of t_o: $\circ$ located between points (f) and (g) and $\bullet$ located on point (g). (iv) Disturbance field $\theta'\theta'(x,y,t)$ measured at the end of the curves corresponding to $\circ$ and $\bullet$.

due to a localised accumulation of energy inside the fluid which is followed by a sudden transition. One could argue that, when localised accumulation is sufficient, a reversal event takes place even if the external thermal forcing is thereafter suppressed. A second approach, which is non-linear, is based on this idea and confirms point (g) as a transition point associated to a threshold state.

First, let us consider the conditionally averaged fields $(\theta^o(x,y,t_o)$ and $\vec{u}^o(x,y,t_o))$ obtained at time t_o for the standard RB problem, see figure 7. Starting from such fields labeled by time t_o, we perform a direct numerical simulation of the non-linear Boussinesq equations changing boundary conditions from isothermal to adiabatic on the top and bottom plates. This effectively suppresses the external thermal forcing since $\Phi_{b1} = \Phi_{b2} = 0$ and limits the amount of thermal energy contained inside the cavity. Note that, different initial conditions i.e. different t_o lead to different trajectories for the adiabatic problem.

Evolution of the normalised kinetic energy $\text{E}_{\text{kin}}/\overline{|\text{E}_{\text{kin}}|}$ and the normalised angular impulse $\text{L}_{2D}/\overline{|\text{L}_{2D}|}$ can be seen in figure 21, where each curve corresponds to different t_o (shown as $\circ$ marks) inside the accumulation phase. Dashed (resp. solid) lines indicate negative (positive) values of $\text{L}_{2D}/\overline{|\text{L}_{2D}|}$. For simulations preceding the transition point (g) a decay in both the angular impulse and the kinetic energy are observed. On the contrary, from point (g) on, a change from negative to positive values of $\text{L}_{2D}/\overline{|\text{L}_{2D}|}$ simultaneously as peak values in $\text{E}_{\text{kin}}/\overline{|\text{E}_{\text{kin}}|}$ are observed, before the ensuing decay. To illustrate this
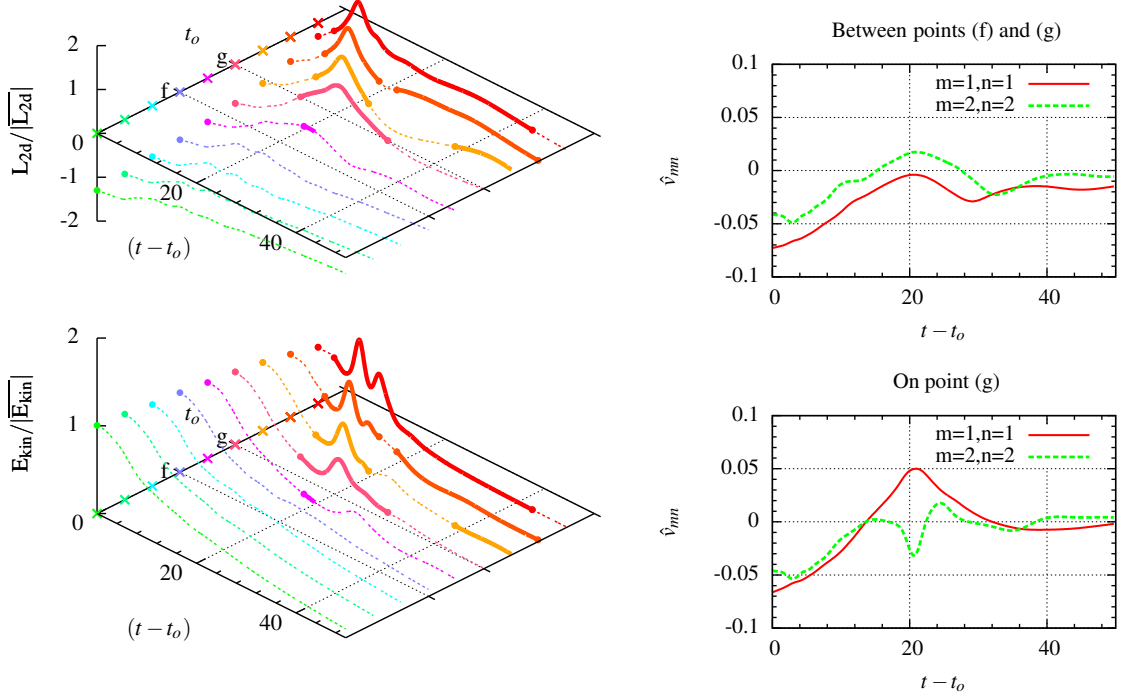
FIGURE 21. Left panel: normalized angular impulse $|L_{2D}|/\overline{|L_{2D}|}$ (top) and normalized kinetic energy $E_{kin}/\overline{|E_{kin}|}$ (bottom) for $(Ra = 5 \cdot 10^7, Pr = 3.0)$ as a function of t_o characterizing the base state and time $(t - t_o)$. Each curve represents different initial conditions i.e. different t_o, where solid lines indicate when a flow reversal takes place (see text). Right panel: Evolution of modal coefficients $\hat{v}_{mn}$ from two initial conditions: before and at point (g).

transition we follow the evolution of Fourier modes $\hat{v}_{mn}$ of the vertical velocity for two initial conditions before and after point (g) as seen on figure 21. For initial conditions preceding $I_a = 0$, an already weakened central vortex is unable to contain the corner-flows in place but does not break (the mode $\hat{v}_{11}$ which is related to the monopole decreases but remains negative). On the contrary, for initial conditions following the transition point (g), Fourier coefficient $\hat{v}_{11}$ changes sign and thus indicates a LSC reversal, before the subsequent decay.

8. Comparison with previous works

The present DNS results and their interpretation in terms of dynamical processes may be discussed by comparison with previous experimental data and models. Experimental data (Brown & Ahlers (2006); Xi & Xia (2008a,b)), and models like (Brown & Ahlers (2007, 2008)) are devoted to the study of cylindrical 3D convection cells, where the LSC plane oscillates. They are mostly focused on the dynamics of the angle of the LSC plane which is a different phenomenon from the dynamics studied in this work. Similarly models like (Sreenivasan *et al.* (2002); Benzi (2005)) which are based on non-linear one-dimensional stochastic models, have been compared against experimental data in cylindrical cells. Mainly they attempt to recover the exponential distribution for the PDF of the inter-switch intervals. In 2D systems, such distribution is not observed and again this is probably due to the difference between cessations-driven and rotation-led reversals. Sreenivasan *et al.* (2002) states that reversals can be understood in terms of an imbalance between buoyancy effects and friction, where inertia is playing only a secondary role. In the present study, reversals do require the accumulation of potential energy and point (g) is associated to a threshold state pinpointed by the change of sign of

I_a a quantity related to wall friction. However, the model proposed in Sreenivasan *et al.* (2002) is a local one, which follows a single parcel of fluid, while our understanding of the dynamics depends on the existence of global flow structures. It is also mentioned in Sreenivasan *et al.* (2002) the possible role of side-wall thermal conductivity on reversals, which is excluded here. The model by Araujo *et al.* (2005) is based on the inertia of a plume to initiate the reversal. In our case, inertial effects appear during the rebound: as mentioned in §6.1, the newly formed circulation is able to advect thermal blobs against the action of buoyancy forces. However, this is a direct consequence of the reversal and not the triggering factor. Low order models could be based also on POD modes (Podvin & Sergent (2015, 2016)). This approach allows to rebuild the full dynamics of the velocity and temperature fields. The model proposed in Podvin & Sergent (2015) that uses 3 leading modes, is able to reproduce large-scale features of our DNS results when noise is introduced: reversal and cessation dynamics, and growth of corner flows during the accumulation phase. It is also able to reproduce the characteristic time scales as given in §4. However, the phases predominantly associated in the present work to small scales, such as the acceleration and second part of the release, are by construction not recovered by the model described in Podvin & Sergent (2015). Going back to the threshold state on point (g), the existence of such a point has also been identified through a large scale description of reversals by a POD approach (Podvin & Sergent (2016)). The scenario of the growth of corner flows leading to the release in the case of a square RB cell has been previously proposed by (Chandra & Verma (2013); Sugiyama *et al.* (2010)). Both papers pointed out the feeding of the corner flows by plumes detached from horizontal boundary layers. Our results agree with these findings. But we present this process in a more quantitative way through the use of field $\Pr(y_r - y)\theta$ (see figure 11): in this way, we are able to show that E_{apot} is stored mainly in the corner flows. Neither of the two previous papers quantified the energy exchange between kinetic and potential energy during the release. In the present paper, the energy exchange is clearly demonstrated on figures 8 and 9. Furthermore, the figure 12 shows that the energy exchange takes place between the corner flows and the bulk.

9. Concluding remarks

In this paper we used long-term data from two-dimensional DNS in square RB cells inside the CR regime to perform a statistical characterisation of reversals. Once having removed the samples not contained in the CR regime, a simple time rescaling allowed us to identify a generic reversal cycle in terms of the evolution of three global quantities: the global angular impulse, the global kinetic energy, and available potential energy. Consistent dynamical features were found for different values of $(\mathrm{Ra}, \mathrm{Pr})$, and suggested the existence of a generic reversal mechanism, composed of three successive phases: accumulation, release, and acceleration.

The accumulation phase is characterised by a progressive build-up of thermal energy almost exclusively inside the corners thereby inducing them to grow. During the release phase, an energy exchange takes place from available potential energy to global kinetic energy: the opposing corner-flows connect to form a new central vortex and the thermal energy contained from small-scales is suddenly released into the bulk. A newly formed vortex may complete several turnovers before the temperature differences inside the bulk are reduced. Strong fluctuations in both the angular impulse and the kinetic energy are observed during this process, referred to as a rebound. During the acceleration phase, the global angular impulse and the kinetic energy increase as a result of spontaneous self-organisation of the flow into a large diagonal vortex and two small counter-rotating

corner-flows. During this phase, increased mixing inside the central vortex results in a very homogeneous bulk temperature and almost constant potential energy. We complement this view in terms of the evolution of energy transfer rates.

Finally, in order to identify the presence of a transition between accumulation and release, we propose two approaches. First a linear stability analysis is performed around generic fields $\vec{u}^o(x, y, t_o)$ and $\theta^o(x, y, t_o)$ (obtained as the ensemble average over long term DNS results). A sharp increase in the exponential growth rate σ is shown before the beginning of the release phase. In a second approach, the same transition zone is put into evidence by suppressing the external thermal forcing and letting the system evolve from different initial conditions inside the accumulation phase. The presence of a reversal-type event is an indication that a sufficient amount of thermal energy already being stored in the system triggers the reversal.

This work can be easily extended for 2D cells with different geometries or different boundary conditions. This could provide a complementary view to improve the understanding of reversals in 2D convection, in particular to the role of corner flows. In a future work, we intend to compare more precisely the present findings with results from POD-based models proposed in Podvin & Sergent (2015, 2016). In RB 3D cells, the energy budget has already been used but it was considered only in a time-averaged sense. The instantaneous energy budget used here and the way it is related to flow structures can be extended to 3D cells. Indeed, this approach is currently being implemented by the authors in the particular case of a 3D cell which is very much confined in the transversal direction. Our statistical approach however might be difficult to use in cylindrical convection cells for two reasons: first, one needs a long time signal containing a sufficient number of events. This is a difficult thing to achieve in a fully resolved 3D DNS. Second, the situation is more complex in 3D than 2D since in cessation-led (resp. rotation-led) reversals, the LSC plane changes in time abruptly (resp. through azimuthal or torsional motions). This implies to identify or develop a new criteria to follow the evolution of the LSC. This is a limiting factor for expanding the method to 3D convection case in a cylindrical domain.

Acknowledgements

REFERENCES

Araujo, Francisco Fontenele, Grossmann, Siegfried & Lohse, Detlef 2005 Wind reversals in turbulent Rayleigh-Bénard convection. *Physical Review Letters* **95**, 084502.

Bailon-Cuba, J., Emran, M. S. & Schumacher, J. 2010 Aspect ratio dependence of heat transfer and large-scale flow in turbulent convection. *Journal of Fluid Mechanics* **655**, 152–173.

Bell, Jb, Colella, P & Glaz, Hm 1989 A second-order projection method for the incompressible Navier-Stokes equations. *Journal of Computational Physics* **283**, 257–283.

Benzi, Roberto 2005 Flow reversal in a simple dynamical model of turbulence. *Physical Review Letters* **95** (2), 024502.

Brown, Eric & Ahlers, Guenter 2006 Rotations and cessations of the large-scale circulation in turbulent Rayleigh–Bénard convection. *Journal of Fluid Mechanics* **568**, 351–386.

Brown, Eric & Ahlers, Guenter 2007 Large-scale circulation model for turbulent Rayleigh–Bénard convection. *Physical Review Letters* **98** (13), 134501.

Brown, Eric & Ahlers, Guenter 2008 A model of diffusion in a potential well for the

dynamics of the large-scale circulation in turbulent Rayleigh–Bénard convection. *Physics of Fluids (1994-present)* **20** (7), 075101.

CHANDRA, MANI & VERMA, MAHENDRA K 2011 Dynamics and symmetries of flow reversals in turbulent convection. *Physical Review E* **83** (6), 067303.

CHANDRA, MANI & VERMA, MAHENDRA K. 2013 Flow reversals in turbulent convection via vortex reconnections. *Physical Review Letters* **110**, 114503.

CLERCX, HJH, MAASSEN, SR & VAN HEIJST, GJF 1998 Spontaneous spin-up during the decay of 2d turbulence in a square container with rigid boundaries. *Physical Review Letters* **80** (23), 5129.

FUNFSCHILLING, DENIS, BROWN, ERIC & AHLERS, GUENTER 2008 Torsional oscillations of the large-scale circulation in turbulent Rayleigh-Bénard convection. *Journal of Fluid Mechanics* **607**, 119–139.

GROSSMANN, SIEGFRIED & LOHSE, DETLEF 2003 On geometry effects in Rayleigh-Bénard convection. *Journal of Fluid Mechanics* **486**, 105–114.

HUGHES, GRAHAM O., GAYEN, BISHAKHDATTA & GRIFFITHS, ROSS W. 2013 Available potential energy in Rayleigh-Bénard convection. *Journal of Fluid Mechanics* **729**, R3.

LHUILLIER, FLORIAN, HULOT, GAUTHIER & GALLET, YVES 2013 Statistical properties of reversals and chrons in numerical dynamos and implications for the geodynamo. *Physics of the Earth and Planetary Interiors* **220**, 19–36.

LORENZ, EDWARD N 1955 Available potential energy and the maintenance of the general circulation. *Tellus* **7** (2), 157–167.

MOLENAAR, D., CLERCX, H. J H & VAN HEIJST, G. J F 2004 Angular momentum of forced 2D turbulence in a square no-slip domain. *Physica D: Nonlinear Phenomena* **196**, 329–340.

NI, RUI, HUANG, SHI-DI & XIA, KE-QING 2015 Reversals of the large-scale circulation in quasi-2D Rayleigh–Bénard convection. *Journal of Fluid Mechanics* **778**, R5.

NIEMELA, JJ, SKRBEK, L, SREENIVASAN, KR & DONNELLY, RJ 2001 The wind in confined thermal convection. *Journal of Fluid Mechanics* **449**, 169–178.

PETSCHEL, K, WILCZEK, M, BREUER, M, FRIEDRICH, R & HANSEN, U 2011 Statistical analysis of global wind dynamics in vigorous Rayleigh-Bénard convection. *Physical Review E* **84** (2), 026309.

PODVIN, BÉRENGÈRE & SERGENT, ANNE 2015 A large-scale investigation of wind reversal in a square Rayleigh-Bénard cell. *Journal of Fluid Mechanics* **766**, 172–201.

PODVIN, BÉRENGÈRE & SERGENT, ANNE 2016 On a precursor mechanism for wind reversal in a square Rayleigh-Bénard cell. *submitted* .

VAN DER POEL, ERWIN P., STEVENS, RICHARD J. A. M. & LOHSE, DETLEF 2011 Connecting flow structures and heat flux in turbulent Rayleigh-Bénard convection. *Physical Review E* **84**, 045303.

POPINET, S. 2016 Basilisk. Website, http://basilisk.fr.

RESAGK, CHRISTIAN, DU PUITS, RONALD, THESS, ANDRÉ, DOLZHANSKY, FELIX V., GROSSMANN, SIEGFRIED, FONTENELE ARAUJO, FRANCISCO & LOHSE, DETLEF 2006 Oscillations of the large scale wind in turbulent thermal convection. *Physics of Fluids* **18** (9), 095105.

SHRAIMAN, BORIS I. & SIGGIA, ERIC D. 1990 Heat transport in high-Rayleigh-number convection. *Physical Review A* **42**, 3650–3653.

SREENIVASAN, KATEPALLI R, BERSHADSKII, ALEXANDER & NIEMELA, JJ 2002 Mean wind and its reversal in thermal convection. *Physical Review E* **65** (5), 056306.

STEVENS, RICHARD J. A. M., VERZICCO, ROBERTO & LOHSE, DETLEF 2010 Radial boundary layer structure and Nusselt number in Rayleigh-Bénard convection. *Journal of Fluid Mechanics* **643**, 495–507.

SUGIYAMA, KAZUYASU, NI, RUI, STEVENS, RICHARD J. A. M., CHAN, TAK SHING, ZHOU, SHENG-QI, XI, HENG-DONG, SUN, CHAO, GROSSMANN, SIEGFRIED, XIA, KE-QING & LOHSE, DETLEF 2010 Flow reversals in thermally driven turbulence. *Physical Review Letters* **105**, 034503.

SUTHERLAND, BRUCE R 2010 *Internal gravity waves*. Cambridge University Press.

TSENG, YU HENG & FERZIGER, JOEL H. 2001 Mixing and available potential energy in stratified flows. *Physics of Fluids* **13** (5), 1281–1293.

VALET, JEAN-PIERRE, FOURNIER, ALEXANDRE, COURTILLOT, VINCENT & HERRERO-BERVERA,

EMILIO 2012 Dynamical similarity of geomagnetic field reversals. *Nature* **490** (7418), 89–93.

VERMA, MAHENDRA K., AMBHIRE, SIDDHESH C. & PANDEY, AMBRISH 2015 Flow reversals in turbulent convection with free-slip walls. *Physics of Fluids* **27** (4), 047102.

WAGNER, SEBASTIAN & SHISHKINA, OLGA 2013 Aspect-ratio dependency of Rayleigh-Bénard convection in box-shaped containers. *Physics of Fluids* **25** (8), 085110.

WICHT, JOHANNES, STELLMACH, STEPHAN & HARDER, HELMUT 2009 Numerical models of the geodynamo: From fundamental cartesian models to 3D simulations of field reversals. In *Geomagnetic Field Variations*, pp. 107–158. Springer Berlin Heidelberg.

WINTERS, KRAIG B., LOMBARD, PETER N., RILEY, JAMES J. & D'ASARO, ERIC A. 1995 Available potential energy and mixing in density-stratified fluids. *Journal of Fluid Mechanics* **289**, 115–128.

XI, HENG-DONG & XIA, KE-QING 2008*a* Azimuthal motion, reorientation, cessation, and reversal of the large-scale circulation in turbulent thermal convection: a comparative study in aspect ratio one and one-half geometries. *Physical Review E* **78** (3), 036326.

XI, HENG-DONG & XIA, KE-QING 2008*b* Flow mode transitions in turbulent thermal convection. *Physics of Fluids* **20** (5), 055104.

XIA, KE-QING, SUN, CHAO & ZHOU, SHENG-QI 2003 Particle image velocimetry measurement of the velocity field in turbulent thermal convection. *Physical Review E* **68**, 066303.
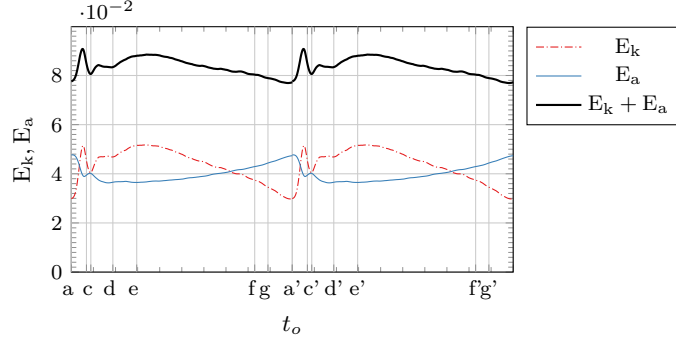
Figure 4.1: Evolution of the kinetic energy E_k and the available potential energy E_a during a generic reversal for $Ra = 5 \cdot 10^7$ and $Pr = 3$.

Additional remarks added after publication

Figure 8 of the present paper illustrates a competing behavior between the kinetic E_k and the total and available potential energies, E_p and E_a respectively. This behavior may give the impression that the sum of E_k and E_a to be nearly constant during reversals as expected in the inviscid limit. This is not the case, see figure 4.1. It is convenient to note, that this difference may be accounted for by fluctuations of the internal energy, and to a smaller degree to the Boussinesq approximation, which neglects the heating due to viscous dissipation of energy.

Chapter 5

Coherent structures during flow reversals and cessations

For turbulent Rayleigh-Bénard cells, modal analysis can be used to separate the effects of large- and small-scale flow in order to highlight the spatio-temporal dynamics of the large-scale circulation. So far two types of modal analyses have been used: Fourier analysis (Chandra and Verma, 2011; Chandra and Verma, 2013) and proper orthogonal decomposition (POD) analysis (Verdoold et al., 2009; Bailon-Cuba et al., 2010; Podvin and Sergent, 2012; Podvin and Sergent, 2015; Podvin and Sergent, 2017). The POD basis is orthogonal, is derived exclusively from observations and the resulting modes are arranged 'optimally' regarding their energetic contents. Unlike the Fourier modes, the POD can be applied to different geometries and boundary conditions.

We chose the latter approach to provide a low-order description of two-dimensional Rayleigh-Bénard dynamics inside the regime of consecutive reversals and the regime of extended cessations in terms of the evolution of the most energetic structures, see §2.6.2. This chapter was built upon existing works (Podvin and Sergent, 2015; Podvin and Sergent, 2017) and complements the statistical approach presented in §4.

This chapter is divided in five main parts. In the first part we compare different POD formulations on the reconstruction of primitive fields as presented in (Podvin and Sergent, 2015). Additionally we compare the reconstruction of the mechanical energy during a generic reversal in order to select the formulation of the POD and the number of modes for a low-order description. Next, DNS data is divided on two subsets: one subset which corresponds to the regime of consecutive reversals only, and one subset which excludes this regime. The second part of the chapter is devoted to the POD analysis of the consecutive reversals exclusively. This is seen as complementary to the statistical interpretation of the generic reversals. This approach is extended to regime of cessations in the third part of the chapter. Then we compare both regimes in the fourth part, by fixing the set of POD modes. Finally, in the fifth chapter, we follow the energy contents of the different modes as we increase Ra to provide insight on the evolution of the large-scale dynamics.

5.1 Comparison of the different POD formulations for convection problems

The idea behind any decomposition is to be able to represent a given quantity as the sum of a series of simpler expressions. If all of the terms are retained, one is expected to recover the original data, regardless of the method used. For a finite number of POD modes, one formulation might reconstruct more accurately the evolution the quantities we are interested in. Consider the three different formulations of the POD which were presented earlier on §2.6.2: formulation (A) based on the temperature field, formulation (B) based on the velocity vector field, and formulation (C) which combines the temperature and velocity fields.

For convection problems a mixed formulation is generally preferred (Sirovich, 1987; Park and Sirovich, 1990). In the study of flow reversals inside square Rayleigh-Bénard cells, (Podvin and Sergent, 2015) compared different formulations and obtained similar coherent structures for each one. Based on these observations, three-mode and five-mode models were proposed (Podvin and Sergent, 2015 and Podvin and Sergent, 2017, respectively) that reproduce many of the key features of the large-scale flow reversals.

In the following sections, we validate our approach by comparing against reference results (Podvin and Sergent, 2015; Podvin and Sergent, 2017). Having validated our POD code, we proceed to compare, for a mixed formulation the influence of the low-order truncation on the reconstruction of flow structures and global quantities which characterize the reversal process. In addition, we compare the results obtained from a six-mode reconstruction of the kinetic and potential energies during a generic reversal.

5.1.1 Comparison of POD modes for the different formulations

In order to validate our approach we compare to published results by (Podvin and Sergent, 2015; Podvin and Sergent, 2017). Converged results were obtained for $(\mathrm{Ra} = 5 \cdot 10^7, \mathrm{Pr} = 4.3)$ from 1200 snapshots taken every 5 convective time units. Results change very little when using a larger number of snapshots or a different time interval between snapshots. These snapshots correspond to the time series displayed in figure 5.1a.

An initial comparison is based on the POD spectra and the eigenvalues λ_i (see equation (2.65)) displayed on figure 5.1b for the first 20 modes. For each formulation (A,B,C) the contributions from mode $k = 1$ are at least 3 orders of magnitude larger than contributions from mode $k = 20$. For formulation (A), apart from the first and second modes, the energetic content from each mode was found to be quite small and evenly distributed among the different modes. As a consequence, if we consider the cumulative energy defined as $\sum_{i=1}^{k} \lambda_i / \sum_{i=1}^{\infty} \lambda_i$, the amount of energy contained inside a fixed number of modes is smaller for formulation (A) than for formulations (B) and (C). For instance, the cumulative energy inside the first 6 modes in formulation (A) is only of 0.80, whereas this value is close to 0.90 (resp. 0.88) for formulations (B) (resp. (C)), see figure 5.1c. From this point of view, formulation (A) is deemed less favorable for a low-order description than formulations (B) and (C).

The resulting POD modes and corresponding educed modes are displayed on figure 5.2:

(a) Time series of the global angular impulse

(b) POD spectra

(c) Cumulative energy
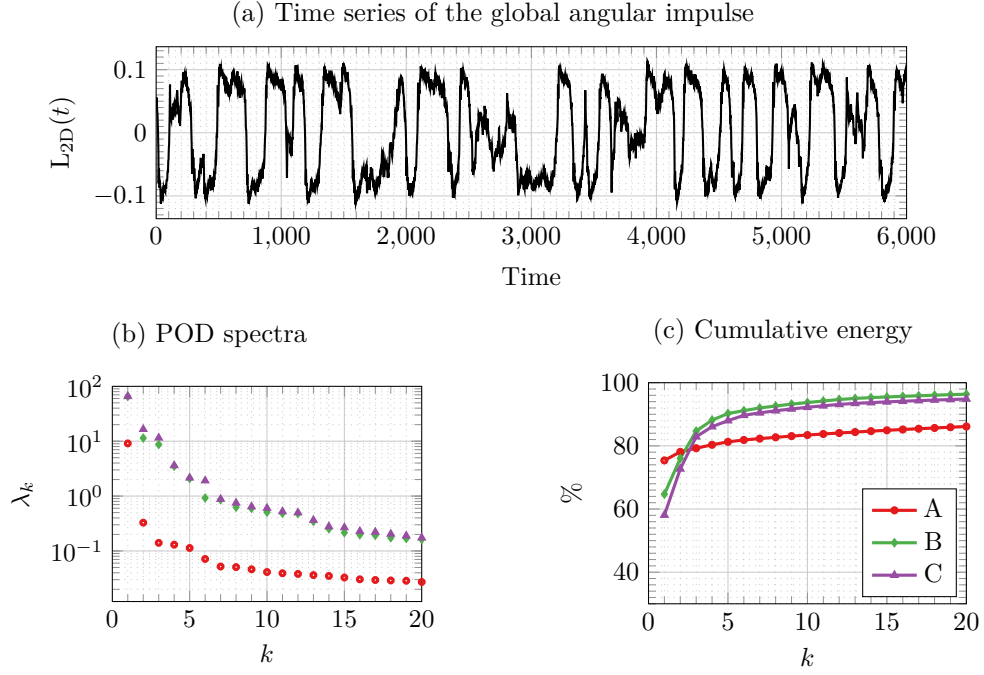
Figure 5.1: (a) Time series of L_{2D} during the sampled interval for $(Ra = 5 \cdot 10^7, Pr = 4.3)$. (b) Eigenvalues obtained for the first 20 POD modes; (c) $100 \sum_{i=1}^{k} \lambda_i / \sum_{i=1}^{\infty} \lambda_i$. POD analysis based on temperature formulation (A); on the velocity formulation (B); or the joint velocity-temperature formulation (C).

the first row corresponds to the temperature mode $\phi_k^{(\theta)}$ and the second row corresponds to the stream-function of the velocity modes, i.e. $(\phi_k^{(u)}, \phi_k^{(v)})$. The bottom row corresponds to contributions from each mode to the convective heat-flux in the vertical direction, i.e. $\phi_k^{(v)} \phi_k^{(\theta)}$. Results in figures 5.2a and 5.2b have been normalized by a factor such that $\langle \phi_j^{(\theta)} \phi_k^{(\theta)} \rangle + \langle \phi_j^{(u)} \phi_k^{(u)} \rangle + \langle \phi_j^{(v)} \phi_k^{(v)} \rangle = c_{jk}$, as to facilitate the comparison. For formulation (C) c_{jk} corresponds to the Kronecker delta δ_{jk}. However for formulations (A) and (B), since the educed modes are not orthogonal $c_{jj} = 1$ and $c_{jk} \neq 0$ for $j \neq k$.

We validate our implementation of the POD by comparing our results with those from (Podvin and Sergent, 2015): For formulations (B) and (C), we recover the same type of flow structures and the energetic content of each mode is in good agreement. For the formulation (A), the two most energetic modes are identical. For modes $k \geq 3$, we obtain a similar set of modes although in a different order. If we consider a POD spectra in which several modes have a similar energetic content, the order of these modes could be influenced by the sampled interval. For instance, the third to fifth modes in formulation (A). As observed by Podvin and Sergent, 2015, all three formulations produce the same type of coherent structures with only a different distribution of the energy contents and can be grouped together based on their natural symmetries $\mathbb{S}_x$, $\mathbb{S}_y$, R_π described in 2.5, see table 5.1. For consistency, we will use the same notation as (Podvin and Sergent, 2015; Podvin and Sergent, 2017).

Consider the results obtained using formulation (C). As shown by (Podvin and Sergent, 2015; Podvin and Sergent, 2017), the first (denoted L) and fourth (denoted L*) most energetic modes have the same symmetry group: both are antisymmetric with respect to the $\mathbb{S}_x$ and $\mathbb{S}_y$ symmetries, and symmetric with respect to R_π. The mode L corresponds to
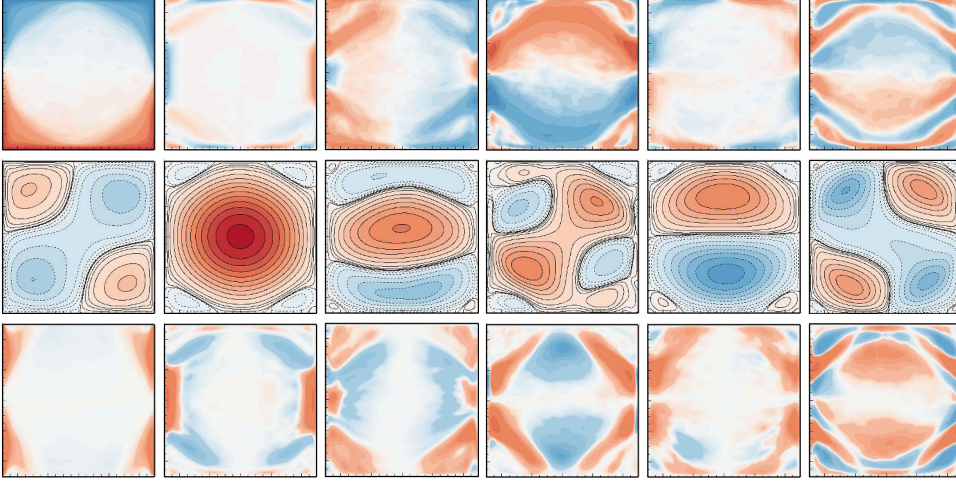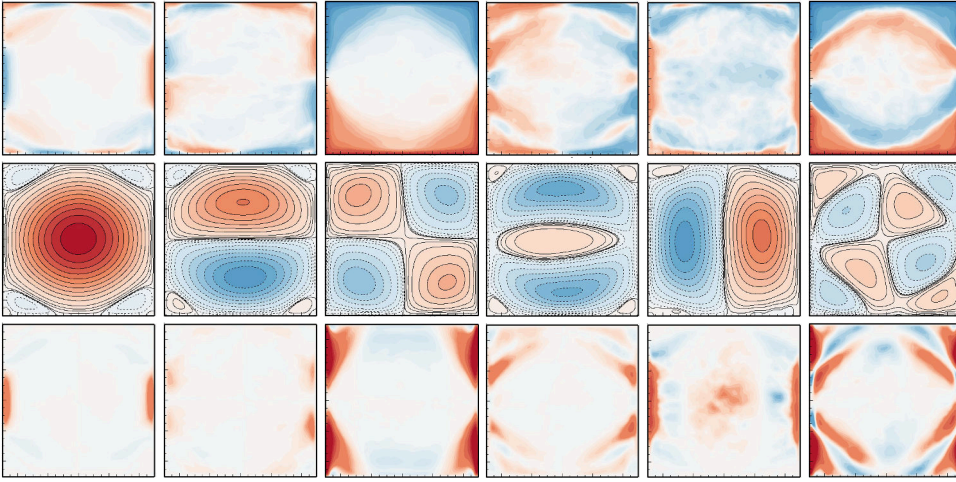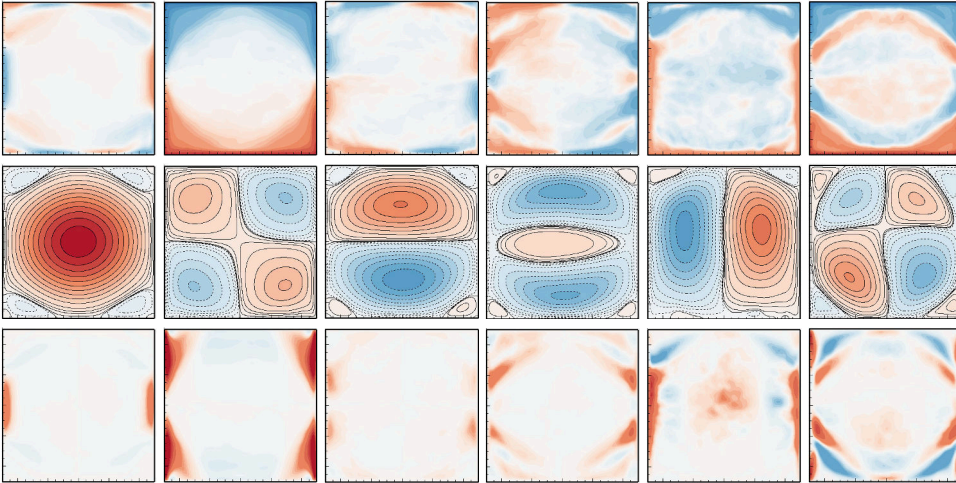
Figure 5.2: Six most energetic POD modes obtained using formulations (A), (B), and (C) for $(\text{Ra} = 5 \cdot 10^7, \text{Pr} = 4.3)$. For each formulation the top row corresponds to the temperature modes, the middle row to the stream-function of the velocity modes and the bottom row to the advective heat-flux in the vertical direction, i.e. $\phi_k^{(v)} \phi_k^{(\theta)}$. Results by a common factor as to facilitate the comparison, see text.

	Mode-L	Mode-Q	Mode-S_y	Mode-L*	Mode-S_x	Mode-Q*
Formulation (C)	1	2	3	4	5	6
Formulation (B)	1	3	2	4	5	6
Formulation (A)	2	1	5	3		4
Symmetry $\mathbb{S}_x$	AS	S		AS	S	S
Symmetry $\mathbb{S}_y$	AS	S	S	AS		S
Symmetry R_π	S	S		S		S

Table 5.1: Hierarchy of modes in each POD formulation for $(\mathrm{Ra} = 5 \cdot 10^7, \mathrm{Pr} = 4.3)$. For each mode, we indicate if the mode is symmetric (S) or antisymmetric (AS) with respect to $\mathbb{S}_x$, $\mathbb{S}_y$, R_π described in 2.5.

a large-scale single-roll mode with small recirculation cells in the corners, whereas mode L* corresponds roughly to three vertically stacked rolls. The second (denoted Q) most energetic mode is symmetric with respect to $\mathbb{S}_x$ and $\mathbb{S}_y$ and corresponds to a four-roll mode. This mode bears a strong resemblance to the mean fields (Podvin and Sergent, 2015). The sixth most energetic mode is similar to Q, but displays a pattern consisting of eight rolls: four in the center and four in the corners. This mode is characterized by having blobs of hot (resp. cold) fluid inside the bulk just opposite to the cold (resp. hot) thermal boundary layers. Since this mode belongs to the same symmetry group as Q, we denote this mode as Q*. The third and fifth most energetic modes are symmetric with respect to either $\mathbb{S}_x$ or to $\mathbb{S}_y$. Mode S_y consists on a vertically stacked double roll mode, which is symmetric with respect to the horizontal axis, hence the name. Conversely, mode S_x consists on two horizontally stacked rolls, which is symmetric with respect to the vertical axis. All of these modes have a positive overall contributions to the vertical heat-flux. However, the modes S_x and Q* display zones with important negative heat-flux near the corners.

We would like to compare how low-order reconstructions using the different formulations are able to describe the main flow features of the generic reversal and recover the evolution of different global quantities which characterize the reversal process, namely the global kinetic, total potential and available potential energies. Before making such comparison, it is necessary to fix a number of modes for the low-order reconstructions. In the following section we focus on influence of the low-order truncation on the reconstructed fields and the global quantities.

5.1.2 Influence of the low-order truncation on the reconstructed fields using the mixed POD formulation (C)

In order to illustrate the influence of the truncation on a low-order reconstruction, let us compare the DNS results against reconstructions obtained using the mixed POD modes for $(\mathrm{Ra} = 5 \cdot 10^7, \mathrm{Pr} = 4.3)$. Reconstructed fields are obtained using the three, six, nine, and twelve most energetic modes: modes $k = 1$ to $k = 6$ are displayed on figure 5.2, while modes $k = 7$ to $k = 12$ are displayed on figure 5.3. We are primarily interested in the evolution of the global kinetic and the total potential energies. First, one reconstructs the primitive fields $(\tilde{\theta}, \tilde{u}, \tilde{v})$ using a fixed number of POD modes, then compute $\widetilde{E_k}$ and $\widetilde{E_p}$ from these reconstructed fields. Last, one evaluates the absolute deviation from the DNS

k=7	k=8	k=9	k=10	k=11	k=12
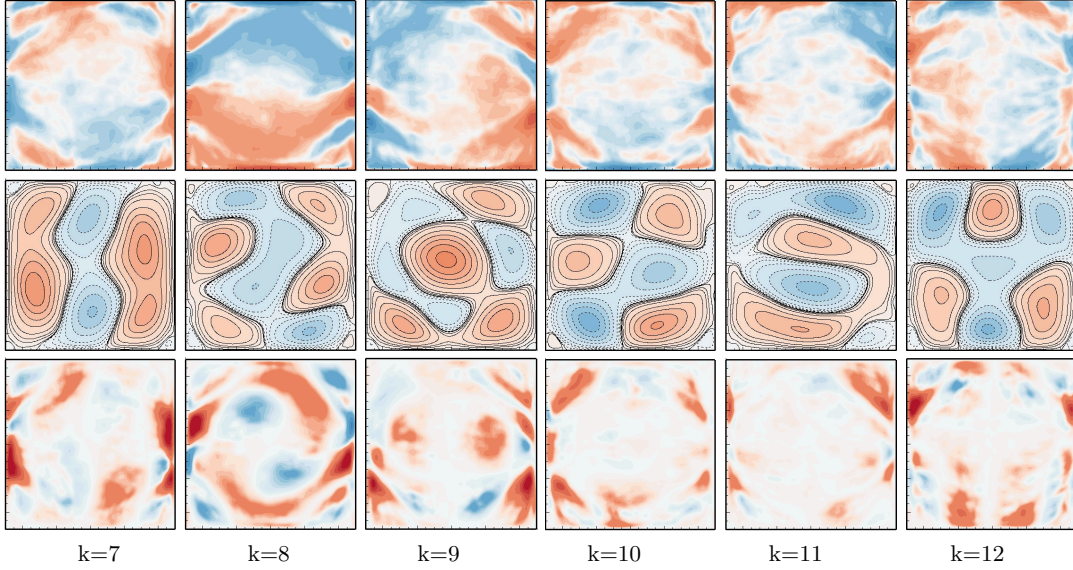
Figure 5.3: Modes $k = 7$ to $k = 12$ obtained using formulation (C) for $(\mathrm{Ra} = 5 \cdot 10^7, \mathrm{Pr} = 4.3)$. Continues from figure 5.2.

results

$$\%\mathrm{Error}(\mathrm{E_k}) = 100 \frac{\widetilde{\mathrm{E_k}} - \mathrm{E_k}}{\mathrm{E_k}} \qquad \%\mathrm{Error}(\mathrm{E_p}) = 100 \frac{\widetilde{\mathrm{E_p}} - \mathrm{E_p}}{\mathrm{E_p}} \qquad (5.1)$$

as function of time. Note that contributions from each mode to $\mathrm{E_k}$ are always positive, whereas the contribution to $\mathrm{E_p}$ can be both positive and negative. Furthermore, contributions to $\mathrm{E_p}$ from modes antisymmetric with respect to $\mathbb{S}_x$ are zero, for instance modes L and L*.

Consider the time series of $\mathrm{Error}(\mathrm{E_k})$ and $\mathrm{Error}(\mathrm{E_p})$ displayed in figure 5.4 during a particular reversal. A time-series of $\mathrm{L_{2D}}$ is displayed for reference. Let us focus on the three-mode reconstruction. During the first part of the accumulation phase (see plateau in $\mathrm{L_{2D}}$), there is little difference from the reconstruction of $\mathrm{E_k}$ to the DNS. However, by the end accumulation phase (∘ mark in figure 5.4a), the value of $\mathrm{Error}(\mathrm{E_k})$ begins to increase with respect to the other reconstructions until the end of the acceleration. The picture for $\mathrm{E_p}$ is similar but deviations are accentuated positively or negatively from the end of the accumulation until the end of the acceleration. A six-mode reconstruction works better during both phases (compare ∘ and ● marks in figures 5.4a and 5.4b) and has a consistent behavior with the nine- and twelve-mode reconstructions.

The larger deviations during the release and acceleration phases suggest an increased activity of the smaller scales. To illustrate this we compare four snapshots issued from the DNS against their respective POD reconstructions (figures 5.5a to 5.5d): the first snapshot takes place during the accumulation phase; the second one takes place during the release phase, just before the corner-rolls are merged; the third snapshot is taken during the rebound; and the last one during the acceleration phase corresponds to the rotation of the central vortex. For the first and last snapshots, one is able to recover most of the flow features using a three-mode reconstruction (figures 5.5a and 5.5d). However, during the release this reconstruction fails to reproduce the merging of the corner flows (figure 5.5b). In addition, during the rebound, the three-mode reconstruction fails to recover
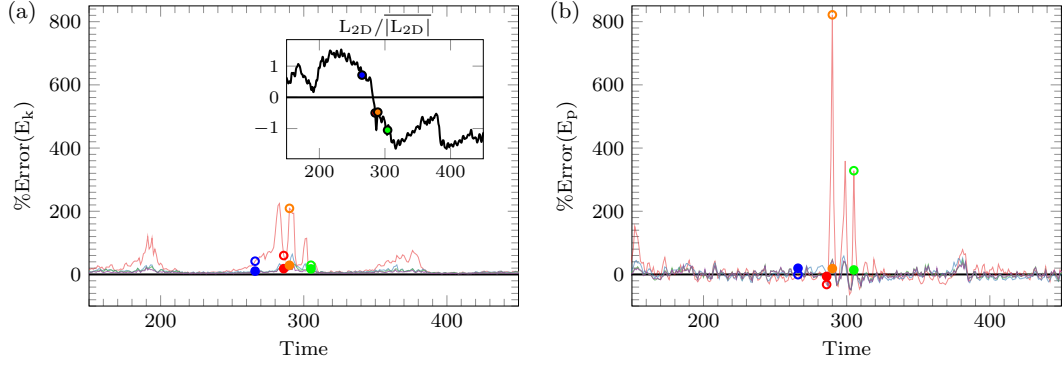
Figure 5.4: Evolution of the error in the low-order reconstructions of E_k and E_p during a particular reversal for $(\text{Ra} = 5 \cdot 10^7, \text{Pr} = 4.3)$. Color indicates the number of POD modes: three-modes (red lines), six-modes (blue lines), nine-modes (green lines) and twelve-modes (purple lines). Inset displays the evolution of L_{2D} for reference. Hollow $\circ$ (resp. solid $\bullet$) marks indicate results to a three-modes (resp. six-modes) reconstruction corresponding to snapshots displayed on figure 5.5.

the detachment of the central vortex from the upper and lower walls (figure 5.5c). For all of the snapshots, the small-scale plumes are smoothed out and the blobs of hot/cold fluid inside the corner-rolls are barely visible. Furthermore, thermal boundary layers are missing from a three-mode reconstruction during the rebound and during the acceleration (figures 5.5c and 5.5d).

It is clear that a three-mode reconstruction is insufficient to recover the energetic and some key features of a particular flow reversal. However, it is more difficult to state how many modes are actually required. At least six modes are required to prevent unphysical results such as the vanishing of the boundary layers. Incremental improvements are observed as one includes additional modes, but it is difficult to extract a general trend. For this reason it may be interesting to compare the reconstructions of the generic reversal instead of a particular one. In the following section, we take this approach to compare the different formulations of the POD using a six-mode reconstruction of the generic reversal.

5.1.3 Comparison of a six-mode reconstruction of the energetics of a generic reversal for the different formulations of the POD

In order to illustrate the differences between the POD formulations, let us consider the generic reversal cycles obtained by the DNS results against six-mode reconstructions. We use the following procedure to build a generic reversal from the reconstructed fields:

1. Project primitive fields and obtain modal coefficients $\alpha_k(t)$ for each formulation.

2. Evaluate a six-mode reconstruction of the primitive fields $\tilde{\psi} = (\tilde{\theta}, \tilde{u}, \tilde{v})$.

3. Evaluate the global kinetic energy $\tilde{E}_k(t)$, the potential energy $\tilde{E}_p(t)$, and the available potential energy $\tilde{E}_a(t)$, based on the reconstructed fields $\tilde{\psi} = (\tilde{\theta}, \tilde{u}, \tilde{v})$. For practical purposes we approximate the reference height as $\tilde{y}_r = y_r(\tilde{\theta})$.

4. Apply the conditional average presented in §4 to each quantity based on the amplitude of mode L (by analogy to L_{2D}).

85
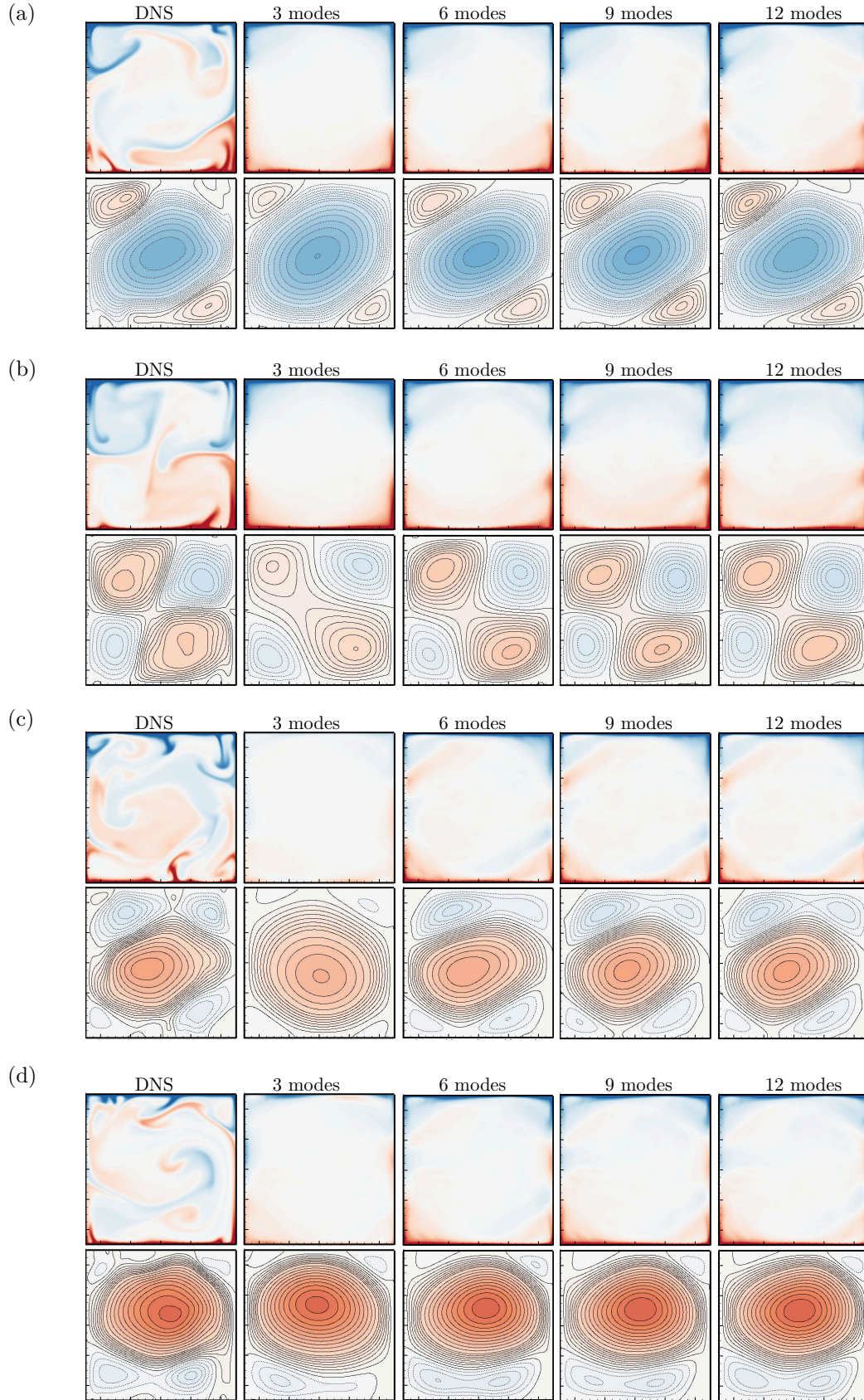
Figure 5.5: DNS results compared to a reconstruction obtained using POD modes for $(Ra = 5 \cdot 10^7, Pr = 4.3)$. Snapshots correspond to instants identified as solid marks in figure 5.4; (a•) during the accumulation phase ; (b•) during the release phase ; (c•) the rebound ; and (d•) during the acceleration phase. For each figure, the top row corresponds to the temperature field and the bottom row to the stream-function.
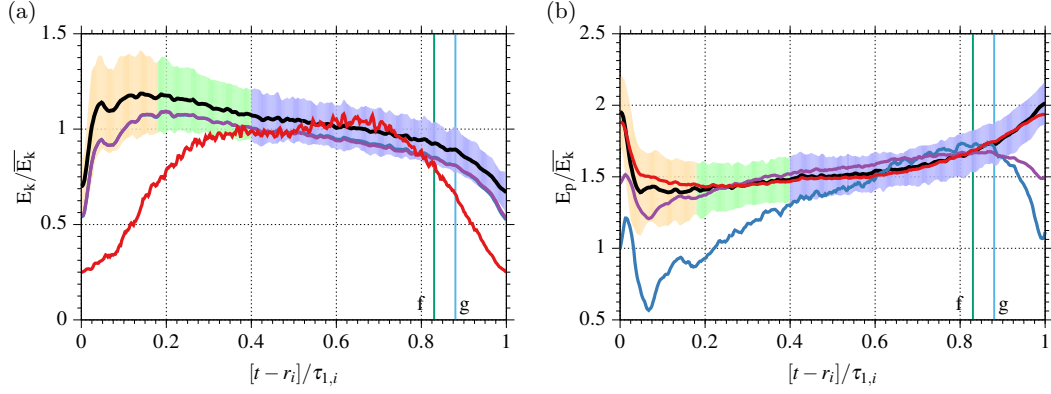
Figure 5.6: Kinetic and potential energy during a generic reversal: DNS results (black lines) are compared to the conditional averaged values obtained from the first six POD modes using different formulations for $(\mathrm{Ra} = 5 \cdot 10^7, \mathrm{Pr} = 4.3)$: (A) in red, (B) in blue, and (C) in purple. Shaded region represents one standard deviation from the DNS results in three phases: release (orange), acceleration (green), and accumulation (blue). The transition points, (f) and (g) defined in the previous chapter are shown for reference.

Results obtained using each formulation are displayed in a different color on figure 5.6. Using formulation (C), one is able to recover the approximate shape and order of magnitude of E_k throughout the cycle, although the reconstruction only contains 91% of E_k. For E_p the picture is slightly more complicated and two major deviations from the generic cycle are observed (figure 5.6b). The first deviation is observed during the rebound, where the value of E_p is underestimated. The second deviation is observed during the accumulation phase: E_p grows linearly but stagnates near the transition points (f) and (g), before decreasing instead of increasing faster as observed from the DNS. This suggests that, near the end of the accumulation phase, thermal energy is being stored inside smaller scales, absent from the six-modes reconstruction.

For formulation (B velocity-based), the reconstruction of E_k is roughly the same as in formulation (C), whereas for formulation (A temperature-based), the reconstruction of E_p now follows closely the generic cycle. This improvement is reflected on the amount of energy contained inside these modes, see table 5.2. The improvement also suggests that one of the six temperature-based modes from figure 5.2, which is not included in the first six mixed-modes, becomes the carrier of thermal energy just before the reversal. Now consider using formulation (A) to evaluate E_k and formulation (B) to evaluate E_p. The reconstruction of the potential (resp. kinetic) energy using only the velocity (resp. temperature) based modes, fares much worse than results produced from formulation (C).

Before moving on to the next section, let us consider the case of a reconstruction of the available potential energy E_a (see figure 5.7a). Observe that $\widetilde{E_a}$ has the same shape as the reconstructions of E_p, but underestimates its value by as much a 20% with respect to the DNS. This deficit is nearly constant all along the cycle and is observed in all three formulations, even for the temperature-based one. Let us remind that E_p depends on the probability distribution of the temperature field which is required to compute y_r. A low-order reconstruction does not preserve the bounds nor the probability distribution of the temperature field (see figure 5.7b), making very difficult to compute E_a accurately.

Formulation	$\langle\tilde{\psi}^2\rangle/\langle\psi\rangle$	$\widetilde{E_k}/E_k$	$\widetilde{E_p}/E_p$	$\widetilde{E_a}/E_a$
A	80%	-	99%	88%
B	90%	91%	-	-
C	88%	91%	97%	85%

Table 5.2: Comparison of the generic reversal cycle using different formulations of the POD. Six-mode reconstruction of the combined energy $\langle\tilde{\psi}^2\rangle/\langle\psi^2\rangle$ with $\tilde{\psi} = (\tilde{\theta}, \tilde{u}, \tilde{v})$ (resp. $\psi = (\theta, u, v)$), and reconstructions of the kinetic, potential, and available potential energies measured with respect to DNS results.
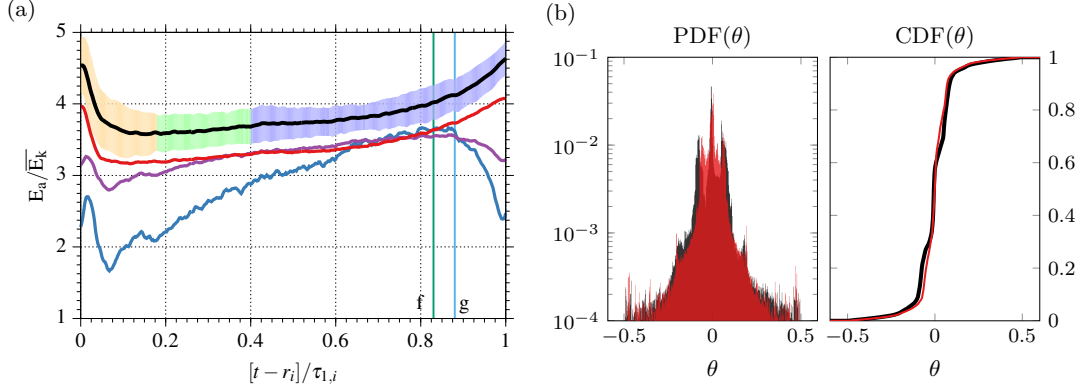
Figure 5.7: Left: Available potential energy during a generic reversal compared to the conditional averaged values obtained from the first six POD modes for $(\mathrm{Ra} = 5 \cdot 10^7, \mathrm{Pr} = 4.3)$. Layout is similar to figure 5.6. Right: Probability density and cumulative density functions of an instantaneous temperature field $\theta(\mathbf{x}, t)$ corresponding to the release phase of a particular reversal, compared to a six-mode reconstruction using formulation (A).

Using separate expansions for the temperature and velocity field gives better results but comes at the expense of losing the coupling between the velocity and temperature fields. If we opt for a single expansion, then formulation (C) gives better results. This comparison makes a good case for using a mixed formulation for POD analysis inside Rayleigh-Bénard cells. This comparison does not change our previous conclusion that six-modes are sufficient to provide a simplified description of the reversal process. In the following we focus on results obtained using formulation (C).

5.2 Dynamics inside of the 'regime of consecutive reversals' using mixed POD modes

Let us separate our data into two sub-sets using the filtering procedure presented in §4. For $(\mathrm{Ra} = 5 \cdot 10^7, \mathrm{Pr} = 4.3)$ the first set is composed of 3150 snapshots taken every 4 convective time units belonging to the 'regime composed of continuous reversals' (CR), while the second one excludes snapshots from this regime. For consistency, we repeat this procedure for $(\mathrm{Ra} = 5 \cdot 10^7, \mathrm{Pr} = 3.0)$ using 1500 snapshots inside the CR regime. In this section, we focus on the POD analysis performed on the CR subset.

5.2.1 Leading POD modes in the 'regime of consecutive reversals'
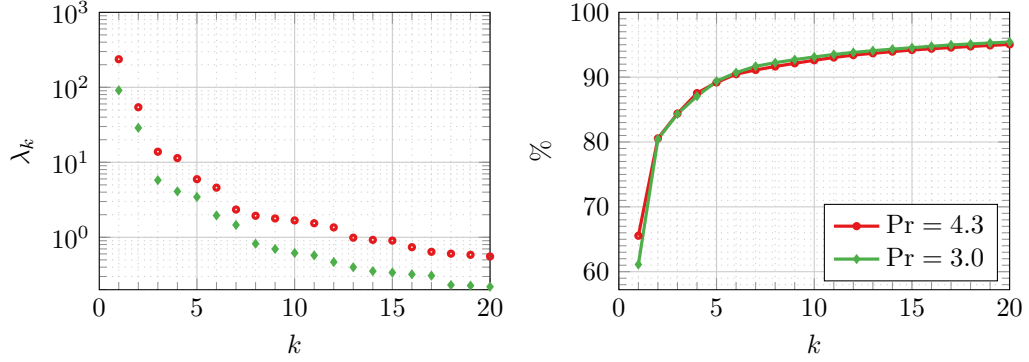
Figure 5.8: POD analysis of the filtered subset corresponding to the CR regime for $Ra = 5 \cdot 10^7$. (a) Eigenvalues obtained for the first 20 POD modes; (b) $100 \sum_{i=1}^{k} \lambda_i / \sum_{i=1}^{\infty} \lambda_i$.

The POD spectra and the eigenvalues λ_i (see equation (2.65)) are displayed on figure 5.8 for the first 20 modes. Contributions from the most energetic mode are at least 3 orders of magnitude larger than contributions from mode $k = 20$, whereas the the cumulative energy contained inside the first 6 modes is close to 0.90 for both values of (Ra, Pr), compared to 0.88 when using the complete series.

The resulting POD modes are displayed in figure 5.9. In both cases, we recover a similar set of coherent structures. Since the complete series features prominently the CR regime, it comes as no surprise that CR modes and modes obtained from the entire set resemble each other (compare figures 5.2c and 5.9a). The filtered modes are cleaner and more symmetric. Modes L, Q, L* and Q* are nearly identical to those from the complete set, but the two other modes are slightly different from S_y and S_x. In the following we refer to these modes as S and S*, since S is antisymmetric (resp. symmetric) with respect to $\mathbb{S}_x$ (resp. $\mathbb{S}_y$) whereas S* is antisymmetric (resp. symmetric) with respect to $\mathbb{S}_y$ (resp. $\mathbb{S}_x$), making both modes antisymmetric with respect to $\mathbb{R}_\pi$.

In the following sections, we focus on the time evolution of these modes using a six-modes reconstruction of the generic reversal cycle.

5.2.2 Time evolution of the leading POD modes of the CR subset

We project the modes displayed in figure 5.9 into the temperature and velocity fields to obtain the modal coefficients α_k for the entire set. The evolution of the amplitude of mode L is nearly identical to L_{2D} (not shown), thus allowing us to apply the filtering procedure presented in §4 and separate the CR regime, the EC regime, and intermediate flow regimes. The curves of the modal coefficients during each reversal are stacked together to obtain conditionally-averaged (or generic) coefficients for each POD mode, see figures 5.10 and 5.11, where each mode is observed to display a characteristic behavior.

Let us consider the time evolution for $Pr = 3.0$. First, note that L and L* are the only modes that display a reversal at the same time. The mode L mirrors the evolution of L_{2D} and alternates between a positive and a negative *plateau* states. The evolution of mode L* is tied to the sign of L and to the different phases of a generic reversal (figures 5.10(1) and

(a)

L Q S L* Q* S*

(b)

L Q L* S Q* S*
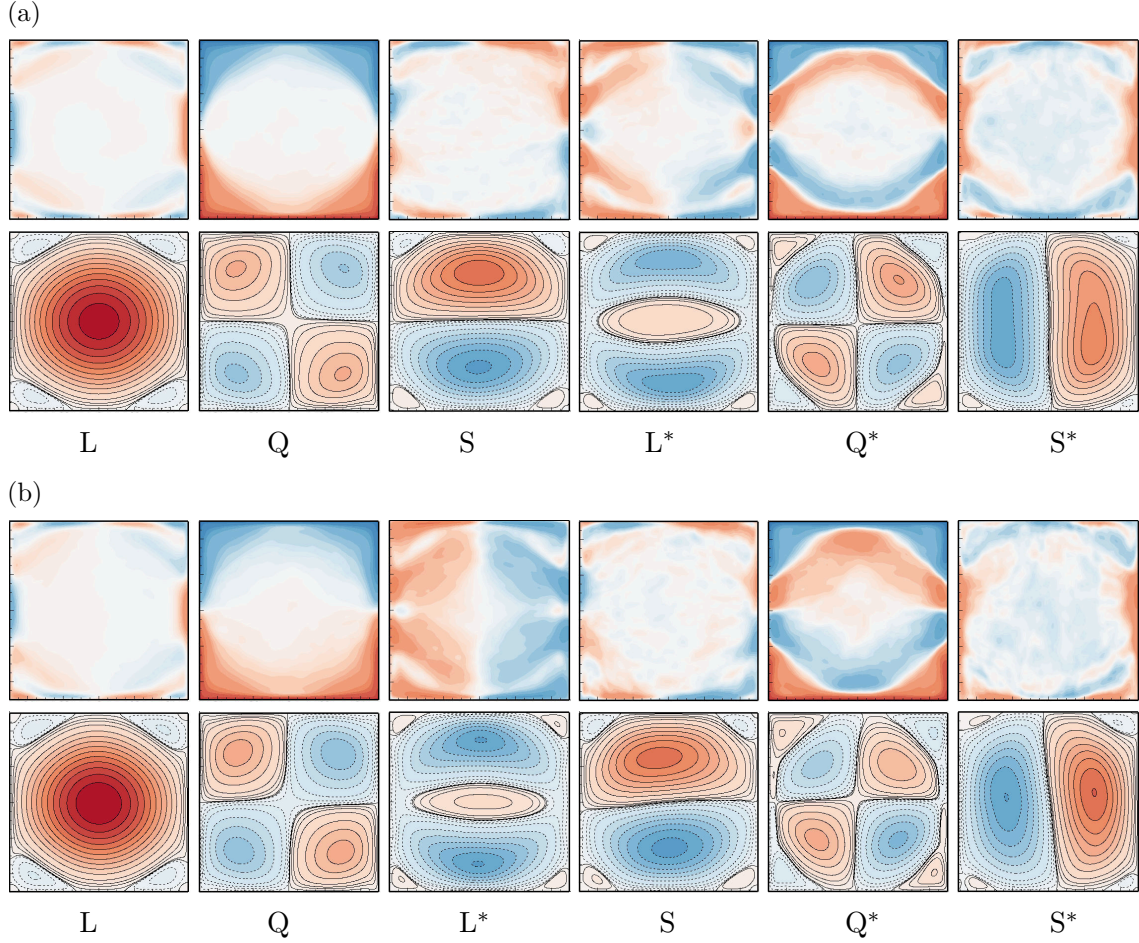
Figure 5.9: POD modes obtained from a filtered subset including only the regime of 'consecutive reversals' for (a) $(\mathrm{Ra} = 5 \cdot 10^7, \mathrm{Pr} = 4.3)$ and (b) $(\mathrm{Ra} = 5 \cdot 10^7, \mathrm{Pr} = 3.0)$. Layout is identical to that of figure 5.2.

5.10(2)). Consider the case with a positive L. At the beginning of the accumulation L* is negative, effectively aiding the main circulation. During the accumulation, the value of L* increases slowly until it becomes positive. As noted by (Podvin and Sergent, 2017), when L and L* have the same sign, the flow is weakened along the upper and lower boundary layers. Then, mode L* continues to increase at a faster rate, which coincides with a more pronounced decrease in L observed from the transition points (f) and (g). Then, during the reversal the value of L* suddenly drops to negative values and bounces back during the release phase. Last, modes L and L* have opposite signs, consistent with the acceleration phase of the generic cycle.

The evolution of the fully symmetric modes Q and Q* are tied to the phases of a generic cycle, but not to the sign of mode L. Mode Q is mostly positive and is reminiscent of the evolution of E_p described in §4: Mode Q increases progressively during the accumulation phase (figure 5.10(3)), exhibits a sudden drop during the reversal, which is followed by a rebound. On the contrary, the value of Q* is centered around zero, but is highly correlated to value of Q: the value of Q* decreases as Q increases and *vice versa*. Both Q and Q* are strongly related to the thermal boundary conditions and enforce the global unstable temperature stratification. In this sense, Q* serves to compensate for changes in Q. Observe that Q* changes sign during the accumulation around the transition point (g), whereas
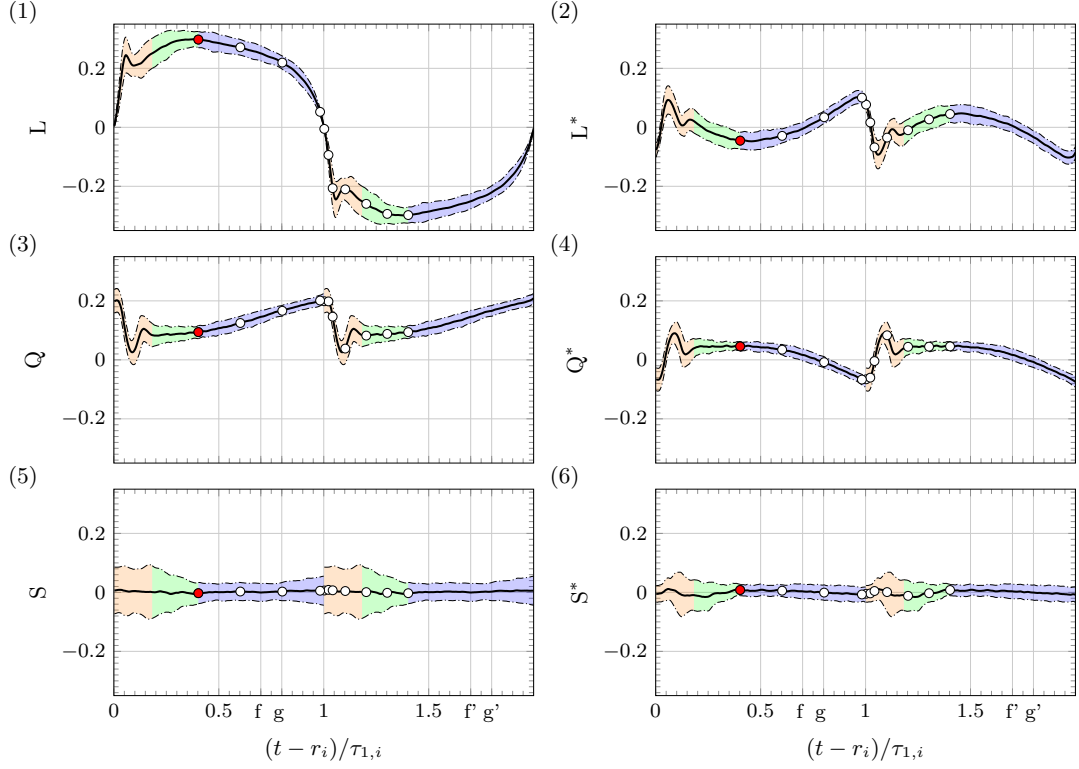
Figure 5.10: Evolution of modal coefficients for $(\mathrm{Ra} = 5 \cdot 10^7, \mathrm{Pr} = 3.0)$. Conditional averages are obtained using the procedure described in §4. Generic curves displayed in solid lines, shaded region indicates one standard deviation with each phase of the reversal in color: release (orange), acceleration (green), and accumulation (blue). Marks ∘ correspond to the fields in figures 5.13(i) to 5.13(x). where (i) is indicated by a ● mark.
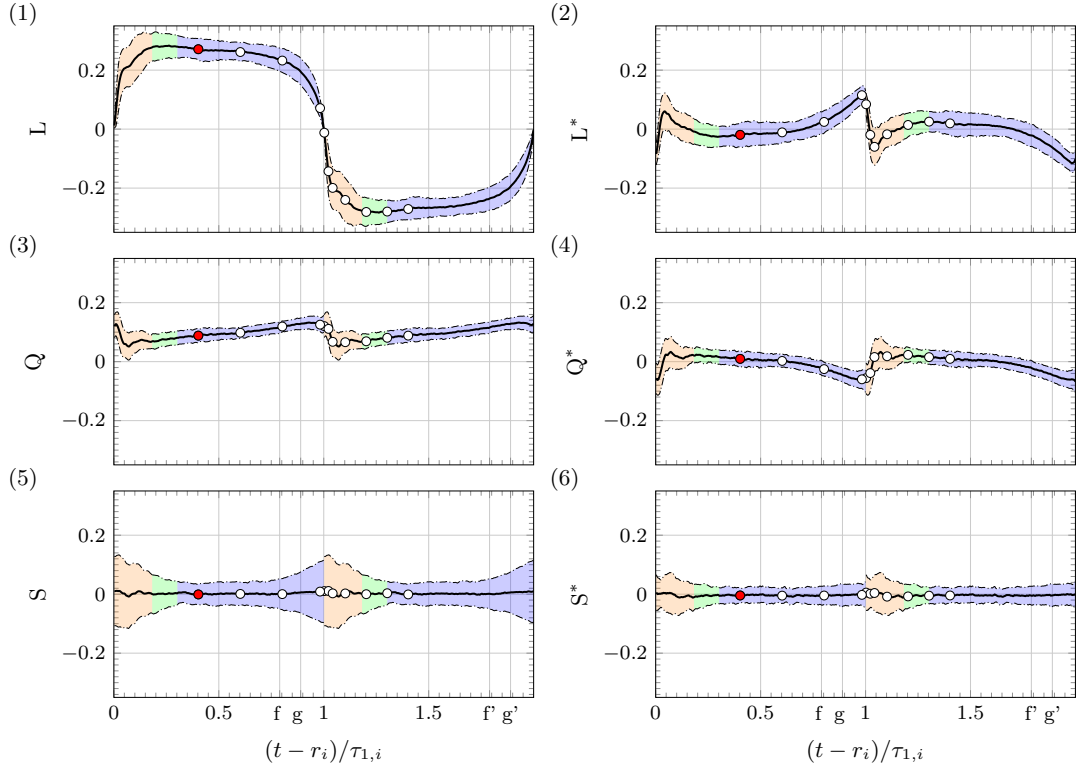
Figure 5.11: Same as in figure 5.11 for $(\mathrm{Ra} = 5 \cdot 10^7, \mathrm{Pr} = 4.3)$. Marks ∘ corresponds to the fields in figures 5.14(i) to 5.14(x) where (i) is indicated by a ● mark.
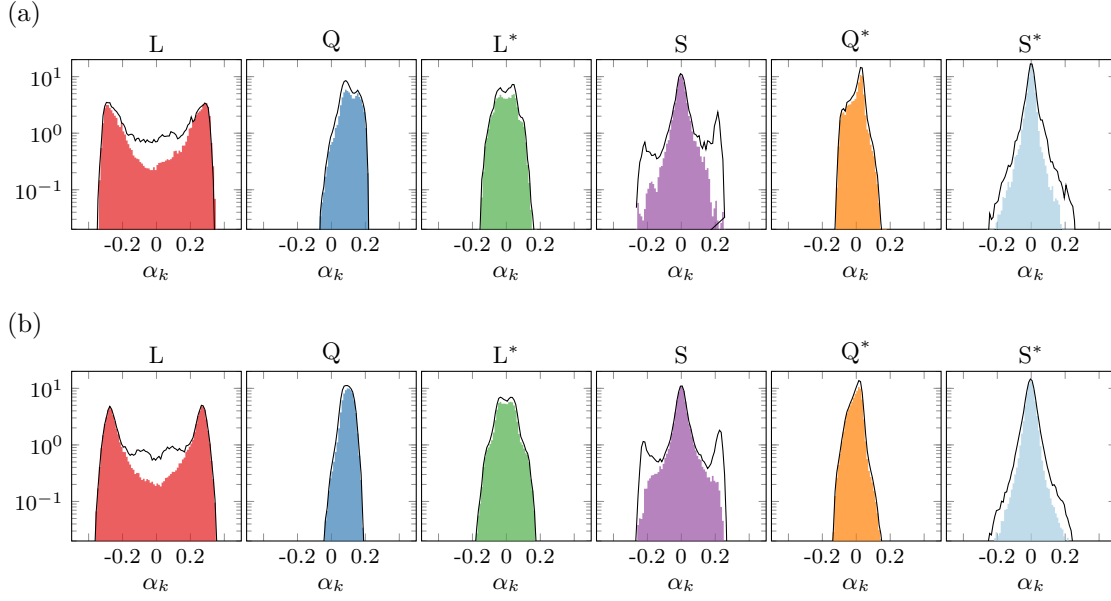
Figure 5.12: Conditional PDF of the modal coefficients $\alpha_k(t)$ inside the CR regime displayed in color, PDF of the complete series shown in black. (a) $(\mathrm{Ra} = 5 \cdot 10^7, \mathrm{Pr} = 3.0)$ and (b) $(\mathrm{Ra} = 5 \cdot 10^7, \mathrm{Pr} = 4.3)$.

the sign switch in L* is closer to the transition point (f). After both modes switch signs, they contribute to the accumulation of thermal energy inside the corner rolls and to the detachment of the large diagonal vortex.

The horizontally and vertically stacked dipoles (modes S and S*) play no dominant role during the generic cycle: their generic curves are essentially zero, but have a larger fluctuations during the release phase. Similar trends in the evolution of the modal coefficients are observed for $\mathrm{Pr} = 4.3$. However, the placement of the sign switch in modes L* and Q* relative to the transition points (f) and (g) is less clear (see figure 5.11).

In order to illustrate the variability of the modal coefficients, let us consider their probability density functions as well. To focus on the behavior of the CR regime, figure 5.12 displays conditional probability density functions (PDF) superimposed to the PDF of the entire set. Inside the CR regime, the antisymmetric modes (L and L*) display a bimodal probability distribution, whereas the symmetric modes (Q and Q*) have asymmetric distributions. Additionally, modes S and S* are consistent with a double exponential distribution centered around zero. This suggest their evolution in time to be driven by a random (stochastic) process, which may explain why the generic curve is flat. This is consistent with observations for $\mathrm{Pr} = 1$ (Verma et al., 2015).

To verify if the evolution of these six POD modes is representative of the reversal process, we perform a reconstruction of the generic reversal using the POD modes and the generic modal coefficients presented here and compare it against the conditionally-averaged fields presented in §4.
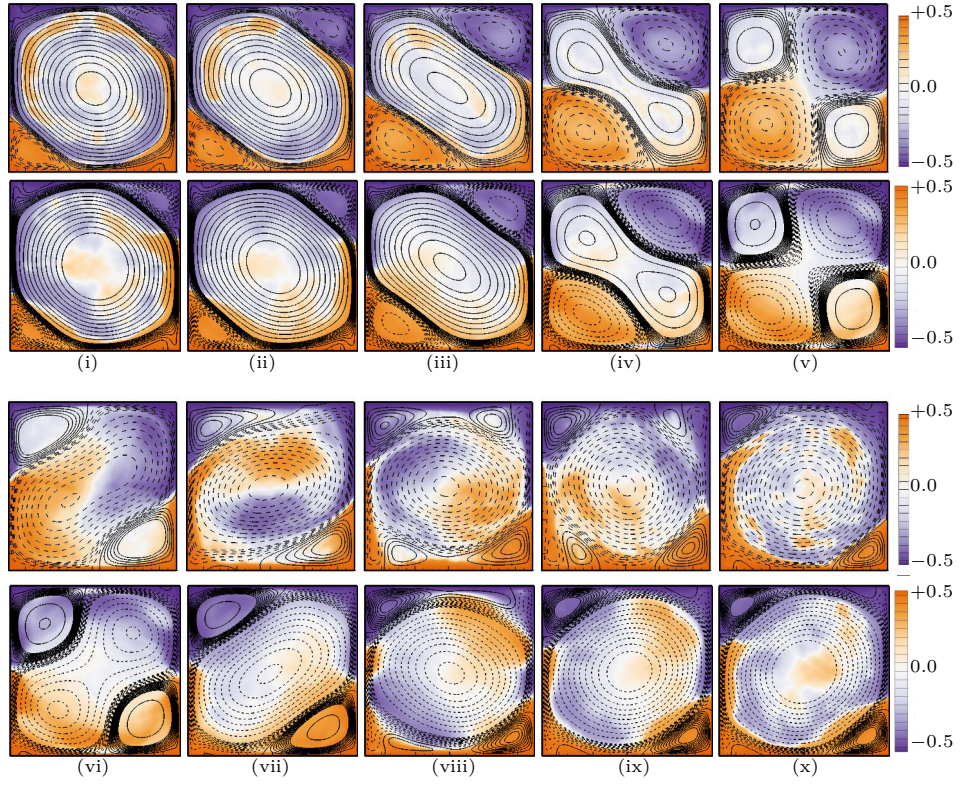
Figure 5.13: Generic fields (top) compared to reconstructed fields using coefficients from figure 5.10 (bottom) for $(\mathrm{Ra} = 5 \cdot 10^7, \mathrm{Pr} = 3.0)$. Streamlines are superposed to a color-map of field $y_r(\mathbf{x}, t)$. Snapshots correspond to a mark in figure 5.10.
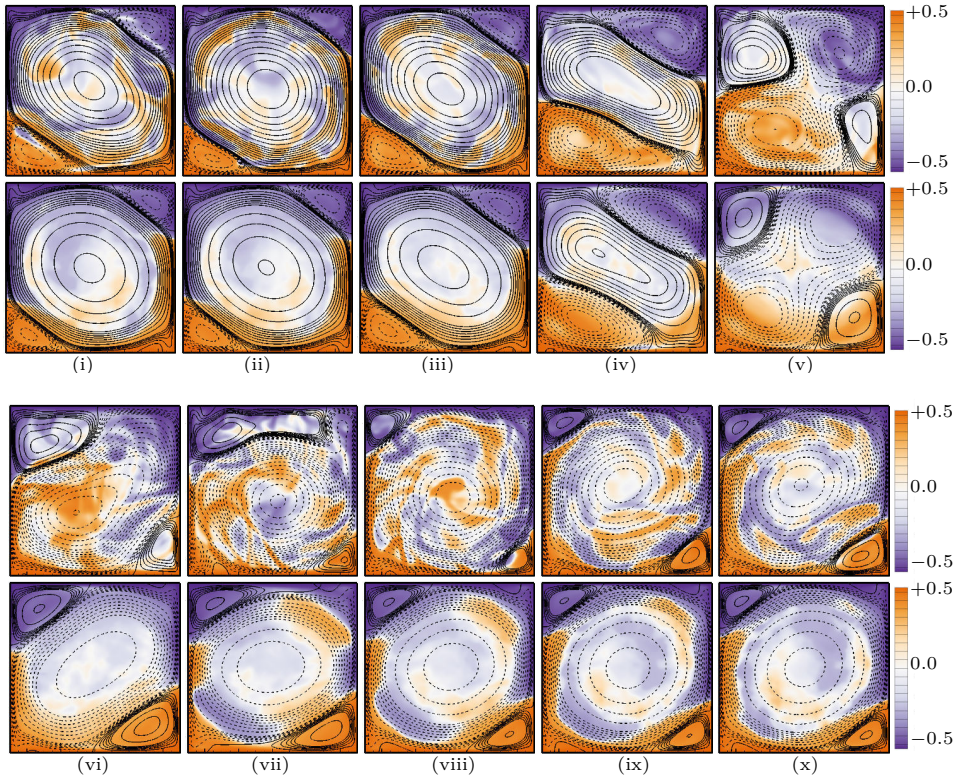
Figure 5.14: Same as in figure 5.13 for $(\mathrm{Ra} = 5 \cdot 10^7, \mathrm{Pr} = 4.3)$. Each snapshot correspond to a mark in figure 5.11.
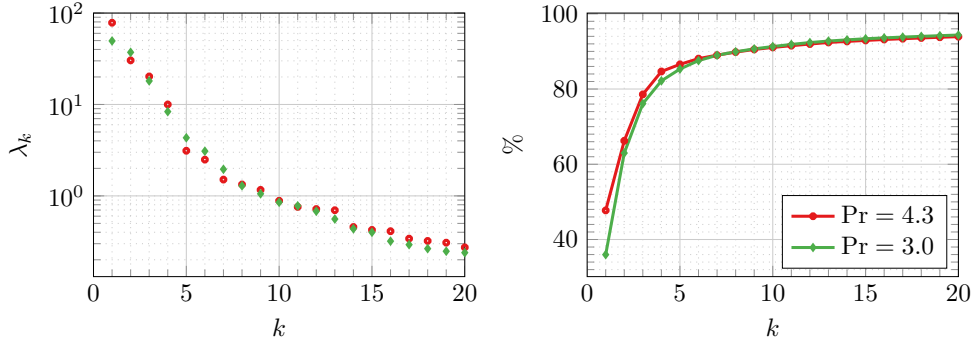
Figure 5.15: POD spectra obtained using formulation (C) from a filtered subset excluding only the regime of 'consecutive reversals' for $Ra = 5 \cdot 10^7$. Eigenvalues obtained for the first 20 POD modes (left panel) and cumulative energy $100 \sum_{i=1}^{k} \lambda_i / \sum_{i=1}^{\infty} \lambda_i$ (right panel).

5.2.3 A six-modes reconstruction of the reversal cycle based on the generic modal coefficients

We use the generic modal coefficients from figure 5.10 and the corresponding POD modes to obtain a six-mode reconstruction of a generic reversal for $(Ra = 5 \cdot 10^7, Pr = 3.0)$. Reconstructed fields are compared to the generic fields obtained in §4, see figure 5.13. Each field correspond to one of the marks in figure 5.11, where the first snapshot (i) is indicated with a ● mark. A similar exercise is performed for $Pr = 4.3$ using the generic modal coefficients from figure 5.11 and the corresponding POD modes.

For both values of Pr, the reconstructed fields reproduce the main features of the accumulation (i to iv) and acceleration (ix to x) phases identified by the conditional averages of the primitive variables §4: a large diagonal roll squeezed by growing counter-rotating corner-rolls and large thermal plumes located along the opposite side-walls. However, the release of thermal energy into the bulk is not recovered with the same level of detail (v to vi): the breakup of the large-scale circulation and the formation of a new one are clearly visible, however, the continuous rotation of the newly formed circulation and the temperature field inside the bulk are missing. This was expected, since small-scale plumes are not recovered by the reconstructed fields by construction. Indeed, the conditional average of the primitive variables preserves the most representative spatial small-scales, as seen from the comparison for $Pr = 4.3$ in figure 5.14.

Both approaches are seen as complementary to each other and give a different perspective of the same physical process with consistent results.

5.3 Dynamics outside of the 'regime of consecutive reversals' using mixed POD modes

In the previous section we separated our data into sub-sets: a first one belonging to the CR regime, and a second one excluding the CR regime composed of 1900 snapshots taken every 2 convective time units for $(Ra = 5 \cdot 10^7, Pr = 4.3)$. In this section, we concentrate on the POD analysis performed on the second set which contains snapshots taken from the 'regime of extended cessations' (EC) and from an intermediate regime, referred to as

94
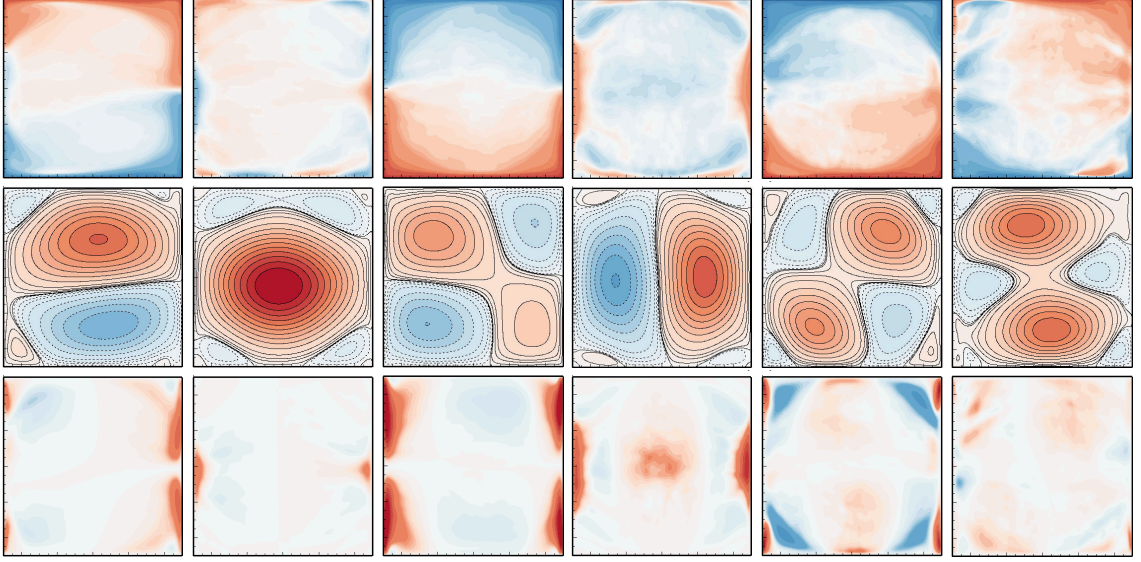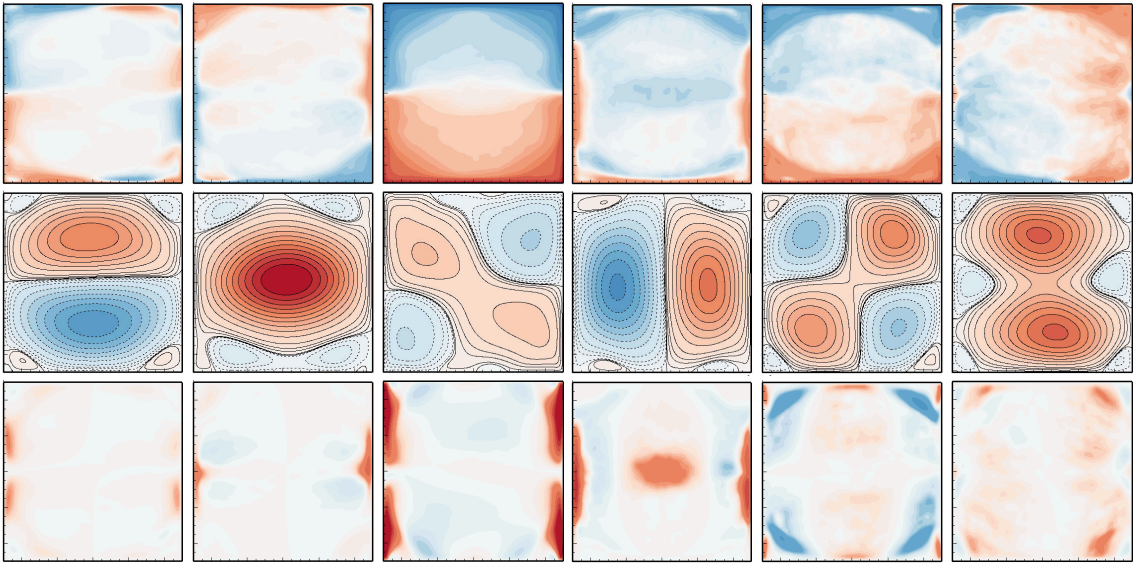
Figure 5.16: Six most energetic POD modes obtained using formulation (C) and a filtered subset which excludes the regime of 'consecutive reversals' for (a) (Ra $= 5 \cdot 10^7$, Pr $= 3.0$) and (b) (Ra $= 5 \cdot 10^7$, Pr $= 4.3$). From top to bottom: temperature field, stream-function, and vertical heat-flux. Layout is identical to figure 5.2.

95

rogue reversals in §4. The main idea is to determine if there exists a particular type of flow structure strictly related to cessations, that is hidden or distorted due to the presence of the CR regime. This is a challenging thing to do for several reasons. For the selected values of (Ra, Pr) the amount of time spent inside extended cessations is only a small fraction of the total length. The limited number of snapshots available inside this regime also makes very difficult to verify the convergence of our POD analysis. In order to validate our results, we repeated this procedure for (Ra $= 5 \cdot 10^7$, Pr $= 3.0$) using a total of 1600 snapshots. Since cessations are less common for this value of (Ra, Pr) and our observations are shorter, snapshots in the subset excluding reversals are taken every convective time unit.

The resulting POD spectra is shown in figure 5.15 for the first 20 modes. Results for both values of (Ra, Pr) are consistent with each other: cumulative energy contained inside the first 6 and 20 POD modes of 0.88 and 0.94, respectively, and at least 2 decades of decay are observed between modes $k = 1$ and $k = 20$.

Figure 5.16 displays the corresponding POD modes. A different set of energetic structures is observed inside and outside the CR regime. Outside the CR regime, the most energetic mode is a double-roll mode similar to mode S_y. Similarly, the fourth most energetic mode is similar to S_x. It is reminded that, S_y and S_x correspond to the double-roll patterns extracted from the complete series (see figure 5.2c). The second most energetic mode corresponds to a central vortex which is detached from the top and bottom walls. This mode is a combination of modes L and L* as shown in (Podvin and Sergent, 2017). The third and fifth most energetic modes are distorted versions of the modes Q and Q*, or combinations of these modes. The sixth most energetic mode was not shown previously and it is composed of two central rolls surrounded by six smaller counter-rotating rolls. This mode is approximatively antisymmetric with respect to $\mathbb{S}_x$ and $\mathbb{S}_y$, the same symmetry group of modes L and L*. This mode is not present in the first twelve modes displayed in figures 5.2 and 5.3. Some of the POD modes obtained from the snapshots including and excluding the CR regime are similar, while others are specific to one regime or the other. A POD analysis of the complete series is shown to mix these modes.

5.4 Comparison inside and outside the 'regime of consecutive reversals'

In order to compare the CR and EC regimes we fix a set of modes ϕ_k that allows for a direct comparison. In this case, ϕ_k corresponds to the POD modes obtained inside the CR regime.

5.4.1 Time evolution of the modal coefficients inside the EC regime using the leading POD modes of the CR regime

Figure 5.17 displays the modal coefficients obtained by projection into the POD modes displayed in 5.9. Inside the EC regime (shaded region), the mode S becomes dominant and alternates between positive and negative *plateau* states. Mode S* displays stronger fluctuations but lacks a well defined behavior. The coefficient for mode L oscillates around

(a)
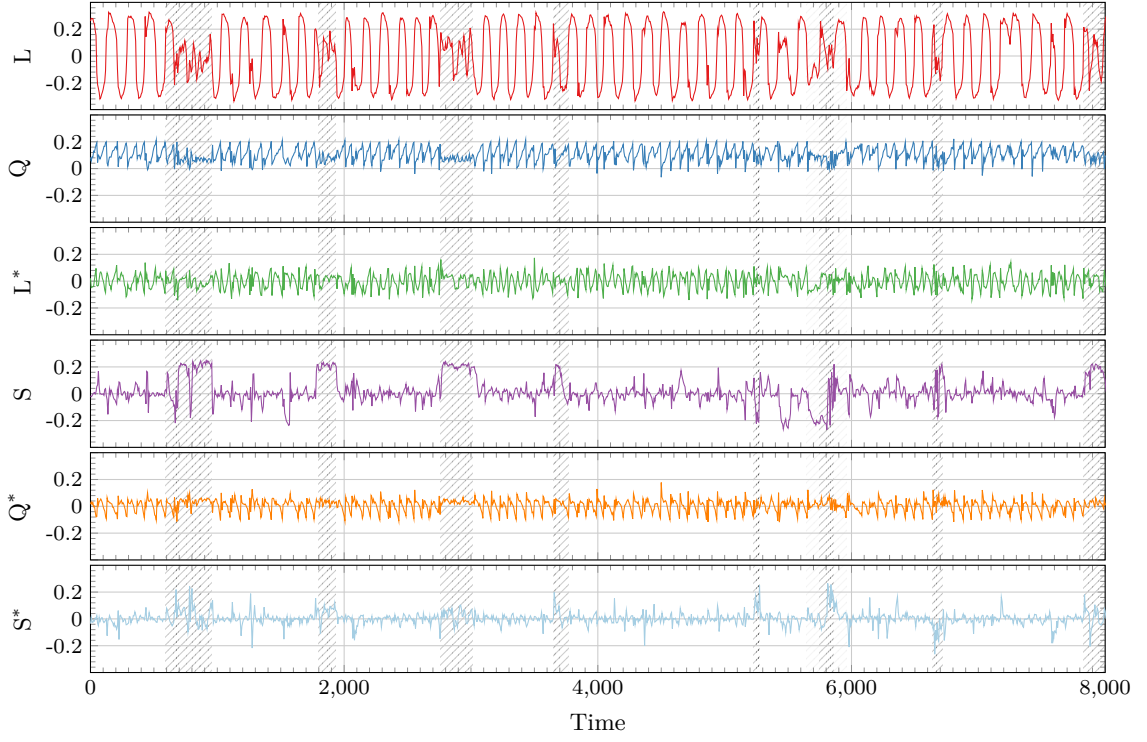
(b)
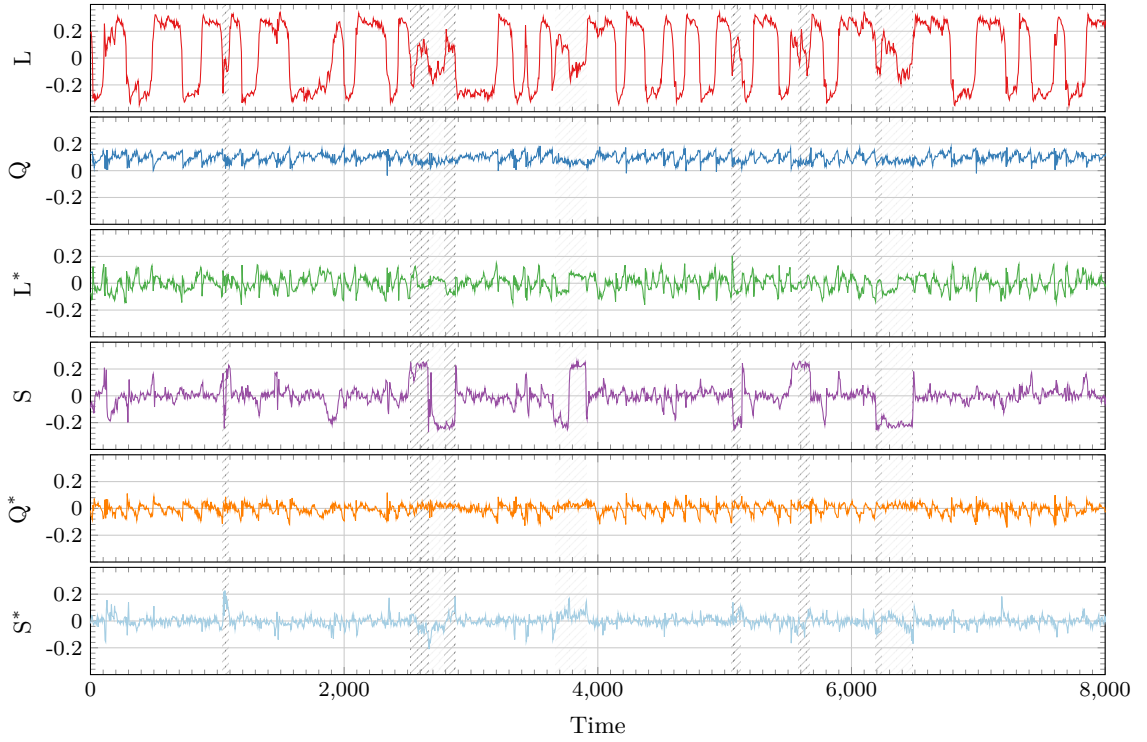
Figure 5.17: Time series of modal coefficients $\alpha_k(t)$ for (a) ($\mathrm{Ra} = 5 \cdot 10^7, \mathrm{Pr} = 3.0$) and (b) ($\mathrm{Ra} = 5 \cdot 10^7, \mathrm{Pr} = 4.3$). Shaded (resp. white) regions are used to identify an EC (resp. CR) regime on the time series.
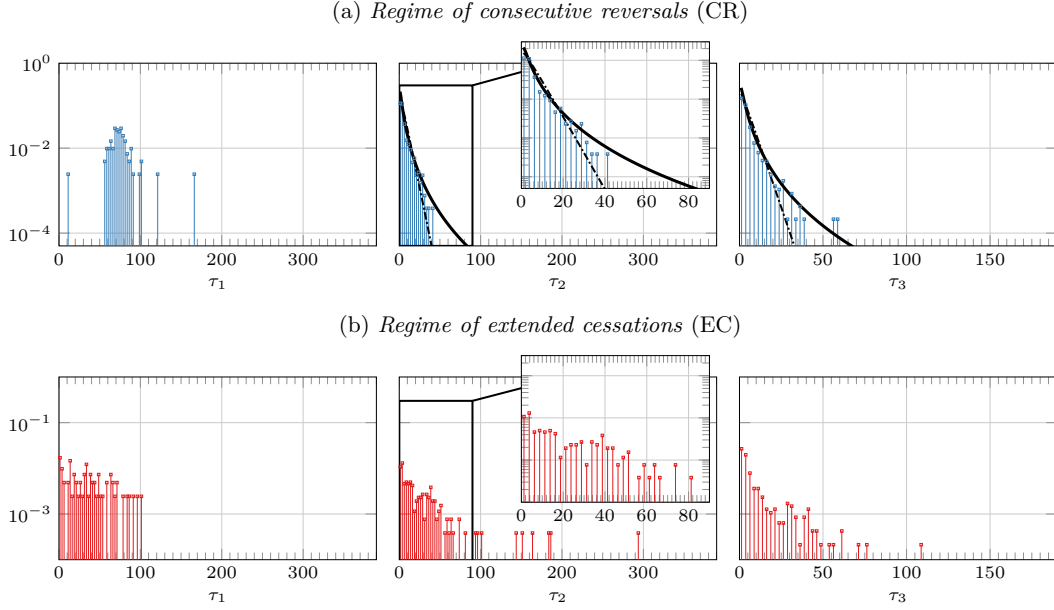
Figure 5.18: Conditional PDF of τ_1, τ_2, and τ_3 for (Ra $= 5 \cdot 10^7$, Pr $= 3.0$), where τ_1, τ_2, and τ_3 correspond to the inter-switch interval in modes L, S, and S*, respectively. (a) belongs to the CR regime, (b) belongs to the EC regime. For τ_2 and τ_3, a continuous (resp. dashed) line corresponds to a data fit to a Log-normal (resp. Gamma) distribution. Coefficients given in text.

zero and occasionally displays shorter and less intense *plateau* states than inside the CR regime. The evolution of mode L* does not exhibit any clear trend. Modes Q and Q* oscillate around the same constant values as in the CR regime but their fluctuations are less intense.

The time evolution of mode S during the EC regime is reminiscent of the evolution of mode L in the CR regime. This suggests we can follow the evolution of mode S to characterize the EC regime. For this reason we compute the inter switch time τ_2 of mode S, similarly as the interval τ_1 of mode L presented §4. For the sake of completeness, we extend this analysis to S*.

Consider a set of consecutive times s_i (resp. t_j) at which the modal coefficient S (resp. S*) changes sign. One evaluates the time interval $\tau_{2,i} = s_{i+1} - s_i$ (resp. $\tau_{3,j} = t_{j+1} - t_j$). The PDFs of τ_1, τ_2, and τ_3 for (Ra $= 5 \cdot 10^7$, Pr $= 3.0$) are compared on figure 5.18. Inside the CR regime, one of the main features of τ_1 is the absence of short inter-switch timescales, while this is the opposite in the EC regime. In contrast to τ_1, inside the CR regime the distributions of τ_2 and τ_3 exhibit short inter-switch times, while inside the EC regime, the distributions are more dispersed. It appears that the distributions of τ_2 and τ_3 fit well to a Log-normal distribution

$$P(\tau) = \frac{1}{\tau} \frac{1}{\sigma_\tau \sqrt{2\pi}} \exp\left(-\frac{(\ln \tau - \mu_\tau)^2}{2\sigma_\tau^2}\right) \tag{5.2}$$

inside the CR regime. Here μ_τ (resp. σ_τ) is the mean (resp. standard deviation) of the natural logarithm of the variable τ.

One alternative used in the characterization of the reversals of the geo-dynamo involves

98

(a) *Regime of consecutive reversals* (CR)

(b) *Regime of extended cessations* (EC)
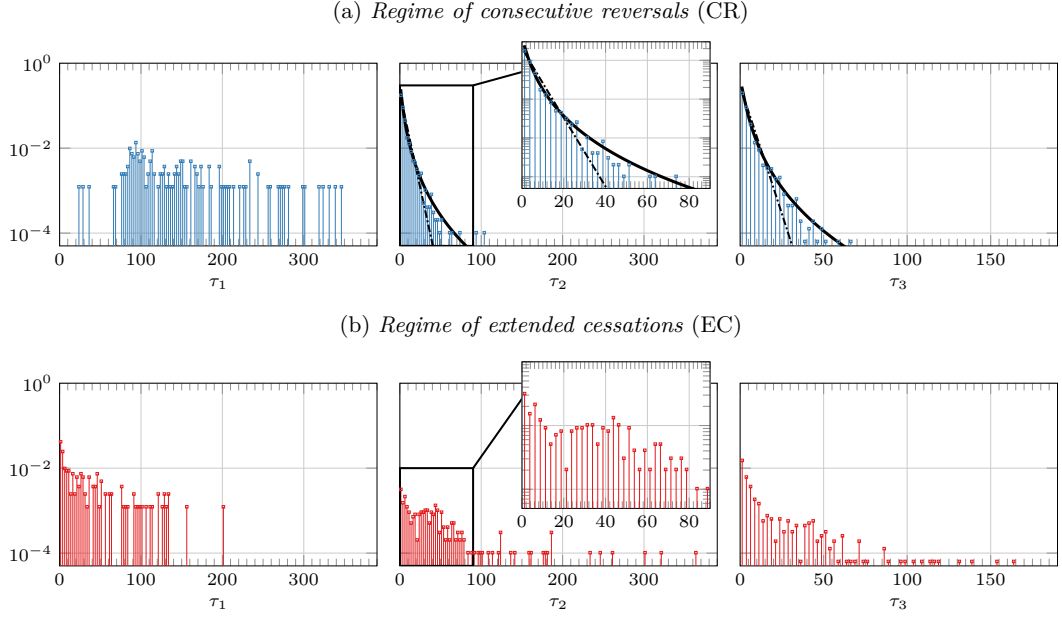
Figure 5.19: Same as in figure 5.18 but for $(\mathrm{Ra} = 5 \cdot 10^7, \mathrm{Pr} = 4.3)$.

considering a Gamma distribution (Lhuillier et al., 2013). For such process, the PDF of the inter-switch interval has the following form

$$P(\tau, k) = \left(\frac{k}{\mu}\right)^k \frac{\tau^{k-1}}{\Gamma(k)} \exp\left(-k\frac{\tau}{\mu}\right) \tag{5.3}$$

where $\Gamma(k)$ is the Gamma function of the shape parameter k, and μ the expected mean value of τ. A Gamma process has a memory of previous events when $k \neq 1$. A special case is observed for $k = 1$ and corresponds to a Poisson process (Parker, 1997).

A data fit of τ_1 inside the CR regime returns a shape parameter $k(\tau_1) = 16.35$ with an expected mean value $\mu(\tau_1) = 77.05$. In contrast, a data fit of τ_2 returns a shape parameter $k(\tau_2) = 0.97$ and expected mean value $\mu(\tau_2) = 4.78$, whereas τ_3 yields a shape parameter $k(\tau_3) = 1.07$ and $\mu(\tau_3) = 3.78$. We repeated this procedure for $(\mathrm{Ra} = 5 \cdot 10^7, \mathrm{Pr} = 4.3)$ seen on figure 5.19 and obtained the shape parameters $k(\tau_2) = 5.00$, $k(\tau_2) = 1.12$ and $k(\tau_3) = 1.10$, with the expected mean values $\mu(\tau_1) = 138.09$, $\mu(\tau_2) = 4.56$ and $\mu(\tau_3) = 3.70$, respectively. These observations would suggest that reversals of mode L are influenced by previous events, whereas the evolution of mode S and mode S* follows Poissonian statistics. This behavior is very different from other systems which display field reversals, such as the cessation-led reversals inside 3D cells (Brown and Ahlers, 2006) and the reversals of Earth's magnetic field (Lhuillier et al., 2013).

In this sense, the 'regime of consecutive reversals' contains elements of a deterministic system (Araujo et al., 2004; Castillo-Castellanos et al., 2016) and noise. The evolution of certain POD modes (L, Q, L*, and Q*) displays a consistent dynamical pattern for each reversal, while the modes S and S* appear to be driven by a random process. It is through these modes that 'randomness' appears to be introduced into the reversal process. Our observations are consistent with results from (Podvin and Sergent, 2017) in which a three-mode model using modes L, Q, and L*, results in periodic reversals.

In §5.2.2 we mentioned the existence of well-defined relations between different modes

inside the CR regime. Our observations suggest there exists, at least in the average sense, a particular relation between different pairs of modes: modes L and L*, Q and Q*, S and S*, and so on. In the following section we focus on how the interaction between different pairs of modes changes inside and outside of the CR regime.

5.4.2 A note on the coexistence between modes

We use a bivariate histogram to illustrate the relation between different pairs of modes. In order to highlight the differences between the CR and EC regimes, we have produced separate histograms for each in figures 5.20 to 5.23. For the CR regime, we also display the generic curves and identified each of the phases and functional instants which characterize the reversal cycle.

Inside the CR regime, the *accumulation* (resp. *release*) phase corresponds to the upper (resp. lower) branches in the (L,Q) plane, with the *acceleration* phase connecting the upper and lower branches. Two attractive fixed points are observed in the (L,S) and (L,S*) planes. Outside of the CR regime, two attractive fixed points are observed in the (L,Q) and (L,S) planes. These observations are consistent with the phase portraits in the (L,Q) and (L,S) planes and to the near-heteroclinic cycle identified by (Podvin and Sergent, 2015). Observations are also consistent with the phase space projections of Fourier modes by (Petschel, Wilczek, et al., 2011; Verma et al., 2015) in a similar system using stress-free boundaries and Pr $= \infty$.

A strong relation between modes L and L* is also shown to exist. As noted by (Podvin and Sergent, 2017), the quadrants LL$^* > 0$ are predominantly occupied during the CR regime. As the intensity of L decreases near the end of the accumulation phase, the mode L* does just the opposite, see figure 5.20(4). During reversals, the inversion of mode L passes systematically through rapid inversions in mode L*. During cessations the relation between both modes changes as both modes are locked in the quadrants LL$^* < 0$, see 5.21(4). These attractors would correspond to a clockwise or counter-clockwise central vortex that is fully detached from the top and bottom walls (Podvin and Sergent, 2017). This is also consistent with the second most energetic mode obtained from the EC subset displayed in figure 5.16.

A relation between modes Q and Q* is shown to be quite robust and does not appear to be affected by the change of regime between reversals and cessations, see figures 5.20(6) and 5.21(6). Inside the CR regime, the generic cycle makes evidence the presence of lower and upper branches corresponding to the release and accumulation phases, respectively.

Modes S and S* belong to the same symmetry group. During the CR both modes oscillate randomly around zero (figure 5.20(5)), whereas during the EC regime we observe three attractive points in the (S,S*) plane.

So far we have established a relation between the intensity of the leading modes and specific parts of the reversal process. Dominant L and Q modes are related to the accumulation phase. The intensity of modes L* and Q* increase during the end of the accumulation phase and during the transition. On the other hand, modes S and S* are predominantly active during cessations. In this sense, the strength of one mode relative to the others

might provide some insight on the large-scale dynamics. In the following section, we follow this relative strength as function of Ra.
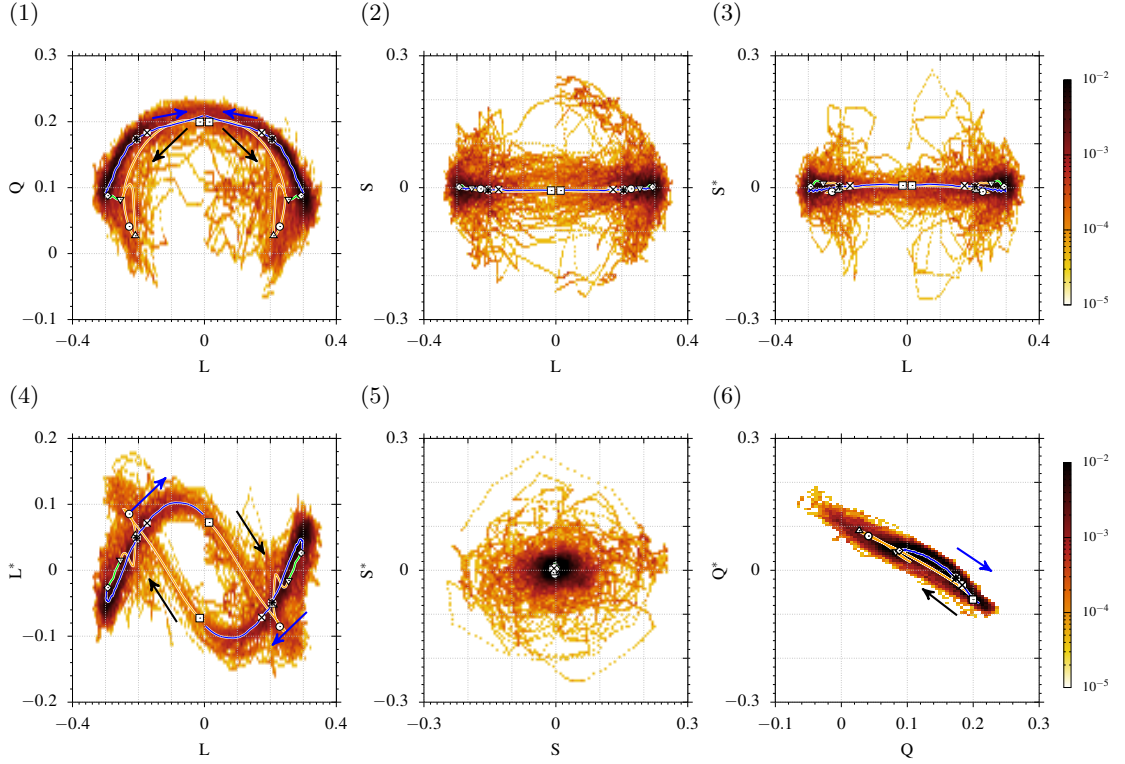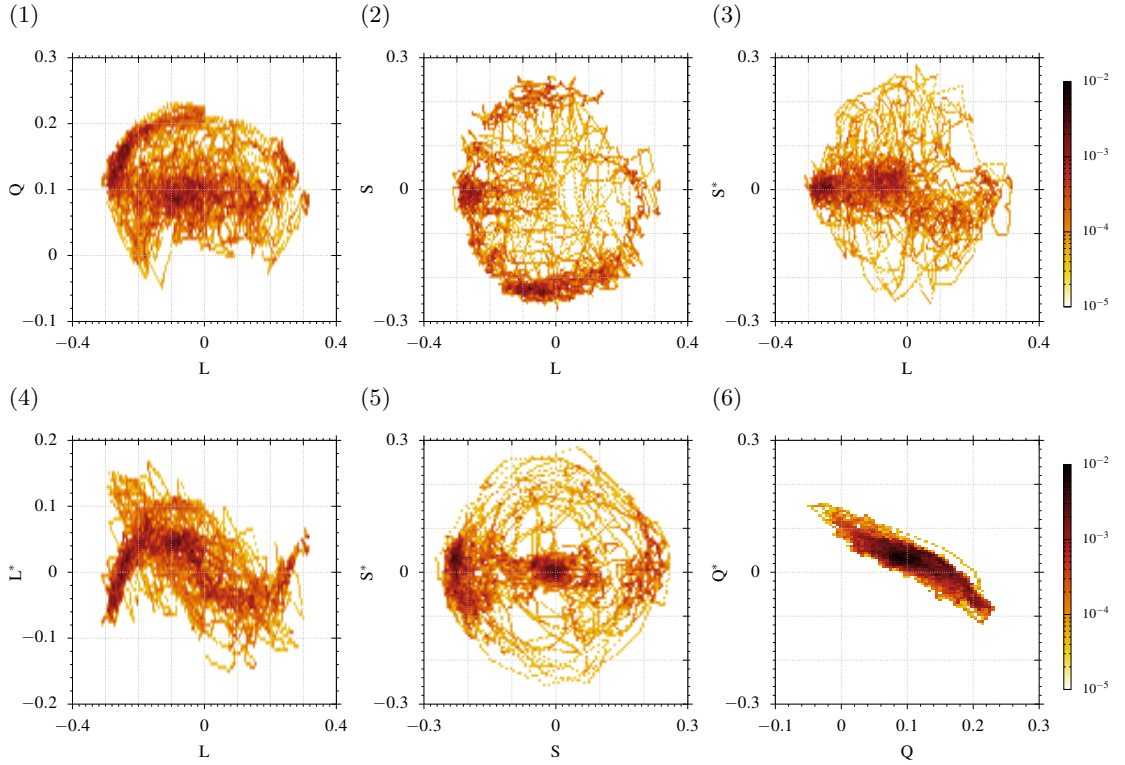
Figure 5.21: Bivariate histogram of modal coefficients for $(\mathrm{Ra} = 5 \cdot 10^7, \mathrm{Pr} = 3.0)$ excluding contributions from the CR regime.
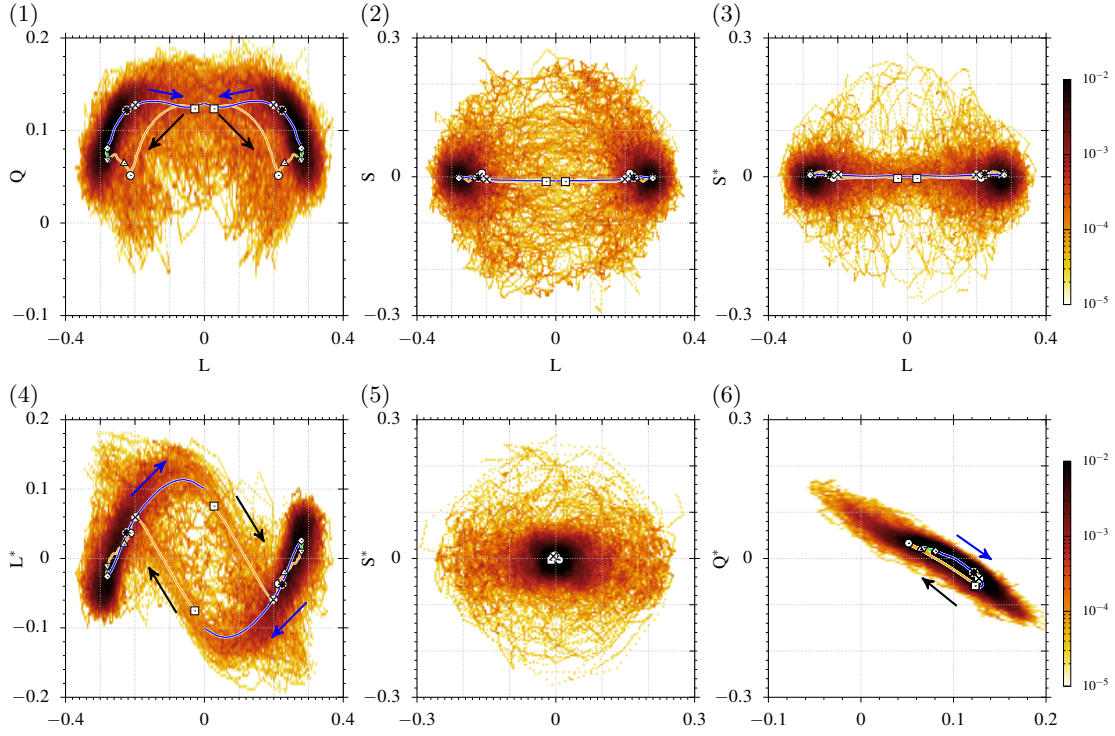
Figure 5.23: Bivariate histogram of modal coefficients for $(\mathrm{Ra} = 5 \cdot 10^7, \mathrm{Pr} = 4.3)$ excluding contributions from the CR regime.

5.5   Evolution of the leading POD modes as function of Ra
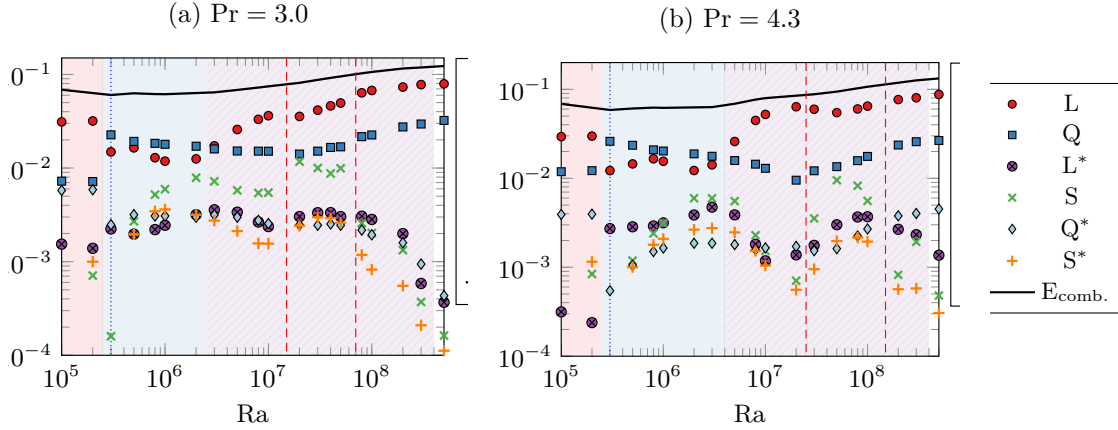
Figure 5.24: Evolution of $\overline{\alpha_k \alpha_k}$ as function of Ra and two different Pr. Here $\overline{\alpha_k \alpha_k}$ corresponds to the mean part of the combined energy projected on the ϕ_k-axis, whereas ϕ_k corresponds to the first 6 POD modes obtained from the CR subset for Ra $= 5 \cdot 10^7$. The total combined energy $\overline{\langle \psi | \psi \rangle}$ is displayed in black lines (Tot.). The values of Ra where flow reversals are observed are enclosed in the hatched area, whereas the combination of the EC and CR regimes is observed between the red dashed lines.

For each Pr, we fix a set of modes $\phi_k(\mathbf{x}, t)$. Here, ϕ_k corresponds to the POD modes obtained from the CR subset for Ra $= 5 \cdot 10^7$. For this comparison we perform a phase-space projection of the instantaneous velocity and temperature fields on the ϕ_k-axis

$$\alpha_k(t) = \langle \psi(\mathbf{x}, t) | \phi_k(\mathbf{x}, t) \rangle \qquad \text{with } \psi = (\theta, u, v) \qquad (5.4)$$

where $\langle . | . \rangle$ is the inner product operator defined in §2.6. For each value of (Ra, Pr), we compute $\overline{\alpha_k \alpha_k}$, which corresponds to the mean part of the combined energy $\overline{\langle \psi | \psi \rangle}$ contained inside the mode ϕ_k. In general, the selected POD modes are deemed as representative of the (Ra, Pr) considered here: the amount of combined energy contained inside these six modes represents between 80% and 95% of $\overline{\langle \psi | \psi \rangle}$ for all Ra.

If we follow the evolution of $\overline{\alpha_k \alpha_k}$ as function of Ra, it is possible to identify different regions based on the relative intensity of the different modes (figure 5.24). Each region is associated to a particular type of dynamics displayed on figure 5.25.

As both values of Pr display many similarities on their behavior, let us consider the case for Pr $= 3.0$. For values below Ra $= 3 \cdot 10^5$, mode L is clearly dominant and the corresponding flow is a steady-state single roll. A second region is observed between Ra $= 3 \cdot 10^5$ and Ra $= 3 \cdot 10^6$, where the mode Q becomes slightly dominant over mode L. However, the value of Q decreases slowly as we increase Ra, while the remaining modes are shown to increase. Inside this region we observe periodic or chaotic reversals *sans* the accumulation phase, i.e. no plateau is visible in L$_{2D}$. An almost periodic oscillatory solution is observed for Ra $= 3 \cdot 10^5$. This is exclusively composed of the release phase of the CR regime, similar to periodic oscillatory solutions of the flywheel mechanism by (Lappa, 2011; Chandra and Verma, 2013). A third region appears for Ra $\geq 3 \cdot 10^6$, where the mode L becomes clearly dominant again. Inside this region, we observe intermittent flow reversals containing the three phases described by the generic cycle. Mode Q is the second most energetic mode.

(a)

(b)
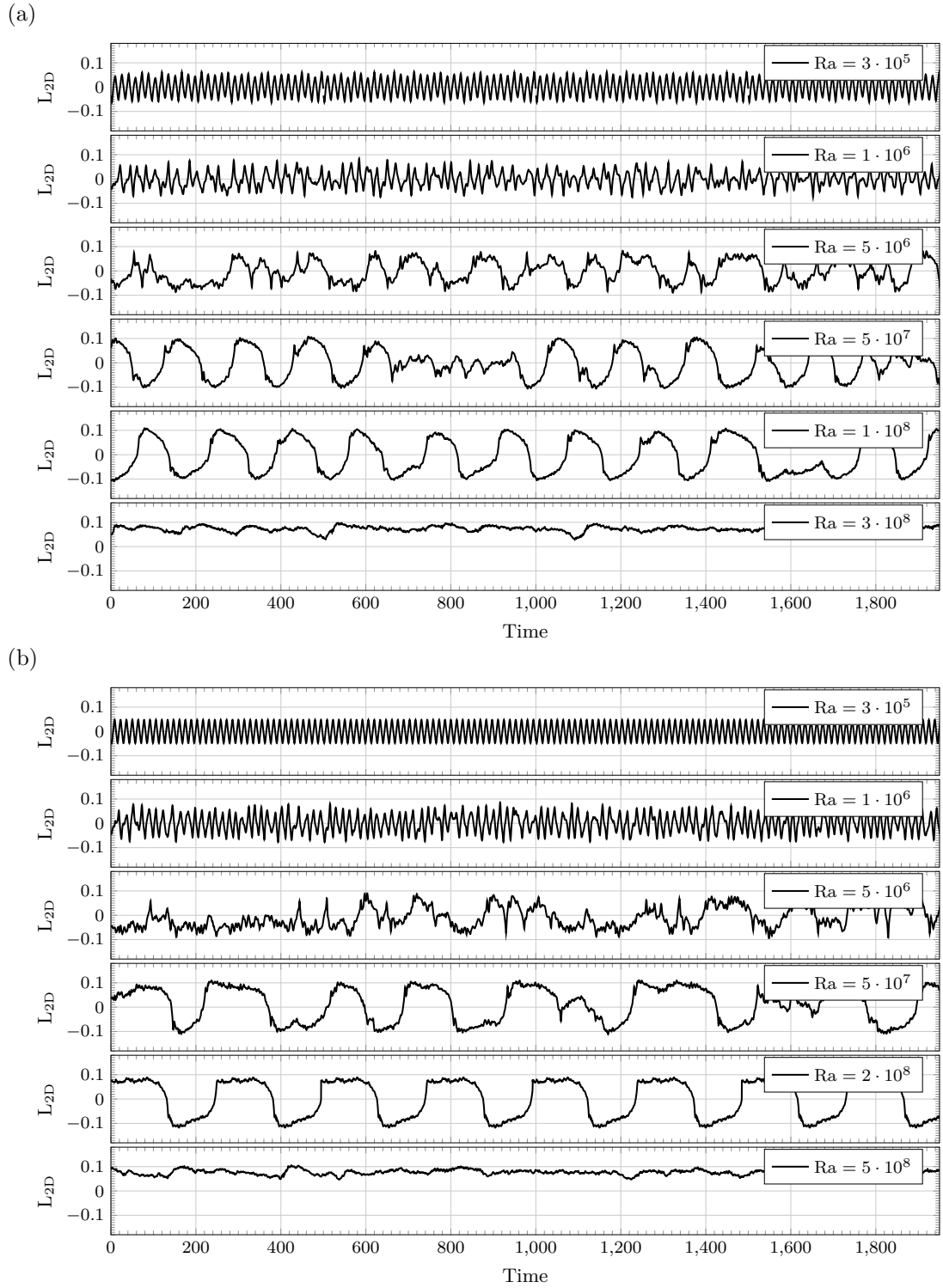
Figure 5.25: Time series of the global angular impulse L_{2D} for different Ra and (a) Pr = 3.0 and (b) Pr = 4.3. From top to bottom: periodic reversal without accumulation phase, chaotic reversals without accumulation phase, reversals with accumulation phase, consecutive reversals and extended cessations, consecutive reversals without extended cessations, long stable plateaus.

All other modes are smaller by an order of magnitude except in a particular range of Ra where the mode S becomes comparable to Q. Inside this range, extended cessations coexists with the consecutive reversals. Above this range, cessations disappear almost completely as the plateau duration increases progressively, as presented in §4. Above a certain value of Ra, it becomes increasingly difficult to observe any reversals at all.

It is difficult to compare this sequence of regimes to the description provided by (Chandra and Verma, 2013) using Fourier modes of the vertical velocity. Several reasons may account for these differences: different values of Pr are used, a different decomposition, and the fact that our simulations may be too short to ensure the statistical convergence.

Conclusions of this chapter

In this chapter we used a POD analysis to characterize the reversal regime inside a square Rayleigh-Bénard cells. A reconstruction of the mechanical energy from three different formulations was compared against the generic reversal curves. In agreement with the existing literature, the mixed velocity-temperature formulation was found to provide the best results. A six-mode representation of flow reversal retains the most important features of the reversal process and is deemed as a good compromise.

We performed a POD analysis of the CR and EC regimes separately. Inside the CR regime, we followed the evolution of the six most energetic POD modes during the generic cycle. Two of these modes exhibit a reversal (L and L*), two others (Q and Q*) follow a dynamical pattern but do not reverse, whereas the other two (S and S*) oscillate around zero. Both regimes (EC and CR) are characterized by the same set of coherent structures, except for one mode present in the EC regime and not observed in the CR regime. This made possible to perform a direct comparison of the dynamics of the CR and EC regime. Finally, we followed the energy contents of the different modes as function of Ra to illustrate the limited range in which consecutive flow reversals are observed and the presence of extended cessations within this range.

Complementary material: Simulation Parameters

(a) Pr = 3.0

Ra	Grid	Length	$\overline{Nu}_{bot}$	$\overline{Nu}_{top}$	$\overline{Nu}_{vol}$	$\overline{Nu}_\epsilon$	$\overline{Nu}_d$	$\overline{Nu}_\theta$	$\overline{Nu}$	%
$1 \cdot 10^6$	512	4,500	6.60	6.60	6.60	6.60	6.59	6.59	6.60	0.2
$3 \cdot 10^6$	512	4,500	8.82	8.82	8.84	8.82	8.80	8.81	8.82	0.4
$5 \cdot 10^6$	512	4,500	10.11	10.10	10.12	10.10	10.08	10.09	10.10	0.4
$8 \cdot 10^6$	512	4,500	11.61	11.62	11.63	11.61	11.55	11.58	11.60	0.7
$1 \cdot 10^7$	512	9,600	12.54	12.54		12.52		12.50	12.50	0.3
$2 \cdot 10^7$	512	9,600	15.52	15.52		15.49		15.46	15.50	0.4
$3 \cdot 10^7$	512	9,600	17.68	17.69		17.64		17.59	17.60	0.5
$4 \cdot 10^7$	512	9,600	19.42	19.42		19.36		19.30	19.30	0.6
$5 \cdot 10^7$	512	9,600	20.75	20.75		20.68		20.61	20.70	0.7
$8 \cdot 10^7$	512	5,000	23.95	23.94	24.00	23.87	23.42	23.57	23.79	2.5
$1 \cdot 10^8$	512	20,000	25.65	25.65	25.67	24.98	24.98	25.35	25.38	2.8
$3 \cdot 10^8$	1024	4,600	35.19	35.18	35.23	35.13	34.69	34.93	35.06	1.5
$5 \cdot 10^8$	1024	4,800	41.01	41.01	41.05	40.93	40.06	40.52	40.76	2.5

(b) Pr = 4.3

Ra	Grid	Length	$\overline{Nu}_{bot}$	$\overline{Nu}_{top}$	$\overline{Nu}_{vol}$	$\overline{Nu}_\epsilon$	$\overline{Nu}_d$	$\overline{Nu}_\theta$	$\overline{Nu}$	%
$1 \cdot 10^6$	512	4,500	6.83	6.83	6.84	6.84	6.83	6.83	6.83	0.2
$3 \cdot 10^6$	512	4,500	9.10	9.09	9.11	9.09	9.07	9.08	9.09	0.4
$5 \cdot 10^6$	512	4,500	10.48	10.48	10.50	10.48	10.45	10.46	10.47	0.5
$8 \cdot 10^6$	512	3,500	12.16	12.16	12.17	12.15	12.08	12.12	12.14	0.7
$1 \cdot 10^7$	512	9,600	13.07	13.07	13.08	13.03		13.05	13.06	0.3
$3 \cdot 10^7$	512	19,000	18.37	18.37	18.38	18.31		18.04	18.29	0.2
$5 \cdot 10^7$	512	29,000	21.01	21.01	21.03	20.86		20.95	20.97	0.7
$8 \cdot 10^7$	512	5,000	24.13	24.11	24.17	24.05	23.56	23.72	23.96	2.6
$1 \cdot 10^8$	512	19,000	25.88	25.88	25.90	25.19	25.21	25.58	25.61	2.8
$3 \cdot 10^8$	1024	4,600	35.64	35.62	35.68	35.58	35.13	35.35	35.50	1.6
$5 \cdot 10^8$	1024	4,800	41.37	41.35	41.40	41.28	40.29	40.82	41.09	2.8

Table 5.3: Convergence of Nusselt number; Rayleigh number, grid size, and lenght of simulation. Time-averaged values of Nu, averaged Nusselt number $\overline{Nu}$ and % maximum relative difference.

Part III

Influence of boundary conditions: stress-free surface on a square Rayleigh-Bénard cell

Chapter 6

Influence of imposing a stress-free surface on a square Rayleigh-Bénard cell

In the study of classic Rayleigh-Bénard cells, one assumes the Oberbeck-Boussinesq (OB) approximation and considers the same type of boundary conditions imposed on the top and bottom plates. In a such case, the reflection with respect to the horizontal plane $\mathbb{S}_y$ (see §2.5) is a natural symmetry of the system (Golubitsky et al., 1984). Recent studies in natural convection have been focused on systems which lack this reflection symmetry either due to the presence of non-Oberbeck-Boussinesq (NOB) effects (Zhang et al., 1997; Horn et al., 2013; Ahlers, Brown, et al., 2006; Sugiyama, Calzavarini, et al., 2009; Xia, Shu-Ning et al., 2016) or trough the use of asymmetric boundary conditions, for instance due to the use of a bottom rough plate (J. C. Tisserand, et al., 2011; Salort et al., 2014; Liot et al., 2016) or due to the use of different mechanical conditions on the top and bottom plates (Van Der Poel et al., 2014). Other physical systems where field reversals are present, are sensitive to asymmetric boundary conditions. For instance, periodic or random reversals of the magnetic field generated by a fluid dynamo in the Von Karman Sodium (VKS) experiment are observed only when different angular rotation velocities are imposed on the top and bottom lids (Berhanu et al., 2007; Gallet et al., 2012). For the Rayleigh-Bénard studies, the influence of the asymmetry is centered on the flow structures and on different global quantities. Deviations from the symmetric case are best observed on the mean temperature profiles, since the mean temperature at the center is no longer expected to correspond to the median temperature. For global quantities, the system response ranges from a modest increase in heat-flux to a transition to a different flow regime (Van Der Poel et al., 2014). One may also study the influence of asymmetry on stability. For instance, (Xia, Shu-Ning et al., 2016) focuses on the impact of NOB effects on the stability of flow structures during flow reversals. As the asymmetry increases, flow reversals are found to cover a wider range of the parameter space $(\mathrm{Ra}, \mathrm{Pr})$ than before.

In this chapter, we consider an asymmetric cell: stress-free (resp. no-slip) mechanical boundary condition imposed on the top (resp. bottom). This configuration is relevant for different systems, such as the convective boundary layer in the atmosphere. In the following the asymmetric cells are denoted as ST cells, whereas classic RB cells are denoted

as NT cells.

6.1   Model equations and numerical method

The governing equations are again the Boussinesq equations (2.22), with the same boundary conditions as in the previous chapters, except that a free-slip condition is now imposed on the top plate $y = 0.5$.

For the 2-D numerical simulations, we consider values of $\mathrm{Ra} \in [10^4, 5 \cdot 10^8]$ with $\mathrm{Pr} = 3.0$ and $\mathrm{Pr} = 4.3$. This range of values covers the onset of convective motion, the apparition of periodic and oscillatory solutions, and the transition to a (weakly-)turbulent regime. Simulations have been performed using Basilisk on a regular Cartesian grid, with a variable time-step that verifies the condition CFL< 0.5. Initial conditions correspond to no-motion and a linear temperature gradient. Spatial resolution is verified by following the procedure described in §3.2.2: one checks numerically the exact relations between the instantaneous rates-of-change (see equation (3.11)) and energy transfer rates. The second check concerns the statistical convergence of time-averaged Nusselt numbers proposed by (R. Stevens, Verzicco, et al., 2010). The average values of $\overline{\mathrm{Nu}}_{\mathrm{vol}}$, $\overline{\mathrm{Nu}}_{\mathrm{top}}$, $\overline{\mathrm{Nu}}_{\mathrm{bot}}$, $\overline{\mathrm{Nu}}_{\epsilon}$, $\overline{\mathrm{Nu}}_{\theta}$, $\overline{\mathrm{Nu}}_{\mathrm{d}}$, and $\overline{\mathrm{Nu}}$ as well as the maximum relative difference %Diff are listed in tables 6.1a and 6.1b (see §2.2.7 for definitions). These quantities are shown to converge within 2% when averaged over the entire length of the simulation except for the highest Ra.

In the following, for visualization we use the reference height $y_r(\mathbf{x}, t)$, instead of the temperature field $\theta(\mathbf{x}, t)$. Field $y_r(\mathbf{x}, t)$ is indeed a one-to-one mapping of the temperature field, which ensures that $y_r(\theta(\mathbf{x}, t)) < 0$ for 'cold' fluid parcels $\theta(\mathbf{x}, t) < \langle \theta \rangle_{\mathrm{xy}}$ and *vice versa*, thus composing a good candidate for (visually) separating thermal boundary layers from the bulk (see figure 6.1).

6.2   Overview of the flow dynamics for $10^5 < \mathrm{Ra} < 10^8$ inside free-slip (ST) cells

6.2.1   Steady-state solutions $(\mathrm{Ra} < 10^5, \mathrm{Pr} = 4.3)$

Let us consider the results for $\mathrm{Pr} = 4.3$. For this range of Ra, one obtains a single-roll and double-roll solutions (figure 6.1). The choice between one state or another depends on the value of Ra: from the same initial condition (no-motion and unstable temperature gradient with added noise), a single-roll state was obtained for $\mathrm{Ra} = 10^4$ and $\mathrm{Ra} = 8 \cdot 10^4$, whereas double-roll modes were obtained for $\mathrm{Ra} = 3 \cdot 10^4$ and $\mathrm{Ra} = 5 \cdot 10^4$. However, the choice depends as well on the initial conditions: if we start from an initial condition corresponding to a single-roll and increase Ra, we keep the single-roll structure. The presence of this type of multi-stable solutions is reflected on the different global quantities. This multi-stability is commonly observed in classic Rayleigh-Bénard cells (see for instance Mizushima and Adachi, 1997; Lappa, 2009).

Whenever convective motion is present for this range of Ra, the system reaches after a

(a) Single roll

(c) Temperature profiles
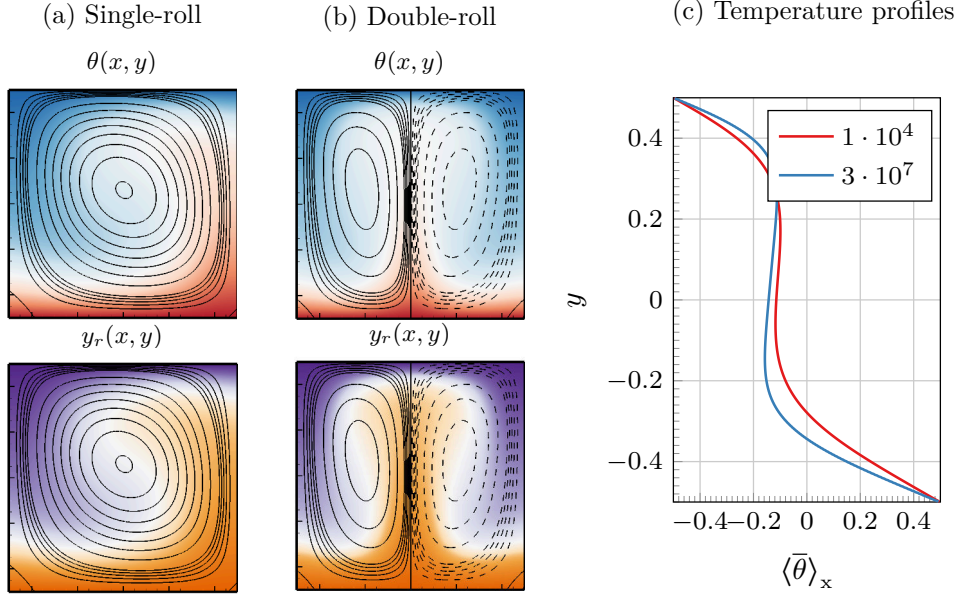
Figure 6.1: Steady-state solutions inside free-slip cells (ST) for $Pr = 4.3$: (a) $Ra = 10^4$ and (b) $Ra = 3 \cdot 10^4$. streamlines are superposed over the color map of field $\theta(x,y)$ (resp. $y_r(x,y)$). Fig. (c) displays the vertical temperature profile $\langle \theta \rangle_x$ for both Ra.

transition period a steady-state[1] with a lower mean temperature $\langle \theta \rangle_{xy}$ than the median temperature $(\theta_{top} + \theta_{bot})/2$ (figure 6.1c). This is allowed since the top/bottom symmetry no longer exists. This effect is further explored in the following sections.

6.2.2 Oscillatory and intermittent flows $(10^5 < Ra \leq 3 \cdot 10^5)$

The transition towards unsteady flows is observed near $Ra = 10^5$. Two types of oscillatory solutions are identifiable for both $Pr = 4.3$ and $Pr = 3.0$: a flow regime composed of a central vortex and another regime composed of two vertically stacked rolls. The apparent significance of these solutions will be discussed on the following sections.

Oscillatory one- and four-roll pattern

In the first type of oscillatory solution, a single-roll and four-roll pattern appears cyclically resulting in a periodic reversal of the large-scale circulation. A close inspection of the instantaneous fields (top part of figure 6.2) reveals the counter-rotating vortex is larger on the lower half than on the upper half of the cell. This difference shifts the rotation center of the central vortex slightly upwards. This type of solution is known to exist in classic RB cells at similar Ra, see (Mizushima and Adachi, 1997; Shimizu et al., 2015; Lappa, 2011), and is clearly reminiscent of the release phase of a generic flow reversal presented in chapter 4. To illustrate the difference between the solutions observed inside free-slip (ST) and no-slip (NT) cells, figure 6.2 displays a time-series of the angular impulse L_{2D}, the spatially averaged vorticity C and the normalized Nusselt numbers at the top and bottom plates, Nu_{top} and Nu_{bot}, for both cells. The evolution of L_{2D} is similar in both

---

[1] We use the L_∞ norm of the change in the horizontal velocity observed during two consecutive convective time units and fix 10^{-8} as our tolerance criteria to define a steady-state solution.
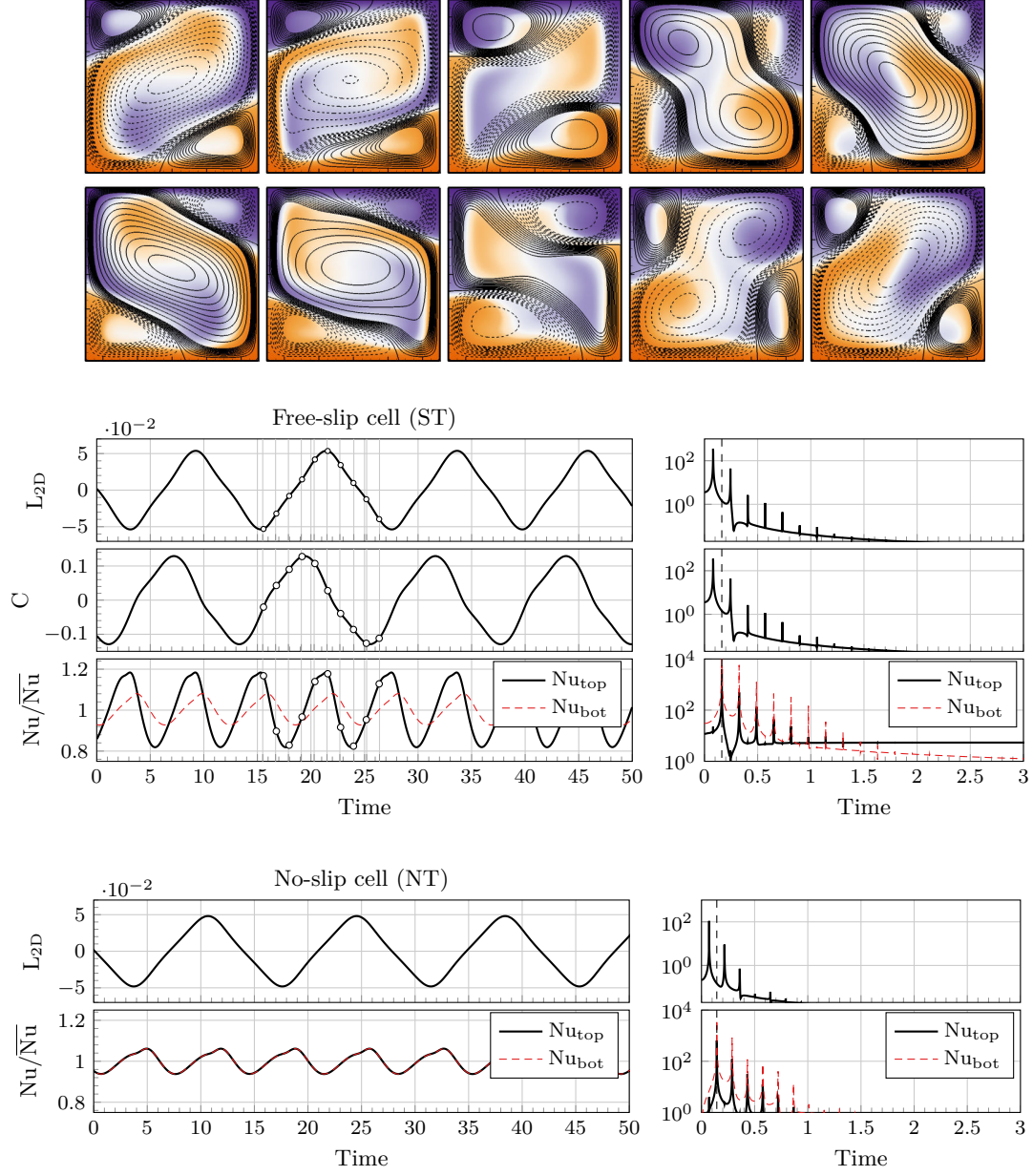
Figure 6.2: Oscillatory solutions for $(\mathrm{Ra} = 3 \cdot 10^5, \mathrm{Pr} = 4.3)$ for a free-slip (ST) cell. Top: Streamlines superposed to field $y_r(\mathbf{x}, t)$ corresponding to the oscillatory one- and four-roll pattern. Snapshots correspond to marks indicated on the time series below. Middle: Time series of L_{2D}, C, $\mathrm{Nu_{top}}$ and $\mathrm{Nu_{bot}}$ (see §2.2 and 2.3), and corresponding frequency spectra. Bottom: Time series and frequency spectra for the NT cell shown for reference.
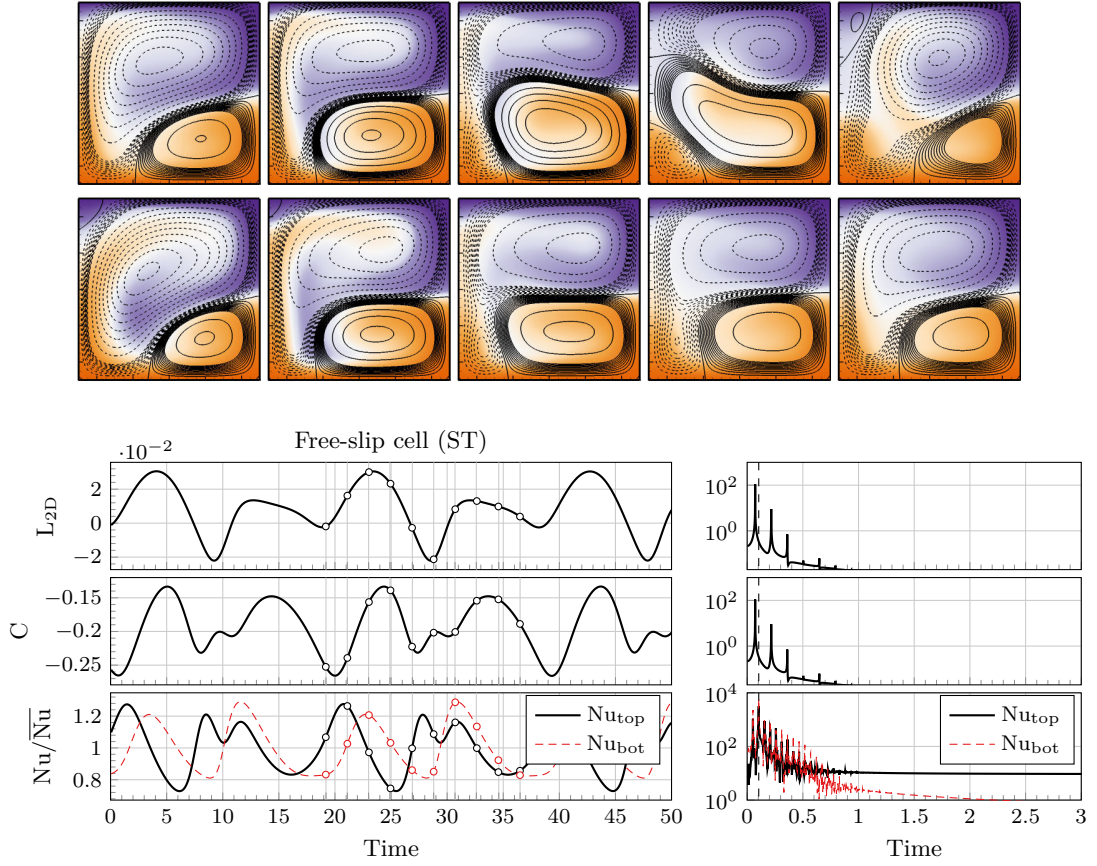
Figure 6.3: Same as in figure 6.2 for $(\mathrm{Ra} = 1 \cdot 10^5, \mathrm{Pr} = 4.3)$. An equivalent solution was not found for NT cells for $\mathrm{Pr} = 4.3$, see text.

cells, but the ST cell displays a larger amplitude and shorter period: the characteristic frequency of $\mathrm{L_{2D}}$ being $f = 0.081$ against $f = 0.072$ for the NT cell. In addition, for the modified cells C is non-zero and has the same dominant frequency as $\mathrm{L_{2D}}$ ($f = 0.072$) but is shifted in time with respect to $\mathrm{L_{2D}}$ by 2.8 convective time units. The evolution of $\mathrm{Nu_{top}}$ is different from the NT case, while $\mathrm{Nu_{bot}}$ is similar. For the ST and NT cells, $\mathrm{Nu_{top}}$ and $\mathrm{Nu_{bot}}$ have twice the frequency of $\mathrm{L_{2D}}$ and similar triangular shapes. However, in the ST cell the fluctuations of $\mathrm{Nu_{top}}$ are twice as large as those of $\mathrm{Nu_{bot}}$. Also, $\mathrm{Nu_{top}}$ is delayed 0.85 convective time units with respect to $\mathrm{Nu_{bot}}$, instead of being in phase as in the NT case.

Oscillatory double-roll pattern

A second type of oscillatory solution is observed on the ST cells. This solution is characterized by two opposing thermal plumes locked along the right wall and a single ascending plume along the left wall. This solution does not respect the top/bottom symmetry. The left/right symmetry is not respected either, but a mirror opposite configuration may be observed. Dominant flow structures correspond to two vertically stacked rolls, pushing back and forth one another, with one smaller corner roll which appears every half cycle, see bottom part of figure 6.3 at $t = 25$. This solution is not perfectly periodic as indicated by the noise in the spectra. A similar periodic solution is reported to exist in classic Rayleigh-Bénard cells for $(\mathrm{Ra} = 10^7, \mathrm{Pr} = 1.0)$ (Chandra and Verma, 2013, Supplementary

115
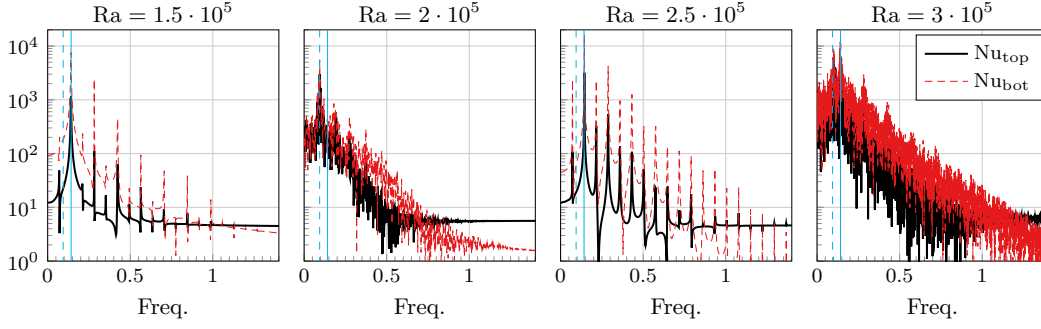
Figure 6.4: Time-frequency spectra of Nu_{bot} and Nu_{top} for $Pr = 3.0$ and different Ra: $Ra = 1.5 \cdot 10^5$, $Ra = 2 \cdot 10^5$, $Ra = 2.5 \cdot 10^5$, and $Ra = 3 \cdot 10^5$.
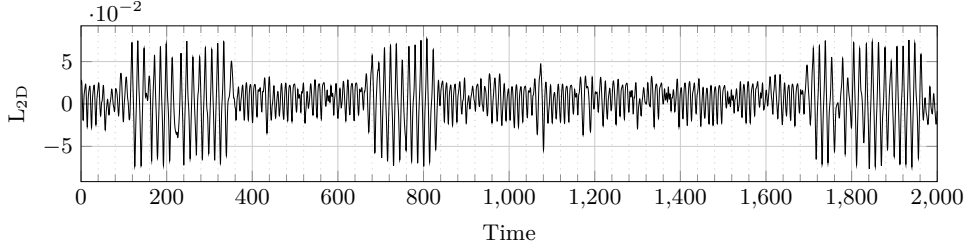
Figure 6.5: Time series of L_{2D} for $(Ra = 3\cdot10^5, Pr = 3.0)$ displays both oscillatory solutions intermittently.

material) but was not observed in our simulations.

The lack of top/bottom symmetry implies the value of L_{2D} might have a positive mean value (dashed lines on figure 6.3), or a negative one if the rotation sense of the rolls is inversed. The amplitude of L_{2D} is half of the amplitude of the first oscillatory solution. Additionally, C remains negative for positive L_{2D} (or *vice versa*) during the full length of the cycle, but displays the same dominating frequencies as L_{2D}. Both Nu_{bot} and Nu_{top} have comparable amplitudes and have the same dominant frequency as L_{2D} (f= 0.104). However, their time evolution is now different: Nu_{top} displays a secondary oscillation for every cycle, not present in Nu_{bot}. A similar solution is obtained for $Pr = 3.0$.

Intermittency and transition towards turbulence

Both types of oscillatory solutions are observed inside a narrow band from $1.5 \cdot 10^5 < Ra < 3 \cdot 10^5$. For $Pr = 3.0$, continuous reversals were observed for $Ra = 1.5 \cdot 10^5$ and $Ra = 2.5 \cdot 10^5$, while the stacked rolls were found for $Ra = 2.0 \cdot 10^5$, see figure 6.4. For $Ra = 3 \cdot 10^5$, both oscillatory solutions are observed intermittently: continuous reversals are seen on the amplitude of L_{2D} (figure 6.5), but also on the characteristic frequencies of the other quantities.

6.2.3 Weakly turbulent flow regime $(3 \cdot 10^5 < Ra < 5 \cdot 10^8)$

Once a (weakly-)turbulent regime is established, one observes the appearance of dynamical flow patterns which are reminiscent of both oscillatory solutions described earlier. Resulting flow structures are very similar to those ones previously observed in the NT

(a)

Cessation-type dynamics ●

Reversal-type dynamics ○

(b)

Reversal-type dynamics ○

(c)

Absence of flow reversals ○
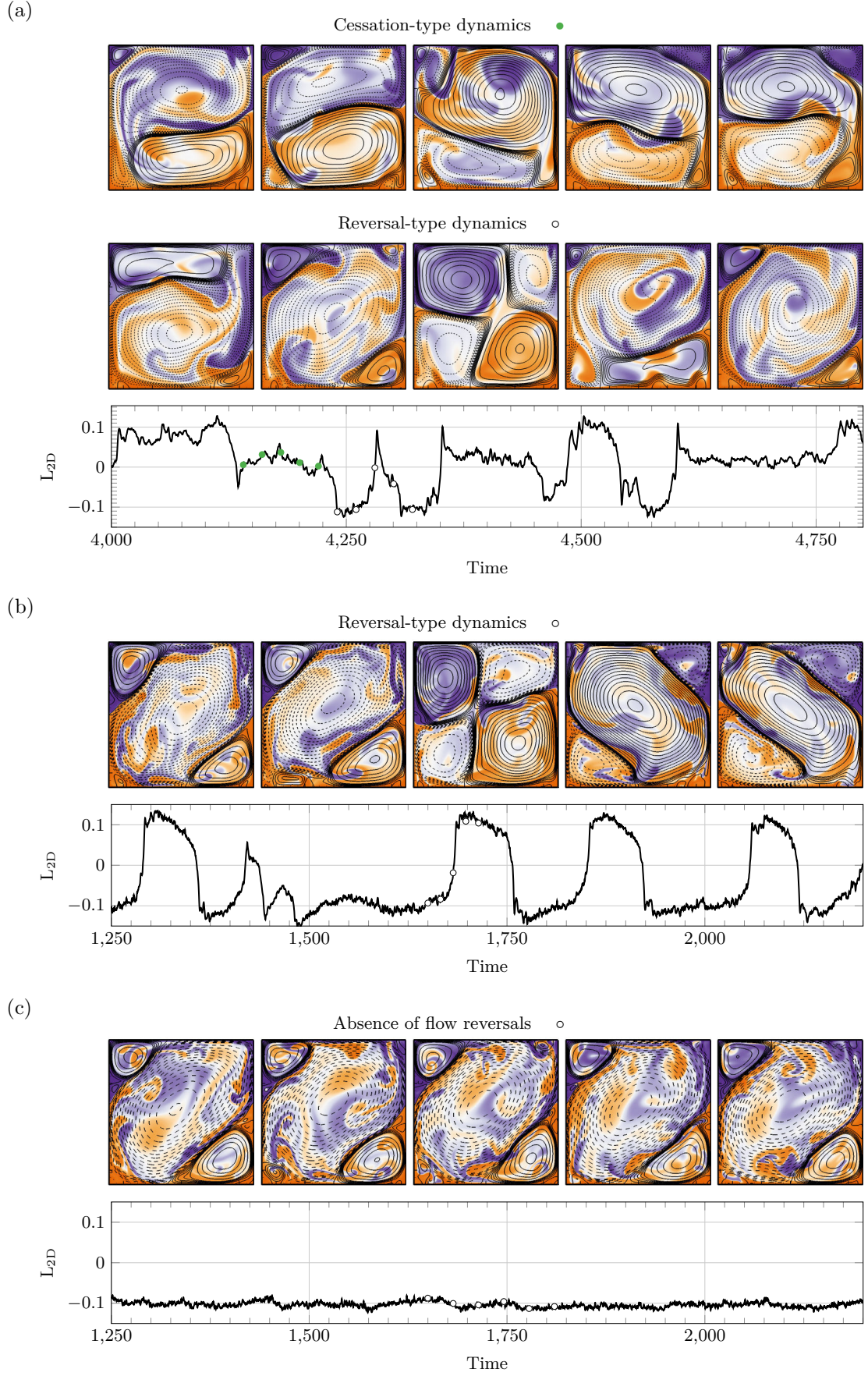
Figure 6.6: Instantaneous streamlines superposed over field $y_r(\mathbf{x}, t)$ and corresponding time series of L_{2D} inside ST cells (a) $(\mathrm{Ra} = 5 \cdot 10^7, \mathrm{Pr} = 4.3)$, (b) $(\mathrm{Ra} = 3 \cdot 10^8, \mathrm{Pr} = 4.3)$ and (c) $(\mathrm{Ra} = 5 \cdot 10^8, \mathrm{Pr} = 3.0)$.

117

cells, complete with the presence of flow regimes analogous to the regime of 'consecutive reversals' (CR) and the regime composed of 'extended cessations' (EC), see figure 6.6. The former regime is associated to a dominant central vortex and counter-rotating corner-rolls, similar to the CR regime presented on the previous chapter. The latter regime is associated to a dominant double-roll pattern which is sustained for relatively long periods of time, before spontaneously re-organizing in the opposite direction (figure 6.6a), similar to the EC regime.

As the value of Ra increases, a series of consecutive reversals are observed with increased regularity, while the extended cessations become less frequent and eventually disappear altogether (figure 6.6b). For higher Ra, an increasingly large amount of time is spent inside the *plateau* state, making the flow reversals difficult to observe (figure 6.6b). The sequence of coexistence of the CR and EC regime, followed by a progressive disappearance of the EC regime, then by an increasingly longer plateau state is consistent with observations inside NT cells presented in §5.5.

While the dominant structures are very similar in nature, the resulting flow dynamics are faster and more complex than for NT cells. In order to perform a direct comparison between the NT and ST cells, a statistical approach is required.

6.3 Statistical characterization: global quantities and spatial distribution

6.3.1 Lower bulk temperature

The modified cells are characterized by having a lower bulk temperature than their no-slip counterpart. This is observed for all flow regimes (steady, oscillatory, and turbulent). For instance for $(\mathrm{Ra} = 5 \cdot 10^7, \mathrm{Pr} = 4.3)$, bulk temperature is up to 10% lower than the median temperature $(\theta_{\mathrm{bot}} + \theta_{\mathrm{top}})/2$, see figure 6.7. To quantify this difference, let us define an asymmetry coefficient

$$\chi = \frac{0.5 - \langle \overline{\theta} \rangle_{\mathrm{xy}}}{\langle \overline{\theta} \rangle_{\mathrm{xy}} + 0.5} \tag{6.1}$$

For the modified cells, the asymmetry coefficient $\chi > 1$ for all of the values of Ra considered (figure 6.7). Three slopes are observed in this figure each associated to the temporal dynamics (steady-state, periodic oscillatory and turbulent flow regime respectively). In each case, the value of χ appears to increase with Ra. This asymmetry was also inside a periodic box with asymmetric (no-slip/free-slip) conditions and $\mathrm{Pr} = 1$ (Van Der Poel et al., 2014). It seems to us that the asymmetry is stronger for our configuration. In the case of an asymmetric cell due to a rough bottom plate and smooth top plates, a similar effect was also observed, but for much higher Ra.
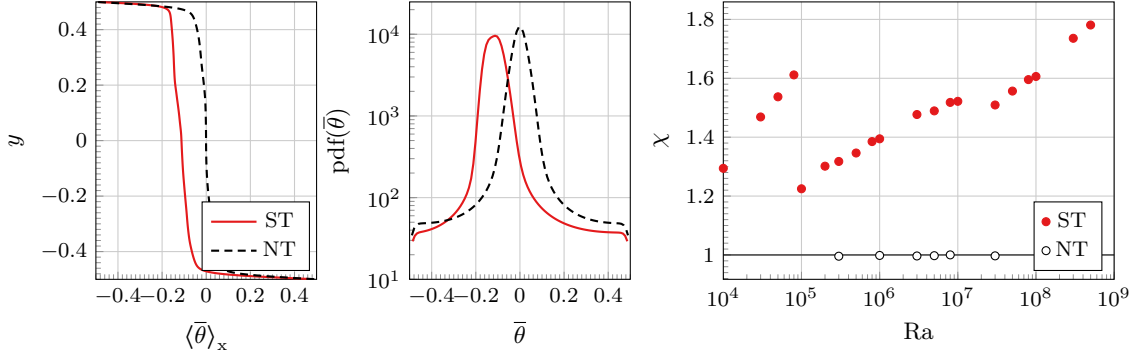
Figure 6.7: Mean temperature profile $\langle \overline{\theta} \rangle_{\mathrm{x}}$ (left) and probability distribution of the mean temperature $\overline{\theta}(\mathbf{x})$ (center) for $(\mathrm{Ra} = 5 \cdot 10^7, \mathrm{Pr} = 4.3)$. Asymmetry coefficient χ as function of Ra for $\mathrm{Pr} = 4.3$ (right).
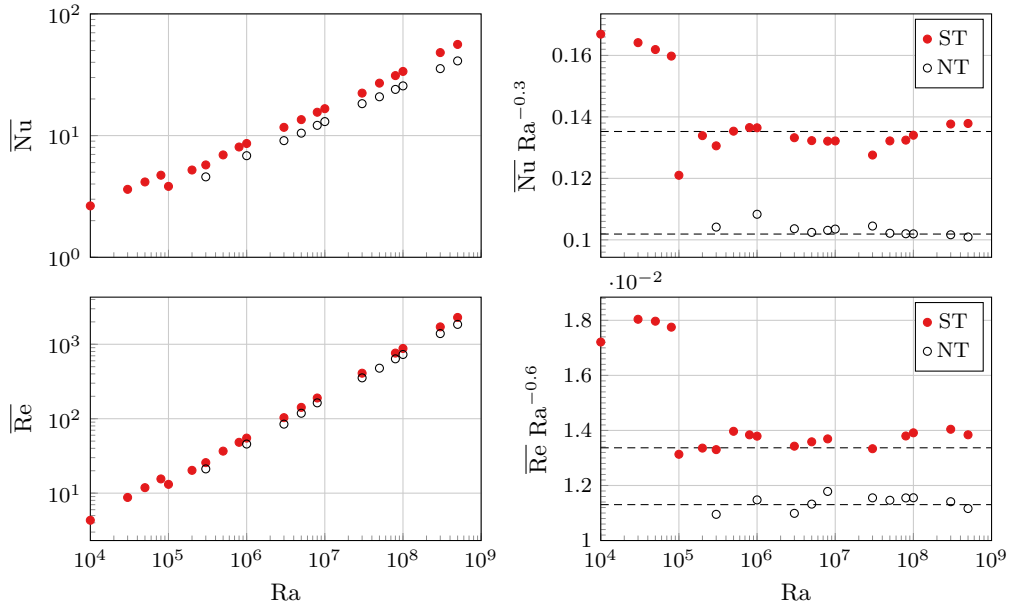
Figure 6.8: Simulations for $\mathrm{Pr} = 4.3$ (Left) Average Nusselt $\overline{\mathrm{Nu}}$ and Reynolds $\overline{\mathrm{Re}}$ number as function of Ra and (right) compensated $\overline{\mathrm{Nu}}$ and $\overline{\mathrm{Re}}$.

6.3.2 Increased heat-flux and turbulent motion

Going from NT to ST, the average Nusselt number $\overline{\mathrm{Nu}}$ increases from 20% to 40%, whereas the average Reynolds number $\overline{\mathrm{Re}}$ based on the mean velocity increases from 15% to 20% (figure 6.8). For both quantities, this increase is reflected on the dependence on Ra on the multiplicative coefficient rather than on the scaling exponents, see comparison between NT and ST in figure 6.8. Note that scaling exponents $\beta_{\mathrm{Nu}} = 0.30$ and $\beta_{\mathrm{Re}} = 0.60$ for $\mathrm{Pr} = 4.3$, were obtained by performing a power law fit of the NT cells.

Let us now consider the temporal fluctuations of the Nusselt around the mean, more precisely the probability density functions of the instantaneous Nusselt integrated along the fluid domain $\mathrm{Nu_{vol}}$ and the Nusselt numbers evaluated at the bottom and top plates, $\mathrm{Nu_{bot}}$ and $\mathrm{Nu_{top}}$, (figure 6.9). Values are normalized by $\overline{\mathrm{Nu}}$ to facilitate the comparison between the NT and ST cells. For the modified cell, the PDFs of $\mathrm{Nu_{vol}}$ and $\mathrm{Nu_{bot}}$ have the same overall shape with slightly longer tails. For $\mathrm{Nu_{top}}$, both configurations display a
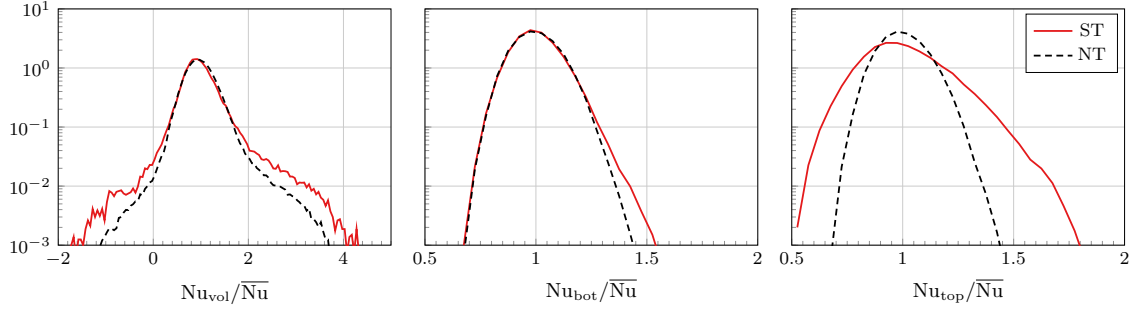
Figure 6.9: Probability density functions of the instantaneous Nusselt numbers $\mathrm{Nu_{vol}}$, $\mathrm{Nu_{bot}}$, and $\mathrm{Nu_{top}}$ for $(\mathrm{Ra} = 5 \cdot 10^7, \mathrm{Pr} = 4.3)$.
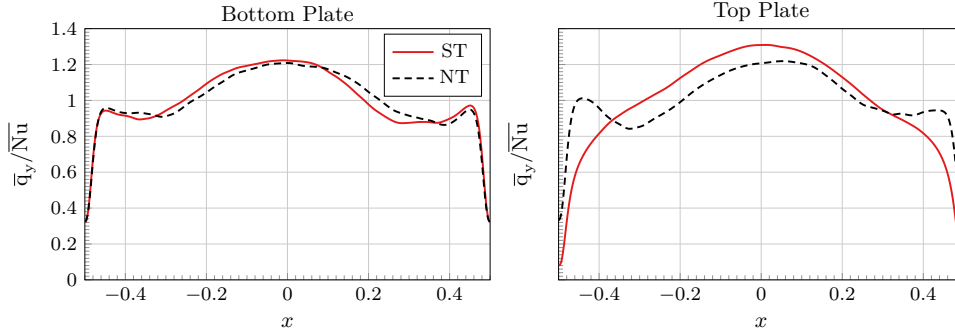
Figure 6.10: Normalized local heat flux $\overline{q}_y$ evaluated at the top and bottom plates for $(\mathrm{Ra} = 5 \cdot 10^7, \mathrm{Pr} = 4.3)$.

positive skewed distribution. However, since the thermal boundary layer interacts directly with the bulk flow, fluctuations are more intense in the modified cell: $\sigma(\mathrm{Nu_{top}})$ almost doubles with respect to the to $\sigma(\mathrm{Nu_{bot}})$, while the value of $\sigma(\mathrm{Nu_{bot}})/\overline{\mathrm{Nu}}$ is comparable in the ST and NT cells.

6.3.3 Changes in the spatial distributions of different quantities

Let us consider the spatial distribution for different fields. In order to facilitate the comparison between the ST and NT cells, let us focus on results for $(\mathrm{Ra} = 5 \cdot 10^7, \mathrm{Pr} = 4.3)$.

Vertical heat-flux at the top and bottom plates

For the contributions to $\mathrm{Nu_{bot}}$ and $\mathrm{Nu_{top}}$, we consider the local heat flux $\overline{q}_y$ evaluated on the top $(y = 0.5)$ and bottom $(y = -0.5)$ plates as a function of x (figure 6.10). For the bottom plate, the profiles are very similar in both cases. For the top plate, different profiles are observed: unlike the NT case, the ST profile decreases monotonically as one gets away from the center. This might be related the effect of top/bottom asymmetry prominently during the extended cessations or due to changes in the upper corner flows due to the free-slip condition.

120

Figure 6.[...] [...] of contribution [...]ion $\overline{\partial_j\theta\partial_j\theta}(\mathbf{x})$ for (Ra = [...] (a) ST and (b) [...] correspond to $\overline{\partial_j\theta\partial_j\theta} = 100$.
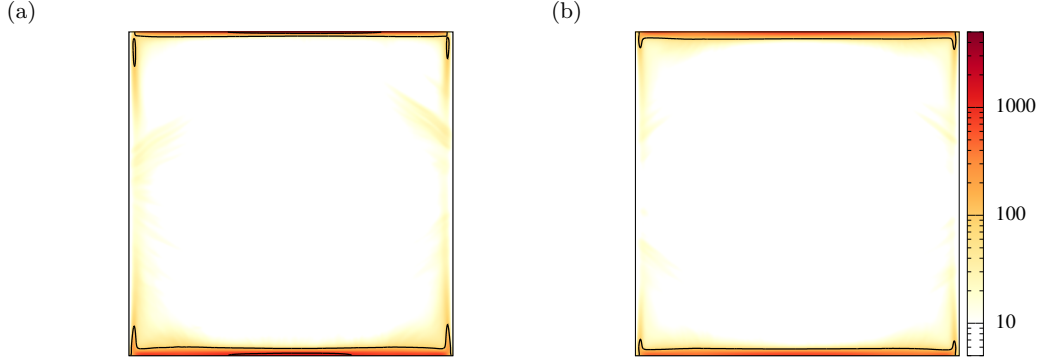
Figure 6.12: Spatial distribution of contributions to the viscous dissipation $\overline{\partial_j u_i \partial_j u_i}(\mathbf{x})$ for (Ra = $5 \cdot 10^7$, Pr = 4.3) inside (a) ST and (b) NT cells. Solid lines correspond to $\overline{\partial_j u_i \partial_j u_i} = 100$. Dashed horizontal lines located at $y = \pm 0.4$ for reference.

Thermal and viscous dissipation rates

Because of the increase in $\overline{\mathrm{Nu}}$ and the relations in (2.50), the total thermal dissipation ϵ_θ and total viscous dissipation ϵ increase as well when going from NT to ST cells. For both cells, the thermal dissipation rate ϵ_θ is highly localized near the top and bottom plates inside thermal boundary layers (figure 6.11). Also, the thermal boundary layer for the ST cells is thinner at the top plate than at the bottom plate.

In both cells, the viscous dissipation rate ϵ is very localized near the no-slip walls, particularly along the side-walls (figure 6.12). Additional, less intense contributions are observed near the corners. For the ST cell, a dissipation layer is observed just below the top plate, in which the dissipation has a comparable intensity to the corners. The viscous dissipation inside the bulk region ($-0.4 < x < 0.4$ and $-0.4 < y < 0.4$) is similar for both cells: 46% (resp. 45%) of ϵ for the ST (resp. NT) cells. Since the viscous dissipation barely changes in the bulk, the absence of dissipation at the top plate, should be compensated by remaining no-slip walls.

Temporal and spatial fluctuations in the modified cell near the (no-slip) bottom plate are similar to those in both plates of the no-slip cell. This suggests a disconnection between the top and bottom plates, which interact directly with the bulk flow but not with each other,
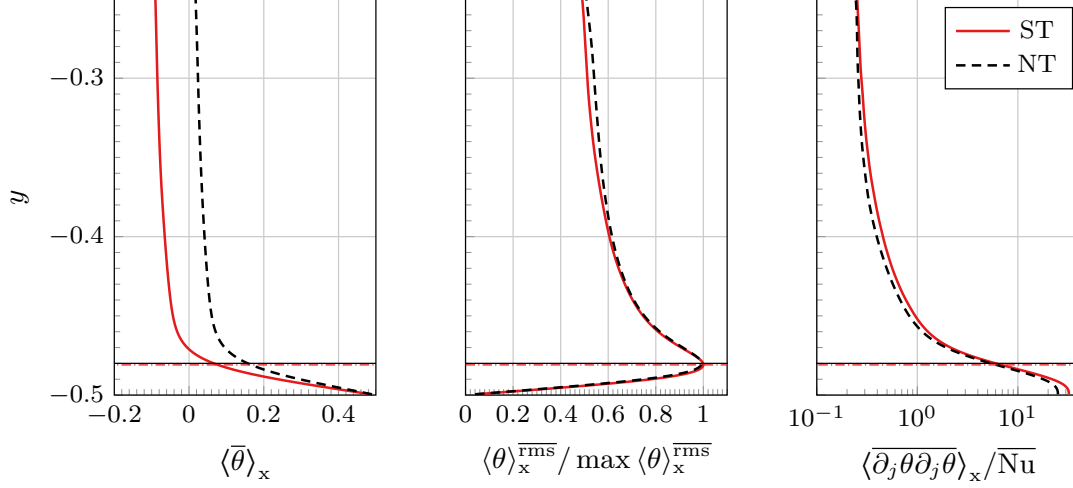
Figure 6.13: Vertical profiles for the mean temperature $\langle\overline{\theta}\rangle_{\mathrm{x}}$, temperature fluctuations $\langle\theta\rangle_{\mathrm{x}}^{\overline{\mathrm{rms}}}$, and normalized thermal dissipation $\langle\overline{\partial_j\theta\partial_j\theta}\rangle_{\mathrm{x}}$ in the lower half-cell for (Ra $= 5\cdot10^7$, Pr $= 4.3$). A horizontal line indicates the thickness $\delta_{\theta,\mathrm{bot}}$.

consistent with observations from other asymmetric systems such as (J. C. Tisserand, et al., 2011). In order to explore such hypothesis, let us take a closer look at the differences in the flow structure near the top and bottom plates.

Comparison between the lower and upper half-cells

Consider the mean temperature and temperature fluctuation profiles in both the ST and NT cells near the bottom plate (figure 6.13). As we mentioned earlier, the ST cell displays a larger temperature difference $\theta_{\mathrm{bot}} - \langle\overline{\theta}\rangle_{\mathrm{xy}}$ across the bottom thermal boundary layer, but its thickness $\delta_{\theta,\mathrm{bot}}$ is comparable in both ST and NT cells. Near the bottom plate, the vertical profiles of temperature fluctuations as well as the thermal dissipation are similar in the ST and NT cases. The vertical profiles near the top plate are different. For the ST cell, both the temperature difference $\langle\overline{\theta}\rangle_{\mathrm{xy}} - \theta_{\mathrm{top}}$, thickness $\delta_{\theta,\mathrm{top}}$ are smaller than in the NT cell. However, the slope of the mean temperature profile near the top wall is similar in both cells (figure 6.14). Temperature fluctuations near the top plate are smaller than fluctuations near the bottom plate for the ST cell, while contributions from the thermal dissipation are much more localized near the top plate.

The vertical profiles based on the velocity also support the separation between the upper and lower half-cells: the vertical profiles of the spatio-temporal velocity fluctuations close to the bottom plate, and the viscous dissipation profile in the lower half-cell are very similar for both NT and ST cells (figure 6.15). For the modified cell, the spatio-temporal fluctuations of the horizontal velocity are maximum and the contributions to the viscous dissipation are minimum at the top plate (figure 6.16). However, the contributions from the dissipation layer are larger than in the no-slip case. Since the contributions from the bulk change little, this increase is likely to come from the viscous boundary layers at the side-walls.

Let us define Rayleigh and Nusselt numbers based on the temperature difference between each plate and the bulk as done in other asymmetric configurations (see for instance J.-C.
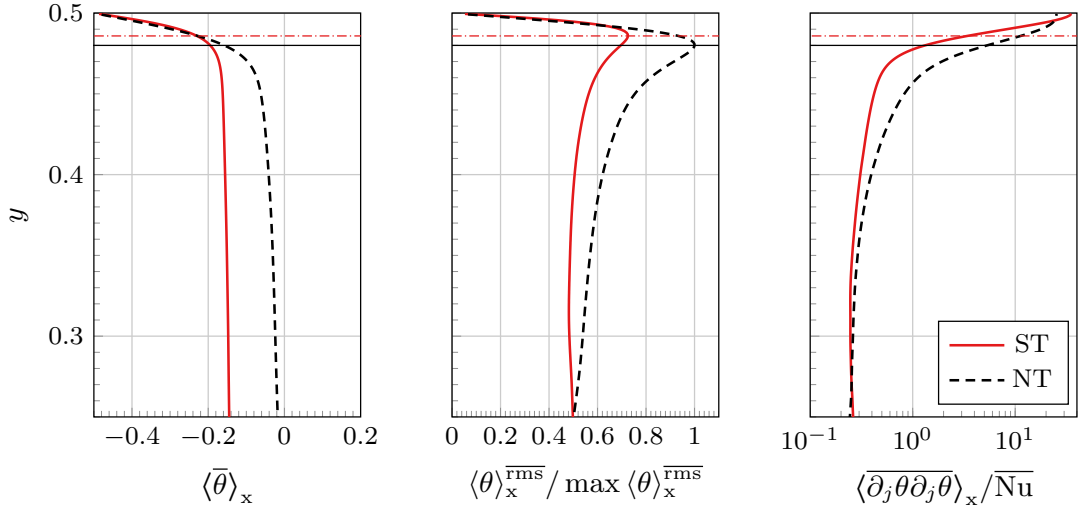
Figure 6.14: Same as in figure 6.13 but for the upper half-cell. A horizontal line indicates the value of $\delta_{\theta,\text{top}}$.
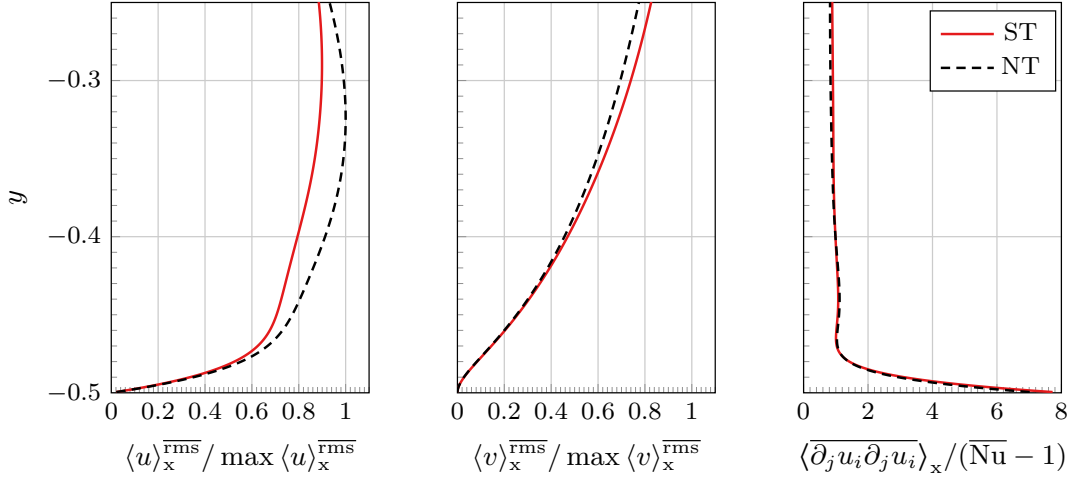
Figure 6.15: Vertical profiles for the normalized velocity fluctuations $\langle u \rangle_{\text{x}}^{\overline{\text{rms}}}$ and $\langle v \rangle_{\text{x}}^{\overline{\text{rms}}}$, and normalized viscous dissipation $\langle \overline{\partial_j u_i \partial_j u_i} \rangle_{\text{x}}$ in the lower half-cell for $(\text{Ra} = 5 \cdot 10^7, \text{Pr} = 4.3)$.
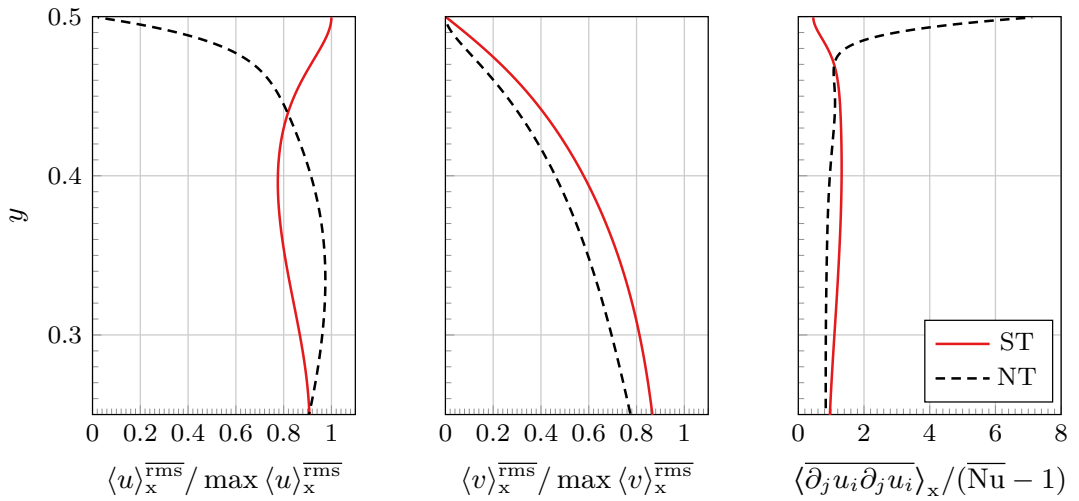
Figure 6.16: Same as in figure 6.15 but for the upper half-cell.

Tisserand, et al., 2011; Salort et al., 2014). This is equivalent to defining two virtual cells, which are symmetric (no-slip/no-slip and free-slip/free-slip), have an homogeneous bulk temperature and have the same temperature difference across the thermal boundary layers as the asymmetric cell (no-slip/free-slip). The Rayleigh number associated to the no-slip plate is defined as

$$\mathrm{Ra_n} = \frac{2\beta(\mathrm{T_{bot}} - \langle\overline{\mathrm{T}}\rangle_{\mathrm{xy}})gH^3}{\kappa\nu} = \frac{1}{2(0.5 - \langle\overline{\theta}\rangle_{\mathrm{xy}})}\,\mathrm{Ra} \tag{6.2}$$

and a corresponding Nusselt number

$$\overline{\mathrm{Nu_n}} = \frac{\langle\overline{v\mathrm{T}}\rangle - \kappa\partial_y\langle\overline{\mathrm{T}}\rangle}{2\kappa(\mathrm{T_{bot}} - \langle\overline{\mathrm{T}}\rangle_{\mathrm{xy}})/H} = 2(0.5 - \langle\overline{\theta}\rangle_{\mathrm{xy}})\,\overline{\mathrm{Nu}} \tag{6.3}$$

Similarly for the free-slip plate, we define a Rayleigh number

$$\mathrm{Ra_s} = \frac{2\beta(\langle\overline{\mathrm{T}}\rangle_{\mathrm{xy}} - \mathrm{T_{top}})gH^3}{\kappa\nu} = \frac{1}{2(\langle\overline{\theta}\rangle_{\mathrm{xy}} + 0.5)}\,\mathrm{Ra} \tag{6.4}$$

and a corresponding Nusselt number

$$\overline{\mathrm{Nu_s}} = \frac{\langle\overline{v\mathrm{T}}\rangle - \kappa\partial_y\langle\overline{\mathrm{T}}\rangle}{2\kappa(\langle\overline{\mathrm{T}}\rangle_{\mathrm{xy}} - \mathrm{T_{top}})/H} = 2(\langle\overline{\theta}\rangle_{\mathrm{xy}} + 0.5)\,\overline{\mathrm{Nu}} \tag{6.5}$$

The resulting $\mathrm{Ra_n}$, $\mathrm{Ra_s}$, $\overline{\mathrm{Nu_n}}$ and $\overline{\mathrm{Nu_s}}$ are given in figure 6.17. Let us discuss these results separately. One the one had, results for the free-slip plate now reflect the three different regimes associated to the temporal evolution (steady, oscillatory and turbulent regimes). For values of $\mathrm{Ra_s} > 10^7$, a power law $\overline{\mathrm{Nu_s}} \sim \mathrm{Ra_s^{0.34}}$ is observed. On the other hand, results for the no-slip plate follow a power law scaling $\overline{\mathrm{Nu_n}} \sim \mathrm{Ra_n^{0.30}}$ which is comparable to previous measurements in the NT cells, but the multiplicative factor of the power law is 15% larger. These measurements appear to be insensitive to the change in regime on the free-slip plate and suggest the behavior of both plates to be rather independent from each other.

However, since results from a symmetric free-slip/free-slip cell with adiabatic no-slip side-walls are not available at this time, we are unable to verify if the $\overline{\mathrm{Nu_s}} \sim \mathrm{Ra_s^{0.34}}$ scaling is representative of such cells, or if it corresponds to a transition between different flow regimes. Additional simulations for higher Ra would help clarify this point.
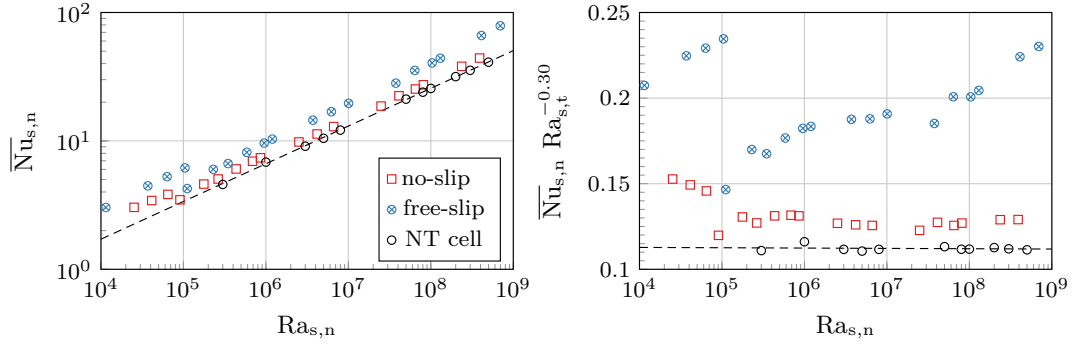
Figure 6.17: Evolution of $\overline{\mathrm{Nu}}_n$ (resp. $\overline{\mathrm{Nu}}_s$) as function of Ra_n (resp. Ra_s) for $\mathrm{Pr} = 4.3$. Values of $\overline{\mathrm{Nu}}$ as function of Ra for the NT cell are displayed as reference.

6.4 Statistical characterization of temporal dynamics

(a)

(b)
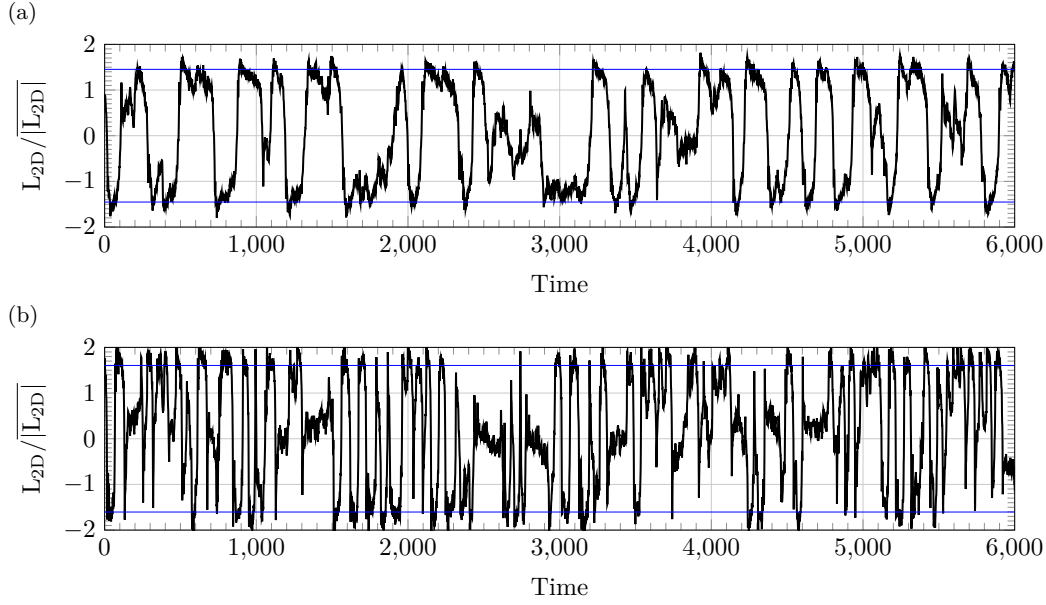
Figure 6.18: Time evolution of $L_{2D}/\overline{|L_{2D}|}$ for $(\text{Ra} = 5 \cdot 10^7, \text{Pr} = 4.3)$ inside a (a) NT cell and (b) ST cell. The two continuous lines correspond to the thresholds used by the filtering procedure. Value of the normalised standard deviation $\sigma(|L_{2D}|)/\overline{|L_{2D}|} = 0.452$ for the NT cell and $\sigma(|L_{2D}|)/\overline{|L_{2D}|} = 0.603$ for the ST cell.

To conclude this chapter, let us consider the influence of imposing the free-slip condition on the dynamics of the large-scale flow by extending the statistical characterization presented on §4 to the modified cells. More precisely, we are interested in the changes between the regime of 'consecutive reversals' and the regime of 'extended cessations' for $(\text{Ra} = 5 \cdot 10^7, \text{Pr} = 4.3)$.

We follow the procedure described in §4: first we consider the evolution of the global angular impulse L_{2D} (figure 6.18), then we identify a set of consecutive times r_i at which L_{2D} changes sign and define a time interval $\tau_{i,1} = r_{i+1} - r_i$. We use the amplitude-based filter to separate the CR and EC regimes and compute percentage of time spent in each regime, p_{cr} and $p_{ec} = 1 - p_{cr}$, as well as the duration of the jump τ_d.

The number of sign switches of L_{2D} increases significantly from 375 events in the NT cell to over 1160 events on the modified cell in the same interval of 29,000 convective time units. In addition, the number of sign switches associated to flow reversals increases from 161 to 358 in the same period. Additionally, the amount of time spent inside the CR regime decreases from $p_{cr} = 83\%$ to $p_{cr} = 79\%$, suggesting that flow reversals are shorter and more frequent.

Consider the probability distribution of τ_1 inside the CR and EC regimes (figure 6.19). The ST cells display an average inter-switch interval of $\overline{\tau_1} = 151$ convective time units, which is comparable to $\overline{\tau_1} = 159$ for the NT cell. However, the values are not distributed in the same way, in general reversals in the modified cell are faster and more frequent: the peak probability distribution of the inter-switch interval (resp. duration of the jump) is $\tau_1 = 53$ compared to $\tau_1 = 103$ (resp. $\tau_d = 3.2$ compared to $\tau_d = 11.2$) for the NT cell. For the ST cell, the EC regime is characterized by a short inter-switch interval ($\tau_1 < 50$),

(a)

NT cell

(b)
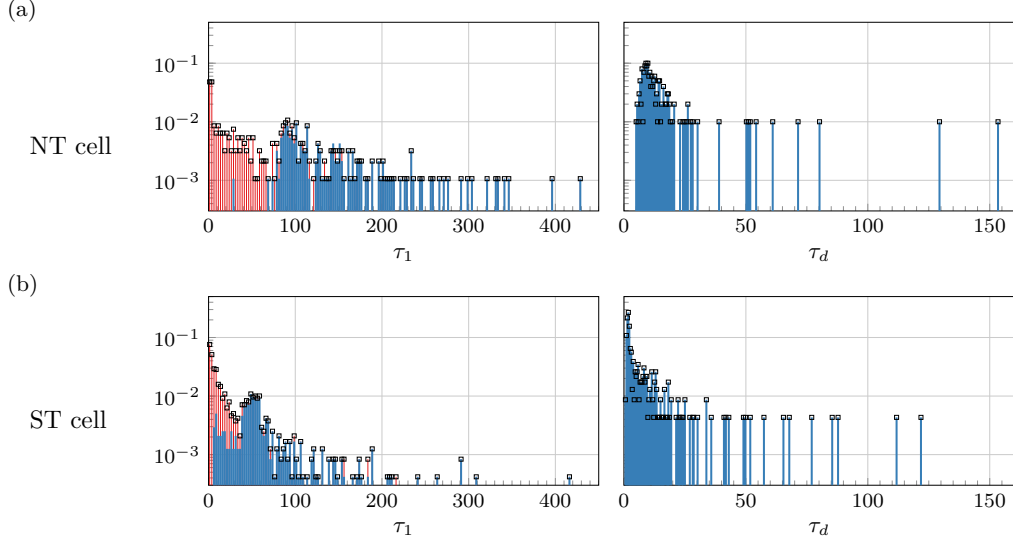
ST cell

Figure 6.19: PDF of τ_1 and τ_d for $(\mathrm{Ra} = 5 \cdot 10^7, \mathrm{Pr} = 4.3)$ inside a (a) NT and (b) ST cell. The PDF value is represented by $\circ$ marks. For τ_1 it is the sum of two conditional PDFs: one shown by a thick blue line corresponding to the CR regime, the other shown by a fine red line corresponding to the EC regime.
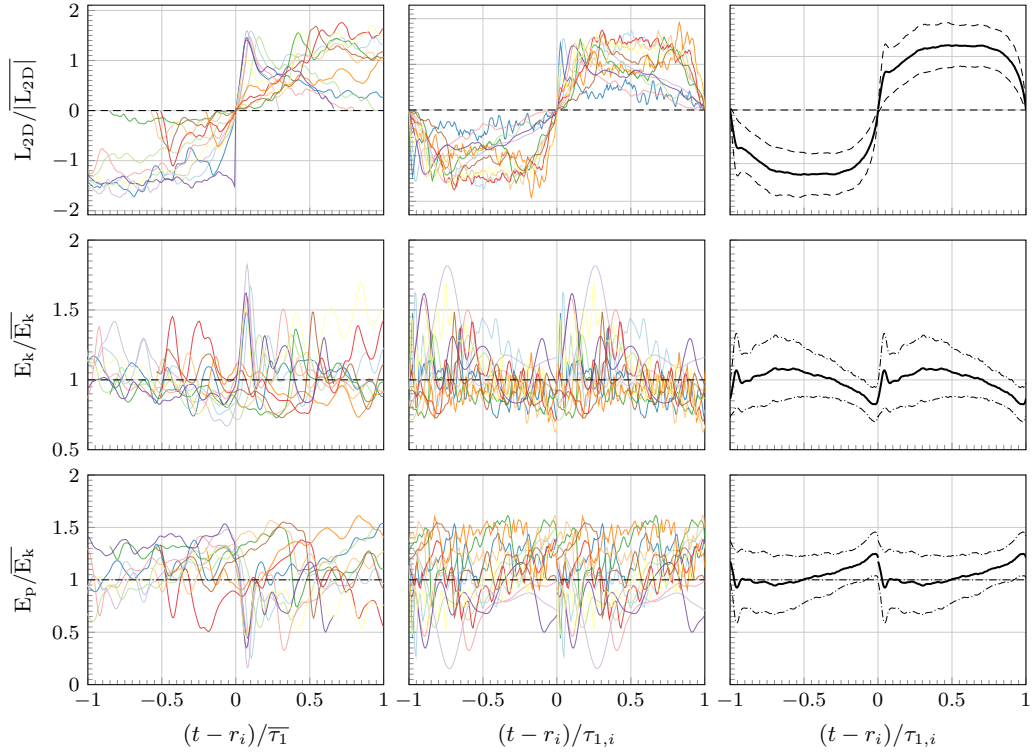
Figure 6.20: Normalized global angular impulse $\mathrm{L_{2D}}/\overline{|\mathrm{L_{2D}}|}$, kinetic energy $\mathrm{E_k}/\overline{\mathrm{E_k}}$ and potential energy $\mathrm{E_p}/\overline{\mathrm{E_k}}$ for $(\mathrm{Ra} = 5 \cdot 10^7, \mathrm{Pr} = 4.3)$ inside a free-slip (ST) cell. Layout is similar to figure 5 in chapter 4: Each curve is centered and its time is rescaled by $\overline{\tau_1}$ or by $\tau_{1,i}$, accordingly. The leftmost figures correspond to average value of rescaled curves (thick lines) and curves corresponding to one standard deviation (dashed lines).

127

whereas the values of τ_1 are distributed over a wider range ($10 < \tau_1 < 400$) in the CR regime. Both regimes overlap each other such that a separation time-scale τ_c may not be defined.

In order to illustrate the variability of the results, consider the evolution of L_{2D}, E_k, and E_p, displayed in figure 6.20 for a dozen reversals representative of the entire series to avoid cluttered graphs: roughly half of the events assigned to the CR regime display the dynamical pattern of the generic cycle presented in §4, while the other half does not appear to follow any particular trend. While it is still possible to use the conditionally averaged curves and identify a generic reversal cycle with roughly the same features as in the no-slip case, the standard deviation from the generic cycle is larger.

6.5   Conclusions of this chapter

We have studied the influence of mechanical boundary conditions on Rayleigh-Bénard convection. The main differences between the classic and modified cells, concern the change in the bulk temperature and an increase in both Nusselt and Reynolds numbers. Our observations support a simplified description where the system can be viewed as being composed of two half-cells interacting directly with the bulk flow but not with each other. The lower half-cell is similar in many aspects (temporal fluctuations, boundary layers) to the no-slip cell, except for the larger temperature gradient. The upper half cell lacks a kinetic boundary layer, which leaves a thinner thermal boundary layer exposed to the turbulent bulk flow.

The dynamics of the large scale flow are reminiscent of the regime of consecutive reversals and of extended cessations observed in the no-slip cells, but the separation between both regimes is less clear. Modified cells are characterized by the same type of flow structures than the no-slip case, but their temporal evolution is quite different. Reversals are faster and more frequent, whereas the extended cessations are more frequently observed. The reversal mechanism is identical for both cells, but larger deviations from the generic reversal are commonly observed.

Complementary material: Simulation Parameters

(a)

Ra	Grid	Length	$\overline{Nu}_{bot}$	$\overline{Nu}_{top}$	$\overline{Nu}_{vol}$	$\overline{Nu}_{\epsilon}$	$\overline{Nu}_{d}$	$\overline{Nu}_{\theta}$	$\overline{Nu}$	%	$\langle\overline{\theta}\rangle_{xy}$
$1\cdot10^4$	512	$*$	2.63	2.63	2.63	2.63	2.63	2.63	2.63	0.3	-0.063
$3\cdot10^4$	512	$*$	3.35	3.36	3.36	3.36	3.35	3.36	3.36	0.3	-0.091
$5\cdot10^4$	512	$*$	3.89	3.90	3.90	3.90	3.89	3.90	3.89	0.3	-0.108
$8\cdot10^4$	512	$*$	4.70	4.71	4.71	4.71	4.70	4.71	4.71	0.3	-0.115
$1\cdot10^5$	512	$*$	5.00	5.00	5.00	5.00	4.99	5.00	5.00	0.3	-0.120
$1.5\cdot10^5$	512	500†	4.44	4.44	4.44	4.43	4.42	4.43	4.43	0.4	-0.052
$2\cdot10^5$	512	500‡	4.56	4.55	4.55	4.55	4.54	4.54	4.55	0.4	-0.054
$2.5\cdot10^5$	512	500†	5.23	5.24	5.24	5.24	5.22	5.23	5.24	0.3	-0.060
$3\cdot10^5$	512	2,000†‡	5.42	5.42	5.42	5.42	5.40	5.42	5.42	0.4	-0.061
$5\cdot10^5$	512	4,000	6.41	6.41	6.42	6.41	6.39	6.40	6.41	0.4	-0.075
$8\cdot10^5$	512	4,000	7.41	7.41	7.41	7.40	7.38	7.39	7.40	0.4	-0.087
$1\cdot10^6$	512	4,000	7.98	8.00	7.99	7.99	7.96	7.99	7.98	0.5	-0.088
$3\cdot10^6$	512	4,000	11.12	11.13	11.14	11.12	11.08	11.09	11.11	0.6	-0.091
$5\cdot10^6$	512	4,000	12.91	12.92	12.92	12.90	12.83	12.86	12.89	0.7	-0.096
$8\cdot10^6$	512	4,000	14.69	14.68	14.68	14.66	14.56	14.58	14.64	0.9	-0.092
$3\cdot10^7$	512	5,000	22.06	22.04	22.07	21.99	21.70	21.74	21.94	1.7	-0.099
$5\cdot10^7$	1024	29,000	26.92	26.72	26.63	26.77	26.41	26.51	26.66	0.5	-0.111
$8\cdot10^7$	1024	4,800	31.44	31.47	31.47	31.42	31.20	31.26	31.37	0.9	-0.120
$1\cdot10^8$	1024	4,200	33.39	33.46	33.45	33.38	33.11	33.20	33.33	1.0	-0.121
$3\cdot10^8$	1024	4,400	47.55	47.60	47.63	47.47	46.61	46.90	47.29	2.2	-0.136
$5\cdot10^8$	1024	4,200	57.33	57.33	57.37	57.18	55.69	56.15	56.84	3.0	-0.143

(b)

Ra	Grid	Length	$\overline{Nu}_{bot}$	$\overline{Nu}_{top}$	$\overline{Nu}_{vol}$	$\overline{Nu}_{\epsilon}$	$\overline{Nu}_{d}$	$\overline{Nu}_{\theta}$	$\overline{Nu}$	%	$\langle\overline{\theta}\rangle_{xy}$
$1\cdot10^4$	512	$*$	2.65	2.64	2.65	2.65	2.65	2.65	2.65	0.3	-0.064
$3\cdot10^4$	512	$*$	3.61	3.62	3.62	3.62	3.61	3.62	3.62	0.3	-0.095
$5\cdot10^4$	512	$*$	4.16	4.15	4.16	4.16	4.16	4.16	4.16	0.2	-0.106
$8\cdot10^4$	512	$*$	4.73	4.72	4.73	4.73	4.73	4.72	4.73	0.2	-0.117
$1\cdot10^5$	512	500†	3.83	3.82	3.82	3.82	3.83	3.83	3.83	0.3	-0.051
$2\cdot10^5$	512	500†	5.22	5.22	5.21	5.22	5.21	5.21	5.21	0.2	-0.066
$3\cdot10^5$	512	1,000‡	5.74	5.75	5.75	5.75	5.73	5.74	5.74	0.3	-0.069
$5\cdot10^5$	512	4,000	6.94	6.94	6.95	6.94	6.92	6.93	6.94	0.4	-0.074
$8\cdot10^5$	512	4,000	8.06	8.06	8.07	8.06	8.03	8.05	8.06	0.4	-0.081
$1\cdot10^6$	512	4,000	8.60	8.63	8.62	8.61	8.58	8.61	8.61	0.5	-0.082
$3\cdot10^6$	512	4,000	11.70	11.71	11.71	11.70	11.64	11.67	11.69	0.6	-0.096
$5\cdot10^6$	512	4,000	13.54	13.55	13.57	13.54	13.47	13.49	13.53	0.7	-0.098
$8\cdot10^6$	512	4,000	15.59	15.59	15.61	15.57	15.47	15.50	15.55	0.9	-0.103
$3\cdot10^7$	512	5,000	22.46	22.45	22.48	22.40	22.07	22.14	22.33	1.8	-0.101
$5\cdot10^7$	1024	4,200	27.34	27.67	27.61	27.53	27.37	27.52	27.51	0.3	-0.109
$8\cdot10^7$	1024	4,200	31.17	31.21	31.21	31.16	30.93	31.00	31.11	0.9	-0.115
$1\cdot10^8$	1024	4,200	33.71	33.80	33.79	33.72	33.45	33.54	33.67	1.0	-0.116
$3\cdot10^8$	1024	4,400	48.32	48.39	48.41	48.29	47.43	47.66	48.08	2.1	-0.134
$5\cdot10^8$	1024	3,600	56.59	56.67	56.67	56.50	54.84	55.46	56.12	3.3	-0.140

Table 6.1: Convergence of Nusselt number for (a) Pr = 3.0 and (b) Pr = 4.3. Rayleigh number, grid size, and length of simulation. Time-averaged values of Nu, average Nusselt number $\overline{Nu}$, % maximum relative difference and mean temperature $\langle\overline{\theta}\rangle_{xy}$. A $*$ symbol indicates a steady-state solution, while † and ‡ indicate one of two periodic solutions, see text.

Part IV

Influence of boundary conditions: severe lateral confinement on a rectangular Rayleigh-Bénard cell

Chapter 7

Confined cells with adiabatic side-walls

7.1 Preamble

Under the Boussinesq approximation, the 3-D RB system is fully defined by the *Rayleigh* and *Prandtl* numbers, by the cell geometry (in particular the aspect ratio along the transversal direction Γ_z) and the boundary conditions. The influence of geometrical parameters on the large scale circulation has been the subject of many studies in cylindrical vessels or rectangular boxes. In the latter case, numerical or experimental studies (S. Wagner, and Shishkina, 2013; S. D. Huang, et al., 2013; Kaczorowski et al., 2014; Ni et al., 2015) have focused on the influence of the aspect ratio Γ_z on global properties as well as the large-scale flow. In the numerics, for instance, the global Nusselt and Reynolds numbers display a strong dependence on Γ_z for Ra $\sim 10^5 - 10^7$ (S. Wagner, and Shishkina, 2013). This geometrically induced heat-transfer enhancement was confirmed experimentally and numerically by (S. D. Huang, et al., 2013) and was explained by the formation of vertical turbulent channels instead of a large-scale roll. Experimentally, the influence of confinement on the dynamics of these large-scale circulation has been also discussed by (Ni et al., 2015).

Studies by (Chong, S.-D. Huang, et al., 2015; Chong and Xia, 2016) identified three different flow regimes denoted as I, II, and III, see figure 7.1. The differences between the regimes can be illustrated by considering an horizontal slice inside the bottom boundary layer. Regime I is the classical regime in which thermal plumes are arranged into sheet-like structures with no preferential alignment, except close to the side-walls (figure 7.1a). When the characteristic size of the plumes is comparable to the transversal size of the box, plumes do not split but in turn transform into sheets of constant width oriented along the transversal direction. This corresponds to regime II (figure 7.1b). Inside regime III we observe clear indications of a (quasi-)two-dimensional flow consistent with Hele-Shaw cells: a transversal velocity close to zero and a Poiseuille-type velocity profile (figures 7.1c and 7.1d). To illustrate these changes in 3-D we consider instantaneous isotherms for different aspect ratios displayed on figure 7.2. During transition from II to III the large thermal structures locked near the corners which were separated (figure 7.2b) tend to merge and form a single plume (figures 7.2c and 7.2d). Note that, the separation between regimes II
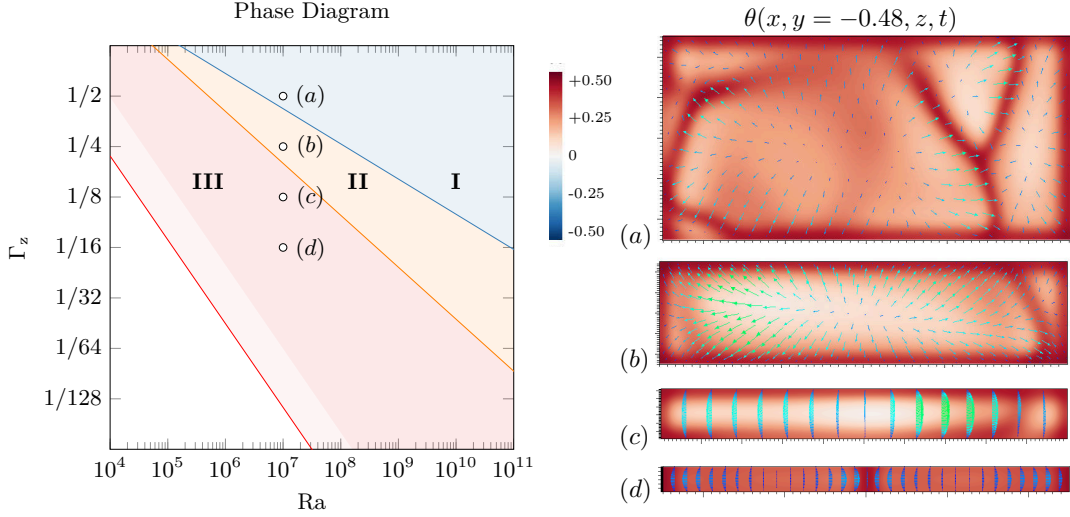
Figure 7.1: (Left panel) Different regimes of heat transport under geometrical confinement borrowed from Chong and Xia, 2016 for Pr = 4.38. Regime I represents the classical three-dimensional case; Regime II is the plume-controlled regime; and regime III the severely confined regime. A blue line ($\Gamma_z = 12.42\mathrm{Ra}^{-0.21}$) separates regimes I and II, an orange one ($\Gamma_z = 29.37\mathrm{Ra}^{-0.31}$) separates regimes II and III, and a red line ($\Gamma_z = 21.96\mathrm{Ra}^{-0.5}$) indicates the onset of convection. Note that for a given Γ_z, the light area inside III separates the Ra at the onset of convection to five times this value. (Right panel) Horizontal slice of the temperature and velocity field in a plane in proximity of the bottom boundary layer ($x, y = -0.48, z$). Each slice corresponds to a mark on the left panel: (a) $\Gamma_z = 1/2$, (b) $\Gamma_z = 1/4$, (c) $\Gamma_z = 1/8$, and (d) $\Gamma_z = 1/16$.

and III ($\Gamma_z = 29.37\mathrm{Ra}^{-0.31}$) corresponds to the aspect ratio at which the average Nusselt number reaches a maximum value while keeping Ra constant and increasing Γ_z (Chong and Xia, 2016).

Thermal and solutal convection in Hele-Shaw cells has been the subject of several experimental (Hartline and Lister, 1977; Ozawa et al., 1992), numerical (Bizon et al., 1997) and analytical (Graham et al., 1992) studies. Such systems model fluid filtration in saturated porous media (Gorin, 2012; Nield and Bejan, 2013). The most striking feature is again, the suppression of a system-wide circulation in favor of the formation of large plumes (or clusters of plumes) along the vertical direction. The scaling exponents of the Nusselt and Reynolds numbers deviate from the exponents observed in cubic Rayleigh-Bénard convection. To the best of my knowledge, this case is not considered by the unifying theory of thermal convection (Grossmann and Lohse, 2000; Grossmann and Lohse, 2003).

In the present chapter, we identify the main dynamical features of confined cells through the use of fully resolved 3-D DNS in regime III. Note that in this regime, the observed large-scale dynamic is very different from the one of pure two-dimensional turbulent convection presented in chapters 4 and 5 of this thesis. In the subsequent chapter we compare results from the 3-D DNS with two simplified models, which are used to explore the parameter space and to study long-term dynamics for which the use of 3-D DNS is prohibitively expensive.
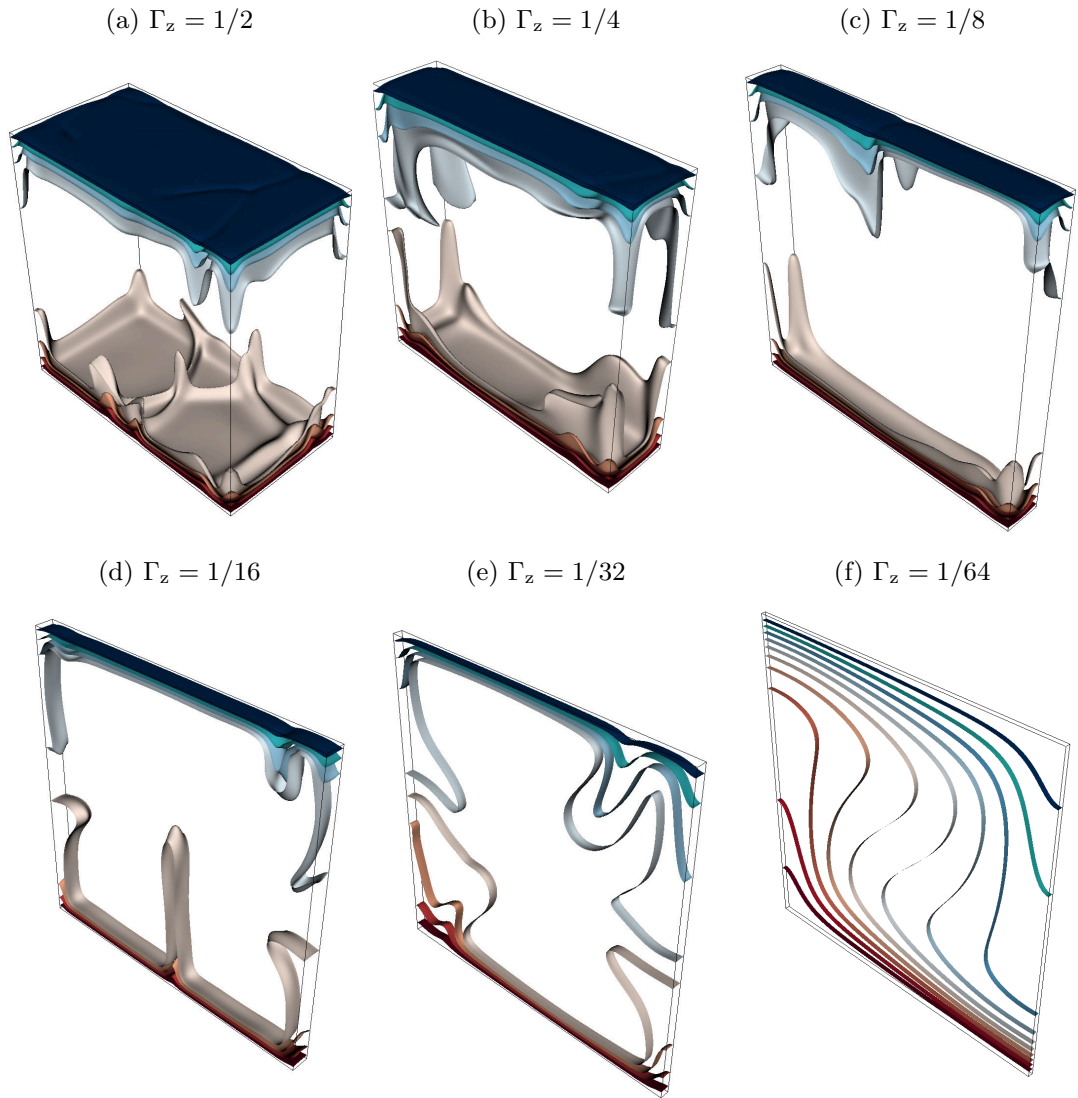
Figure 7.2: Instantaneous isotherms for $\{\pm 0.45, \pm 0.35, \pm 0.25, \pm 0.15\}$ and $(\mathrm{Ra} = 10^7, \mathrm{Pr} = 4.38)$. Figure (a) corresponds to regime I, figure (b) corresponds to regime II, and figures (c-f) correspond to regime III.

7.2 Numerical approach

We explore here regime III, where we fixed $\mathrm{Pr} = 4.38$ and varied Ra from 10^6 to 10^9. Different aspect ratios $1/64 \leq \Gamma_{\mathrm{z}} \leq 1/8$ were also considered. Direct numerical simulations were performed using the code Basilisk described in section 3.1.2. It is reminded that one solves the Boussinesq equations

$$\partial_i u_i + \partial_z w = 0 \tag{7.1a}$$

$$\partial_t u_i + \partial_j(u_j u_i) + \partial_z(w u_i) = -\partial_i \mathrm{p} + \mathrm{Pr}\mathrm{Ra}^{-0.5}(\partial_j\partial_j u_i + \partial_z^2 u_i) + \mathrm{Pr}\theta\delta_{iy} \tag{7.1b}$$

$$\partial_t w + \partial_j(u_j w) + \partial_z(w w) = -\partial_z \mathrm{p} + \mathrm{Pr}\mathrm{Ra}^{-0.5}(\partial_j\partial_j w + \partial_z^2 w) \tag{7.1c}$$

$$\partial_t \theta + \partial_j(u_j \theta) + \partial_z(w\theta) = \mathrm{Ra}^{-0.5}(\partial_j\partial_j \theta + \partial_z^2 \theta) \tag{7.1d}$$

Here the Einstein notation is used only for the in-plane components, i.e. indices $i, j = x, y$. The domain is defined as $[-0.5, 0.5] \times [-0.5, 0.5] \times [-\Gamma_{\mathrm{z}}/2, \Gamma_{\mathrm{z}}/2]$, with $\Gamma_{\mathrm{z}} \ll 1$. Velocity is zero on all walls. On the top (resp. bottom) walls, the reduced temperature is imposed to be $\theta(y = 0.5) = -0.5$ (resp. $\theta(y = -0.5) = 0.5$). Side-walls are adiabatic i.e. $\partial_n \theta = 0$.

Results were obtained on uniform Cartesian grids with a variable time-step that verifies CFL < 0.5. As a general rule, the distribution of grid points must be able to resolve the steep gradients in the velocity and temperature fields near the walls (Grötzbach, 1983). This is a difficult thing to do using regular Cartesian grids for confined cells since the number of points along the transversal direction is usually small. A second, more subtle limitation is a slow time evolution since velocities are quite small, making fully resolved direct simulations increasingly onerous for $\Gamma_{\mathrm{z}} < 1/64$.

Spatial resolution is verified to be adequate by following the procedure described on §3.2.2: one checks numerically whether the exact relations between the instantaneous rates-of-change (see equation (3.11)) and energy transfer rates are verified. A small residual value is an indication that spatial resolution is adequate. The second check concerns the statistical convergence of time-averaged Nusselt numbers proposed by (R. Stevens, Verzicco, et al., 2010). The average values of $\overline{\mathrm{Nu}}_{\mathrm{vol}}$, $\overline{\mathrm{Nu}}_{\mathrm{top}}$, $\overline{\mathrm{Nu}}_{\mathrm{bot}}$, $\overline{\mathrm{Nu}}_{\epsilon}$, $\overline{\mathrm{Nu}}_{\theta}$, $\overline{\mathrm{Nu}}_{\mathrm{d}}$, and $\overline{\mathrm{Nu}}$ as well as the maximum relative difference %Diff are listed in table 7.1 (see §2.2.7 for definitions). For the finer grids, these quantities are shown to converge within 3% of $\overline{\mathrm{Nu}}$ for the range of $(\mathrm{Ra}, \mathrm{Pr})$ presented. In addition, the average Nusselt number $\overline{\mathrm{Nu}}$ is in good agreement with published results from Chong and Xia, 2016.

Γ_z	Ra	t.u.	Grid	$\overline{\mathrm{Nu}}_\mathrm{top}$	$\overline{\mathrm{Nu}}_\mathrm{bot}$	$\overline{\mathrm{Nu}}_\mathrm{vol}$	$\overline{\mathrm{Nu}}_\epsilon$	$\overline{\mathrm{Nu}}_\mathrm{d}$	$\overline{\mathrm{Nu}}_\theta$	$\overline{\mathrm{Nu}}$	%Diff
1/8	10^6	750	$256^2 \times 32$	5.18	5.18	5.17	5.16	5.16	5.17	5.17	0.5
	$5 \cdot 10^6$	750	$256^2 \times 32$	10.70	10.72	10.70	10.61	10.60	10.62	10.66	1.0
	10^7	†	$512^2 \times 64$	14.87	14.87	14.87	14.83	14.81	14.82	14.85	0.4
	$5 \cdot 10^7$	1,600	$512^2 \times 64$	28.44	28.44	28.45	28.30	28.19	28.17	28.33	1.0
	10^8	1,800	$512^2 \times 64$	35.00	35.01	35.01	34.75	34.62	34.53	34.82	1.4
1/16	10^6	∗	$256^2 \times 16$	4.12	4.12	4.11	4.07	4.11	4.11	4.11	1.0
	$5 \cdot 10^6$	1,000	$256^2 \times 16$	7.17	7.17	7.16	7.08	7.14	7.14	7.15	1.2
	10^7	5,000‡	$512^2 \times 32$	9.42	9.44	9.43	9.40	9.40	9.41	9.41	0.4
	$2 \cdot 10^7$	2,500	$512^2 \times 32$	15.40	15.40	15.40	15.33	15.31	15.33	15.37	0.6
	$5 \cdot 10^7$	1,750	$512^2 \times 32$	22.76	22.76	22.76	22.63	22.58	22.59	22.68	0.8
	10^8	2,250	$512^2 \times 32$	29.48	29.49	29.50	29.28	29.06	29.11	29.32	1.5
1/32	$5 \cdot 10^6$	∗	$512^2 \times 16$	5.33	5.33	5.33	5.27	5.32	5.32	5.32	1.0
	10^7	1,000	$1024^2 \times 32$	6.52	6.54	6.53	6.52	6.52	6.52	6.52	0.3
	$5 \cdot 10^7$	750	$1024^2 \times 32$	14.48	14.49	14.47	14.43	14.44	14.45	14.46	0.4
	10^8	1,000	$1024^2 \times 32$	19.94	19.88	19.91	19.85	19.85	19.86	19.88	0.5
	10^9	1,000	$1024^2 \times 32$	62.11	62.04	61.92	61.58	61.34	61.17	61.69	1.5
1/64	10^7	∗	$1024^2 \times 16$	3.69	3.67	3.68	3.65	3.68	3.68	3.68	1.2
	$5 \cdot 10^7$	1,200	$1024^2 \times 16$	7.84	7.87	7.85	7.76	7.85	7.85	7.84	1.0
	10^8	1,200	$1024^2 \times 16$	12.61	12.59	12.60	12.47	12.58	12.60	12.58	1.1
	$2 \cdot 10^8$	1,000	$1024^2 \times 16$	19.39	19.42	19.51	19.29	19.31	19.35	19.38	1.1
	10^9	2,000	$1024^2 \times 16$	46.83	46.85	46.85	46.28	46.31	46.30	46.57	1.2

Table 7.1: Time-averaged Nusselt numbers and maximum relative difference between them for the finest grid used. Here t.u. indicates the length of the simulation. Symbol † indicates a periodic solution, ‡ an intermittent solution, and ∗ a steady-state.

7.3 Dynamics of the confined regime in RB cells

7.3.1 Large-scale plume dynamics

Flow dynamics is mostly defined by the competition between friction and buoyancy forces. For severely confined cells, the frictional drag on the front and back walls ($z = \pm\Gamma_z/2$) favors the formation of large plume clusters along the vertical direction (also called turbulent channels) instead of a system-scale circulation observed in pure 2-D or in conventional 3-D convection. Figure 7.3 illustrates the evolution of flow structures as we decrease Γ_z for ($\mathrm{Ra} = 10^7, \mathrm{Pr} = 4.38$). The plume width increases with the confinement. The resulting flow is mainly controlled by the motion of the turbulent channels. Some channels cross the domain unopposed from top to bottom or *vice versa*, as seen near the center of the cavity in figures 7.3a to 7.3c. Other channels may collide with each other as they traverse the domain. Such head-on collisions are typically found along the vertical side-walls, in which the plumes are deviated in the horizontal direction.

For ($\Gamma_z = 1/8, \mathrm{Ra} = 10^7$) the top-bottom symmetry is not observed and side-wall plumes collide at a nearly constant height close to top or bottom plates. The interaction of side-wall plumes with the central plume creates a *periodic* sweeping motion, which is reflected on the the evolution of $\mathrm{Nu_{bot}}$, $\mathrm{Nu_{top}}$, and $\mathrm{Nu_{vol}}$. A dominant frequency of $f = 0.12$ is clearly observed for $\mathrm{Nu_{vol}}$ (see figure 7.3a).

For ($\Gamma_z = 1/16, \mathrm{Ra} = 10^7$) the collision of the side-wall plumes takes place near the mid-height of the cavity. The interaction between the side-wall plumes and the central plume leads to a *chaotic* motion with a dominant frequency $f = 0.036$. The side-wall plumes can be moving in-phase or out-of-phase. During the in-phase motions the side-plumes keep the central plume locked in place, whereas during the out-of-phase motions the side-plumes push back and forth the central plume. In some instances, the coordinated motion pushes the central plume into a wall which then merges with a side-wall plume.

For ($\Gamma_z = 1/32, \mathrm{Ra} = 10^7$) one observes two types of periodic solutions: a flow with a central plume locked in place (see figure 7.3c), and a flow without a central plume (see figure 7.3d). In the former case, the motions of the side-wall plumes are coordinated, pumping hot fluid from the bottom to the top or *vice versa*. In the latter case, the side-wall plumes move out-of-phase to form a large-scale circulation and prevent other plumes to settle. Both solutions have the same dominant frequency $f = 0.025$, suggesting the oscillating motion of the side-plumes remains unchanged.

For the most confined cell ($\Gamma_z = 1/64, \mathrm{Ra} = 10^7$), one arrives to a steady single-roll configuration with one ascending and one descending plume (not shown in figure 7.3).

Figures 7.4 to 7.7 display the dynamics for $\Gamma_z = 1/64$ and different Ra. The plume width is shown to decrease as we increase Ra. The relative plume size with respect to the size of the cavity seems to play an important role in the overall dynamics. As such, similar flow regimes may be observed for different combinations of Ra and Γ_z with a similar plume size. For ($\mathrm{Ra} = 5 \cdot 10^7, \Gamma_z = 1/64$) we observe two types of solutions. In the first one (figure 7.4a), the coordinated motion of the side-wall plumes prevents the center plume from moving and one obtains a periodic oscillatory solution similar to the one displayed on figure 7.3c. The second kind of solution (figure 7.4b) is a chaotic one, but different
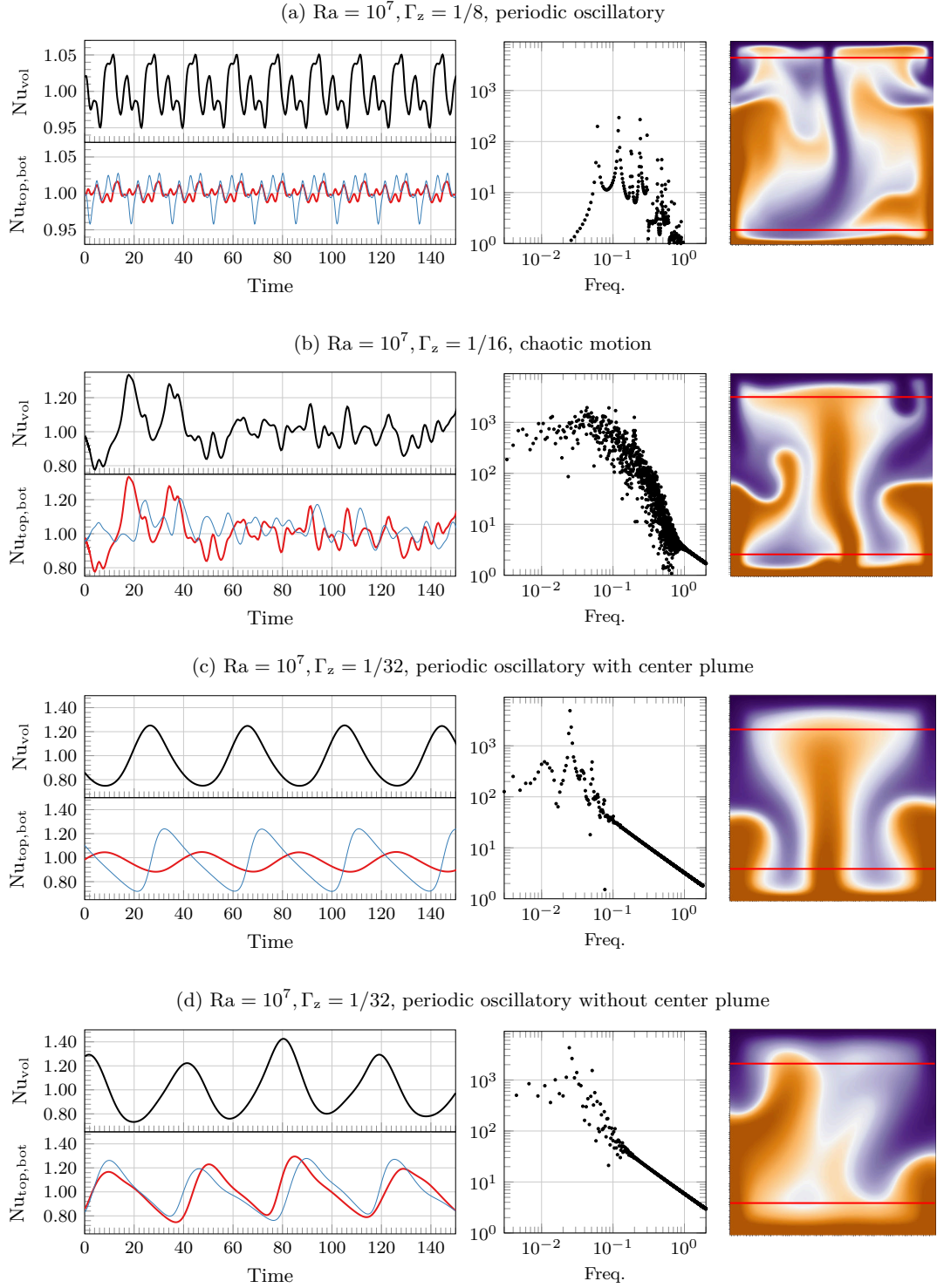
Figure 7.3: DNS results for $(\mathrm{Ra} = 10^7, \mathrm{Pr} = 4.38)$ and different Γ_z. (Left) Time series of $\mathrm{Nu}_{\mathrm{vol}}$ (black), $\mathrm{Nu}_{\mathrm{top}}$ (blue) and $\mathrm{Nu}_{\mathrm{bot}}$ (red); (Middle) Time-frequency spectra of $\mathrm{Nu}_{\mathrm{vol}}$; (Right) Snapshot of the reference height $y_r(x, y, 0, t)$ (see §2.2.4). Horizontal lines correspond to $y = \pm(0.5 - \frac{1}{\mathrm{Nu}})$.

(a) $\mathrm{Ra} = 5 \cdot 10^7, \Gamma_z = 1/64$, oscillatory periodic with center plume

(b) $\mathrm{Ra} = 5 \cdot 10^7, \Gamma_z = 1/64$, chaotic motion without center plume
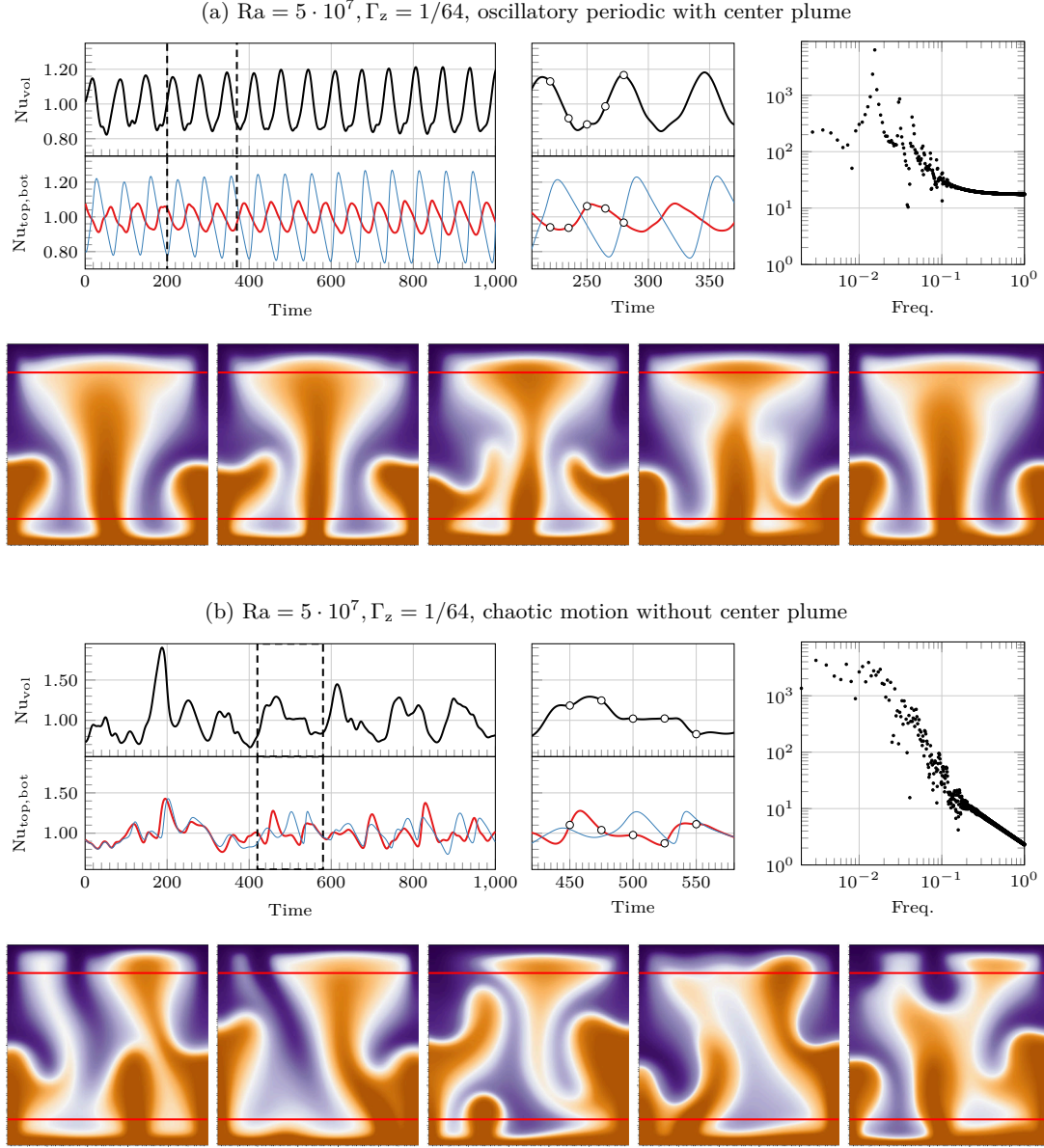
Figure 7.4: DNS results for $(\Gamma_z = 1/64, \mathrm{Ra} = 5 \cdot 10^7, \mathrm{Pr} = 4.38)$. The two sequences (a) and (b) correspond to different stable solutions, see text. First row: Time series of $\mathrm{Nu}_{\mathrm{vol}}$ (black), $\mathrm{Nu}_{\mathrm{top}}$ (blue) and $\mathrm{Nu}_{\mathrm{bot}}$ (red); a close-up view of the time-series inside the interval indicated in dashed lines ; and time-frequency spectra of $\mathrm{Nu}_{\mathrm{vol}}$. Second row: snapshots of the reference height $y_r(x, y, 0, t)$ (see §2.2.4), where times corresponding to snapshots are indicated in the time series by a ∘ mark. Thick horizontal lines correspond to $y = \pm(0.5 - \frac{1}{\mathrm{Nu}})$ for reference.
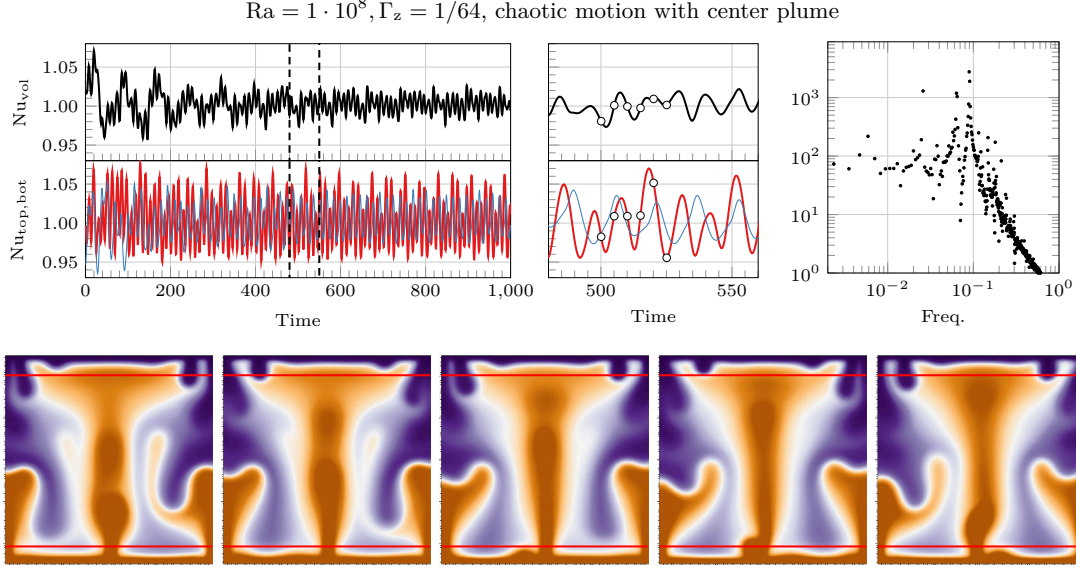
Figure 7.5: Same as in figure 7.4 but for Ra $= 10^8$.

from the one in figure 7.3b. Here the side-wall plumes move back and forth independently from one another. One ascending and one descending central plume are observed almost simultaneously, which repel each other to the sides as they collide, thus creating a system-wide circulation.

Dynamics for (Ra $= 10^8, \Gamma_z = 1/64$) are determined by the interaction between the side-wall plumes and one ascending (or descending) central plume (figure 7.5). This configuration results in a chaotic motion with characteristic frequency $f = 0.1$. This solution similar to the one displayed on figure 7.3b.

When Ra is further increased, additional channels are allowed to form (figures 7.6 and 7.7). For (Ra $= 2 \cdot 10^8, \Gamma_z = 1/64$) in addition to having side-wall plumes of different heights, we identify one ascending and one descending channels near the center of the cavity (figure 7.6). Unlike configurations with a single central plume, this solution is nearly centro-symmetric. The interaction between multiple turbulent channels leads to rather complex dynamics characterized by a dominant frequency near $f = 0.05$.

For (Ra $= 10^9, \Gamma_z = 1/64$) thermal plumes are clustered into four ascending and three descending turbulent channels (figure 7.7). Intervals of light (lower than average) and intense (higher than average) heat-transfer alternate roughly every 100 convective time units (see $\mathrm{Nu_{vol}}(t)$ in figure 7.7). Light periods often coincide with the merging of hot (resp. cold) plumes into large clusters close to the lower (resp. upper) thermal boundary layers. These clusters detach from the boundary layers and make their way into the bulk. The intense periods coincide with the collision of said clusters against the upper (resp. lower) plate. The formation of multiple turbulent channels is consistent with observations from (Bizon et al., 1997). Near the onset of convection, the sequence of conductive, stationary, and oscillatory flow patterns is also consistent with experiments in Hele-Shaw cells (Ozawa et al., 1992).

Finally, note a strong similarity between the turbulent channels and the type of convective structures observed in similar systems where the third dimension is partially suppressed due to the action of stabilizing forces. Examples include strong magnetic fields, a rapid

Ra $= 2 \cdot 10^8, \Gamma_z = 1/64$, chaotic motion with two center plumes
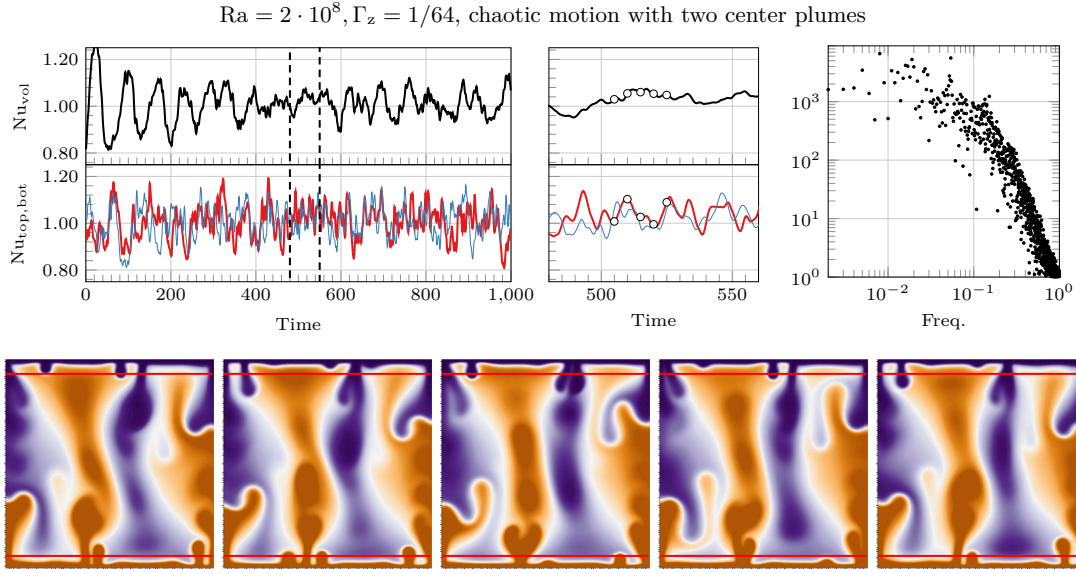
Figure 7.6: Same as in figure 7.4 but for Ra $= 2 \cdot 10^8$.

Ra $= 1 \cdot 10^9, \Gamma_z = 1/64$, turbulent flow with multiple plumes
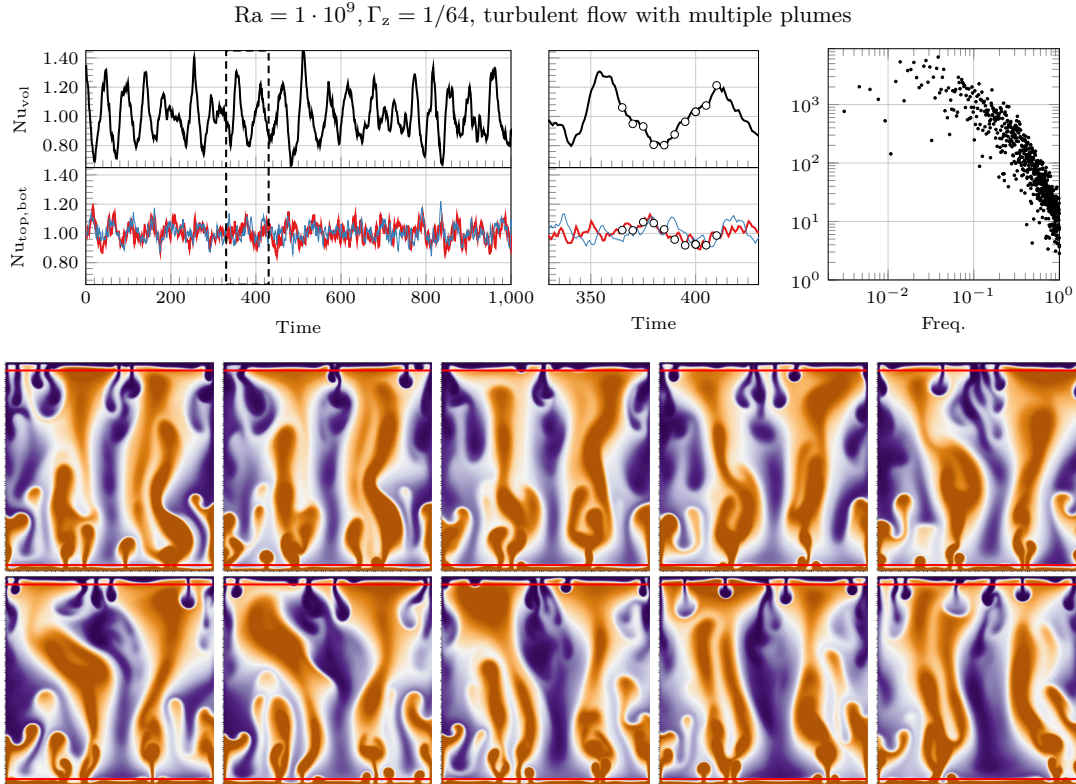
Figure 7.7: Same as in figure 7.4 but for Ra $= 10^9$. One additional row of snapshots is displayed to illustrate the sequence from below average to above average heat-flux.

		Viscous dissipation		Thermal dissipation		diapycnal mixing	
Ra	Γ_z	$\overline{(\epsilon^{(z)}/\epsilon)}$	$\sigma(\epsilon^{(z)}/\epsilon)$	$\overline{(\epsilon_\theta^{(xy)}/\epsilon_\theta)}$	$\sigma(\epsilon_\theta^{(xy)}/\epsilon_\theta)$	$\overline{(\Phi_d^{(xy)}/\Phi_d)}$	$\sigma(\Phi_d^{(xy)}/\Phi_d)$
$1 \cdot 10^7$	1/8	0.738	0.006	0.803	0.002	0.574	0.005
$5 \cdot 10^7$	1/8	0.778	0.017	0.776	0.011	0.501	0.027
$1 \cdot 10^8$	1/8	0.777	0.018	0.788	0.009	0.498	0.026
$1 \cdot 10^7$	1/16	0.824	0.011	0.976	0.004	0.949	0.007
$5 \cdot 10^7$	1/16	0.826	0.016	0.774	0.014	0.516	0.027
$1 \cdot 10^8$	1/16	0.798	0.021	0.727	0.020	0.452	0.025
$1 \cdot 10^7$	1/32	0.952	0.004	0.998	0.001	0.996	0.001
$5 \cdot 10^7$	1/32	0.922	0.005	0.978	0.003	0.956	0.005
$1 \cdot 10^8$	1/32	0.906	0.009	0.932	0.025	0.873	0.037
$1 \cdot 10^9$	1/32	0.876	0.020	0.703	0.018	0.396	0.036
$1 \cdot 10^7$	1/64	0.984	0.000	1.000	0.000	1.000	0.000
$5 \cdot 10^7$	1/64	0.976	0.003	0.999	0.000	0.999	0.000
$1 \cdot 10^8$	1/64	0.972	0.001	0.997	0.000	0.995	0.000
$1 \cdot 10^9$	1/64	0.952	0.005	0.817	0.013	0.707	0.020

Table 7.2: Evolution of different global quantities as function of Ra and Γ_z. Time averaged value and standard deviation of the ratios $(\epsilon^{(z)}/\epsilon)$, $(\epsilon_\theta^{(xy)}/\epsilon_\theta)$, and $(\Phi_d^{(xy)}/\Phi_d)$.

rotation around the vertical axis, the presence of an additional density gradient (Chong, Kai Leong et al., 2017), or geometric confinement like in porous media (Otero et al., 2004; D. R. Hewitt, et al., 2012; D. Hewitt, et al., 2014). The loss of three-dimensionality may be illustrated through the various dissipative terms in (3.11): the viscous dissipation rate ϵ, the thermal dissipation rate ϵ_θ and the diapycnal mixing Φ_d. Each of these terms may be split in two parts: one part due to contributions from gradients along the transversal direction z, and another due to gradients along the in-plane components x and y

$$\epsilon^{(z)} \equiv \langle (\partial_z u_i)(\partial_z u_i) + (\partial_z w)^2 \rangle_{xyz} \qquad \epsilon^{(xy)} \equiv \epsilon - \epsilon^{(z)} \tag{7.2a}$$

$$\epsilon_\theta^{(z)} \equiv \langle (\partial_z \theta)^2 \rangle_{xyz} \qquad \epsilon_\theta^{(xy)} \equiv \langle (\partial_j \theta)(\partial_j \theta) \rangle_{xyz} \tag{7.2b}$$

$$\Phi_d^{(z)} \equiv \langle (\partial_z y_r)(\partial_z \theta) \rangle_{xyz} \qquad \Phi_d^{(xy)} \equiv \langle (\partial_j y_r)(\partial_j \theta) \rangle_{xyz} \tag{7.2c}$$

The relative contributions from $\epsilon^{(z)}/\epsilon$, $\epsilon_\theta^{(xy)}/\epsilon_\theta$, and $\Phi_d^{(xy)}/\Phi_d$ provide a good measurement of the bi-dimensionalization of the flow structures (see table 7.2). First, $\epsilon^{(z)}$ corresponds to the energy lost due to frictional drag along the front and back walls ($z = \pm\Gamma_z/2$). As we decrease the aspect ratio Γ_z, $\epsilon^{(z)}$ contributes anywhere from 70% up to 98% of the total viscous dissipation ϵ (see table 7.2). Second, $\epsilon_\theta^{(xy)}$ represent from 70% to nearly 100% of the total thermal dissipation, whereas $\Phi_d^{(xy)}$ represent from 50% to nearly 100% of the total mixing rate Φ_d. This is expected in confined cells where adiabaticity of the front and back walls imposes small temperature gradients along z.

7.3.2 Flow reversals inside the laterally confined geometry

A pure 2-D turbulent convection can be described by the superposition of a large-scale flow over a incoherent turbulent background (see chapters 4 and 5). This large-scale flow is mainly characterized by a single-roll structure which is sustained for extended periods of time. However, a spontaneous re-organization takes place (known as a flow reversal), changing the sense of rotation of the roll, thus restoring the statistical symmetry of the

(a) Sequence of snapshots for a reversal

(a.i)   (a.ii)   (a.iii)   (a.iv)   (a.v)

(a.vi)   (a.vii)   (a.viii)   (a.ix)   (a.x)

(b) Time-series (and close-up view) of the Half-range Fourier coefficients $\hat{u}_{pq}$

(c) Time-series (and close-up view) of the kinetic and available potential energies
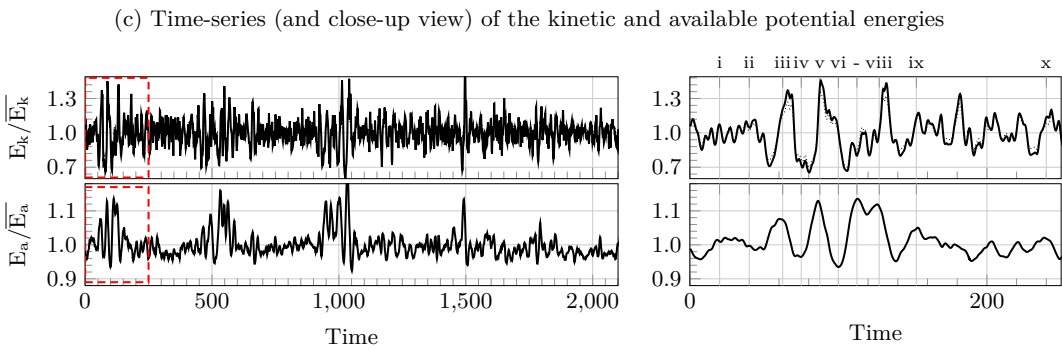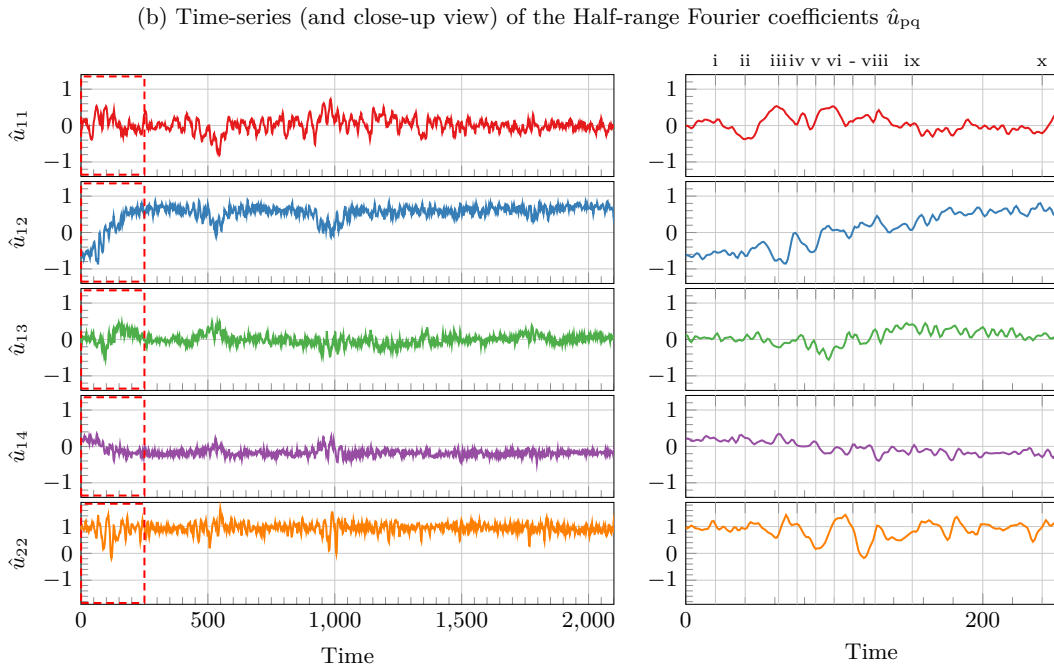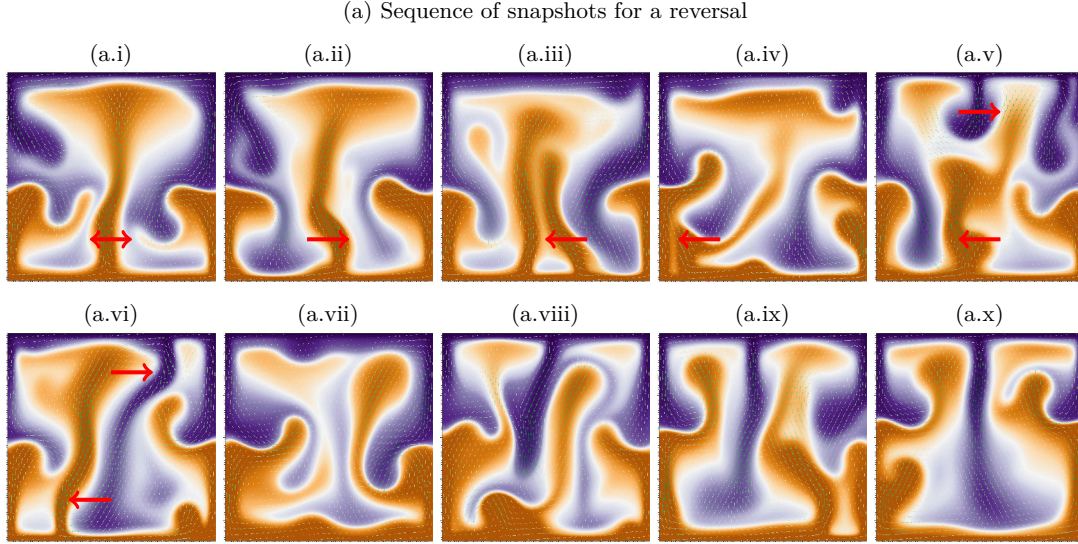
Figure 7.8: Flow reversal observed for DNS at $Ra = 2 \cdot 10^7$ and $\Gamma_z = 1/16$. (a) A sequence of snapshots of field $y_r(x, y, 0, t)$ during the reversal. (b) Time-series of the half-range Fourier coefficients of the horizontal velocity $\hat{u}_{pq}$. Modal coefficients are multiplied by a factor 10^2. The dashed box indicates the time interval where the reversal occurs. This interval is displayed on the right indicating the times corresponding to the snapshots. (c) Time-series (and its close-up view) of the normalized kinetic and the available potential energies, E_k and E_a.

144

system. In 3-D rectangular cells, flow reversals have been observed for different values of Ra and Pr. For $\Gamma_z = 0.3$, this was seen by Sugiyama, Ni, et al., 2010, for $\Gamma_z = 0.2$ by Vasiliev and Frick, 2011, and for $0.84 \leq \Gamma_x \leq 1.10$ and $0.33 \leq \Gamma_z \leq 0.25$ by Ni et al., 2015. In the present work, we report a reversal process for more confined 3-D cells, which corresponds to a different large-scale flow.

A configuration with one ascending plume near the center of the cavity (fig. 7.8a.i) may be sustained for over 1,000 convective time units. Since the central plume collides against the top plate, cold fluid is pushed towards the side-walls and suppresses the formation of additional large-scale plumes. Due to a coordinated motion of the side-wall plumes, the central plume (the direction of its motion is indicated by a red arrow) is displaced (fig. 7.8a.ii) and allows a second plume to appear on its left (fig. 7.8a.iii). Thereafter, the central plume swings back towards the left, sweeping the newly formed plume towards the side-wall leading to the destruction of both central plumes (fig. 7.8a.iv). In the absence of a single central plume, ascending and descending plumes form simultaneously and actively repel each other (fig. 7.8a.v-a.viii). They coexist until one is swept away and the other becomes dominant (figs. 7.8a.ix-a.x).

This sequence is quite different from the reversals observed in pure 2-D. This is illustrated based on a half-range Fourier decomposition of the horizontal velocity, see §2.5. In pure 2-D, the reversal of the large diagonal vortex occurs after being squeezed by counter-rotating corner-rolls and it is characterized by the evolution of the first 2-D Fourier modes (in particular modes (1,1),(1,3),(1,2) and (2,2)). Reversals are evidenced by a change in sign in the mode (1,1). Let us consider a similar approach for the laterally confined cells and follow the evolution 2-D Fourier modes in the transversal mid-plane $z = 0$ (see figure 7.8b). In laterally confined 3-D cells, the mode $\hat{u}_{1,1}$ is not dominant and oscillates around zero, whereas the leading modes correspond to $\hat{u}_{2,2}$, and $\hat{u}_{1,2}$ instead. The value of $\hat{u}_{2,2}$ is mostly positive, while $\hat{u}_{1,2}$ and $\hat{u}_{1,4}$ switch signs during the flow reversal near $t = 100$. In this sense, $\hat{u}_{1,2}$ is a natural choice to characterize the presence of flow reversals in this geometry. Furthermore, near $t = 550$, $t = 1000$, and to a lesser degree for $t = 1500$ one observes failed reversals: these coefficients drop to zero, before returning to the same plateau.

In 2-D reversals, the whole process is driven by localized and progressive accumulation of thermal energy inside the corner-rolls, which eventually overcomes the central vortex. In the confined geometry, the reversal is characterized by strong oscillations in E_k, E_a and Nu_{vol} (figure 7.8c), but it is less clear if there is a progressive build-up of thermal energy as in pure 2-D. No noticeable change in size of the thermal structures was observed. Note that reversal are rare and it is difficult to perform a detailed study using DNS. This constitutes one of the motivations for developing the reduced order models presented in the next chapter.

7.4 Statistical characterization of the confined regime: number of plumes and average plume width

We take a statistical approach to characterize the turbulent flow and the persistent large-scale structures. In the context of the confined regime, we are interested in the number

and size of large-scale turbulent channels that controls the flow dynamics. Given the loss of three-dimensionality of the thermal structures along the transversal direction, we can focus our observations on the transversal mid-plane $z = 0$.

From figure 7.9a, two type of plumes can be distinguished. Near the bottom plate we observe three narrow ascending plumes (in orange) just detached from the boundary layers, and two wider descending plumes (in blue) which are about to impact against the bottom boundary layer. Similarly, near the upper plate we observe two narrow descending plumes (in blue) and one wider ascending plume (in orange). A geometric characterization of such individual plumes is a complex task. Different alternatives are available, see for instance (Shishkina and C. Wagner, 2008). Here, a simple method is proposed taking advantage of the alignment of sheet-like plumes perpendicular to the front and back walls ($z = \pm\Gamma_z/2$) in the confined regime. To compute the position of the narrow plumes just detached from the boundary layer, one focuses on the height $y = \pm(0.5 - 1/\overline{\mathrm{Nu}})$, i.e. twice the thermal boundary layer thickness. Since plumes are the main carriers of heat across the domain, it is reasonable to associate a plume to each local maxima in $\langle\phi^2\rangle_z(x,t)$ where $\phi(x,t) = v\theta - \langle v\theta\rangle_x$ denotes the deviations from the mean instantaneous vertical heat-flux. Hence, the location of the plumes is estimated by searching for the number and positions of these local maxima (indicated in figure 7.9 by ▲ marks).

The number of plumes at a given time depends on length Γ_x (here kept at $\Gamma_x = 1$), and on the geometry of the plumes, which depends on Ra and Γ_z. For $(\mathrm{Ra} = 10^8, \Gamma_z = 1/64)$ one identifies from 3 to 4 plumes near the bottom plate and from 3 to 4 others near the top plate (figures 7.9a to 7.9c), whereas for $(\mathrm{Ra} = 10^9, \Gamma_z = 1/64)$ one identifies from 6 to 10 plumes near the bottom plate and a similar amount near the top plate (figures 7.9d to 7.9f). Ejected plumes are not evenly distributed but have instead the tendency to form clusters (see figures 7.9e and 7.9f). Hence the distance between contiguous ejected plumes, denoted by d_0, is not necessarily equal to the length of the cavity divided by the number of plumes. Figure 7.10a displays the probability distribution of d_0 for $(\Gamma_z = 1/64, \mathrm{Pr} = 4.38)$ and different values of Ra.

For $\mathrm{Ra} = 5 \cdot 10^7$, plume spacing near the bottom plate peaks near $d_0 = 0.5$, i.e. the distance between the side-walls and the central plume, while near the top plate a peak is observed near $d_0 = 0.95$, i.e. the distance between the side-wall plumes. For $\mathrm{Ra} = 10^8$, a central plume is observed at the bottom and two side-wall plumes at the top, but additional plumes form near both plates, which are pushed towards the center or towards the side-walls. The plume spacing d_0 is distributed over a wider range due to the horizontal displacements of the plumes, while a second smaller length scale reflects the motion of the new plumes (see top part of figure 7.10a). Unlike $\mathrm{Ra} = 5 \cdot 10^7$ and $\mathrm{Ra} = 10^8$, a transition towards a symmetric configuration is observed for $\mathrm{Ra} = 2 \cdot 10^8$ and $\mathrm{Ra} = 10^9$. This results in a similar distributions of d_0 at the top and bottom plates. Finally, for $\mathrm{Ra} = 10^9$ the motion of several turbulent channels that are formed, pushed and merged continuously with each other is reflected on a smoother distribution of d_0.

One may estimate a characteristic width of the ejected (narrow and intense) plumes. This is done by computing the time averaged spatial auto-correlation function of ϕ

$$f_{\mathrm{corr}}(r) = \overline{\left(\frac{\langle\phi(x,y,z,t)\phi(x+r,y,z,t)\rangle_x}{\langle\phi(x,y,z,t)\phi(x,y,z,t)\rangle_x}\right)} \qquad \text{at } y = \pm(0.5 - 1/(2\overline{\mathrm{Nu}})), z = 0 \qquad (7.3)$$

$$\mathrm{Ra} = 10^8, \Gamma_z = 1/64$$

(a) Snapshot $t = t_0$

(b) Lower boundary layer

(c) Upper boundary layer

$$\mathrm{Ra} = 10^9, \Gamma_z = 1/64$$

(d) Snapshot $t = t_0$

(e) Lower boundary layer

(f) Upper boundary layer
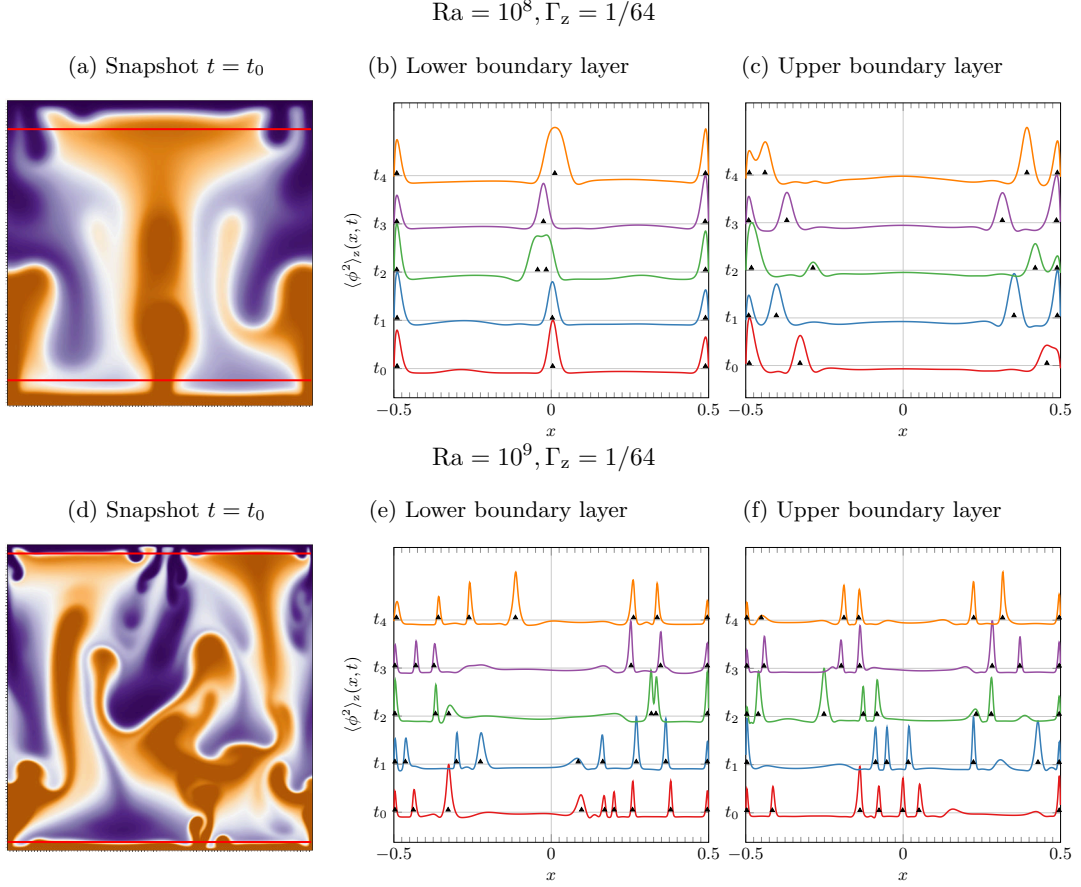
Figure 7.9: Plume characterization for $(\Gamma_z = 1/64, \mathrm{Pr} = 4.38)$ for (a,b,c) $\mathrm{Ra} = 10^8$ and (d,e,f) $\mathrm{Ra} = 10^9$. Figures (a,d) display the reference height $y_r(x, y, 0, t_0)$, whereas figures (b,e) and (c,f) correspond to $\langle \phi^2 \rangle_z(x, t)$ with $\phi = v\theta - \langle v\theta \rangle_x$ for 5 consecutive instants (t_0 to t_4), each in a different color. Measurements taken at $y = \pm(0.5 - 1/\overline{\mathrm{Nu}})$. The number of plumes is deduced from local maxima in $\langle \phi^2 \rangle_z(x, t)$ (each shown as ▲).

(a) Inter-plume spacing

(b) Spatial auto-correlation
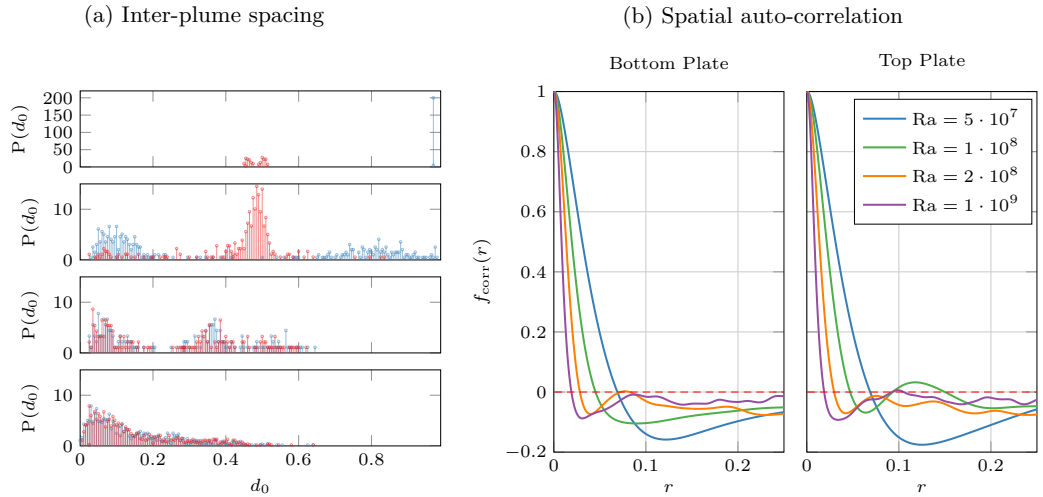
Figure 7.10: (a) Probability distribution of the inter-plume spacing d_0 measured near the top (blue) and bottom (red) boundary layers for $\mathrm{Pr} = 4.38$ and $\Gamma_z = 1/64$. From top to bottom: $\mathrm{Ra} = 5 \cdot 10^7$ (w/central plume), $\mathrm{Ra} = 10^8$, $\mathrm{Ra} = 2 \cdot 10^8$, and $\mathrm{Ra} = 10^9$. (b) Spatial auto-correlation for $\mathrm{Pr} = 4.38$ and $\Gamma_z = 1/64$ used to illustrate the plume width.

Ra	Γ_z	No.	$\overline{d_0}/\delta_\theta^{(1)}$	$\overline{r_0}/\delta_\theta^{(1)}$	$\mathcal{L}_0/\delta_\theta^{(1)}$	No.	$\overline{d_0}/\delta_\theta^{(1)}$	$\overline{r_0}/\delta_\theta^{(1)}$	$\mathcal{L}_0/\delta_\theta^{(1)}$
			Plumes near top BL			Plumes near bottom BL			
$1 \cdot 10^7$	1/8	3.6	10.87	4.21	0.90	3.6	10.92	4.90	1.50
$5 \cdot 10^7$	1/8	4.7	14.49	8.69	2.99	4.7	14.50	9.47	3.23
$1 \cdot 10^8$	1/8	4.8	16.55	10.56	2.72	5.0	16.22	11.10	2.74
$1 \cdot 10^7$	1/16	3.0	8.96	1.05	0.46	2.6	11.09	1.05	0.50
$5 \cdot 10^7$	1/16	3.2	20.25	4.92	1.45	3.3	19.36	6.96	0.90
$1 \cdot 10^8$	1/16	4.5	16.33	4.64	1.52	4.1	18.54	5.90	1.64
$1 \cdot 10^7$	1/32	2.7	7.17	1.17	0.53	2.8	7.08	1.17	0.54
$5 \cdot 10^7$	1/32	3.5	11.42	1.09	0.55	4.0	9.45	1.00	0.47
$1 \cdot 10^8$	1/32	4.5	11.04	1.18	0.54	4.5	11.10	1.25	0.59
$1 \cdot 10^9$	1/32	6.8	21.09	15.62	3.03	7.2	19.96	16.58	2.68
$1 \cdot 10^7$	1/64	2.0	6.95	1.34	0.61	2.0	6.96	1.35	0.61
$5 \cdot 10^7$	1/64	2.9	7.92	1.07	0.51	2.9	7.94	1.09	0.51
$1 \cdot 10^8$	1/64	3.2	11.01	1.17	0.55	3.5	9.96	1.12	0.51
$1 \cdot 10^9$	1/64	8.0	13.24	1.68	0.78	7.7	13.84	1.77	0.78

Table 7.3: Geometric characterization of plumes for $y = \pm(0.5 - 1/\overline{\mathrm{Nu}})$: Average number of plumes (No.), average plume spacing $\overline{d_0}$, mean correlation distance r_0 and integral scale $\mathcal{L}_0$. Values normalized by $\delta_\theta^{(1)} = 1/(2\overline{\mathrm{Nu}})$ for reference.

and measuring the distance r_0 as the first zero-crossing of $f_{\mathrm{corr}}(r_0) = 0$, i.e. the distance at which the plumes are no longer correlated to themselves (figure 7.10b). The distance r_0 is then used to compute an integral length scale of the vertical heat-flux $\mathcal{L}_0$

$$\mathcal{L}_0 = \int_{-r_o}^{r_0} f_{\mathrm{corr}}(r) \ \mathrm{d}r \tag{7.4}$$

The value $\mathcal{L}_0$ is considered to be representative of the average plume width. Note that the value of $\mathcal{L}_0$ is comparable to $\delta_\theta^{(1)} = 1/(2\overline{\mathrm{Nu}})$ (see table 7.3). This is consistent with observations in cylindrical cells (Shishkina and C. Wagner, 2008) in which the thickness of sheet-like plumes was found to be of the same order of the thermal boundary layer.

7.5 Statistical characterization of the confined regime: mean profiles and boundary layer thickness

Turbulent convection is divided spatially into thermal and kinetic boundary layers and a turbulent background away from the boundaries. Traditionally, in order to provide a simplified description of the turbulent flow, one considers vertical profiles of different quantities. In our particular case, the influence of the aspect ratio Γ_z is also explored through the use of profiles of the viscous dissipation in the transversal direction.

7.5.1 Vertically averaged profiles

Consider the thermal vertical profiles displayed on figure 7.11: the spatio-temporal fluctuations $\langle\theta\rangle_{\mathrm{xz}}^{\overline{\mathrm{rms}}}$ and the plane and time-averaged thermal dissipation rate $\langle\overline{\partial_j\theta\partial_j\theta}\rangle_{\mathrm{xz}}$. Two regimes are identifiable. In the first one, fluctuation profiles are similar to the typi-
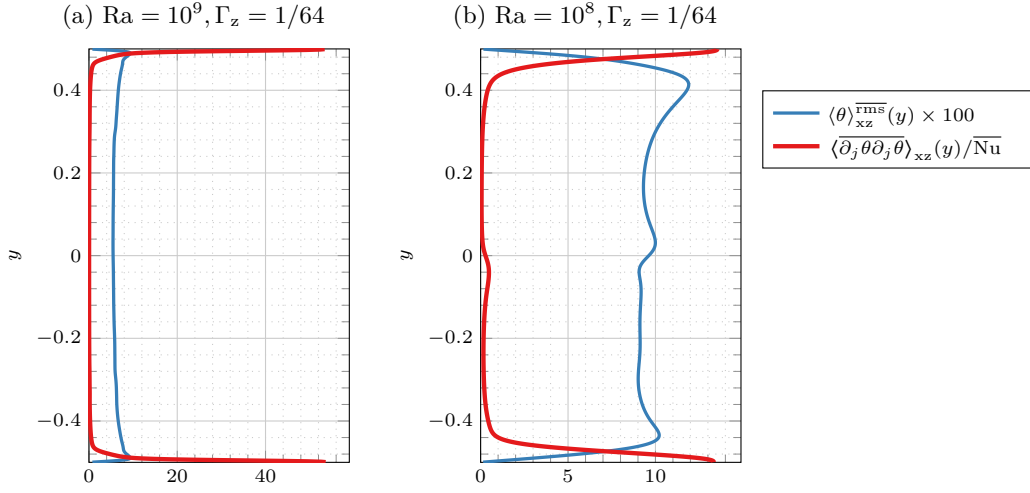
Figure 7.11: DNS results for $(\Gamma_z = 1/64, \mathrm{Pr} = 4.38)$ and different Ra. Spatio-temporal fluctuations $\langle \theta \rangle_{\mathrm{xz}}^{\overline{\mathrm{rms}}}(y)$, and time-averaged thermal dissipation rate $\langle \overline{\partial_j \theta \partial_j \theta} \rangle_{\mathrm{xz}}(y)$.
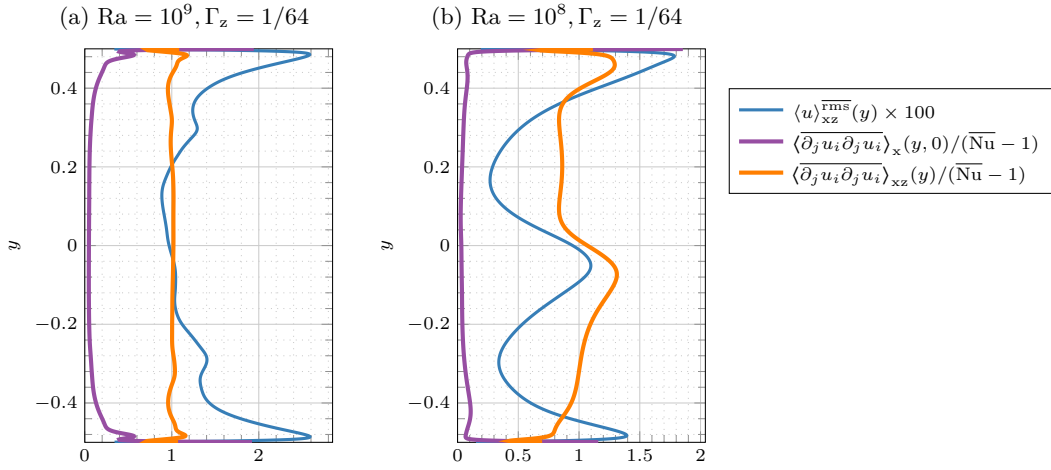
Figure 7.12: DNS results for $(\Gamma_z = 1/64, \mathrm{Pr} = 4.38)$ and different Ra. Spatio-temporal fluctuations $\langle u \rangle_{\mathrm{xz}}^{\overline{\mathrm{rms}}}(y)$, time-averaged viscous dissipation $\langle \overline{\partial_j u_i \partial_j u_i} \rangle_{\mathrm{xz}}(y)$ averaged along the z direction, and time-averaged viscous dissipation $\langle \overline{\partial_j u_i \partial_j u_i} \rangle_{\mathrm{x}}(y, 0)$ at the transversal mid-plane $(z = 0)$.

cal profiles found on unconfined turbulent convection cells (Kerr, 1996). This is the case for $(\Gamma_z = 1/64, \mathrm{Ra} = 10^9)$ (figure 7.11a) but also for $(\Gamma_z = 1/32, \mathrm{Ra} = 10^8)$ and $(\Gamma_z = 1/32, \mathrm{Ra} = 10^9)$ (not shown): temperature fluctuations reach a peak value close to the top and bottom plates, indicating the presence of thermal boundary layers, whereas a nearly constant temperature fluctuation is observed in the bulk. Additionally, thermal dissipation is localized near the top and bottom plates. The second regime corresponds to configurations where a central plume is observed to remain in place for long periods of time. This is the case for $(\mathrm{Ra} = 10^8, \Gamma_z = 1/64)$ (figure 7.11b) but also for $(\Gamma_z = 1/64, \mathrm{Ra} = 5 \cdot 10^7)$ (not shown). In such cases, the vertical profiles are asymmetric by exchanging the lower and upper half-cells inside the bulk. In addition to the features of the first regime, the temperature fluctuations display a peak in the bulk, more precisely at an intermediate height where the ascending and descending plumes collide. A small increase in thermal dissipation is also observed at the same height.

These two regimes have a counterpart in the vertical velocity profiles of the spatio-temporal fluctuations $\langle u \rangle_{\mathrm{xz}}^{\overline{\mathrm{rms}}}(y)$, the plane-averaged viscous dissipation rate $\langle \overline{\partial_j u_i \partial_j u_i} \rangle_{\mathrm{xz}}$ and the viscous dissipation rate $\langle \overline{\partial_j u_i \partial_j u_i} \rangle_{\mathrm{x}}$ at the median plane $z = 0$ (figure 7.12). In the first regime, the horizontal velocity fluctuations display a peak value close to the top and bottom plates and comparatively smaller values in the bulk (figure 7.12a). Unlike the model profiles by (Kerr, 1996), the transversally averaged dissipation profile $\langle \overline{\partial_j u_i \partial_j u_i} \rangle_{\mathrm{xz}}$ is nearly constant in the bulk due to frictional drag along the front and back walls. If we consider the dissipation profile at the median plane instead of the transversally averaged one, the viscous dissipation is localized near the top and bottom plates. For the second regime, additional peaks in the velocity fluctuations and in the viscous dissipation are observed at intermediate heights where the ascending and descending side-wall plumes collide (figure 7.12b).

7.5.2   Mean thermal and kinetic boundary layers

In this section, we focus on the relation between the thermal and kinetic boundary layers. In confined convection, the thickness of the thermal boundary layer depends not only on Ra and Pr, as in the conventional convection, but also on Γ_z. The situation for the kinetic boundary layer is different: for the confined case, its thickness depends mostly on Γ_z. This implies that the ratio between thermal and kinetic boundary layers is no longer defined by Pr as conventional (unconfined) convection, and leads to a situation where the thermal boundary layer interacts directly with the bulk even for $\mathrm{Pr} > 1$, which is not possible in conventional convection.

Thermal boundary layer thickness at the top and bottom plates

We provide different estimates of the thermal boundary layer thickness presented in §2.4: namely, thickness $\delta_\theta^{(1)} = 1/(2\overline{\mathrm{Nu}})$; a thickness $\delta_\theta^{(2)}$ defined as the distance between the closest peak in $\langle \theta \rangle_{\mathrm{xz}}^{\overline{\mathrm{rms}}}$ to the top and bottom plates; and thickness $\delta_\theta^{(3)}$ defined as the closest distance between the position where $\langle \overline{\partial_j \theta \partial_j \theta} \rangle_{\mathrm{xz}}(y) = \overline{\mathrm{Nu}}$ and the top and bottom plates. To measure such thicknesses, we could have used the profiles at the transversal mid-plane ($z = 0$) instead of the transversally averaged profiles, since $\langle \overline{\partial_j \theta \partial_j \theta} \rangle_{\mathrm{x}}(y, z)$ for
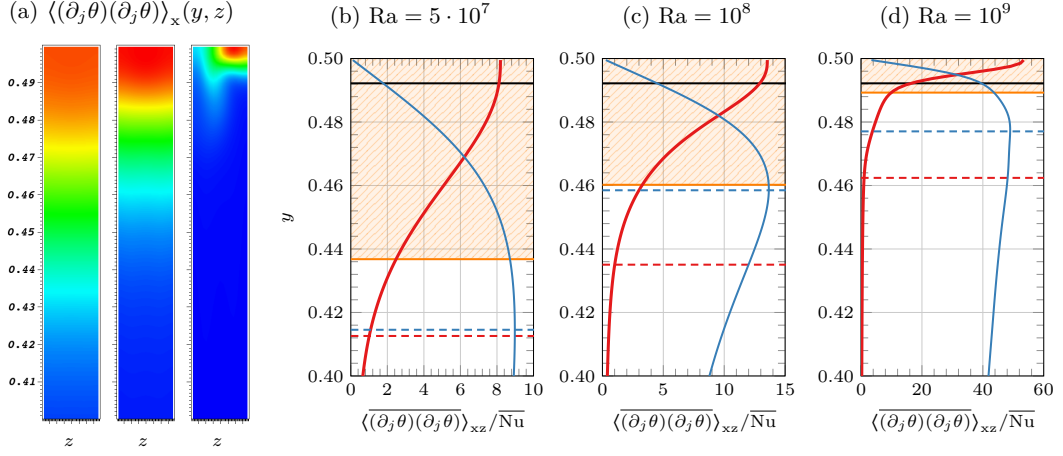
Figure 7.13: Thermal dissipation for $\Gamma_z = 1/64$ and $\text{Pr} = 4.38$. Figure (a) displays $\langle \overline{\partial_j \theta \partial_j \theta} \rangle_x (y, z)$ for $\text{Ra} = 5 \cdot 10^7$ (left), $\text{Ra} = 10^8$ (center), and $\text{Ra} = 10^9$ (right). Figures (b-d) display vertical profiles for $\langle \theta \rangle_{xz}^{\overline{\text{rms}}}$ (blue lines) and $\langle \overline{\partial_j \theta \partial_j \theta} \rangle_{xz} (y) = \overline{\text{Nu}}$ (red lines). The horizontal lines $y = 0.5 - \delta_\theta^{(1)}$, $y = 0.5 - \delta_\theta^{(2)}$, and $y = 0.5 - \delta_\theta^{(3)}$ are displayed in orange, dashed blue, and dashed red lines, respectively, and $y = 0.5 - \Gamma_z/2$ is shown in black for reference.

$\text{Ra} = 5 \cdot 10^7$, $\text{Ra} = 10^8$, and $\text{Ra} = 10^9$ illustrating a small dependence on z of the thermal dissipation, except for the largest Ra (figure 7.13).

A close-up of the vertical profiles near the top plate allows to compare the values of $\delta_\theta^{(1)}$, $\delta_\theta^{(2)}$, and $\delta_\theta^{(3)}$ as we increase Ra for $\Gamma_z = 1/64$ (figure 7.13). In most cases, $\delta_\theta^{(1)}$ was found to be the smallest value and $\delta_\theta^{(3)}$ was the largest one, see table 7.4. Since our main concern is the relative thickness of the thermal and kinetic boundary layers, we will take the low end estimate of the thickness, i.e. $\delta_\theta^{(1)}$, to define the thermal boundary layer thickness (hatched region in figures 7.13b to 7.13d).

Kinetic boundary layers on the top and bottom plates

In turbulent Rayleigh-Bénard convection, a kinetic boundary layer develops in the vicinity of the plates and of the side-walls (figure 7.14). In this section we focus on the kinetic boundary layer of thickness δ_p on the top and bottom walls. Different estimations for δ_p were presented in §2.4. First, a thickness $\delta_p^{(1)}$ defined based on the distance between the closest peak in $\langle u \rangle_{xz}^{\overline{\text{rms}}}$ to the top and bottom plates (see §2.4.2i). Second, a thickness $\delta_p^{(2)}$ based on the closest distance between the position where $\langle \overline{\partial_j u_i \partial_j u_i} \rangle_x (y, 0) = (\overline{\text{Nu}} - 1)$ to the top and bottom plates. The plane $z = 0$ is chosen in order to reduce the influence of the side-walls on the measurements on the top and bottom plates.

Figure 7.15 displays a close-up of the vertical profiles near the bottom plate for $\Gamma_z = 1/64$. In most cases, the thickness $\delta_p^{(1)}$ is larger than $\delta_p^{(2)}$ and is comparable to Γ_z. In the following, we use the thickness $\delta_p = \delta_p^{(1)}$ to define the kinetic boundary layer thickness at the top and bottom plates (blue hatched region in figures 7.15b to 7.15d).

Γ_z	Ra	$\delta_\theta^{(1)}/\Gamma_z$	Bottom $\delta_\theta^{(2)}/\Gamma_z$	Top $\delta_\theta^{(2)}/\Gamma_z$	Bottom $\delta_\theta^{(3)}/\Gamma_z$	Top $\delta_\theta^{(3)}/\Gamma_z$
1/8	$1 \cdot 10^7$	0.27	0.26	0.27	0.52	0.45
1/8	$5 \cdot 10^7$	0.14	0.13	0.13	0.35	0.35
1/8	$1 \cdot 10^8$	0.11	0.10	0.10	0.34	0.34
1/16	$1 \cdot 10^7$	0.85	1.05	1.27	1.02	1.20
1/16	$5 \cdot 10^7$	0.35	0.36	0.36	0.77	0.77
1/16	$1 \cdot 10^8$	0.27	0.23	0.23	0.83	0.77
1/32	$1 \cdot 10^7$	2.45	3.20	3.17	2.52	2.55
1/32	$5 \cdot 10^7$	1.11	1.70	2.42	1.83	1.89
1/32	$1 \cdot 10^8$	0.81	0.95	1.11	1.64	1.61
1/32	$1 \cdot 10^9$	0.26	0.20	0.20	1.42	1.39
1/64	$5 \cdot 10^7$	4.04	6.28	6.22	4.22	5.59
1/64	$1 \cdot 10^8$	2.54	4.16	5.53	3.84	4.16
1/64	$2 \cdot 10^8$	1.65	3.41	3.34	3.16	3.09
1/64	$1 \cdot 10^9$	0.69	0.66	0.66	2.41	2.34

Table 7.4: Different estimations for the thickness of the thermal boundary layers: $\delta_\theta^{(1)}$, $\delta_\theta^{(2)}$, and $\delta_\theta^{(3)}$. Values are normalized by Γ_z for reference.
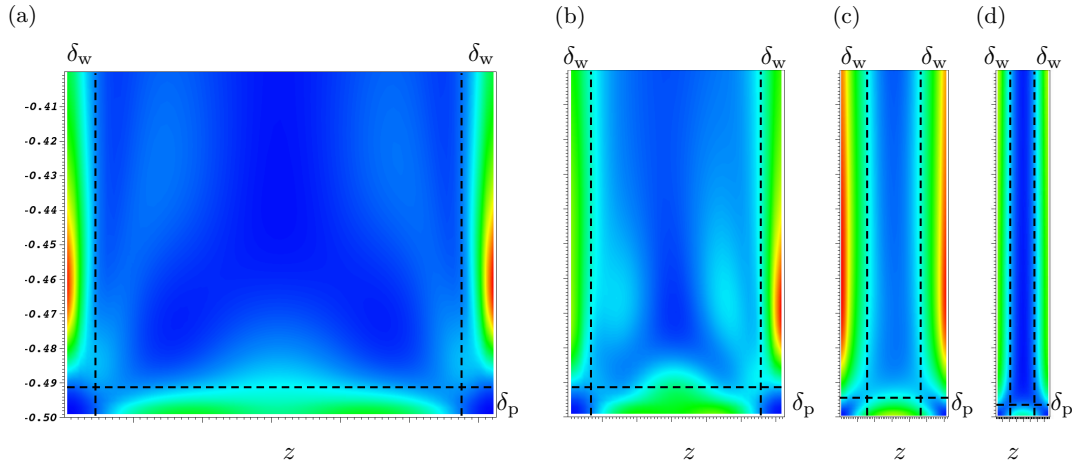
Figure 7.14: Spatial distribution of the viscous dissipation $\langle \overline{\partial_j u_i \partial_j u_i} \rangle_x (y,z)$ near the bottom for Ra $= 10^8$, Pr $= 4.38$ and for: (a) $\Gamma_z = 1/8$, (b) $\Gamma_z = 1/16$, (c) $\Gamma_z = 1/32$, and (d) $\Gamma_z = 1/64$. Boundary layer thicknesses at the plates δ_p and side-walls δ_w shown for reference.

(a) $\langle \overline{\partial_j u_i \partial_j u_i} \rangle_{\mathrm{x}}(y,z)$

(b) $\mathrm{Ra} = 5 \cdot 10^7$

(c) $\mathrm{Ra} = 10^8$

(d) $\mathrm{Ra} = 10^9$

$\langle \overline{\partial_j u_i \partial_j u_i} \rangle_{\mathrm{x}}/(\overline{\mathrm{Nu}} - 1)$
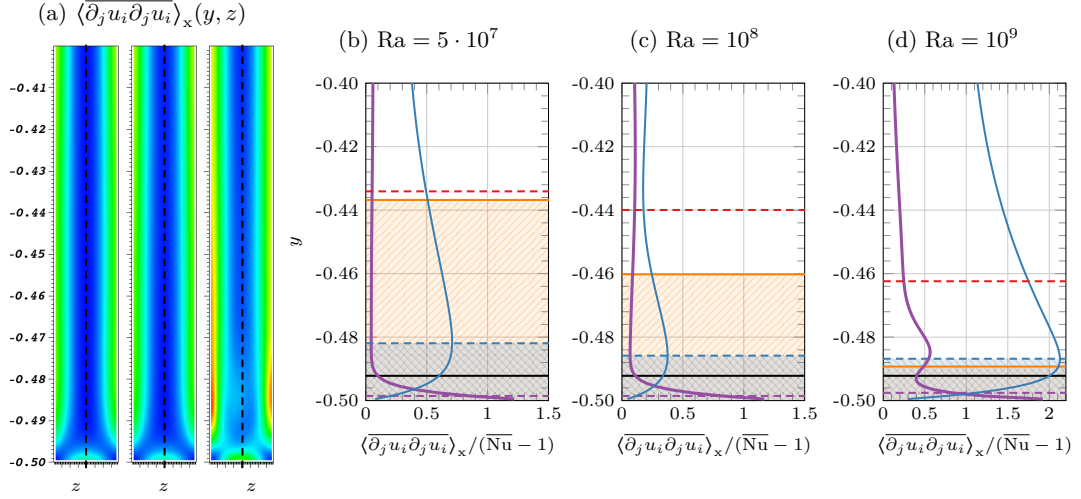
Figure 7.15: Viscous dissipation for $\Gamma_{\mathrm{z}} = 1/64$ and $\mathrm{Pr} = 4.38$. Figure (a) displays $\langle \overline{\partial_j u_i \partial_j u_i} \rangle_{\mathrm{x}}(y,z)$ for $\mathrm{Ra} = 5 \cdot 10^7$, $\mathrm{Ra} = 10^8$, and $\mathrm{Ra} = 10^9$. Figures (b-d) display vertical profiles for $\langle u \rangle_{\mathrm{xz}}^{\overline{\mathrm{rms}}}$ (in blue lines) and $\langle \overline{\partial_j u_i \partial_j u_i} \rangle_{\mathrm{x}}(y,0)$ (in purple lines). Thickness $\delta_{\mathrm{p}}^{(1)}$ (resp. $\delta_{\mathrm{p}}^{(2)}$) displayed in blue (resp. purple) horizontal lines. Thickness $\delta_{\theta}^{(1)}$ (resp. $\delta_{\theta}^{(3)}$) are displayed in orange (resp. red) horizontal lines. The area hatched in blue corresponds to the kinetic boundary layer, while the thermal one is displayed in orange. Here $\Gamma_{\mathrm{z}}/2$ is shown in black for reference.

| | | Kinetic BL thickness | | Ratio between thermal and kinetic BL thicknesses | | | | |
| | | Bottom | Top | | Bottom | Top | Bottom | Top |
Γ_{z}	Ra	$\delta_{\mathrm{p}}^{(1)}/\Gamma_{\mathrm{z}}$	$\delta_{\mathrm{p}}^{(1)}/\Gamma_{\mathrm{z}}$	$\delta_{\mathrm{p}}^{(1)}/\delta_{\theta}^{(1)}$	$\delta_{\mathrm{p}}^{(2)}/\delta_{\theta}^{(1)}$	$\delta_{\mathrm{p}}^{(2)}/\delta_{\theta}^{(1)}$	$\delta_{\mathrm{p}}^{(3)}/\delta_{\theta}^{(1)}$	$\delta_{\mathrm{p}}^{(3)}/\delta_{\theta}^{(1)}$
1/8	$1 \cdot 10^7$	0.45	0.30	1.4	1.7	1.1	0.9	0.7
1/8	$5 \cdot 10^7$	0.29	0.29	2.0	2.2	2.2	0.8	0.8
1/8	$1 \cdot 10^8$	0.26	0.26	2.2	2.5	2.5	0.8	0.8
1/16	$1 \cdot 10^7$	0.58	0.70	0.8	0.6	0.6	0.6	0.6
1/16	$5 \cdot 10^7$	0.67	0.67	1.9	1.9	1.9	0.9	0.9
1/16	$1 \cdot 10^8$	0.45	0.48	1.7	1.9	2.1	0.5	0.6
1/32	$1 \cdot 10^7$	1.02	1.02	0.4	0.3	0.3	0.4	0.4
1/32	$5 \cdot 10^7$	0.80	0.98	0.8	0.5	0.4	0.4	0.5
1/32	$1 \cdot 10^8$	0.86	0.73	1.0	0.9	0.7	0.5	0.5
1/32	$1 \cdot 10^9$	0.52	0.52	2.0	2.5	2.5	0.4	0.4
1/64	$5 \cdot 10^7$	1.22	1.22	0.3	0.2	0.2	0.3	0.2
1/64	$1 \cdot 10^8$	1.09	1.22	0.5	0.3	0.2	0.3	0.3
1/64	$2 \cdot 10^8$	0.97	0.97	0.6	0.3	0.3	0.3	0.3
1/64	$1 \cdot 10^9$	0.91	0.91	1.3	1.4	1.4	0.4	0.4

Table 7.5: Estimation for the thickness of the kinetic boundary layers at the top and bottom plates $\delta_{\mathrm{p}}^{(1)}$ and ratios between $\delta_{\mathrm{p}}^{(1)}$ and the estimated thicknesses of the thermal boundary layers: $\delta_{\theta}^{(1)}$, $\delta_{\theta}^{(2)}$, and $\delta_{\theta}^{(3)}$. Color red indicates the kinetic boundary is nested inside the thermal one.
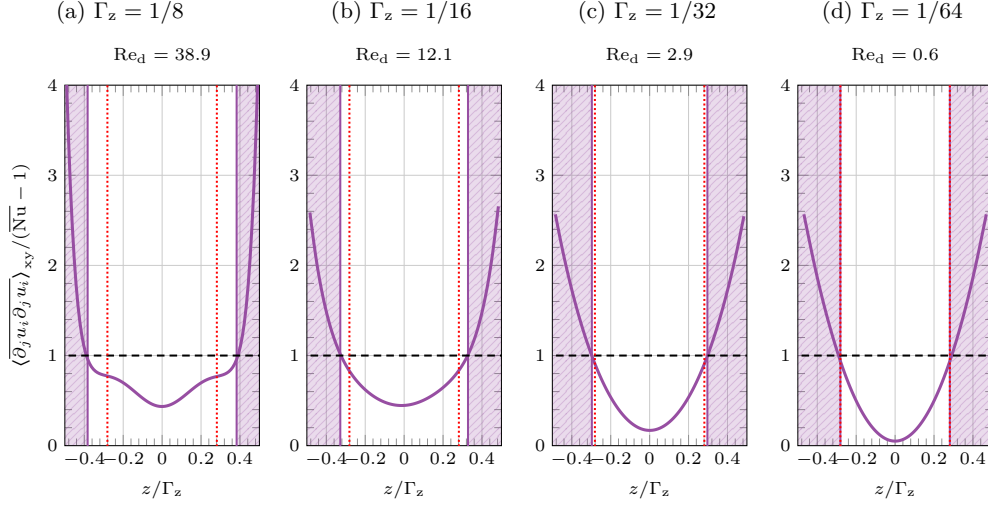
Figure 7.16: DNS results for $(\text{Ra} = 10^8, \text{Pr} = 4.38)$ and different Γ_z. Time-averaged dissipation profiles in the transversal direction (purple lines). The shaded area of size δ_w/Γ_z corresponds to the kinetic boundary layers on the front and back walls. The value δ_w/Γ_z is compared to the value $\delta_w/\Gamma_z = 0.211$ (red dotted lines).

Ratio between the thermal and kinetic boundary layers at the plates

For conventional (unconfined) cells, the ratio between δ_p and δ_θ is mostly defined by the value of Pr: δ_θ is expected to be smaller than δ_p for $\text{Pr} > 1$ and *vice versa*. However, for very confined cells, the thickness δ_θ increases as the convective transfer, i.e. Nusselt (see table 7.1) is hampered by the confinement, while δ_p depends mostly on Γ_z and not on Ra (see table 7.5). In this sense, the ratio δ_p/δ_θ is expected to become smaller as Γ_z decreases regardless of the value of Pr. This a major difference between the unconfined and confined regimes, which is consistent with observations from (Chong, Kai Leong et al., 2017). This behavior is independent of the two regimes mentioned earlier on figures 7.11 and 7.12, which are related to behavior of thermal plumes and the asymmetry of the vertical profiles. Both regimes are observed for $\delta_p/\delta_\theta > 1$ and $\delta_p/\delta_\theta < 1$ alike. Examples of the second regime include $(\text{Ra} = 5 \cdot 10^7, \Gamma_z = 1/8)$ and $(\text{Ra} = 10^8, \Gamma_z = 1/8)$ for $\delta_p/\delta_\theta > 1$, and $(\text{Ra} = 10^7, \Gamma_z = 1/8)$ and $(\text{Ra} = 10^8, \Gamma_z = 1/16)$ for $\delta_p/\delta_\theta < 1$.

Kinetic boundary layers on the front and back walls

The second major difference from unconfined convection concerns the kinetic boundary layers on the front and back walls which become dominant for geometrical reasons. To define the boundary layer thickness, we consider the transversal profiles of the time-averaged viscous dissipation $\langle \overline{\partial_j u_i \partial_j u_i} \rangle_{xy}$ (figure 7.16) and compute the positions z where $\langle \overline{\partial_j u_i \partial_j u_i} \rangle_{xy} = \langle \overline{\partial_j u_i \partial_j u_i} \rangle_{xyz} = (\overline{\text{Nu}} - 1)$. The smallest distance between these points and the front or back walls is taken as the thickness δ_w.

Locally, the velocity field along the side-walls may be considered as a wall-bounded flow. For such a velocity field, the thickness δ_w is expected to increase as the Reynolds number decreases and *vice versa*. This Reynolds number is based on the mean velocity magnitude

Γ_z	Ra	$\overline{\mathrm{Re}}_d$	$\dfrac{\delta_p^{(1)}}{\delta_\theta^{(1)}}$	$\dfrac{\delta_w}{\Gamma_z}$	$\dfrac{\Delta z}{\Gamma_z}$	$\dfrac{\epsilon^{(bl)}}{\epsilon}$	Γ_z	Ra	$\overline{\mathrm{Re}}_d$	$\dfrac{\delta_p^{(1)}}{\delta_\theta^{(1)}}$	$\dfrac{\delta_w}{\Gamma_z}$	$\dfrac{\Delta z}{\Gamma_z}$	$\dfrac{\epsilon^{(bl)}}{\epsilon}$
1/8	$1\cdot10^7$	9.7	1.4	0.15	0.02	0.52	1/32	$1\cdot10^7$	0.5	0.4	0.22	0.03	0.79
1/8	$5\cdot10^7$	26.5	2.0	0.13	0.02	0.50	1/32	$5\cdot10^7$	1.8	0.8	0.21	0.03	0.75
1/8	$1\cdot10^8$	38.9	2.2	0.12	0.02	0.49	1/32	$1\cdot10^8$	2.9	1.0	0.21	0.03	0.74
1/16	$1\cdot10^7$	2.4	0.8	0.21	0.03	0.69	1/32	$1\cdot10^9$	15.5	2.0	0.21	0.03	0.71
1/16	$5\cdot10^7$	7.7	1.9	0.19	0.03	0.62	1/64	$5\cdot10^7$	0.3	0.3	0.23	0.06	0.81
1/16	$1\cdot10^8$	12.1	1.7	0.19	0.03	0.61	1/64	$1\cdot10^8$	0.6	0.5	0.23	0.06	0.80
							1/64	$2\cdot10^8$	1.1	0.6	0.23	0.06	0.80
							1/64	$1\cdot10^9$	3.7	1.3	0.22	0.06	0.77

Table 7.6: Most conservative estimate of the ratio $\delta_p^{(1)}/\delta_\theta^{(1)}$ which indicates whether the kinetic BL is nested inside the thermal one (shown in purple) or *vice versa*; average thickness of the kinetic boundary layer at the front/back walls δ_w and contributions to the viscous dissipation from the front/back kinetic boundary layers. Grid spacing in the transversal direction Δz is shown to illustrate the incertitude in the measurement of δ_w.

and on the depth of the cavity, that is

$$\overline{\mathrm{Re}}_d = \frac{\Gamma_z \mathrm{Ra}^{0.5}}{\mathrm{Pr}} \langle \overline{\mathbf{u}^2} \rangle_{\mathrm{xyz}}^{0.5} \tag{7.5}$$

At some level of confinement, the value of δ_w loses its Reynolds dependence being bounded by the depth of the cavity. This process is illustrated in figure 7.16. As Γ_z decreases, the dissipation becomes increasingly parabolic: dissipation peaks at the front and back walls and is close to zero at the transversal mid-plane. Furthermore, the boundary layer thickness 'saturates' to a constant value $\delta_w = 0.211\Gamma_z$ (indicated by a red dotted line in figure 7.16). This value can be equally obtained by assuming the velocity profile to be parabolic. For such a parabolic profile, the viscous dissipation at the front and back walls ($z/\Gamma_z = \pm 0.5$) tends to $\langle \overline{\partial_j u_i \partial_j u_i} \rangle_{\mathrm{xy}} \approx 3(\overline{\mathrm{Nu}} - 1)$ and the dissipation $\epsilon^{(bl,w)}$ inside the region enclosing the front and back kinetic boundary layers accounts for 80.7% of the total dissipation ϵ. This peak dissipation at the front and back walls (see figure 7.14d) and the value of the ratio $\epsilon^{(bl,w)}/\epsilon$ (see table 7.6) are observed in our simulations.

The transition towards $\delta_p^{(1)}/\delta_\theta^{(1)} < 1$ is observed around $\mathrm{Re}_d \sim 2$ and often coincides with the saturation the boundary layer thickness at the front and back walls to a constant value $\delta_w = 0.211\Gamma_z$ indicating the transition to a parabolic velocity profile in the transversal direction (table 7.6). In the following section, we explore how these deviations from the conventional (unconfined) convection are reflected on the behavior of the Nusselt and Reynolds numbers.

7.6 Nu and Re as function of Ra and Γ_z: scaling exponents

In order to characterize respectively, the heat-flux and the turbulent motion we use the average Nusselt number defined in (2.50), and a Reynolds number

$$\overline{\mathrm{Re}} = \Gamma_y \frac{\mathrm{Ra}^{0.5}}{\mathrm{Pr}} \overline{U} \qquad\qquad \overline{U} = \overline{\sqrt{\langle \mathbf{u}^2 \rangle_{\mathrm{xyz}}}} \tag{7.6}$$
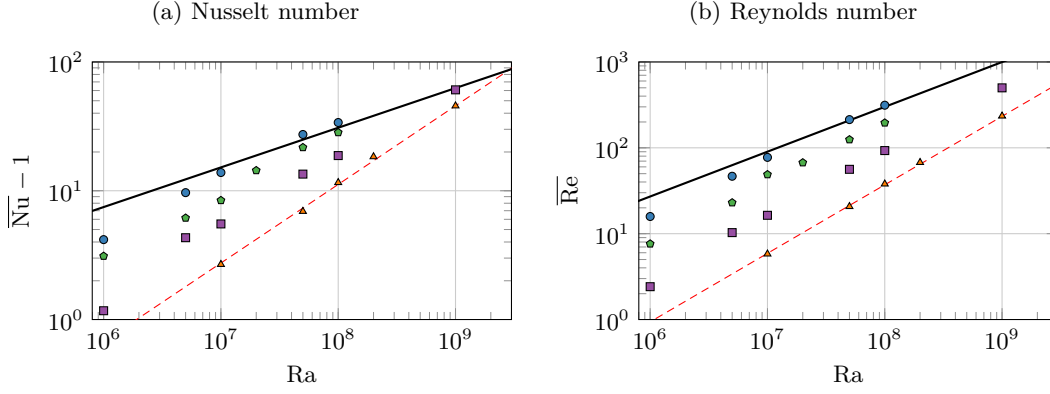
Figure 7.17: (a) Average Nusselt and (b) Reynolds numbers as a function of Ra and Γ_z for Pr = 4.38. Symbols indicate the aspect ratios: $\circ$ $\Gamma_z = 1/8$, $\diamondsuit$ $\Gamma_z = 1/16$, $\square$ $\Gamma_z = 1/32$, and $\triangle$ $\Gamma_z = 1/64$. A black (resp. red) line corresponds to the scaling for $\Gamma_z = 1$ (resp. $\Gamma_z = 1/64$).

Γ_z	$\beta_{\mathrm{Nu}-1}$	β_{Re}
1/8	0.41 ± 0.16	0.61 ± 0.12
1/16	0.50 ± 0.20	0.65 ± 0.19
1/32	0.51 ± 0.03	0.73 ± 0.01
1/64	0.61 ± 0.10	0.80 ± 0.03

Table 7.7: Scaling exponents from equation (7.7) with 95% confidence bounds.

based on the mean velocity magnitude and on the height of the cavity $\Gamma_y = 1$. Figures 7.17a and 7.17b display $(\overline{\mathrm{Nu}} - 1)$ and $\overline{\mathrm{Re}}$ as function of Ra for different values of Γ_z. Both seem to depend on Ra following a power law

$$(\overline{\mathrm{Nu}} - 1) \sim \mathrm{Ra}^{\beta_{\mathrm{Nu}-1}} \qquad \text{and} \qquad \overline{\mathrm{Re}} \sim \mathrm{Ra}^{\beta_{\mathrm{Re}}} \qquad \text{for constant } \Gamma_z \qquad (7.7)$$

The scaling exponents $\beta_{\mathrm{Nu}-1}$ and β_{Re} are estimated by fitting our data and presented on table 7.7. These exponents are consistent with values found in previous studies (Chong and Xia, 2016).

For confined cells, scaling exponents display a dependence on Γ_z and hence deviate from the Grossmann and Lohse, (2000) theory. For $\Gamma_z = 1/64$ one obtains $\beta_{\mathrm{Nu}-1} = 0.61$ and $\beta_{\mathrm{Re}} = 0.80$ (red lines on figures 7.17a and 7.17b), which are different from $\beta_{\mathrm{Nu}-1} = 0.30$ and $\beta_{\mathrm{Re}} = 0.52$ observed in cubic cells (black lines in figures 7.17a and 7.17b). The latter are compatible with (Grossmann and Lohse, 2000).

Chong and Xia, (2016) followed the evolution of scaling exponents with respect to Γ_z up to $\Gamma_z = 1/128$ and concluded that these exponents were approaching the asymptotic values ($\beta_{\mathrm{Nu}-1} = 0.61$ and $\beta_{\mathrm{Re}} = 0.80$), which we found here for $\Gamma_z = 1/64$. However, for Hele-Shaw cells with aspect ratio $\Gamma_z = 1/240$ using free-slip boundaries, higher exponents have been reported ($\beta_{\mathrm{Nu}-1} = 0.872$ and $\beta_{\mathrm{Re}} = 0.96$) (Bizon et al., 1997). While cells with no-slip and free-slip conditions may have different dynamics, it is reasonable to wonder if the same high exponents exists for no-slip conditions for aspect ratios smaller than $\Gamma_z = 1/128$.

156

Since the kinetic boundary layer thicknesses δ_p and δ_w become increasingly thin with Γ_z, it is quite difficult to perform fully resolved direct numerical simulations in such confined configurations. In order to explore this severely confined regime, it is convenient to take a different approach. In the following chapter, we present a reduced model based on the Hele-Shaw cells which is compared to DNS results. The resulting data is used to explore the long term evolution of the large scale flow and the evolution of different global quantities for $\Gamma_\mathrm{z} \ll 1$, before presenting a scaling theory (see section 8.5) suggesting the asymptotic scaling exponents have different values from those of Chong and Xia, (2016).

Chapter 8

A reduced model for confined cells with adiabatic side-walls

Natural convection in the confined regime (III) is characterized by multiple large-scale turbulent channels along the vertical direction and the flow dynamics is defined by the non-linear interactions between these large-scale channels. In particular, over long periods of time, these structures observe a series of re-configurations. A complete study of the long-term behavior of these structures is deemed too expensive for 3-D DNS. An open question concerns the asymptotic scaling of the Nusselt and Reynolds numbers suggested by (Chong and Xia, 2016). In order to verify this scaling, additional simulations for $\Gamma_z \ll 1$ are required. This is difficult because of the increasingly thin kinetic boundary layers as $\Gamma_z \to 0$. This configuration, however, is well suited for dimensionality reduction.

In this chapter, we focus on two reduced models for convection cells under severe confinement. The first model assumes a Poiseuille-like velocity and constant temperature profiles in the transversal direction. This approach has been used extensively for convection problems inside Hele-Shaw cells (Hartline and Lister, 1977; Vorontsov et al., 1991; Graham et al., 1992; Bizon et al., 1997). A second model is also based on the assumption of a Poiseuille-like velocity profile but takes into account inertial corrections, which play an important role near boundaries. It represents a small but noticeable improvement over the first model. Similar work has been done for Hele-Shaw cells (Gondret and Rabaud, 1997; Ruyer-Quil, 2012). By the end of this chapter, we expect to show how such models may assist in the exploration of the parameter space and provide some insight on the dynamics of the confined regime.

8.1 A 'simple' 2-D model for laterally confined cells

In this section, we consider a simple model for convection inside Hele-Shaw cells. In the following we introduce the small parameter

$$\varepsilon = \frac{\Gamma_z}{2} \tag{8.1}$$

and take the average along the transversal direction (for the present chapter $\langle\ \rangle$ means $\langle\ \rangle_z$) of the Boussinesq equations similar to the technique of von Kármán and Pohlhausen.

$$\partial_i\langle u_i\rangle = 0 \tag{8.2a}$$

$$\partial_t\langle u_i\rangle + \partial_j\langle u_j u_i\rangle = -\partial_i\langle\text{p}\rangle + \text{PrRa}^{-0.5}\left[\partial_j\partial_j\langle u_i\rangle + \partial_z u_i\right]_{-\varepsilon}^{\varepsilon} + \text{Pr}\langle\theta\rangle\delta_{iy} \tag{8.2b}$$

$$\partial_t\langle\theta\rangle + \partial_j\langle u_j\theta\rangle = \text{Ra}^{-0.5}\partial_j\partial_j\langle\theta\rangle \tag{8.2c}$$

If we neglect inertial forces on the fluid inside a very confined cell $\varepsilon \ll 1$, one may consider transversal velocity to be negligible and the pressure to be independent of the transversal direction. The resulting in-plane velocity components are expected to have a Poiseuille-like profile. One may also suppose for a confined system with adiabatic walls the temperature field to have no dependency on the transversal direction. In the first model, we assume the primitive variables to have the following form

$$\theta(x, y, z, t) = \theta(x, y, t) \tag{8.3a}$$

$$\text{p}(x, y, z, t) = \text{p}(x, y, t) \tag{8.3b}$$

$$\mathbf{u}(x, y, z, t) = \mathbf{v}(x, y, t)g(z) \tag{8.3c}$$

where

$$g(z) = \frac{3}{2}\left(1 - \left(\frac{z}{\varepsilon}\right)^2\right) \qquad \text{and} \qquad \mathbf{v} \cdot \mathbf{e}_z = 0 \tag{8.4}$$

Introducing *ansatz* (8.3a) to (8.3c), one evaluates the operator $\langle\ \rangle$ which leads to the following system of equations

$$\boxed{\begin{aligned}
&\nabla_{\text{xy}} \cdot \mathbf{v} = 0 && (8.5a) \\
&\partial_t\mathbf{v} + \frac{6}{5}\mathbf{v} \cdot \nabla_{\text{xy}}\mathbf{v} = -\nabla_{\text{xy}}\text{p} + \text{PrRa}^{-0.5}\nabla_{\text{xy}}^2\mathbf{v} - \lambda_1\mathbf{v} + \text{Pr}\,\theta\mathbf{e}_y && (8.5b) \\
&\partial_t\theta + \mathbf{v} \cdot \nabla_{\text{xy}}\theta = \text{Ra}^{-0.5}\nabla_{\text{xy}}^2\theta && (8.5c)
\end{aligned}}$$

with ∇_{xy} as the operator $\nabla_{\text{xy}} = \mathbf{e}_x\partial_x + \mathbf{e}_y\partial_y$ and λ_1 being a friction coefficient on the front and back walls

$$\lambda_1 = \frac{3}{\varepsilon^2}\text{PrRa}^{-0.5} \tag{8.6}$$

These equations are reminiscent of those developed by (Gondret and Rabaud, 1997) in the study of the Kelvin–Helmholtz instability. In order to compare results from this model against the DNS, it is convenient to express the viscous and thermal energy dissipation rates that is consistent with the simplified model. This is done by introducing (8.3a) to (8.3c) in equations (7.2a) and (7.2b)

$$\epsilon \equiv \epsilon^{(xy)} + \epsilon^{(z)} \quad \text{with } \epsilon^{(xy)} = \frac{6}{5}\langle\nabla_{\text{xy}}\mathbf{v} : \nabla_{\text{xy}}\mathbf{v}\rangle_{\text{xy}} \quad \text{and } \epsilon^{(z)} = \frac{3}{\varepsilon^2}\langle\mathbf{v} \cdot \mathbf{v}\rangle_{\text{xy}} \tag{8.7a}$$

$$\epsilon_\theta \equiv \epsilon_\theta^{(xy)} + \epsilon_\theta^{(z)} \quad \text{with } \epsilon_\theta^{(xy)} = \langle\nabla_{\text{xy}}\theta \cdot \nabla_{\text{xy}}\theta\rangle_{\text{xy}} \quad \text{and } \epsilon_\theta^{(z)} = 0 \tag{8.7b}$$

8.2 A 'better' 2-D model with inertial corrections

In this section, we present a second reduced model which takes into account inertial effects. This is done in the spirit of the work by Ruyer-Quil, 2001 that extended the model by Gondret and Rabaud, 1997. Corrections are based on a classical perturbation technique lying on the existence of a basic state to which deviations are applied: the velocity, pressure and temperature fields are developed in terms of a small formal parameter. The profile of the basic state along z corresponds to the solution profile at order zero: a parabolic profile for the velocity field, a constant profile for the temperature and pressure fields. The model equations may be obtained using two alternative methods: the gradient expansion method and the weighted residuals method (Ruyer-Quil, 2012). For a given order of approximation, both methods yield the same equations. In this work, we chose the weighted residuals approach. The complete computations and approximations required are detailed in annex F.

From this analysis, one obtains the expressions for θ and $\mathbf{u}$

$$\theta = \langle\theta\rangle(x,y,t)f_0(z) + \tilde{\vartheta}^{(1,2)}(x,y,t)f_2(z) \tag{8.8a}$$

$$\mathbf{u} = \langle\mathbf{u}\rangle(x,y,t)g_0(z) + \tilde{\mathbf{a}}^{(1,2)}(x,y,t)g_2(z) + \tilde{\mathbf{a}}^{(1,4)}(x,y,t)g_4(z) \tag{8.8b}$$

in terms of the transversally averaged fields $\langle\theta\rangle$, and $\langle\mathbf{u}\rangle$, as well as the inertial correction terms $\tilde{\vartheta}^{(1,2)}$, $\tilde{a}_i^{(1,2)}$, and $\tilde{a}_i^{(1,4)}$. The functions $f_0(z) = 1$ and $g_0(z) = \frac{3}{2}(1 - (\frac{z}{\varepsilon})^2)$ are given by the solution of the zeroth-order formulation and functions $f_2(z)$, $f_2(z)$, $g_2(z)$, and $g_4(z)$ are the following polynomial functions

$$f_2(z) = \frac{1}{60}(7 - 30(z/\varepsilon)^2 + 15(z/\varepsilon)^4) \tag{8.9a}$$

$$g_0(z) = \frac{3}{2}(1 - (z/\varepsilon)^2) \tag{8.9b}$$

$$g_2(z) = -\frac{1}{8}(7 - 21(z/\varepsilon)^2 + 35(z/\varepsilon)^4) \tag{8.9c}$$

$$g_4(z) = \frac{1}{16}(11 - 165(z/\varepsilon)^2 + 385(z/\varepsilon)^4 - 231(z/\varepsilon)^6) \tag{8.9d}$$

The amplitude of the inertial correction term for the temperature field is expressed by

$$\tilde{\vartheta}^{(1,2)} = -\frac{\varepsilon^2\mathrm{Ra}^{0.5}}{2}\left[\langle\mathbf{u}\rangle \cdot \nabla_{\mathrm{xy}}\langle\theta\rangle\right] \tag{8.10a}$$

while the amplitudes of the corrections for the velocity field read as follows

$$\tilde{\mathbf{a}}^{(1,2)} = -\frac{\varepsilon^2\mathrm{Ra}^{0.5}}{42\mathrm{Pr}}\left[\nabla_{\mathrm{xy}}p + \lambda_1\langle\mathbf{u}\rangle - \mathrm{Pr}\langle\theta\rangle\mathbf{e}_y\right] \tag{8.10b}$$

$$+ \frac{\varepsilon^2\mathrm{Ra}^{0.5}}{49\mathrm{Pr}}\left[\langle\mathbf{u}\rangle \cdot \nabla_{\mathrm{xy}}\langle\mathbf{u}\rangle\right] + \frac{2\varepsilon^4\mathrm{Ra}}{735}\left[\langle\mathbf{u}\rangle \cdot \nabla_{\mathrm{xy}}\langle\theta\rangle\right]\mathbf{e}_y$$

$$\tilde{\mathbf{a}}^{(1,4)} = -\frac{2\varepsilon^2\mathrm{Ra}^{0.5}}{385\mathrm{Pr}}\left[\langle\mathbf{u}\rangle \cdot \nabla_{\mathrm{xy}}\langle\mathbf{u}\rangle\right] + \frac{\varepsilon^4\mathrm{Ra}}{3465}\left[\langle\mathbf{u}\rangle \cdot \nabla_{\mathrm{xy}}\langle\theta\rangle\right]\mathbf{e}_y \tag{8.10c}$$

In this second model, the transversally averaged fields $\langle\theta\rangle$ and $\langle\mathbf{u}\rangle$ satisfy the following

dynamical equations

$$\nabla_{\text{xy}} \cdot \langle \mathbf{u} \rangle = 0 \tag{8.11a}$$

$$\frac{6}{5}\partial_t \langle \mathbf{u} \rangle + \frac{54}{35}\langle \mathbf{u} \rangle \cdot \nabla_{\text{xy}}\langle \mathbf{u} \rangle = -\nabla_{\text{xy}}\text{p} + \frac{6}{5}\text{PrRa}^{-0.5}\nabla_{\text{xy}}^2\langle \mathbf{u} \rangle - \lambda_1\langle \mathbf{u} \rangle$$

$$+ \text{ Pr}\left[\langle \theta \rangle - \frac{1}{\lambda_2}\langle \mathbf{u} \rangle \cdot \nabla_{\text{xy}}\langle \theta \rangle\right]\mathbf{e}_y \tag{8.11b}$$

$$\partial_t\langle \theta \rangle + \langle \mathbf{u} \rangle \cdot \nabla_{\text{xy}}\langle \theta \rangle = \text{Ra}^{-0.5}\nabla_{\text{xy}}^2\langle \theta \rangle \tag{8.11c}$$

with $\nabla_{\text{xy}} = \mathbf{e}_x\partial_x + \mathbf{e}_y\partial_y$, and λ_1 being the same friction coefficient (8.6) as in the previous model and λ_2 being a correction coefficient for the buoyancy term

$$\lambda_2 = \frac{105}{2\varepsilon^2}\text{Ra}^{-0.5} \tag{8.12}$$

This expression resembles equations (8.5a) to (8.5c) but with different coefficients and one supplementary correction term for the buoyancy force.

Once again, in order to be able to compare results from the model against the DNS, it is convenient to find an expression for the viscous and thermal energy dissipation rates that are consistent with the model with inertial corrections.

$$\epsilon = \frac{6}{5}\langle \nabla_{\text{xy}}\langle \mathbf{u} \rangle : \nabla_{\text{xy}}\langle \mathbf{u} \rangle \rangle_{\text{xy}} - \frac{2}{5}\langle \nabla_{\text{xy}}\langle \mathbf{u} \rangle : \nabla_{\text{xy}}\tilde{\mathbf{a}}^{(1,2)} \rangle_{\text{xy}} + \frac{3}{\varepsilon^2}\langle \langle \mathbf{u} \rangle \cdot \langle \mathbf{u} \rangle \rangle_{\text{xy}} \tag{8.13a}$$

$$\epsilon_\theta = \langle \nabla_{\text{xy}}\langle \theta \rangle \cdot \nabla_{\text{xy}}\langle \theta \rangle \rangle_{\text{xy}} \tag{8.13b}$$

8.3 Comparison between the 2-D models and the DNS

8.3.1 Plume dynamics using the reduced (2-D) models

It is important to determine whether the reduced models are able to reproduce the main features of the large-scale flow described in the 3-D DNS for $1/64 \leq \Gamma_z \leq 1/8$. As seen in chapter 7, the confined Rayleigh-Bénard system may posses multiple stable states with different dynamics for some aspect ratios. In order to facilitate the comparison, both models use the same initial condition, which is obtained by averaging the initial condition of the DNS along the transversal direction. The system is let evolve for several hundreds of convective time units before taking any measurements. Figure 8.1 displays one snapshot of the reference height field $\langle y_r \rangle(x, y, t)$ obtained from the reduced model (top), the model with inertial corrections (middle) and from 3-D DNS (bottom) for $(\text{Ra} = 10^7, \text{Pr} = 4.38)$ and different aspect ratio Γ_z. The sequence from left to right shows that the laminarization of the flow observed in the DNS when Γ_z is decreased, is reproduced correctly by both models.

For the least confined geometry $\Gamma_z = 1/8$ (figure 8.1a), the fields already display some of the elements of the DNS: the presence of plumes along the side-walls and a single central plume spanning the height of the cavity. However, both models fail to recover the periodic sweeping motion of the central plume observed in the DNS, returning a chaotic solution with no dominant frequency instead (figure 8.2a). For $\Gamma_z \leq 1/16$ (figures 8.2b to 8.2d) both models are able to reproduce both the size, height and shape of thermal plumes. The
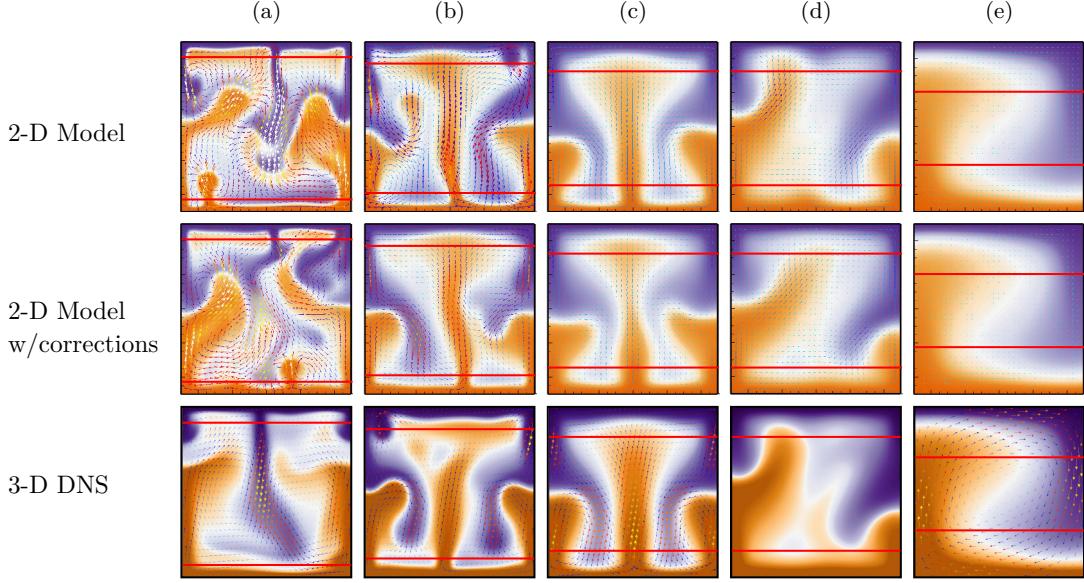
Figure 8.1: Comparison of the reduced model, the model with inertial corrections, and DNS results for $\mathrm{Ra} = 10^7$ and $\mathrm{Pr} = 4.38$. Instantaneous reference height field $\langle y_r \rangle (x, y, t)$ for different Γ_z: (a) $\Gamma_z = 1/8$, (b) $\Gamma_z = 1/16$, (c) $\Gamma_z = 1/32$ almost periodic state with central plume, (d) $\Gamma_z = 1/32$ almost periodic state without central plume, and (e) $\Gamma_z = 1/64$ steady state.

'flapping' motion of side-plumes is now recovered and the time-frequency spectra of $\mathrm{Nu_{vol}}$ is in good agreement with the DNS. For $\Gamma_z = 1/32$, the models recover the multi-state character of the DNS presented in the previous chapter: one almost periodic state with a central plume where the side-wall plumes movements are in-phase (figure 8.2c) and one almost periodic solution without central plume where the side-wall plumes movements are out-of-phase (figure 8.2d). The models also recover the same dominant frequency as the DNS ($f = 0.025$) in both cases (figures 8.2c and 8.2d). For the most confined geometry $\Gamma_z = 1/64$ (figure 8.1e), results from the models are nearly indistinguishable from the DNS.

Figures 8.3a to 8.3d display a sequence of snapshots of the reference height field $\langle y_r \rangle (x, y, t)$ for $(\Gamma_z = 1/64, \mathrm{Pr} = 4.38)$ and different values of Ra. Each sequence from left to right is
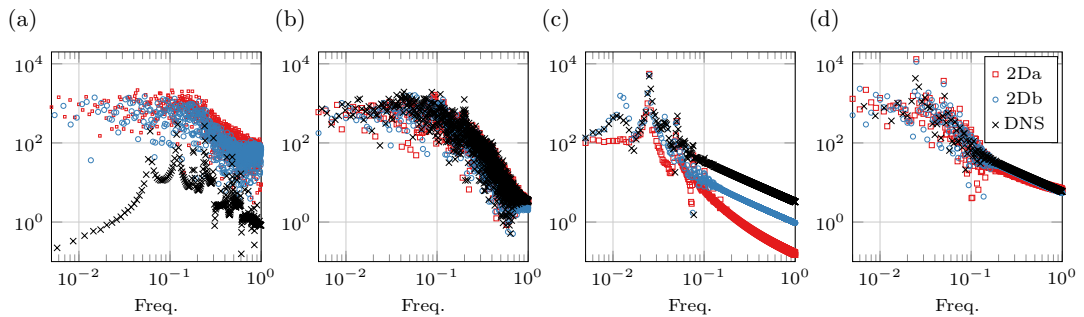
Figure 8.2: Comparison of reduced and DNS for $\mathrm{Ra} = 10^7$ and $\mathrm{Pr} = 4.38$: Time-frequency spectra of $\mathrm{Nu_{vol}}$. Reduced model in red, model with inertial corrections in blue, and DNS in black. (a) $\Gamma_z = 1/8$, (b) $\Gamma_z = 1/16$, (c) $\Gamma_z = 1/32$ almost periodic state with central plume, (d) $\Gamma_z = 1/32$ almost periodic state without central plume.

(a) Ra $= 5 \cdot 10^7, \Gamma_z = 1/64$

(b) Ra $= 10^8, \Gamma_z = 1/64$

(c) Ra $= 2 \cdot 10^8, \Gamma_z = 1/64$
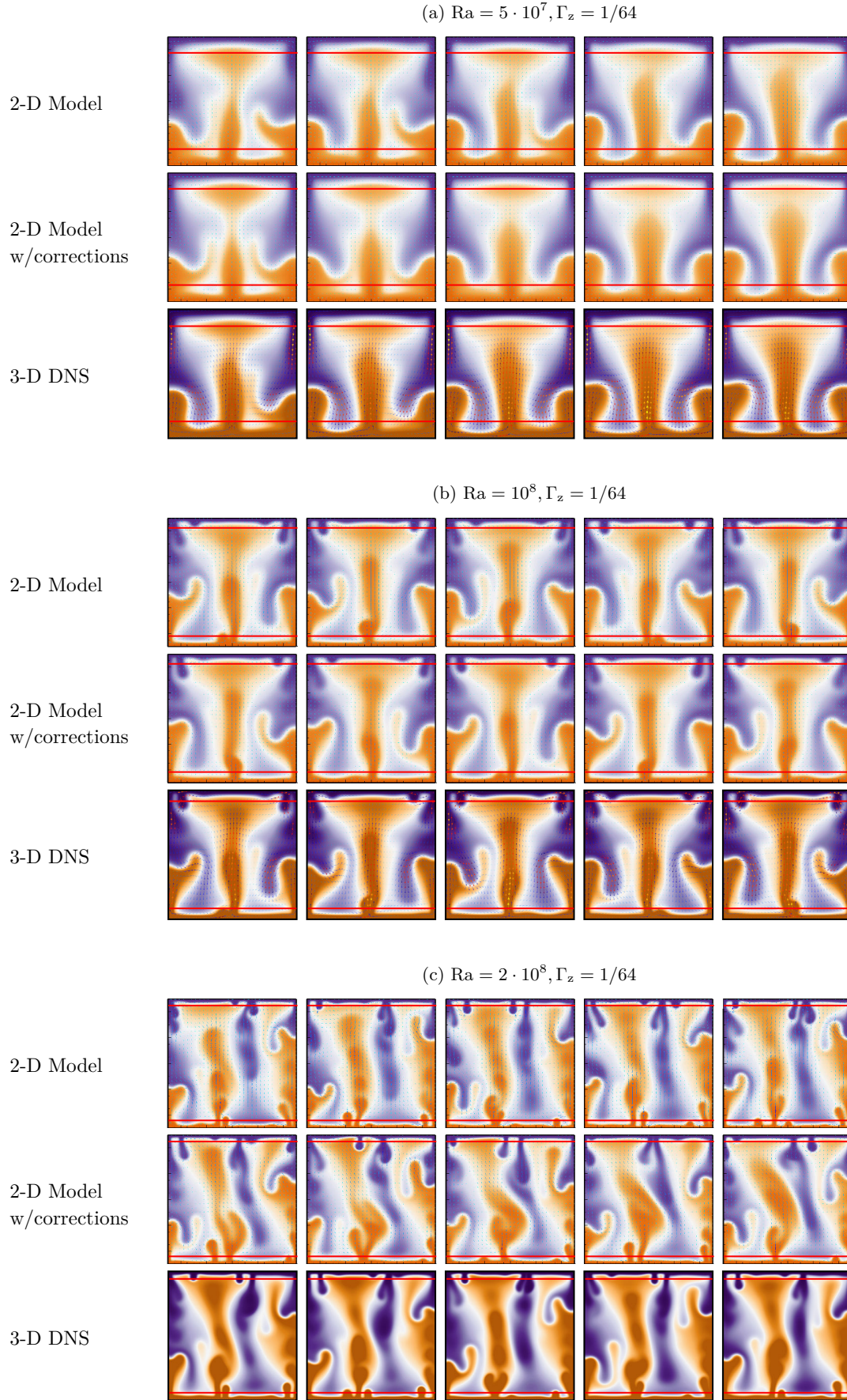
Figure 8.3: Comparison of the reduced model, the model with inertial corrections, and DNS results for $\Gamma_z = 1/64$ and Pr $= 4.38$. Instantaneous reference height field $\langle y_r \rangle (x, y, t)$ for different Ra. The sequence from left to right is taken at the same regular time intervals.

(d) $\mathrm{Ra} = 10^9, \Gamma_z = 1/64$
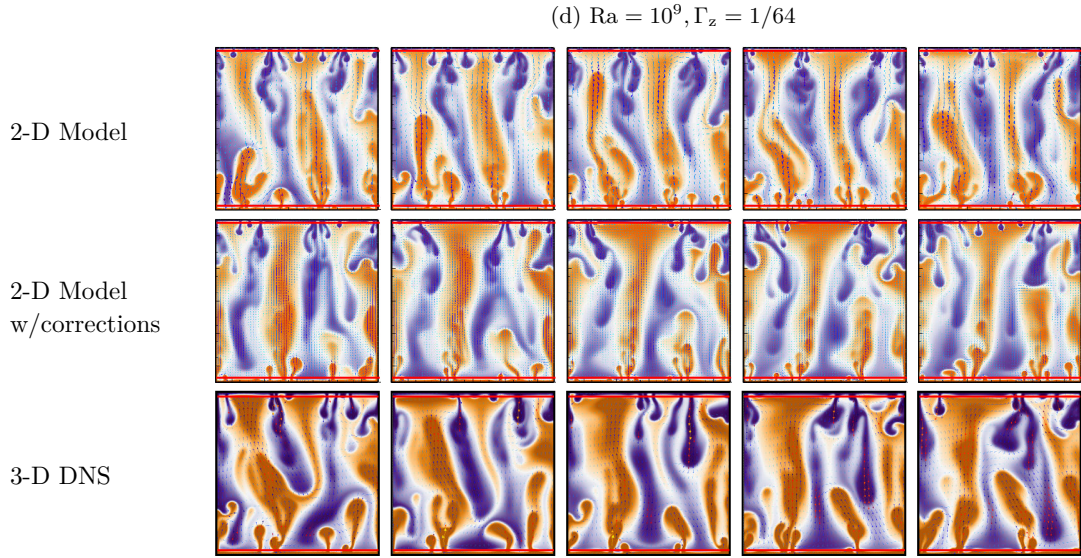
Figure 8.3: Continues from previous page.
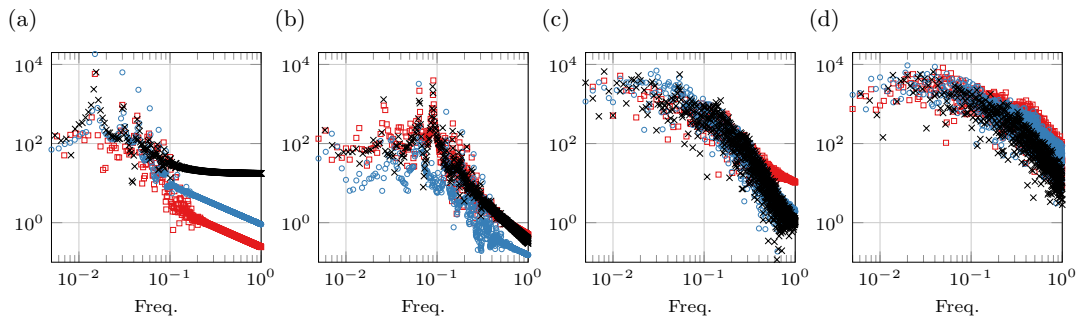
Figure 8.4: Comparison of reduced and DNS for $\Gamma_z = 1/64$ and $\mathrm{Pr} = 4.38$: Time-frequency spectra of $\mathrm{Nu_{vol}}$. Reduced model in red, model with inertial corrections in blue, and DNS in black. (a) $\mathrm{Ra} = 5 \cdot 10^7$, (b) $\mathrm{Ra} = 10^8$, (c) $\mathrm{Ra} = 2 \cdot 10^8$, (d) $\mathrm{Ra} = 10^9$.
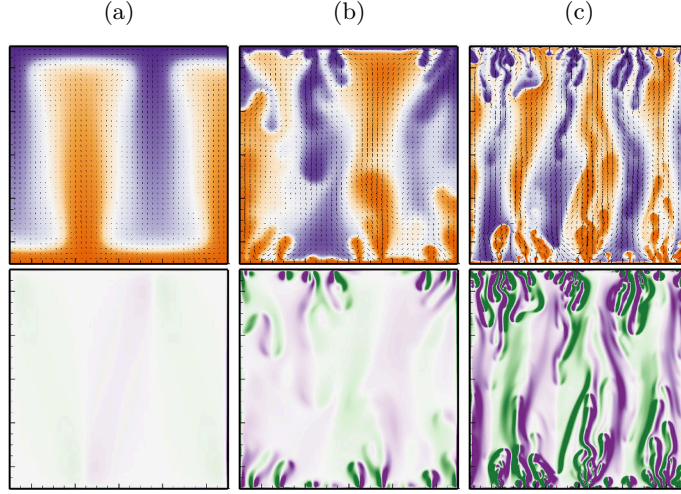
Figure 8.5: Instantaneous reference height field $\langle y_r \rangle (x, y, t)$ (top) and vorticity field $\langle \omega_z \rangle (x, y, t)$ (bottom) obtained using the model with inertial corrections for Pr = 4.38, $\Gamma_z = 1/128$ and: (a) Ra = 10^8, (b) Ra = 10^9, and (c) Ra = 10^{10}. The color map for the vorticity corresponds to the interval $[-1, 1]$. For comparison see Chong and Xia, 2016.

taken at consecutive times every 5 convective units in order to give a sense of the plumes motion. The same type of flow dynamics is recovered in each case.

The configuration with two stable central plumes (one ascending, one descending) displayed on figure 8.3c for Ra = $2 \cdot 10^8$ was initially obtained using the reduced model. We wanted to check if such solution indeed existed for the DNS and the model with inertial corrections. For the DNS we reconstructed the primitive initial fields using instantaneous fields obtained from the model and assuming a constant temperature profile and a parabolic profile for the velocity. For the model with inertial corrections, we used the same instantaneous fields as initial conditions. Both simulations were let evolve for several hundreds of convective time units. In each case, the same configuration was retrieved. This shows that the models can be used to help exploring the parameter space. However, one should be aware that the type of solutions obtained by both models is limited to symmetric solutions with respect to z. Both models are qualitatively well suited to recover the main features of the large-scale flow for the most confined configuration ($\Gamma_z = 1/64$). In the following section, we attempt to perform a quantitative comparison for this value of Γ_z.

Let us end with a side note: the approximate size and shape of the thermal structures presented in figure 8.5 for $\Gamma_z = 1/128$ are in good agreement with the instantaneous fields taken at the vertical mid-plane displayed in figures 5(g) to 5(i) of Chong and Xia, 2016.

8.3.2 Number of plumes and average plume width with the reduced models

As seen on figures 8.3, for the most confined cell ($\Gamma_z = 1/64$), the number, shape, and size of the thermal structures are consistent to the DNS. For Ra = $5 \cdot 10^7$ and Ra = 10^8 a persistent configuration is observed with three ascending (a central plume and the side-wall plumes) and two descending channels. For Ra = $2 \cdot 10^8$ one observes three ascending
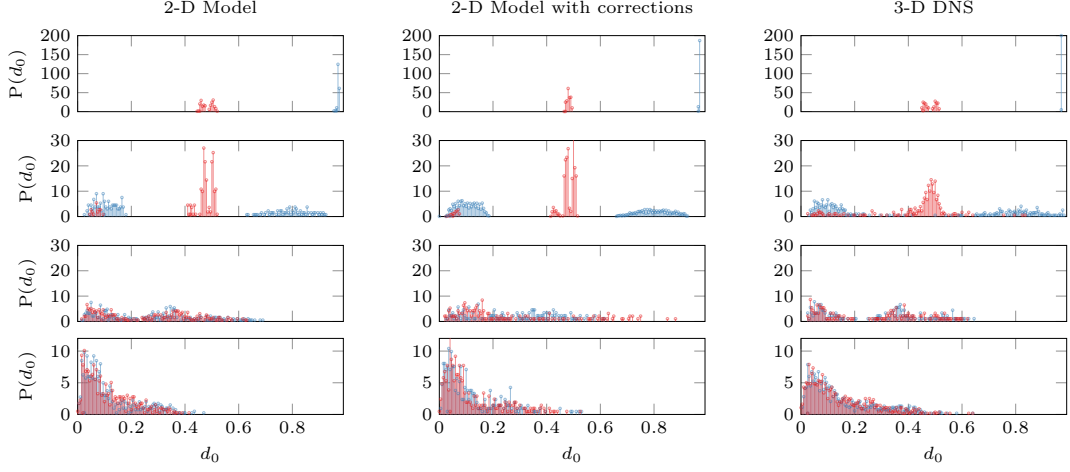
Figure 8.6: Comparison of the 2-D models against DNS results. Probability distribution of the inter-plume distance d_0 measured near the top (blue) and bottom (red) boundary layers for $\mathrm{Pr} = 4.38$ and $\Gamma_z = 1/64$. From top to bottom: $\mathrm{Ra} = 5 \cdot 10^7$, $\mathrm{Ra} = 10^8$, $\mathrm{Ra} = 2 \cdot 10^8$ and $\mathrm{Ra} = 10^9$.

and three descending channels; for $\mathrm{Ra} = 10^9$ more channels are observed.

To quantify this aspect, the probability distribution of the inter-plume distance d_0 is compared for the two models and the DNS in figure 8.6, and the mean spatial auto-correlation of the vertical heat-flux in figure 8.7. Both quantities are in good agreement with the DNS for up to $\mathrm{Ra} \leq 2 \cdot 10^8$. For $\mathrm{Ra} = 10^9$ the correlation distance r_0 and the integral length scale $\mathcal{L}_0$ are underestimated by as much as 15%.

8.3.3   Mean vertical profiles

To illustrate the range of validity in Ra of the models, figures 8.8a to 8.8d display different vertical profiles for $(\Gamma_z = 1/64, \mathrm{Pr} = 4.38)$. Profiles associated to the temperature correspond to mean temperature $\langle \bar{\theta} \rangle_{\mathrm{xz}}$, spatio-temporal fluctuations of the temperature $\langle \theta \rangle_{\mathrm{xz}}^{\overline{\mathrm{rms}}}$, and plane- and time-averaged thermal dissipation $\langle \overline{\partial_j \theta \partial_j \theta} \rangle_{\mathrm{xz}}$, whereas the profiles associated to the velocity field correspond to the (spatio-temporal) fluctuations of the horizontal and vertical velocities, $\langle u \rangle_{\mathrm{xz}}^{\overline{\mathrm{rms}}}$ and $\langle v \rangle_{\mathrm{xz}}^{\overline{\mathrm{rms}}}$ respectively, and to the plane- and time-averaged viscous dissipation $\langle \overline{\partial_j u_i \partial_j u_i} \rangle_{\mathrm{xz}}$.

The reduced model is able to recover the shape of the vertical profiles of the DNS. When using the model with inertial corrections, these results slightly improve for $\mathrm{Ra} \leq 2 \cdot 10^8$ (figures 8.8a to 8.8c). The most visible change being in the viscous dissipation profile near the top and bottom plates, where the reduced model predicts a peak in dissipation not seen on the DNS. For the model with inertial corrections, the position of the peak values in $\langle \theta \rangle_{\mathrm{xz}}^{\overline{\mathrm{rms}}}$ (resp. $\langle u \rangle_{\mathrm{xz}}^{\overline{\mathrm{rms}}}$) close to the top and bottom plates is in good agreement with the DNS. These profiles are used to estimate the thickness of the thermal (resp. kinetic) boundary layers. For the higher Ra ($\mathrm{Ra} = 10^9$), deviations from the DNS become noticeable, but both models still manage to recover the correct orders of magnitude and the approximate shapes (see figure 8.8d).

(a) Ra = $5 \cdot 10^7$ (b) Ra = 10^8 (c) Ra = $2 \cdot 10^8$ (d) Ra = 10^9
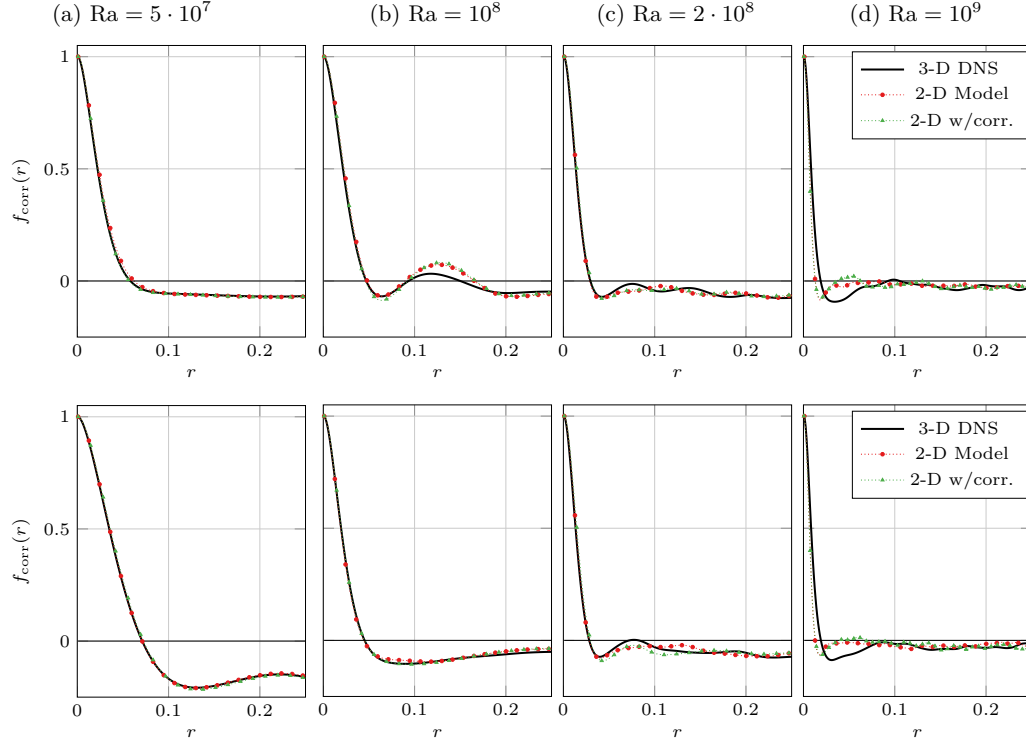
Figure 8.7: Comparison of the 2-D models against DNS results. The top (resp. bottom) row displays the spatial auto-correlation function measured near the upper (resp. lower) boundary layers for Pr = 4.38, $\Gamma_z = 1/64$, and different Ra.

8.3.4   Average Nusselt and Reynolds numbers

The last comparison concerns the time-averaged Nusselt (see §2.50) and time-averaged Reynolds number (see equation (7.6)) for different Γ_z. For the DNS, the time-averaged Nusselt $\overline{\text{Nu}}_{\text{ref}}$, its maximum relative difference %Diff were evaluated in the previous chapter (see table 7.1), and the time-averaged Reynolds number $\overline{\text{Re}}_{\text{ref}}$ is shown in figure 7.17. For the reduced models, we evaluate $\overline{\text{Nu}}_{\text{vol}}$, $\overline{\text{Nu}}_{\text{top}}$, $\overline{\text{Nu}}_{\text{bot}}$, $\overline{\text{Nu}}_\epsilon$, and $\overline{\text{Nu}}_\theta$ and compute again their average value $\overline{\text{Nu}}$ and maximum relative difference %Diff. A time-averaged Reynolds number based on the root mean squared velocity $\overline{\text{Re}}$ is also evaluated. For the 'simple' model, the expressions required to compute these quantities are (8.7a) and (8.7b). For the model with inertial corrections, these expressions are detailed in annex F. In particular, the Reynolds number is obtained using equation (F.44). The accuracy of the models is quantified by %Error($\overline{\text{Nu}}$) (resp. %Error($\overline{\text{Re}}$)) as the deviation from the reference Nusselt $\overline{\text{Nu}}_{\text{ref}}$ (resp. Reynolds $\overline{\text{Re}}_{\text{ref}}$) obtained from 3-D DNS results.

$$\%\text{Error}(\overline{\text{Nu}}) = (\overline{\text{Nu}} - \overline{\text{Nu}}_{\text{ref}})/\overline{\text{Nu}}_{\text{ref}} \times 100 \tag{8.14}$$

$$\%\text{Error}(\overline{\text{Re}}) = (\overline{\text{Re}} - \overline{\text{Re}}_{\text{ref}})/\overline{\text{Re}}_{\text{ref}} \times 100 \tag{8.15}$$

A good convergence in $\overline{\text{Nu}}$ for the models, often coincides with small deviations from the reference results obtained by the DNS (see table 8.1 and 8.2). Inside the range of validity of the models, both models recover the main features of the confined regime, dominated by large-scale coherent plumes and the Nusselt and Reynolds numbers are estimated within a few percent (see tables 8.1 and 8.2) which implies similar scaling laws as the DNS for these configurations.
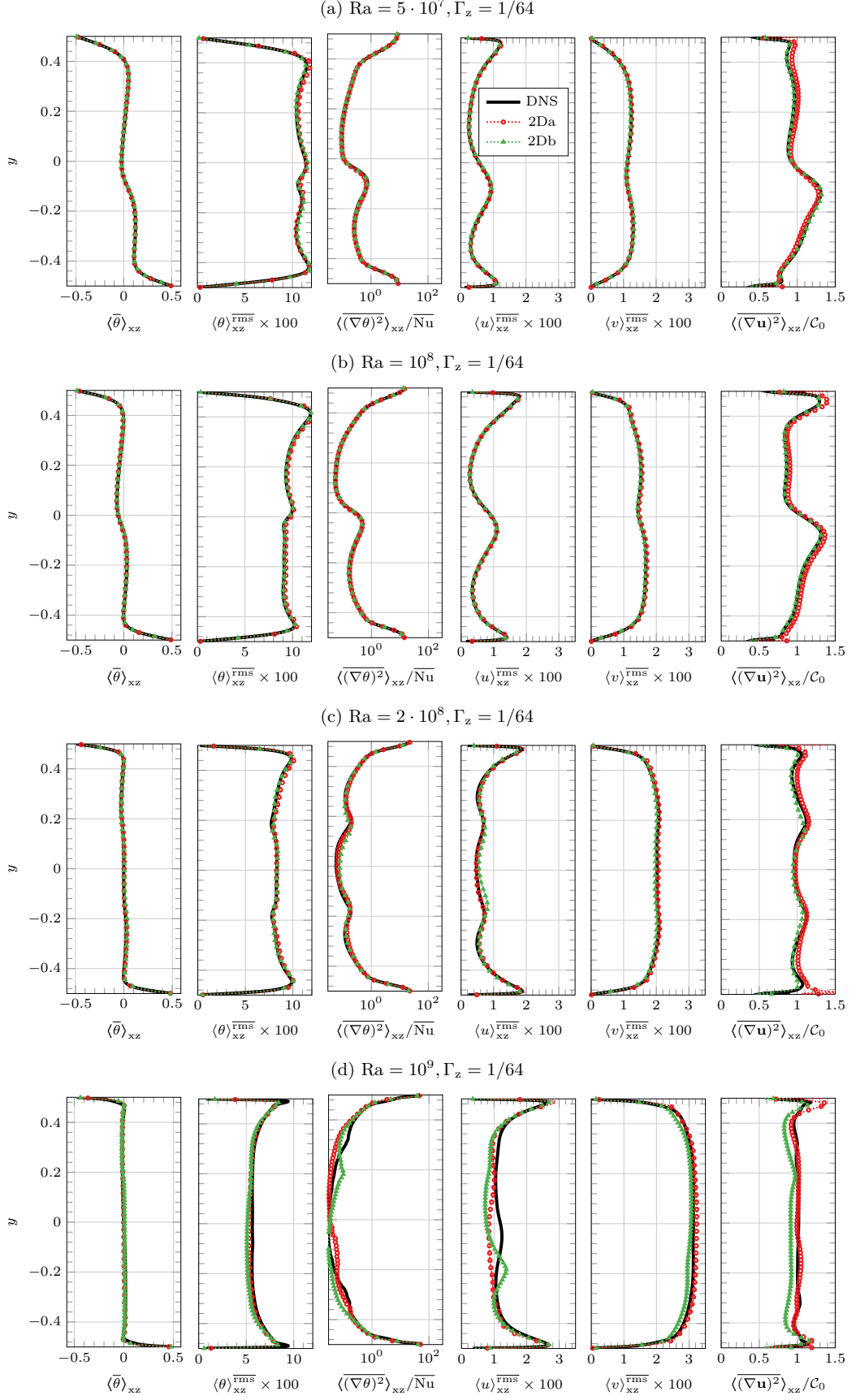
Figure 8.8: Comparison of the vertical profiles for DNS results (solid lines), reduced model (● marks), and model with inertial corrections (▲ marks) for ($\Gamma_z = 1/64, \mathrm{Pr} = 4.38$) and different Ra. From left to right: temperature, RMS temperature, thermal dissipation, RMS velocities and viscous dissipation. Here $\mathcal{C}_0 = \overline{\mathrm{Nu}} - 1$.

Ra	Γ_z	Average Nusselt $\overline{\mathrm{Nu}}$			%Diff		%Error($\overline{\mathrm{Nu}}$)	
		model	w/corr	3D DNS	model	w/corr	model	w/corr
$1 \cdot 10^7$	1/16	10.10	9.36	9.41	3.1	10.6	7.3	0.5
$5 \cdot 10^7$	1/16	19.32	18.81	22.68	6.0	35.8	14.8	17.0
$1 \cdot 10^8$	1/16	24.70	34.42	29.32	8.7	209.2	15.8	-
$1 \cdot 10^7$	1/32	6.39	6.19	6.52	1.3	2.8	2.0	5.0
$5 \cdot 10^7$	1/32	15.28	14.06	14.46	1.9	4.9	5.7	2. 7
$1 \cdot 10^8$	1/32	21.51	19.58	19.88	3.0	7.0	8.2	1.5
$1 \cdot 10^9$	1/32	49.64	87.48	61.69	23.0	381.0	19.5	-
$1 \cdot 10^7$	1/64†	3.69	3.65	3.68	0.2	0.7	0.2	0.8
$5 \cdot 10^7$	1/64	7.97	7.73	7.91	1.1	1.5	0.8	2.3
$1 \cdot 10^8$	1/64	13.02	12.45	12.57	0.6	1.6	3.6	0.9
$2 \cdot 10^8$	1/64	20.26	19.02	19.38	1.6	2.2	4.5	1.8
$1 \cdot 10^9$	1/64	46.55	42.32	46.57	6.9	6.4	0.1	9.1

Table 8.1: Time-averaged Nusselt number and the maximum relative difference between definitions of the Nusselt number %Diff for the reduced models using a 512^2 grid. Measurements are obtained over 1,000 convective time units. Results from the DNS is noted here as $\overline{\mathrm{Nu}}_{\mathrm{ref}}$, while the deviation from the DNS is noted as %Error($\overline{\mathrm{Nu}}$). A † indicates steady-state solutions.

There are incremental improvements when using the model with inertial corrections, most notably on the average Reynolds number and the viscous dissipation but also on the fluctuation profiles. In the following, we only consider results from the model with inertial corrections.

8.4 Using the reduced model with inertial corrections to explore the confined regime

One may use the reduced model with inertial corrections to study the long term evolution of the large-scale flow in order to characterize flow reversals in the confined regime. To illustrate the feasibility of such studies, we perform simulations using a 512^2 grid for $(\Gamma_z = 1/16, \mathrm{Ra} = 2 \cdot 10^7, \mathrm{Pr} = 4.38)$. A flow reversal was observed for this configuration using 3-D DNS in section 7.3.2. The initial condition for the reduced model corresponds to instantaneous fields obtained from the DNS which are averaged over the transversal direction. The system was then evolved for over 35,000 convective time units: several disruptions of the large-scale flow were observed, in particular 4 flow reversals. Each reversal is indicated in the time series (figure 8.9) by marks (i) to (iv). The average time interval between reversals is about 8,500 convective time units. Let us compare figures 8.9 and 7.8. In both cases, a sign switch in the Fourier coefficients of the horizontal velocity $\hat{u}_{1,2}$ and $\hat{u}_{1,4}$ indicates the presence of a flow reversal. The odd Fourier modes $\hat{u}_{1,1}$ and $\hat{u}_{1,3}$ oscillate around zero, and even mode $\hat{u}_{2,2}$ is mostly positive, while fluctuation in both modes are increased during the re-organization periods, consistent with observations from section 7.3.2.

Longer observations may be obtained from the reduced model, which allow us to compute different quantities, such as the probability distributions for each modal coefficient. Note

		Average Reynolds $\overline{\text{Re}}$			%Error($\overline{\text{Re}}$)	
Ra	Γ_z	model	w/corr	3D DNS	model	w/corr
$1 \cdot 10^7$	1/16	36.01	37.29	37.73	4.6	1.2
$5 \cdot 10^7$	1/16	111.04	113.35	123.89	10.4	8.5
$1 \cdot 10^8$	1/16	176.46	187.45	194.19	9.1	3.5
$1 \cdot 10^7$	1/32	14.66	15.70	16.25	9.8	3.4
$5 \cdot 10^7$	1/32	53.05	55.22	56.17	5.6	1.7
$1 \cdot 10^8$	1/32	89.09	91.89	92.50	3.7	0.7
$1 \cdot 10^9$	1/32	429.44	465.43	496.67	13.5	6.3
$1 \cdot 10^7$	1/64†	5.30	5.76	5.80	8.6	0.7
$5 \cdot 10^7$	1/64	18.96	20.35	20.57	7.8	1.1
$1 \cdot 10^8$	1/64	35.25	37.62	37.91	7.0	0.8
$2 \cdot 10^8$	1/64	62.94	66.40	67.45	6.7	1.6
$1 \cdot 10^9$	1/64	215.91	222.04	233.96	7.7	5.1

Table 8.2: Time-averaged Reynolds number for the reduced models using a 512^2 grid. Measurements are obtained over 1,000 convective time units. Results from the DNS is noted here as $\overline{\text{Re}}_{\text{ref}}$, while the deviation from the DNS is noted as %Error($\overline{\text{Re}}$). A † indicates steady-state solutions.
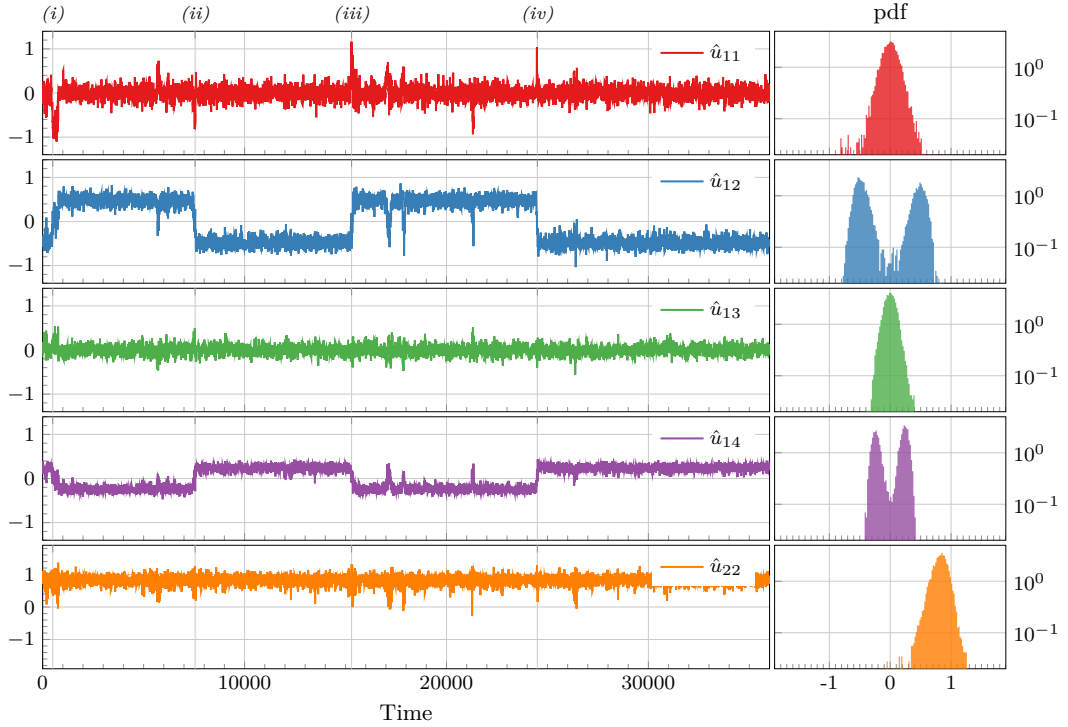
Figure 8.9: Flow reversals obtained using the model with inertial corrections for $\Gamma_z = 1/16$, Ra $= 2 \cdot 10^7$ and Pr $= 4.38$. Each reversal is indicated by a mark (i) to (iv). Time-series of the Fourier coefficients of the horizontal velocity $\hat{u}_{\text{pq}}$ (left) and corresponding probability density distributions (right). Modal coefficients are multiplied by a factor 10^2.
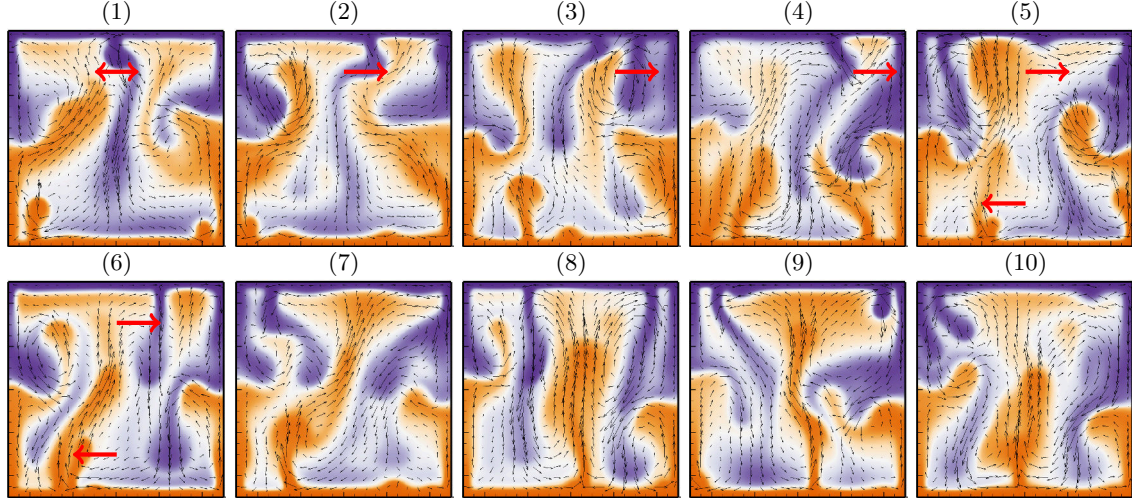
Figure 8.10: Flow reversal observed using the reduced model with inertial corrections for $\mathrm{Ra} = 2 \cdot 10^7$ and $\Gamma_z = 1/16$. Figure displays a sequence of snapshots of field $\langle y_r \rangle (x, y, t)$ superposed to the velocity vector field $\langle \mathbf{u} \rangle (x, y, t)$ during the flow reversal identified as (iv) in figure 8.9.

that, the odd-modes, $\hat{u}_{1,1}$ and $\hat{u}_{1,3}$, have a symmetric PDF, $\hat{u}_{1,2}$ and $\hat{u}_{1,4}$ display a bimodal PDF, and the PDF of $\hat{u}_{2,2}$ is skewed symmetric. The relation between the different modes might be related to the natural symmetries of the Rayleigh-Bénard cells, as in the pure 2-D case.

Figure 8.10 displays a sequence of snapshots describes the evolution of the thermal structures during 100 convective units in which the reversal (iv) is observed. First, due to the action of the side-wall plumes, the central plume is displaced to the sides, thus allowing a second plume to appear (figures 8.10(1) to 8.10(4)). Instead of changing directions and plunging against the left wall, like in the reversal described in figure 7.8, both plumes continue their motion and merge into the right side-wall plume (figure 8.10(5)). Then, ascending and descending plumes form simultaneously (figures 8.10(6) to 8.10(8)) and co-exist until one becomes dominant (figures 8.10(9) to 8.10(10)). Reversals (i) to (iii) follow a similar process, although some variations, like the direction of the plumes motion and the duration of the reversal are observed. Despite these differences, the sequence is considered as representative of the ensemble of flow reversals observed. Our observations suggests the driving force behind flow reversals to be the interaction between the large-scale plumes along the side-walls and near the center of the cavity, consistent with previous observations from DNS results.

In this sense, the model appears to be well adapted for the study the long-term evolution of the large-scale flow. Exploration of the parameter space is required in order to identify a configuration with more frequent reversals in order to verify these observations.

8.5 Scaling exponents of the Nusselt and Reynolds numbers in the severely confined regime

One may use the reduced models with inertial corrections to perform simulations for very small values of Γ_z focusing on the Nusselt and Reynolds scaling exponents in the confined regime. Indeed, one interesting question raised by (Chong and Xia, 2016) concerns the evolution of these scaling exponents towards some asymptotic values. The use of such models could provide some insight on this question by considering values Γ_z which are difficult to access for fully resolved DNS. This is done in §8.5.2, but before we would like to introduce a theoretical prediction for the scaling exponents in the severely confined regime.

8.5.1 A theoretical approach to the scaling exponents in the severely confined regime

Scaling exponent for the Nusselt number

Let us revisit some central elements of Rayleigh-Bénard convection. Under a severe confinement, one may argue that characteristic velocity scales should differ those of equation (1.3): the velocity scale of the heat conduction and the momentum dissipation are based on the depth of the cavity d instead of the height H, while keeping the scale of the buoyancy unchanged

$$U'_{\text{cond}} = \frac{\kappa}{d} \qquad\qquad U'_{\text{visc}} = \frac{\nu}{d} \qquad\qquad U_{\text{buoy}} = \sqrt{\beta \Delta \mathrm{T} g H} \qquad (8.16)$$

Using the ratio between these velocities, we define a new dimensionless *Rayleigh* number

$$\mathrm{Ra_d} \equiv \frac{U_{\text{buoy}}^2}{U'_{\text{cond}} \, U'_{\text{visc}}} = \frac{\beta \Delta \mathrm{T} g H d^2}{\kappa \nu} \qquad (8.17)$$

which is related to the classical *Rayleigh* number as

$$\mathrm{Ra_d} = \Gamma_z^2 \mathrm{Ra} \qquad (8.18)$$

The parameter $\mathrm{Ra_d}$ is reminiscent of the *Darcy-Rayleigh* number used in convection inside fluid-saturated porous media, if the Darcy permeability coefficient (the square of a length scale characterizing the porous medium) is replaced by $\mathrm{K} \sim d^2$, where d is the depth of a Hele-Shaw cell (Nield and Bejan, 2013). The similarities between both systems can be seen in figure 8.11: the large-scale plumes observed in confined convection is analogous to the 'dripping' patterns observed in convection inside porous media (Otero et al., 2004).

In the classical Rayleigh-Bénard, Malkus' and Howard's arguments based on the marginal stability of the boundary layer lead to the classical $\beta_{\mathrm{Nu}-1} = 1/3$ exponent, see table 8.3. Using the same arguments[1], but considering a local $\mathrm{Ra_d}$ as the relevant control parameter

---

[1] This reasoning was already applied to obtain the ultimate regime of convection in porous media (Doering and Constantin, 1998; Otero et al., 2004; D. R. Hewitt, et al., 2012).
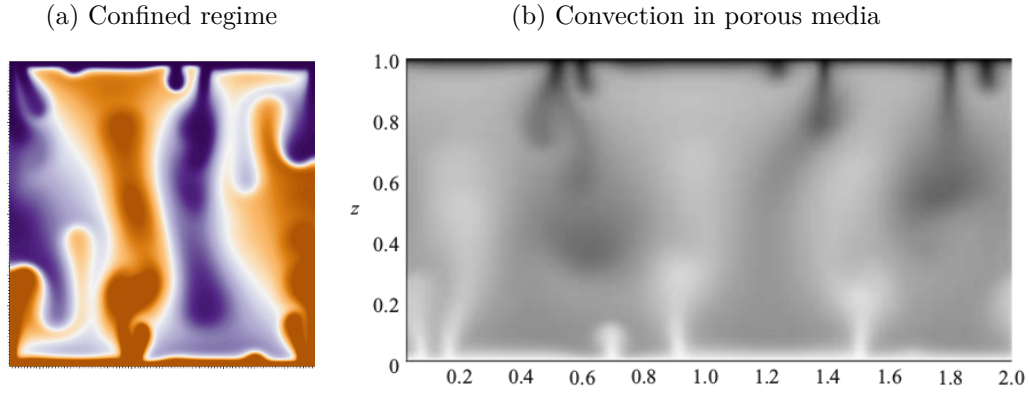
Figure 8.11: a) Snapshot of the reference height $y_r(x, y, 0, t)$ for Ra $= 2 \cdot 10^8$, Pr $= 4.38$, and $\Gamma_z = 1/64$. b) Snapshot of the temperature field for Ra$_d = 1581$ from 2-D Darcy–Oberbeck–Boussinesq equations. Image (b) is taken from (Otero et al., 2004).

Conventional convection	*Severe confinement*
$\delta_\theta = H/(2\overline{\mathrm{Nu}})$	$\delta_\theta = H/(2\overline{\mathrm{Nu}})$
where δ_θ is independent of H.	where δ_θ is independent of H.
$\dfrac{\beta \Delta \mathrm{T} g \delta_\theta^3}{\kappa \nu} = \left(\dfrac{\delta_\theta}{H}\right)^3 \mathrm{Ra} \sim 10^3$	$\dfrac{\beta \Delta \mathrm{T} g \delta_\theta d^2}{\kappa \nu} = \left(\dfrac{\delta_\theta}{H}\right) \mathrm{Ra}_d \sim 10^3$
$\overline{\mathrm{Nu}} \sim \mathrm{Ra}^{1/3}$	$\overline{\mathrm{Nu}} \sim \mathrm{Ra}_d = \Gamma_z^2 \mathrm{Ra}$

Table 8.3: Malkus' and Howard's theory applied to conventional convection (left) and convection under severe confinement (right). The latter is consistent with the ultimate regime in porous media.

instead of a local Ra, one gets (see table 8.3)

$$\overline{\mathrm{Nu}} \sim \mathrm{Ra_d} = \Gamma_z^2 \mathrm{Ra} \qquad\qquad \text{for } \Gamma_z \ll 1 \qquad (8.19)$$

hence $\beta_{\mathrm{Nu}-1} = 1$. This value is larger than the $\beta_{\mathrm{Nu}-1} = 0.872$ observed by (Bizon et al., 1997) and $\beta_{\mathrm{Nu}-1} = 0.61$ observed by (Chong and Xia, 2016).

Scaling exponent for the Reynolds number

The scaling exponent for the Reynolds number may be deduced by following the reasoning from Grossmann-Lohse (GL) scaling theory. The basic element of the GL theory are the exact relations for the viscous dissipation rates derived from the Boussinesq equations, $\bar{\epsilon} = (\overline{\mathrm{Nu}} - 1)$ (Shraiman and Siggia, 1990). This term is decomposed into contributions from the different boundary layers and the viscous bulk and estimates for each term are obtained from dimensional analysis.

Let us focus on the contributions from the kinetic boundary layers at the front and back walls. In the GL scaling theory, the contributions from the side-walls are estimated from dimensional analysis assuming a balance between the advective and viscous terms

$$\epsilon^{bl,w} \sim \frac{\overline{U}^2}{\delta_w^2} \left(\frac{\delta_w}{\Gamma_z} \right) \qquad\qquad (8.20)$$

with $\frac{\delta_w}{\Gamma_z}$ being the fraction of volume occupied by the kinetic boundary layers at the side-walls.

Using DNS results for the most confined cells $\Gamma_z = 1/32$ and $\Gamma_z = 1/64$, we measured the thickness of the kinetic boundary layer at the front and back walls δ_w and the relative contributions to the viscous dissipation from the region enclosing the boundary layers $\epsilon^{bl,w}$ (see table 7.6)

$$\delta_w = 0.211\Gamma_z \qquad\qquad \epsilon^{bl,w} = 0.807\,\bar{\epsilon} \qquad (8.21)$$

It is reminded that both values are consistent with a parabolic velocity profile in the transversal direction. Introducing equation (8.21) into (8.20)

$$0.807\,\bar{\epsilon} \sim \frac{\overline{U}^2}{\Gamma_z^2} \qquad\qquad \text{for } \Gamma_z \ll 1 \qquad (8.22)$$

Introducing equation (7.6) and the exact relation $\bar{\epsilon} = (\overline{\mathrm{Nu}} - 1)$ into (8.22) yields

$$(\overline{\mathrm{Nu}} - 1) = \bar{\epsilon} \sim \frac{\overline{\mathrm{Re}}^2 \mathrm{Pr}^2}{\Gamma_z^2 \mathrm{Ra}} \qquad\qquad (8.23)$$

Bizon et al., 1997 uses a balance between Hele-Shaw plume drag and buoyancy forces to obtain the same results. Note that equation 8.23 imposes a relation between the scaling exponents

$$\beta_{\mathrm{Re}} = (\beta_{\mathrm{Nu}-1} + 1)/2 \qquad\qquad (8.24)$$

Equation (8.23) is combined with (8.19) to obtain the following scaling for the Reynolds

(a) 3-D DNS			
Γ_z	β_{Nu-1}	β_{Re}	$\frac{\beta_{Nu-1}+1}{2}$
1/16	0.50	0.65	0.750
1/32	0.51	0.73	0.755
1/64	0.61	0.80	0.805

(b) Model with inertial corrections			
Γ_z	β_{Nu-1}	β_{Re}	$\frac{\beta_{Nu-1}+1}{2}$
1/16	0.456	0.692	0.728
1/32	0.511	0.728	0.755
1/64	0.565	0.763	0.782
1/128	0.616	0.791	0.808
1/192	0.613	0.789	0.806
1/256	0.617	0.795	0.808

Table 8.4: Scaling coefficients obtained from (a) 3-D DNS and (b) model with inertial corrections.

number

$$\overline{Re} \sim \frac{\Gamma_z^2 Ra}{Pr} \qquad \text{and} \qquad \text{for } \Gamma_z \ll 1 \qquad (8.25)$$

This leads to the theoretical exponents $\beta_{Nu-1} = \beta_{Re} = 1$, which are not identical but closer to the values $\beta_{Nu-1} = 0.872$ and $\beta_{Re} = 0.96$ obtained by (Bizon et al., 1997) for $\Gamma_z = 1/240$ using stress-free boundaries. In order to verify if such scaling may be observed, we perform simulations from reduced model with inertial corrections for up to $\Gamma_z = 1/256$.

8.5.2 Scaling exponents in the severely confined regime using the reduced model with inertial corrections

We compute scaling exponents obtained from simulations of the reduced model with inertial corrections for $\Gamma_z < 1/16$, see table 8.4. Since the kinetic boundary layer thickness is comparable to Γ_z, this value becomes a limiting factor for these simulations. Here, we use a 1024^2 grid for $\Gamma_z = 1/64$, $\Gamma_z = 1/128$, $\Gamma_z = 1/192$, and $\Gamma_z = 1/256$

Figures 8.12a and 8.12b display the compensated Nusselt and Reynolds numbers as function of Ra for different Γ_z from 1/16 to 1/256. Fitted scaling exponents (see table 8.4) are comparable to those obtained from DNS results and to published results (Chong and Xia, 2016): $\beta_{Nu-1} = 0.61$ and $\beta_{Nu-1} = 0.80$ for $\Gamma_z = 1/128$. The relation between the scaling exponents (8.24) also appears to be verified for the most confined cells ($\Gamma_z < 1/32$) in both the DNS and the model. However, a close inspection of figure 8.12 for the more confined cells $\Gamma_z < 1/128$, suggests there is a change of slope. This change is seen in a compensated plot when represented as function of Ra/Ra* (see figure 8.13), where we introduce $1/Ra^* = 1.85 \cdot 10^{-5}\Gamma_z^{3.23}$ as proposed by (Chong and Xia, 2016) to collapse our data.

A first group which corresponds to Ra/Ra* < 0.005 and $\overline{Nu} > 5$ exhibits $\beta_{Nu-1} = 0.82$ and $\beta_{Re} = 0.91$ (dashed red lines in figure 8.13). These scaling exponents are consistent with equation (8.24). A second group which corresponds to Ra/Ra* > 0.005 yields the scaling exponents $\beta_{Nu-1} = 0.44$ and $\beta_{Re} = 0.69$ (dashed green lines in figure 8.13). In contrast, these exponents do not verify equation (8.24). A third group of outliers corresponds to points with $\overline{Nu} < 5$ and Ra/Ra* < 0.005.

The change in slope of the Nusselt and Reynolds numbers observed around Ra/Ra* $\sim$
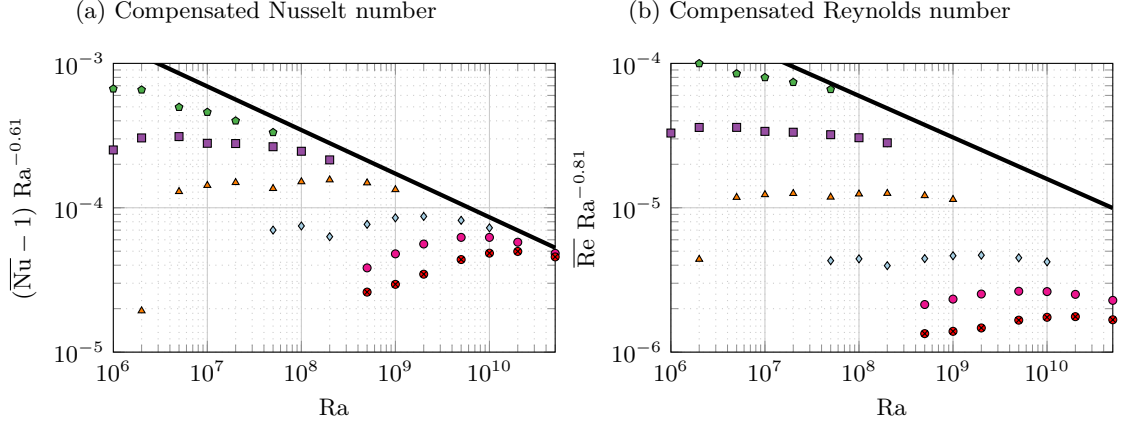
Figure 8.12: Model with inertial corrections: compensated Nusselt and Reynolds numbers using exponents $\beta_{\mathrm{Nu}-1} = 0.61$ and $\beta_{\mathrm{Re}} = 0.81$. A thick solid line indicates the scaling for a cubic cell. Symbols indicate the value of Γ_z: ⬠ $\Gamma_z = 1/16$, ☐ $\Gamma_z = 1/32$, △ $\Gamma_z = 1/64$, ◇ $\Gamma_z = 1/128$, ○ $\Gamma_z = 1/192$, and ⊗ $\Gamma_z = 1/256$.

(a) Compensated Nusselt number

(b) Compensated Reynolds number
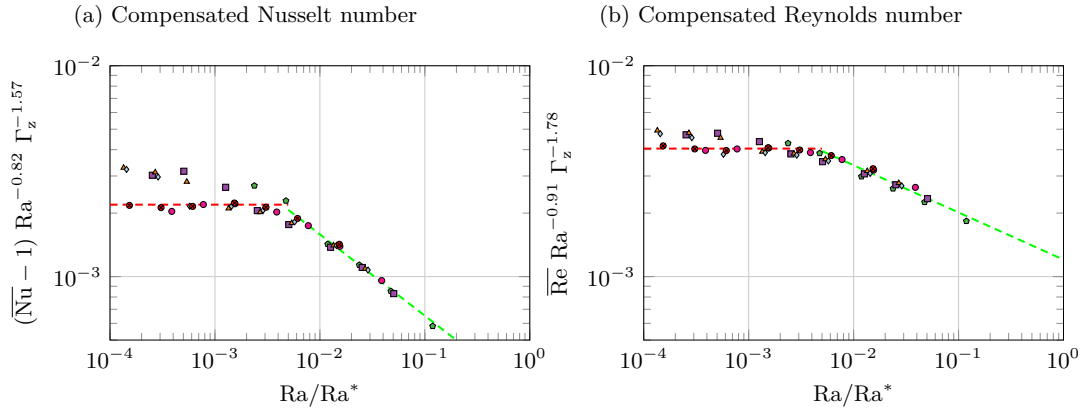
Figure 8.13: Model with inertial corrections: Compensated Nusselt and Reynolds numbers using exponents $\beta_{\mathrm{Nu}-1} = 0.82$ and $\beta_{\mathrm{Re}} = 0.91$ as a function of $\mathrm{Ra}/\mathrm{Ra}^* = 1.85 \cdot 10^{-5} \Gamma_z^{3.23} \mathrm{Ra}$ proposed by (Chong and Xia, 2016). Symbols indicate the value of Γ_z: ⬠ $\Gamma_z = 1/16$, ☐ $\Gamma_z = 1/32$, △ $\Gamma_z = 1/64$, ◇ $\Gamma_z = 1/128$, ○ $\Gamma_z = 1/192$, and ⊗ $\Gamma_z = 1/256$.
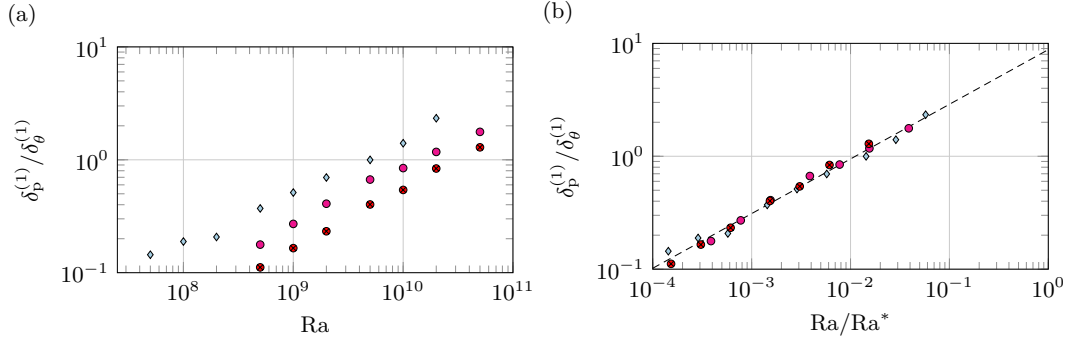
Figure 8.14: Ratio between the kinetic $\delta_\mathrm{p}^{(1)}$ and thermal $\delta_\theta^{(1)}$ boundary layer thicknesses as function of (a) Ra and (b) $\mathrm{Ra}/\mathrm{Ra}^* = 1.85 \cdot 10^{-5} \mathrm{Ra} \Gamma_\mathrm{z}^{3.23}$. Symbols indicate the value of Γ_z: $\diamond$ $\Gamma_\mathrm{z} = 1/128$, $\circ$ $\Gamma_\mathrm{z} = 1/192$, and $\otimes$ $\Gamma_\mathrm{z} = 1/256$.

0.005 suggests a change in the flow structure or in the temporal evolution. Indeed, for $\mathrm{Ra}/\mathrm{Ra}^* < 0.01$ the kinetic boundary layers are nested inside the thermal boundary layers and *vice versa* (see figure 8.14). The inversion of the boundary layers may be related to the change in scaling exponents.

For $\mathrm{Ra}/\mathrm{Ra}^* < 0.005$ and $\overline{\mathrm{Nu}} > 5$, the exponents $\beta_{\mathrm{Nu}-1} = 0.82$ and $\beta_{\mathrm{Re}} = 0.91$, are larger than the asymptotic values estimated by (Chong and Xia, 2016), but differ from the values $\beta_{\mathrm{Nu}-1} = 0.827$ and $\beta_{\mathrm{Re}} = 0.96$ obtained by (Bizon et al., 1997) as well as the theoretical exponents $\beta_{\mathrm{Nu}-1} = \beta_{\mathrm{Re}} = 1$ proposed in section 8.5.1.

There are two possibilities for the differences in the scaling exponents. The first one is that the exponents $\beta_{\mathrm{Nu}-1} = 0.82$ and $\beta_{\mathrm{Re}} = 0.91$ do not correspond yet to the asymptotic regime. To test this affirmation, additional simulations for $\Gamma_\mathrm{z} < 1/256$ should be considered. The second possibility, is that our scaling theory is too simple. In this sense, it could be interesting to extend the Grossmann & Lohse unifying scaling theory as to include the aspect ratio dependency which may provide a better prediction of the scaling exponents confined regime.

Conclusions of chapters 7 and 8

In this part we used data from 3-D DNS in rectangular Rayleigh-Bénard cells for small aspect ratio to highlight the main features of the confined regime III. As one increases the level of confinement, the temperature field becomes independent of the transversal coordinate while the velocity field becomes increasingly parabolic. The confined regime is characterized by the formation of large-scale turbulent channels in the vertical direction and the non-linear interaction between these channels is seen to play a fundamental role on the dynamics of the large-scale flow.

Turbulent convection inside the confined regime may be divided spatially in different regions: thermal and kinetic boundary layers along the top and bottom plates, kinetic boundary layers along the side-walls, and a bulk flow away from the boundaries. Under a severe confinement, the thickness of the kinetic boundary layer at the top and bottom plates becomes comparable to the depth of the cavity. In contrast, the thermal boundary layer becomes increasingly thicker as the convective heat-flux is hindered by the front

and back walls. This leads to a situation where the thermal boundary layer is directly exposed to the bulk flow, even for Pr > 1. Another important difference from conventional (unconfined) convection concerns the thickness of the kinetic boundary layer at the front and back walls, which 'saturates' to a constant value consistent with a parabolic velocity profile.

This configuration is well suited for dimensionality reduction. By analogy to previous works inside Hele-Shaw cells, we extended an reduced model to take into account inertial corrections and performed quantitative comparison of both models to 3-D DNS with good results. Two potential applications of the model with inertial corrections are explored. The first potential use is in the study the long term evolution and the dynamics of reorientations of the large-scale flow. The second potential use concerns the evolution of global quantities for very confined cells. Our observations suggests the presence of a change in flow regime and different scaling laws between confined and severely confined geometries.

Part V

Conclusions and Perspectives

General conclusions

The work exposed in this manuscript is a contribution to the numerical study of large-scale flow dynamics in Rayleigh-Bénard convection. Using a DNS code we simulated the long term evolution for various Rayleigh-Bénard configurations and developed a series of analysis tools for their characterization. A particular attention was given to spontaneous reorientations and reconfigurations of the large-scale flow (or *flow reversals*) over long periods of time by considering a pure 2-D flow inside a square cell, then by considering a slim rectangular cavity. For such long simulations, it is imperative to identify a meaningful quantity, global or local, to guide our observations.

For the 2-D case, a pertinent choice is the global angular impulse. We devised a filtering procedure based on the amplitude of this quantity to separate the different flow regimes, which allowed us to characterize each regime separately. A first regime composed of *consecutive reversals* displays a well defined and consistent dynamical pattern. Using a time rescaling and conditional statistics allowed us to identify a *generic reversal mechanism* in terms of accumulation and exchange of mechanical energy. This work resulted in a publication (Castillo-Castellanos et al., 2016). A second regime composed of *extended cessations* of the large-scale circulation, required to choose a different quantity. A good candidate was obtained from a POD analysis. A statistical characterization suggested this regime to be driven by random stochastic processes.

We extended this analysis to a configuration with a free-slip condition imposed on the top and a no-slip bottom plate. Observations suggest a disconnection between the thermal boundary layer at the top and bottom plates. Both interact directly to the bulk flow but not with each other. This configuration is characterized by the same type of flow structures as in the classical case, but their time evolution is entirely different and the clear separation between the regime of *consecutive reversals* and the regime of *extended cessations* no longer exists. Finally, by considering the plates separately we identified a change of regime in the free-slip plate.

In the last part, we used 3-D DNS to study the flow dynamics inside a slim rectangular cavity. By analogy to other confined systems, such as Hele-Shaw cells and thin liquid films, we proposed a *reduced model with inertial corrections* to mimic the three-dimensional flow. Results from this model agree well with our own 3-D DNS and with existing publications. We successfully tested the feasibility of studying the dynamics of flow reversals inside confined cells by performing long simulations using this model for one configuration and identified a handful of flow reversals. The nature of these reversals is different from pure 2-D reversals. The reduced model also allowed us to identify inside regime III a transition between two different dynamics, which depends on the ratio between the kinetic

and thermal boundary layer thicknesses. A scaling theory for such confined regime was proposed.

Perspectives

In this work we identified a generic reversal mechanism inside square cells in which accumulation of thermal energy inside the counter-rotating corner-rolls is a key process. Since *Prandtl* number is related to diffusion of thermal energy, it might be interesting to examine the influence of this number on the reversal cycle. Another interesting point is to consider the influence of corner-rolls by studying a case in which such rolls are weaker or nonexistent but still experience flow reversals. This would allow us to verify if the main ingredient of flow reversals is related to the localized accumulation of energy somewhere in the flow, or specifically depends on the existence of corner-rolls. For instance, it could be interesting to study from our energetical point of view a 2-D cell with free-slip conditions imposed on all boundaries. Indeed (Verma et al., 2015) showed that this system exhibits reversals without corner-rolls.

Our statistical approach can be extended to 3-D geometries provided one is able to follow the plane of large-scale circulation and that one is able to obtain a long time signal containing a sufficient number of events. However, extending the statistical approach to cubic and cylindrical containers is more challenging because of the meandering of the LSC plane which can also be subject to torsional or sloshing motions. In this work, we were able to contour both limitations when considering a slim rectangular cavity, effectively restricting the large-scale flow to a plane and by proposing a reduced model which is computationally less expensive than using 3-D DNS.

Large-scale flow dynamics inside laterally confined cells are to be further explored. To explore the apparent significance of the ratio between the thickness of the thermal and kinetic boundary layers, a parametric study of the aspect ratio and the *Prandtl* number would be desirable. These observations could eventually allow to include the aspect ratio dependency in the unifying scaling theory of *Grossmann & Lohse*. Such approach would allow for a smooth transition between the different regime and provide a better prediction of the scaling exponents inside the confined regime.

Bibliography

[1] N. Adami, "Surface tension and buoyancy in vertical soap films", PhD thesis (Universié de Liège, 2014).

[2] G. Ahlers, E. Brown, F. F. Araujo, D. Funfschilling, S. Grossmann, and D. Lohse, "Non-Oberbeck–Boussinesq effects in strongly turbulent Rayleigh–Bénard convection", Journal of Fluid Mechanics **569**, 409–445 (2006).

[3] G. Ahlers, S. Grossmann, and D. Lohse, "Heat transfer and large scale dynamics in turbulent Rayleigh-Bénard convection", Reviews of modern physics **81**, 503 (2009).

[4] F. F. Araujo, S. Grossmann, and D. Lohse, "Wind reversals in turbulent Rayleigh-Bénard convection.", Physical Review Letters **95**, 084502 (2004).

[5] J. Bailon-Cuba, M. S. Emran, and J. Schumacher, "Aspect ratio dependence of heat transfer and large-scale flow in turbulent convection", J. Fluid Mech. **655**, 17 (2010).

[6] A. Bejan, Convection heat transfer (John wiley & sons, 2013).

[7] J. Bell, P. Colella, and H. Glaz, "A second-order projection method for the incompressible Navier-Stokes equations", Journal of Computational Physics **283**, 257–283 (1989).

[8] D. Bercovici, "The generation of plate tectonics from mantle convection", Earth and Planetary Science Letters **205**, 107–121 (2003).

[9] M. Berhanu, R. Monchaux, S. Fauve, N. Mordant, F. Pétrélis, A. Chiffaudel, F. Daviaud, B. Dubrulle, L. Marié, F. Ravelet, et al., "Magnetic field reversals in an experimental turbulent dynamo", EPL (Europhysics Letters) **77**, 59001 (2007).

[10] G. Berkooz, P. Holmes, and J. L. Lumley, "The proper orthogonal decomposition in the analysis of turbulent flows", Annual review of fluid mechanics **25**, 539–575 (1993).

[11] C. Bizon, J. Werne, A. Predtechensky, K. Julien, W. McCormick, J. Swift, and H. L. Swinney, "Plume dynamics in quasi-2d turbulent convection", Chaos: An Interdisciplinary Journal of Nonlinear Science **7**, 107–124 (1997).

[12] J. Borée, "Extended proper orthogonal decomposition: a tool to analyse correlated events in turbulent flows", Experiments in Fluids **35**, 188–192 (2003).

[13] E. Brown, and G. Ahlers, "Rotations and cessations of the large-scale circulation in turbulent rayleigh–bénard convection", Journal of Fluid Mechanics **568**, 351–386 (2006).

[14] B. Castaing, G. Gunaratne, F. Heslot, L. Kadanoff, A. Libchaber, S. Thomae, X.-Z. Wu, S. Zaleski, and G. Zanetti, "Scaling of hard thermal turbulence in Rayleigh-Bénard convection", Journal of Fluid Mechanics **204**, 1–30 (1989).

[15] A. Castillo-Castellanos, A. Sergent, and M. Rossi, "Reversal cycle in square Rayleigh–Bénard cells in turbulent regime", Journal of Fluid Mechanics **808**, 614–640 (2016).

[16] M. Chandra, and M. K. Verma, "Flow reversals in turbulent convection via vortex reconnections", Physical Review Letters **110**, 1–4 (2013).

[17] M. Chandra, and M. K. Verma, "On flow reversals in Rayleigh-Bénard convection", Journal of Physics: Conference Series **318**, 082002 (2011).

[18] F. Chillà, and J. Schumacher, "New perspectives in turbulent Rayleigh-Bénard convection", European Physical Journal E **35** (2012) 10.1140/epje/i2012-12058-1.

[19] Chong, Kai Leong, Yang, Yantao, Huang, Shi-Di, Zhong, Jin-Qiang, Stevens, Richard, Verzicco, Roberto, Lohse, Detlef, and K. Q. Xia, "Confined Rayleigh-Bénard, Rotating Rayleigh-Bénard, and Double Diffusive Convection: A unifying view on turbulent transport enhancement through coherent structure manipulation", arXiv preprint arXiv:1702.04522 (2017).

[20] K. L. Chong, S.-D. Huang, M. Kaczorowski, K. Q. Xia, et al., "Condensation of coherent structures in turbulent flows", Physical review letters **115**, 264503 (2015).

[21] K. L. Chong, and K. Q. Xia, "Exploring the severely confined regime in rayleigh–bénard convection", Journal of Fluid Mechanics **805** (2016).

[22] A. J. Chorin, "On the convergence of discrete approximations to the Navier-Stokes equations", Mathematics of computation **23**, 341–353 (1969).

[23] J. A. Clarke, and E. R. Mark, "Enhancements to the extensible data model and format (xdmf)", in Dod high performance computing modernization program users group conference, 2007 (IEEE, 2007), pp. 322–327.

[24] J. A. Clarke, and R. R. Namburu, "A distributed computing environment for interdisciplinary applications", Concurrency and Computation: Practice and Experience **14**, 1161–1174 (2002).

[25] A. Das, U. Ghosal, and K. Kumar, "Asymmetric squares as standing waves in Rayleigh-Bénard convection", Phys. Rev. E **62**, R3051–R3054 (2000).

[26] G. De Vahl Davis, "Natural convection of air in a square cavity: a benchmark solution", Int. J. Num. Methods in Fluids **3**, 249–264 (1983).

[27] J. W. Demmel, Applied numerical linear algebra (Siam, 1997).

[28] C. R. Doering, and P. Constantin, "Bounds for heat transport in a porous layer", Journal of Fluid Mechanics **376**, 263–296 (1998).

[29] C. Egbers, W. Beyer, A. Bonhage, R. Hollerbach, and P. Beltrame, "The geoflow-experiment on iss (part i): experimental preparation and design of laboratory testing hardware", Advances in Space Research **32**, 171–180 (2003).

[30] V. Eijkhout, "Introduction to High Performance Scientific Computing", 446 (2011).

[31] J. H. Ferziger, and M. Perić, Computational methods for fluid dynamics (Springer Berlin Heidelberg, Berlin, Heidelberg, 2002), pp. 157–216.

[32] B. A. Finlayson, The method of weighted residuals and variational principles, Vol. 73 (SIAM, 2013).

[33] D. Funfschilling, and G. Ahlers, "Plume motion and large-scale circulation in a cylindrical rayleigh-bénard cell", Phys. Rev. Lett. **92**, 194502 (2004).

[34] D. Funfschilling, E. Brown, and G. Ahlers, "Torsional oscillations of the large-scale circulation in turbulent rayleigh–bénard convection", Journal of Fluid Mechanics **607**, 119–139 (2008).

[35] B. Gallet, J. Herault, C. Laroche, F. Pétrélis, and S. Fauve, "Reversals of a large-scale field generated over a turbulent background", Geophysical & Astrophysical Fluid Dynamics **106**, 468–492 (2012).

[36] A. Getling, Rayleigh-Bénard Convection: Structures and Dynamics, Advanced series in nonlinear dynamics (World Scientific, 1998).

[37] G. H. Golub, L. C. Huang, H. Simon, and W.-P. Tang, "A fast poisson solver for the finite difference solution of the incompressible navier–stokes equations", SIAM Journal on Scientific Computing **19**, 1606–1624 (1998).

[38] M. Golubitsky, J. W. Swift, and E. Knobloch, "Symmetries and pattern selection in Rayleigh-Bénard convection", Physica D: Nonlinear Phenomena **10**, 249–276 (1984).

[39] P. Gondret, and M. Rabaud, "Shear instability of two-fluid parallel flow in a hele–shaw cell", Physics of Fluids (1994-present) **9**, 3267–3274 (1997).

[40] A. Gorin, "On analogy between convective heat and mass transfer processes in a porous medium and a hele-shaw cell", in Heat and mass transfer in porous media (Springer, 2012), pp. 139–159.

[41] M. D. Graham, U. Müller, and P. H. Steen, "Time-periodic thermal convection in hele–shaw slots: the diagonal oscillation", Physics of Fluids A: Fluid Dynamics **4**, 2382–2393 (1992).

[42] S. Grossmann, and D. Lohse, "On geometry effects in rayleigh–bénard convection", Journal of Fluid Mechanics **486**, 105–114 (2003).

[43] S. Grossmann, and D. Lohse, "Scaling in thermal convection: a unifying theory", Journal of Fluid Mechanics **407**, 27–56 (2000).

[44] G. Grötzbach, "Spatial resolution requirements for direct numerical simulation of the Rayleigh-Bénard convection", Journal of Computational Physics **264**, 241–264 (1983).

[45] J. L. Guermond, P. Minev, and J. Shen, "An overview of projection methods for incompressible flows", Computer Methods in Applied Mechanics and Engineering **195**, 6011–6045 (2006).

[46] H. H. Harlow, and J. E. Welch, "Numerical calculation of time-dependent viscous incompressible flow of fluid with free surface", Phys. Fluids **8**, 2182–2189 (1965).

[47] B. K. Hartline, and C. Lister, "Thermal convection in a hele-shaw cell", Journal of Fluid Mechanics **79**, 379–389 (1977).

[48] D. R. Hewitt, J. A. Neufeld, and J. R. Lister, "Ultimate regime of high rayleigh number convection in a porous medium", Physical Review Letters **108**, 224503 (2012).

[49] D. Hewitt, J. Neufeld, and J. Lister, "High rayleigh number convection in a three-dimensional porous medium", Journal of Fluid Mechanics **748**, 879 (2014).

[50] J. Hinch, L. Petit, J. Hulin, and É. Guyon, Hydrodynamique physique 3e édition (2012), Savoirs Actuels (EDP Sciences, 2012).

[51] P. Holmes, J. L. Lumley, G. Berkooz, and C. W. Rowley, Turbulence, coherent structures, dynamical sy 2nd ed., Cambridge Monographs on Mechanics (Cambridge University Press, 2012).

[52] S. Horn, O. Shishkina, and C. Wagner, "On non-Oberbeck–Boussinesq effects in three-dimensional Rayleigh–Bénard convection in glycerol", Journal of Fluid Mechanics **724**, 175–202 (2013).

[53] S. D. Huang, M. Kaczorowski, R. Ni, and K. Q. Xia, "Confinement-induced heat-transport enhancement in turbulent thermal convection", Physical Review Letters **111**, 4–8 (2013).

[54] G. O. Hughes, B. Gayen, and R. W. Griffiths, "Available potential energy in Rayleigh–Bénard convection", Journal of Fluid Mechanics **729**, R3 (2013).

[55] IDRIS, Ada, Institut du développement et des ressources en informatique scientifique (IDRIS), http://www.idris.fr/ada/, (2016)

[56] IDRIS, Turing, Institut du développement et des ressources en informatique scientifique (IDRIS), http://www.idris.fr/turing/, (2016)

[57] M. Kaczorowski, K.-L. Chong, and K. Q. Xia, "Turbulent flow in the bulk of rayleigh–bénard convection: aspect-ratio dependence of the small-scale properties", Journal of Fluid Mechanics **747**, 73–102 (2014).

[58]S. Kalliadasis, C. Ruyer-Quil, B. Scheid, and M. G. Velarde, <u>Falling liquid films</u>, Vol. 176 (Springer Science & Business Media, 2011).

[59]R. M. Kerr, "Rayleigh number scaling in numerical convection", Journal of Fluid Mechanics **310**, 139–179 (1996).

[60]P. Kundu, and I. Cohen, Fifth Edition (Academic Press, Boston, 2012).

[61]M. Lappa, "Some considerations about the symmetry and evolution of chaotic Rayleigh–Bénard convection: The flywheel mechanism and the "wind" of turbulence", Comptes Rendus Mécanique **339**, 563–572 (2011).

[62]M. Lappa, <u>Thermal convection: patterns, evolution and stability</u> (2009).

[63]P. Le Quéré, "Accurate solutions to the square thermally driven cavity at high Rayleigh number", Computers & Fluids **20**, 29–41 (1991).

[64]P. Le Quéré, and M. Behnia, "From onset of unsteadiness to chaos in a differentially heated square cavity", Journal of fluid mechanics **359**, 81–107 (1998).

[65]R. B. Leighton, "The solar granulation", Annual Review of Astronomy and Astrophysics **1**, 19–40 (1963).

[66]F. Lhuillier, G. Hulot, and Y. Gallet, "Statistical properties of reversals and chrons in numerical dynamos and implications for the geodynamo", Physics of the Earth and Planetary Interiors **220**, 19–36 (2013).

[67]O. Liot, J. Salort, R. Kaiser, R. du Puits, and F. Chillà, "Boundary layer structure in a rough Rayleigh–Bénard cell filled with air", Journal of Fluid Mechanics **786**, 275–293 (2016).

[68]P. W. Livermore, "Galerkin orthogonal polynomials", Journal of Computational Physics **229**, 2046–2060 (2010).

[69]E. N. Lorenz, "Available potential energy and the maintenance of the general circulation", Tellus **7**, 157–167 (1955).

[70]Y. L. Luke, <u>The special functions and their approximations</u>, Vol. 53 (Academic press, 1969).

[71]W. V. Malkus, "The heat transport and spectrum of thermal turbulence", in Proceedings of the royal society of london a: mathematical, physical and engineering sciences, Vol. 225, 1161 (The Royal Society, 1954), pp. 196–212.

[72]J. Mizushima, and T. Adachi, "Sequential transitions of the thermal convection in a square cavity", Journal of the Physical Society of Japan **66**, 79–90 (1997).

[73]D. Molenaar, H. J. H. Clercx, and G. J. F. Van Heijst, "Angular momentum of forced 2D turbulence in a square no-slip domain", Physica D: Nonlinear Phenomena **196**, 329–340 (2004).

[74] NASA / JAXA, <u>Granules-like structure of surface of sun and sunspots</u>, (2015) `https://www.nasa.gov/mission_pages/hinode/solar_022.html` (visited on 04/04/2017).

[75]R. Ni, S.-D. Huang, and K. Q. Xia, "Reversals of the large-scale circulation in quasi-2d rayleigh–bénard convection", Journal of Fluid Mechanics **778**, R5 (2015).

[76]D. A. Nield, and A. Bejan, "Heat transfer through a porous medium", in <u>Convection in porous media</u> (Springer, 2013), pp. 31–46.

[77]J. Niemela, L. Skrbek, K. Sreenivasan, and R. Donnelly, "The wind in confined thermal convection", Journal of Fluid Mechanics **449**, 169–178 (2001).

[78]J. Otero, L. A. Dontcheva, H. Johnston, R. A. Worthing, A. Kurganov, G. Petrova, and C. R. Doering, "High-rayleigh-number convection in a fluid-saturated porous layer", Journal of Fluid Mechanics **500**, 263–281 (2004).

[79]M. Ozawa, U. Müller, I. Kimura, and T. Takamori, "Flow and temperature measurement of natural convection in a Hele-Shaw cell using a thermo-sensitive liquid-crystal tracer", Experiments in Fluids **12**, 213–222 (1992).

[80]H. Park, and L. Sirovich, "Turbulent thermal convection in a finite domain: part ii. numerical results", Physics of Fluids A: Fluid Dynamics **2**, 1659–1668 (1990).

[81]R. L. Parker, "The magnetic field of the earth: paleomagnetism, the core, and the deep mantle", Eos, Transactions American Geophysical Union **78**, 480–480 (1997).

[82]K. Petschel, S. Stellmach, M. Wilczek, J. Lülff, and U. Hansen, "Dissipation Layers in Rayleigh-Bénard Convection: A Unifying View", Physical Review Letters **110**, 114502 (2013).

[83]K. Petschel, M. Wilczek, M. Breuer, R. Friedrich, and U. Hansen, "Statistical analysis of global wind dynamics in vigorous Rayleigh-Bénard convection", Physical Review E **84**, 026309 (2011).

[84]D. Pierce, Empirical Orthogonal Function (EOF) software, `http://meteora.ucsd.edu/~pierce/eof/eofs.html`, 2003.

[85]B. Podvin, "Introduction à la décomposition orthogonale aux valeurs propres (pod)", in (LIMSI-CNRS, 2001).

[86]B. Podvin, and P. Le Quéré, "Low-order models for the flow in a differentially heated cavity", Physics of Fluids (1994-present) **13**, 3204–3214 (2001).

[87]B. Podvin, and A. Sergent, "A large-scale investigation of wind reversal in a square Rayleigh–Bénard cell", Journal of Fluid Mechanics **766**, 172–201 (2015).

[88]B. Podvin, and A. Sergent, "Precursor for wind reversal in a square Rayleigh-Bénard cell", Phys. Rev. E **95**, 013112 (2017).

[89]B. Podvin, and A. Sergent, "Proper orthogonal decomposition investigation of turbulent Rayleigh-Bénard convection in a rectangular cavity", Physics of Fluids (1994-present) **24**, 105106 (2012).

[90]S. Popinet, "Gerris: a tree-based adaptive solver for the incompressible euler equations in complex geometries", J. Comput. Phys. **190**, 572–600 (2003).

[91]S. Popinet, "An accurate adaptive solver for surface-tension-driven interfacial flows", Journal of Computational Physics **228**, 5838–5866 (2009).

[92]S. Rahmstorf, "Thermohaline circulation: the current climate", Nature **421**, 699–699 (2003).

[93]C. Ruyer-Quil, "De la modélisation et des instabilités des films liquides tombants", PhD thesis (2012).

[94]C. Ruyer-Quil, "Inertial corrections to the darcy law in a hele–shaw cell", Comptes Rendus de l'Académie des Sciences - Series {IIB} - Mechanics **329**, 337–342 (2001).

[95]C. Ruyer-Quil, and P. Manneville, "Improved modeling of flows down inclined planes", The European Physical Journal B-Condensed Matter and Complex Systems **15**, 357–369 (2000).

[96]J. Salort, O. Liot, E. Rusaouen, F. Seychelles, J. C. Tisserand, M. Creyssels, B. Castaing, and F. Chillà, "Thermal boundary layer near roughnesses in turbulent Rayleigh-Bénard convection: Flow structure and multistability", Physics of Fluids **26** (2014) `10.1063/1.4862487`.

[97]F. Seychelles, Y. Amarouchene, M. Bessafi, and H. Kellay, "Thermal convection and emergence of isolated vortices in soap bubbles", Physical review letters **100**, 144501 (2008).

[98]X.-D. Shang, X.-L. Qiu, P. Tong, and K.-Q. Xia, "Measured local heat transport in turbulent rayleigh-bénard convection", Physical review letters **90**, 074501 (2003).

[99]M. Shimizu, K. Cho, and G. Kawahara, "Onset of reversal and chaos in thermally driven cavity flow", (2015).

[100]O. Shishkina, A. Shishkin, and C. Wagner, "Simulation of turbulent thermal convection in complicated domains", Journal of Computational and Applied Mathematics **226**, Special Issue: Large scale scientific computations, 336–344 (2009).

[101]O. Shishkina, and C. Wagner, "Analysis of sheet-like thermal plumes in turbulent rayleigh–bénard convection", Journal of Fluid Mechanics **599**, 383–404 (2008).

[102]B. I. Shraiman, and E. D. Siggia, "Heat transport in high-Rayleigh-number convection", Physical Review A **42**, 3650–3653 (1990).

[103]L. Sirovich, "Turbulence and the dynamics of coherent structures part i: coherent structures", Quarterly of applied mathematics **45**, 561–571 (1987).

[104] Stéphane Popinet, Basilisk, http://www.basilisk.fr/, (2016)

[105]B. Stevens, "Atmospheric moist convection", Annual Review of Earth and Planetary Sciences **33**, 605–643 (2005).

[106]R. Stevens, D. Lohse, and R. Verzicco, "Prandtl and rayleigh number dependence of heat transport in high rayleigh number thermal convection", Journal of Fluid Mechanics **688**, 31–43 (2011).

[107]R. Stevens, E. P. van der Poel, S. Grossmann, and D. Lohse, "The unifying theory of scaling in thermal convection: the updated prefactors", Journal of fluid mechanics **730**, 295–308 (2013).

[108]R. Stevens, R. Verzicco, and D. Lohse, "Radial boundary layer structure and Nusselt number in Rayleigh-Benard convection", J. Fluid Mech. **643**, 495–807 (2010).

[109]G. Strang, Computational science and engineering, Vol. 1 (Wellesley-Cambridge Press Wellesley, 2007).

[110]K. Sugiyama, E. Calzavarini, S. Grossmann, and D. Lohse, "Flow organization in two-dimensional non-Oberbeck–Boussinesq Rayleigh–Bénard convection in water", Journal of Fluid Mechanics **637**, 105–135 (2009).

[111]K. Sugiyama, R. Ni, R. Stevens, T. S. Chan, S. Q. Zhou, H. D. Xi, C. Sun, S. Grossmann, K. Q. Xia, and D. Lohse, "Flow reversals in thermally driven turbulence", Physical Review Letters **105**, 1–4 (2010).

[112]B. R. Sutherland, Internal gravity waves (Cambridge University Press, 2010).

[113] The HDF Group, Hierarchical Data Format, version 5, http://www.hdfgroup.org/HDF5/, (2016)

[114]J. C. Tisserand, M. Creyssels, Y. Gasteuil, H. Pabiou, M. Gibert, B. Castaing, and F. Chillà, "Comparison between rough and smooth plates within the same Rayleigh-Bénard cell", Physics of Fluids **23** (2011) 10.1063/1.3540665.

[115]J.-C. Tisserand, M. Creyssels, Y. Gasteuil, H. Pabiou, M. Gibert, B. Castaing, and F. Chilla, "Comparison between rough and smooth plates within the same rayleigh–bénard cell", Physics of Fluids (1994-present) **23**, 015105 (2011).

[116]V. Travnikov, C. Egbers, and R. Hollerbach, "The geoflow-experiment on iss (part ii): numerical simulation", Advances in Space Research **32**, 181–189 (2003).

[117]E. Tric, G. Labrosse, and M. Betrouni, "A first incursion into the 3D structure of natural convection of air in a differentially heated cubic cavity, from accurate numerical solutions", International Journal of Heat and Mass Transfer **43**, 4043–4056 (2000).

[118] D. Tritton, Physical fluid dynamics, The Modern University in Physics Series (Springer Netherlands, 2012).

[119] Y. H. Tseng, and J. H. Ferziger, "Mixing and available potential energy in stratified flows", Physics of Fluids **13**, 1281–1293 (2001).

[120] E. P. Van Der Poel, R. Ostilla-Mónico, R. Verzicco, and D. Lohse, "Effect of velocity boundary conditions on the heat transfer and flow topology in two-dimensional Rayleigh-Bénard convection", Physical Review E - Statistical, Nonlinear, and Soft Matter Physics **90** (2014) 10.1103/PhysRevE.90.013017.

[121] G. J. F. Van Heijst, H. J. H. Clercx, and D. Molenaar, "The effects of solid boundaries on confined two-dimensional turbulence", Journal of Fluid Mechanics **554**, 411–431 (2006).

[122] A. Vasiliev, and P. Frick, "Reversals of large-scale circulation at turbulent convection in rectangular boxes", in Journal of physics: conference series, Vol. 318, 8 (IOP Publishing, 2011), p. 082013.

[123] J. Verdoold, M. J. Tummers, and K. Hanjalić, "Prime modes of fluid circulation in large-aspect-ratio turbulent Rayleigh-Bénard convection", Physical Review E **80**, 037301 (2009).

[124] M. K. Verma, S. C. Ambhire, and A. Pandey, "Flow reversals in turbulent convection with free-slip walls", Physics of Fluids **27**, 047102 (2015).

[125] R. Verzicco, E. van der Poel, and D. Lohse, "High rayleigh number simulations in a slender laterally periodic domain", in Aps meeting abstracts (2015).

[126] S. Vorontsov, A. Gorin, V. Y. Nakoryakov, A. Khoruzhenko, and V. Chupin, "Natural convection in a hele-shaw cell", International journal of heat and mass transfer **34**, 703–709 (1991).

[127] S. Wagner, and O. Shishkina, "Aspect-ratio dependency of Rayleigh-Bénard convection in box-shaped containers", Physics of Fluids **25** (2013) 10.1063/1.4819141.

[128] Wang, J., and Xia, K.-Q., "Spatial variations of the mean and statistical quantities in the thermal boundary layers of turbulent convection", Eur. Phys. J. B **32**, 127–136 (2003).

[129] Wikimedia commons, Montgolfiere hb-byx, (2011) https://commons.wikimedia.org/wiki/File:Ultramagic_F-11_MONTGOLFIERE_2011.JPG (visited on 04/04/2017).

[130] K. B. Winters, P. N. Lombard, J. J. Riley, and E. A. D'Asaro, "Available potential energy and mixing in density-stratified fluids", J. Fluid Mech. **289**, 115 (1995).

[131] XDMF Standard, eXtensible Data Model and Format, http://www.xdmf.org, (2016)

[132] H.-D. Xi, and K. Q. Xia, "Flow mode transitions in turbulent thermal convection", Physics of Fluids **20**, 055104 (2008).

[133] Xia, Shu-Ning, Wan, Zhen-Hua, Liu, Shuang, Wang, Qi, and Sun, De-Jun, "Flow reversals in Rayleigh–Bénard convection with non-Oberbeck–Boussinesq effects", Journal of Fluid Mechanics **798**, 628–642 (2016).

[134] J. Zhang, S. Childress, and A. Libchaber, "Non-boussinesq effect: thermal convection with broken symmetry", Physics of Fluids (1994-present) **9**, 1034–1042 (1997).

[135] Q. Zhou, H.-D. Xi, S.-Q. Zhou, C. Sun, and K. Q. Xia, "Oscillations of the large-scale circulation in turbulent rayleigh–bénard convection: the sloshing mode and its relationship with the torsional mode", Journal of Fluid Mechanics **630**, 367–390 (2009).

Part VI

Appendices

Appendix A

Code FUSION

A.1 Temporal discretization scheme

The time discretization of the equation system is performed by first introducing an increasing sequence if $[t^0, t^1, \cdots, t^n]$ times with $t^n = n\Delta t$ where Δt represents the discrete time-step. The velocity, pressure and temperature fields at time t^n read as

$$\mathbf{u}(\mathbf{x})^n = \mathbf{u}(\mathbf{x}, t^n) \quad , \quad \mathrm{p}(\mathbf{x})^n = \mathrm{p}(\mathbf{x}, t^n) \quad , \quad \theta(\mathbf{x})^n = \theta(\mathbf{x}, t^n) \tag{A.1}$$

We use a second-order backward Euler method to approximate the time derivatives

$$\partial_t u_i^{n+1} = \frac{(3u_i^{n+1} - 4u_i^{n} + u_i^{n-1})}{2\Delta t} + \mathcal{O}(\Delta t)^2 \tag{A.2}$$

Equations are discretised using a semi-implicit method, with viscous terms treated implicitly and advective terms explicitly and approximated as follows

$$\partial_j(u_j u_i)^{n+1} = 2\partial_j(u_j u_i)^{n} - \partial_j(u_j u_i)^{n-1} + \mathcal{O}(\Delta t)^2 \tag{A.3}$$

The discretized equations would have the following form

$$\partial_i u_i^{n+1} = 0 \tag{A.4a}$$

$$\frac{(3u_i^{n+1} - 4u_i^{n} + u_i^{n-1})}{2\Delta t} + \partial_j(2u_j u_i^{n} - u_j u_i^{n-1}) = -\partial_i \mathrm{p}^{n+1} + \mathrm{Pr}\mathrm{Ra}^{-0.5}\partial_j^2 u_i^{n+1} + \mathrm{Pr}\theta^{n+1}\delta_{i2} \tag{A.4b}$$

$$\frac{(3\theta^{n+1} - 4\theta^{n} + \theta^{n-1})}{2\Delta t} + \partial_j(2u_j\theta^{n} - u_j\theta^{n-1}) = \mathrm{Ra}^{-0.5}\partial_j^2\theta^{n+1} \tag{A.4c}$$

In order to solve equations (A.4a) and (A.4b) one must know beforehand the solution for θ^{n+1} from equation (A.4c). This equation has the form of a Helmholtz-Poisson problem and can be treated independently.

Due to the incompressibility condition and the pressure gradient involved, the velocity-pressure coupling is more complex. We use a *rotational incremental-pressure correction* scheme (see for instance Chorin, 1969; Guermond et al., 2006). In this scheme, the

pressure term is treated explicitly to obtain a provisional velocity field $\mathbf{u}^*$ which may not be divergence-free. A correction is obtained by projecting the provisional velocity into a divergence-free space and assume the difference to derived from an scalar function Π, called the pressure potential term.

Solution of the energy equation

In order to obtain θ^{n+1} we need to solve a Helmholtz-Poisson problem; This type of problem can be written in the general form

$$\theta^{n+1} - \frac{1}{\Lambda}\mathrm{Ra}^{-0.5}\partial_j^2\theta^{n+1} = \frac{1}{\Lambda}Q_\theta{}^n \tag{A.5}$$

with $\Lambda = \frac{3}{2\Delta t}$ and $Q_\theta{}^n(\mathbf{x})$ being the source term corresponding to field θ.

$$Q_\theta{}^n(\mathbf{x}) = \frac{(4\theta^n - \theta^{n-1})}{2\Delta t} - \left(2\partial_j(u_j\theta)^n - \partial_j(u_j\theta)^{n-1}\right) \tag{A.6}$$

In order to solve directly this three-dimensional Helmholtz system, we use the Douglas-Rachford *Alternating Direction Implicit* method to separate the operators into one-dimensional components and split the scheme into one sub-step for each coordinate. The main component the ADI method is the factorization of the right-hand side of equation (A.5) as the product of one-dimensional operators in the following form (Ferziger and Perić, 2002).

$$\begin{aligned}\left(1 - \Gamma\partial_j^2\right)\theta^{n+1} &= \left(1 - \Gamma\partial_x^2\right)\left(1 - \Gamma\partial_y^2\right)\left(1 - \Gamma\partial_z^2\right)\theta^{n+1} \\ &\quad - \Gamma^2(\partial_x^2\partial_y^2 + \partial_x^2\partial_z^2 + \partial_y^2\partial_z^2)\theta^{n+1} + \Gamma^3\partial_x^2\partial_y^2\partial_z^2\theta^{n+1}\end{aligned} \tag{A.7}$$

Introducing equation (A.7) into equation (A.5) with $\Gamma = \frac{1}{\Lambda}\mathrm{Ra}^{-0.5}$ and dropping $\mathcal{O}(\Delta t^2 \mathrm{Ra}^{-1})$ terms, leaves the following expression

$$\left(1 - \frac{1}{\Lambda}\mathrm{Ra}^{-0.5}\partial_x^2\right)\left(1 - \frac{1}{\Lambda}\mathrm{Ra}^{-0.5}\partial_y^2\right)\left(1 - \frac{1}{\Lambda}\mathrm{Ra}^{-0.5}\partial_z^2\right)\theta^{n+1} = \frac{1}{\Lambda}Q_\theta{}^n$$

We use a multi-step approach to this problem and solve a one-dimensional Helmholtz problem for each direction.

$$\begin{aligned}\left(1 - \tfrac{1}{\Lambda}\mathrm{Ra}^{-0.5}\partial_x^2\right)\theta^{n+\frac{1}{3}} &= \tfrac{1}{\Lambda}Q_\theta{}^n && \text{w/ BC on } \mathbf{e}_x \\[2mm] \left(1 - \tfrac{1}{\Lambda}\mathrm{Ra}^{-0.5}\partial_y^2\right)\theta^{n+\frac{2}{3}} &= \theta^{n+\frac{1}{3}} && \text{w/ BC on } \mathbf{e}_y \\[2mm] \left(1 - \tfrac{1}{\Lambda}\mathrm{Ra}^{-0.5}\partial_z^2\right)\theta^{n+1} &= \theta^{n+\frac{2}{3}} && \text{w/ BC on } \mathbf{e}_z\end{aligned} \tag{A.8}$$

where $\theta^{n+\frac{1}{3}}$ and $\theta^{n+\frac{2}{3}}$ are the intermediate solutions from the first and second sub-steps, respectively. Observe that each ADI sub-step takes the form of a 1D Helmholtz problem.

Solution of the velocity-pressure coupling: prediction step

We treat the pressure term explicitly in equation (A.4b) leaving the following expression

$$\Lambda u_i{}^* - \text{PrRa}^{-0.5}\, \partial_j^2 u_i{}^* = Q_i{}^n - \partial_i p^n \tag{A.9}$$

with $Q_i{}^n(\mathbf{x})$ being the source term corresponding to the velocity field

$$Q_i{}^n(\mathbf{x}) = \frac{(4u_i{}^n - u_i{}^{n-1})}{2\Delta t} - \left(2\partial_j(u_j u_i)^n - \partial_j(u_j u_i)^{n-1}\right) + \text{Pr}\theta^{n+1}\delta_{i2} \tag{A.10}$$

We then proceed to use ADI method to separate the operators into one-dimensional components and split the scheme into one sub-step for each coordinate

$$\left(1 - \tfrac{1}{\Lambda}\text{PrRa}^{-0.5}\partial_x^2\right) u_i{}^{n+\frac{1}{3}} = \tfrac{1}{\Lambda}Q_i{}^n \qquad \text{w/ BC on } \mathbf{e}_x$$

$$\left(1 - \tfrac{1}{\Lambda}\text{PrRa}^{-0.5}\partial_y^2\right) u_i{}^{n+\frac{2}{3}} = u_i{}^{n+\frac{1}{3}} \qquad \text{w/ BC on } \mathbf{e}_y \tag{A.11}$$

$$\left(1 - \tfrac{1}{\Lambda}\text{PrRa}^{-0.5}\partial_z^2\right) u_i{}^* = u_i{}^{n+\frac{2}{3}} \qquad \text{w/ BC on } \mathbf{e}_z$$

with each ADI sub-step taking the form of a one-dimensional Helmholtz problem.

Solution of the velocity-pressure coupling: projection step

In the projection step, we assume the difference $(\mathbf{u}^{n+1} - \mathbf{u}^*)$ to be derived from a scalar function Π, called the pressure potential term

$$\Lambda(u_i{}^{n+1} - u_i{}^*) \equiv -\partial_i\Pi^{n+1}, \text{ with } u_n{}^{n+1} = u_n{}^* = 0 \text{ on the boundaries} \tag{A.12}$$

Taking the divergence and introducing (A.12) one obtains a Poisson equation

$$\partial_j^2\Pi^{n+1} = \Lambda\partial_i u_i{}^*, \text{ with } \partial_n\Pi^{n+1} = 0 \text{ on the boundaries} \tag{A.13}$$

Solution of the velocity-pressure coupling: correction step

After having obtained a solution for Π^{n+1}, the corrected velocity field is evaluated as

$$u_i{}^{n+1} = u_i{}^* - \frac{1}{\Lambda}\partial_i\Pi^{n+1} \tag{A.14}$$

Note that for the velocity field $\mathbf{u}^{n+1}$ satisfy equation (A.4a) the pressure term must be such that

$$p^{n+1} = p^n + \frac{1}{\Lambda}\Pi^{n+1} - \text{PrRa}^{-0.5}\partial_i u_i{}^* \tag{A.15}$$

Adding equations (A.9) and (A.12) leaves

$$\Lambda u_i{}^{n+1} - \text{PrRa}^{-0.5}\left(\partial_j^2 u_i{}^* - \partial_j\partial_i u_i{}^*\right) = Q_i{}^n - \partial_i p^{n+1} \tag{A.16}$$

197

where $\partial_j^2 u_i^{\mathbf{n+1}} = \partial_j^2 u_i^* - \partial_j \partial_i u_i^*$ may be deduced from equation (A.12). Note that this condition ensures only that the imposed normal velocity be preserved for $\mathbf{u^{n+1}}$ and the splitting error manifest only in the form of an inexact tangential boundary condition on the velocity (Guermond et al., 2006).

A.2 Spatial discretization

We use an staggered grid arrangement (Harlow and Welch, 1965) with a central differentiation scheme (CDS) and linear interpolation for an overall second-order precision. For this arrangement one defines different type of grids. A cell centered grid for the scalar quantities, such as the temperature, pressure and density fields, and one additional grid for each velocity component.

Generation of grid points

The spatial discretization of the system is performed by first introducing an increasing sequence of points $[\mathbf{x_1}, \mathbf{x_2}, \cdots, \mathbf{x_{n_x}}]$ along the x-direction, $[\mathbf{y_1}, \mathbf{y_2}, \cdots, \mathbf{y_{n_y}}]$ along the y-direction, and $[\mathbf{z_1}, \mathbf{z_2}, \cdots, \mathbf{z_{n_z}}]$ along the z-direction.

Let us consider the points $\mathbf{x_i}$: These points can be either regularly spaced

$$\mathbf{x_i} = \Gamma_{\mathbf{x}} \frac{2\mathbf{i} - 3}{2(\mathbf{n_x} - 2)}, \quad \text{for } \mathbf{i} = 1, \cdots \mathbf{n_x} \tag{A.17}$$

where $\Gamma_{\mathbf{x}}$ is the aspect ratio on the x-direction.

Or these points can be spaced following a given function, like the hyperbolic tangent function.

$$\mathbf{x_i} = \begin{cases} -\mathbf{x_2} & \text{for } \mathbf{i} = 1 \\ \frac{1}{2}\Gamma_{\mathbf{x}} \left[1 + \frac{\tanh(\gamma(\frac{\mathbf{i}-1}{\mathbf{n_x}-1} - 0.5))}{\tanh(\gamma/2)} \right] & \text{for } \mathbf{i} = 2, \cdots, \mathbf{n_x} - 1 \\ 2\Gamma_{\mathbf{x}} - \mathbf{x_{n_x-1}} & \text{for } \mathbf{i} = \mathbf{n_x} \end{cases} \tag{A.18}$$

where γ is a coefficient for the stretching function.

We then introduce a second sequence of points along each direction: $[\mathbf{xu_0}, \mathbf{xu_1}, \cdots, \mathbf{xu_{n_x}}]$ along the x-direction, $[\mathbf{yv_0}, \mathbf{yv_1}, \cdots, \mathbf{yv_{n_y}}]$ along the y-direction, and $[\mathbf{zw_0}, \mathbf{zw_1}, \cdots, \mathbf{zw_{n_z}}]$ along the z-direction. Consider the sequence of points $\mathbf{xu_i}$

$$\mathbf{xu_i} = \begin{cases} -\mathbf{xu_2} & \text{for } \mathbf{i} = 0 \\ \frac{1}{2} \left(\mathbf{x_{i+1}} + \mathbf{x_i} \right) & \text{for } \mathbf{i} = 1, \cdots, \mathbf{n_x} - 1 - 1 \\ 2\Gamma_{\mathbf{x}} - \mathbf{xu_{n_x-2}} & \text{for } \mathbf{i} = \mathbf{n_x} \end{cases} \tag{A.19}$$

Distance between points

We will define a quantity $[\Delta\mathbf{x_1}, \Delta\mathbf{x_2}, \cdots, \Delta\mathbf{x_{n_x}}]$ as the length of the segment between the indicated points as follows. First, for each cell we define a forward spacing $\Delta\mathbf{x_i^+}$ and a
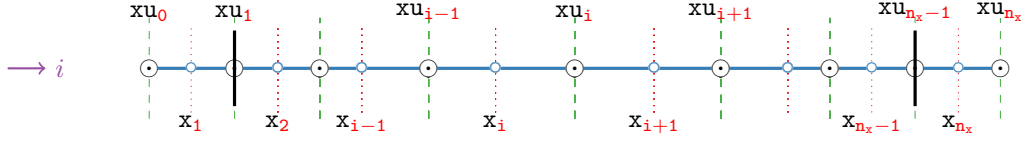
Figure A.1: Distribution of points $\mathtt{x_i}$ and $\mathtt{xu_i}$ along the x-direction. Boundary domains are shown in thick black lines.

backward spacing $\mathtt{\Delta x_i^-}$

$$\mathtt{\Delta x_i^+ = x_{i+1} - x_i} \qquad\qquad \text{for } \mathtt{i} = 1, \cdots, \mathtt{n_x} - 1$$

$$\mathtt{\Delta x_i^- = x_i - x_{i-1}} \qquad\qquad \text{for } \mathtt{i} = 2, \cdots, \mathtt{n_x}$$

and define the length of the segment $\mathtt{\Delta x_i}$

$$\mathtt{\Delta x_i} = \begin{cases} \mathtt{\Delta x_2} & \text{for } \mathtt{i} = 1 \\ \frac{1}{2}(\mathtt{\Delta x_i^+ + \Delta x_i^-}) & \text{for } \mathtt{i} = 2, \cdots, \mathtt{n_x} - 1 \\ \mathtt{\Delta x_{n_x-1}} & \text{for } \mathtt{i} = \mathtt{n_x} \end{cases}$$

In similar fashion, we define a quantity $[\mathtt{\Delta xu_1}, \mathtt{\Delta xu_2}, \cdots, \mathtt{\Delta xu_{n_x}}]$ as the length of the segment between the indicated points as follows. First, one introduces a forward and backward spacing $\mathtt{\Delta xu_i^+}$ and $\mathtt{\Delta xu_i^-}$, respectively

$$\mathtt{\Delta xu_i^+ = xu_{i+1} - xu_i} \qquad\qquad \text{for } \mathtt{i} = 1, \cdots, \mathtt{n_x} - 1$$

$$\mathtt{\Delta xu_i^- = xu_i - xu_{i-1}} \qquad\qquad \text{for } \mathtt{i} = 2, \cdots, \mathtt{n_x}$$

and we proceed to evaluate the length of the segment $\mathtt{\Delta xu_i}$

$$\mathtt{\Delta xu_i} = \begin{cases} 0 & \text{for } \mathtt{i} = 1, \mathtt{n_x} \\ \frac{1}{2}(\mathtt{\Delta x_i^+ + \Delta x_i^-}) & \text{for } \mathtt{i} = 2, \cdots, \mathtt{n_x} - 1 \end{cases}$$

The same process is repeated on the y and z directions.

Staggered grid arrangement

Four different grids are defined in function of these sets of points. We define the following quantities in each grid:

- Grid for the scalar quantities

$$\theta_{\mathtt{i,j,k}} = \theta(\mathtt{x_i, y_j, z_k}) \tag{A.20a}$$

$$\mathtt{p_{i,j,k}} = \mathtt{p}(\mathtt{x_i, y_j, z_k}) \tag{A.20b}$$

$$\Pi_{\mathtt{i,j,k}} = \Pi(\mathtt{x_i, y_j, z_k}) \tag{A.20c}$$

- Grid for the velocity component u_x

$$\mathtt{u_{i,j,k}} = u_x(\mathtt{xu_i, y_j, z_k}) \tag{A.20d}$$

- Grid for the velocity component u_y

$$\mathtt{v_{i,j,k}} = u_y(\mathtt{x_i}, \mathtt{yv_j}, \mathtt{z_k}) \tag{A.20e}$$

- Grid for the velocity component u_z

$$\mathtt{w_{i,j,k}} = u_z(\mathtt{x_i}, \mathtt{y_j}, \mathtt{zw_k}) \tag{A.20f}$$

Additionally, for any given node, for instance $\theta_{\mathtt{i,j,k}}$, one may introduce the following notation for the neighboring points in each direction,

$$\text{For a given point } \theta_{\mathtt{p}} = \theta_{\mathtt{i,j,k}} \qquad \begin{cases} \theta_{\mathtt{e}} = \theta_{\mathtt{i+1,j,k}} & , & \theta_{\mathtt{w}} = \theta_{\mathtt{i-1,j,k}} \\ \theta_{\mathtt{n}} = \theta_{\mathtt{i,j+1,k}} & , & \theta_{\mathtt{s}} = \theta_{\mathtt{i,j-1,k}} \\ \theta_{\mathtt{f}} = \theta_{\mathtt{i,j,k+1}} & , & \theta_{\mathtt{b}} = \theta_{\mathtt{i,j,k-1}} \end{cases}$$

where each subindex alluding the cardinal directions in the plane: east and west along x, north and south along y; and front and back along the transversal direction z.

The finite volume method

The principle of the finite volume method lies on the integration of the model equation over each of the control volumes. Observe that in a staggered arrangement, different control volumes exist for each grid. Consider for instance, field ϕ defined on the scalar grid

$$\int_{\Omega} \phi \; d\Omega - \oint_{\partial\Omega} D(\partial_n \phi) \; d\mathtt{S} = \int_{\Omega} Q \; d\Omega \tag{A.21}$$

where $d\Omega = dxdydz$ represents a differential element of the control volume $\Omega_{\mathtt{p}} = \mathtt{\Delta x_p \Delta y_p \Delta z_p}$ and $d\mathtt{S}$ a differential element of the control surface $\mathtt{S}$ composed of six faces defined as: $\mathtt{S_e = S_w = \Delta y_p \Delta z_p}$, $\mathtt{S_n = S_s = \Delta x_p \Delta z_p}$, and $\mathtt{S_b = S_f = \Delta x_p \Delta y_p}$.

In order to transform our model equation into an algebraic system, we need to approximate the volume (resp. surface) integrals using a simple second-order approximation considering the values at the center of the contol volume (resp. surface) as the mean value of the contol volume (resp. surface).

A.3   Solution for the energy equation

Consider the first ADI sub-step from equation (A.8) integrated over the scalar control volume as follows

$$\int_{\Omega} \theta^{\mathtt{n}+\frac{1}{3}} \; d\Omega - \frac{1}{\Lambda} \mathrm{Ra}^{-0.5} \left[\int \partial_x \theta |_{\mathtt{e}}^{\mathtt{n}+\frac{1}{3}} \; d\mathtt{S_e} - \int \partial_x \theta |_{\mathtt{w}}^{\mathtt{n}+\frac{1}{3}} \; d\mathtt{S_w} \right] = \frac{1}{\Lambda} \int_{\Omega} Q_{\theta}^{\mathtt{n}} \; d\Omega \tag{A.22}$$

Equations for the bulk nodes

Consider the interior points, or <u>bulk points</u>, which correspond to $i = 3, \cdots, n_x - 2$. Introducing the approximations to the volume and surface integrals one obtains

$$\Omega_p \theta_p - \frac{1}{\Lambda} \mathrm{Ra}^{-0.5} \left[S_e \frac{(\theta_e - \theta_p)}{\Delta x_p^+} - S_w \frac{(\theta_p - \theta_w)}{\Delta x_p^-} \right] = \frac{1}{\Lambda} \Omega_p Q_{\theta_p}^n \qquad (A.23)$$

Considering $\Omega_p = \Delta x_p \Delta y_p \Delta z_p$ and $S_e = S_w = \Delta y_p \Delta z_p$, we can rearrange the terms in the following tridiagonal form

$$A_p \theta_p - A_e \theta_e - A_w \theta_w = Q_{\theta_p}^n, \qquad \begin{cases} A_e &= \frac{\mathrm{Ra}^{-0.5}}{\Delta x_p \Delta x_p^+} \\ A_w &= \frac{\mathrm{Ra}^{-0.5}}{\Delta x_p \Delta x_p^-} \\ A_p &= \Lambda + A_e + A_w \end{cases} \qquad (A.24)$$

Before proceeding to solve this system, we have to apply the boundary conditions to the boundary nodes on both ends.

Equations for the boundary nodes

In order to implement the boundary condition additional nodes are placed outside the fluid domain, known as virtual or ghost nodes. These values are a function of the interpolation scheme selected, the values presented in this section correspond to linear interpolation and second order CDS.

Let us consider a node θ_p located on x_{n_x-1}, such that the neighboring node θ_e corresponds to a ghost point on x_{n_x} and the boundary is located on xu_{n_x-1}. On the boundary xu_{n_x-1}, we consider the following Robin boundary condition

$$\frac{(\theta_p + \theta_e)}{2} \mathbf{b} + \frac{(\theta_e - \theta_p)}{\Delta x_p^+} \mathbf{c} = \mathbf{g} \qquad (A.25)$$

with $\mathbf{b}$, $\mathbf{c}$, and $\mathbf{g}$ being the parameters of the boundary condition. The value required at the ghost node θ_e would read as

$$\theta_e = F_e \mathbf{g} + G_e \theta_p, \text{ with } F_e = \frac{2 \Delta x_p^+}{2\mathbf{c} + \mathbf{b}\Delta x_p^+}, \text{ and } G_e = \frac{2\mathbf{c} - \mathbf{b}\Delta x_p^+}{2\mathbf{c} + \mathbf{b}\Delta x_p^+} \qquad (A.26)$$

If we introduce this expression into equation (A.24) one obtains

$$A_p \theta_p - A_w \theta_w = Q_{\theta_p}^n + A_e F_e \mathbf{g}, \qquad \begin{cases} A_e &= \frac{\mathrm{Ra}^{-0.5}}{\Delta x_p \Delta x_p^+} \\ A_w &= \frac{\mathrm{Ra}^{-0.5}}{\Delta x_p \Delta x_p^-} \\ A_p &= \Lambda + A_w - A_e(G_e - 1) \end{cases} \qquad (A.27)$$

Now consider a node θ_p located on x_2, such that the neighboring node θ_w corresponds to a ghost point on x_1 and the boundary is located on xu_1, the value required at the ghost

point would be

$$\theta_{\mathtt{w}} = \mathtt{F_w}\mathbf{g} + \mathtt{G_w}\theta_{\mathtt{p}}, \ \text{with} \ \mathtt{F_w} = \frac{2\Delta\mathtt{x_p^-}}{2\mathbf{c} - \mathbf{b}\Delta\mathtt{x_p^-}}, \ \text{and} \ \mathtt{G_w} = \frac{2\mathbf{c} + \mathbf{b}\Delta\mathtt{x_p^-}}{2\mathbf{c} - \mathbf{b}\Delta\mathtt{x_p^-}} \tag{A.28}$$

and the resulting equation system would read as

$$\mathtt{A_p}\theta_{\mathtt{p}} - \mathtt{A_e}\theta_{\mathtt{e}} = \mathtt{Q}_{\theta\mathtt{p}}^{\mathtt{n}} + \mathtt{A_w}\mathtt{F_w}\mathbf{g}, \qquad
\begin{cases}
\mathtt{A_e} & = \frac{\mathrm{Ra}^{-0.5}}{\Delta\mathtt{x_p}\Delta\mathtt{x_p^+}} \\[2mm]
\mathtt{A_w} & = \frac{\mathrm{Ra}^{-0.5}}{\Delta\mathtt{x_p}\Delta\mathtt{x_p^-}} \\[2mm]
\mathtt{A_p} & = \Lambda + \mathtt{A_e} - \mathtt{A_w}(\mathtt{G_w} - 1)
\end{cases} \tag{A.29}$$

Resulting linear equation system

The resulting system is composed by equation (A.24) for the bulk nodes $\mathtt{i} = 3, \cdots, \mathtt{n_x} - 2$, equation (A.27) for boundary node $\mathtt{i} = \mathtt{n_x} - 1$ and equation (A.29) for boundary node $\mathtt{i} = 2$.

$$\begin{cases}
\mathtt{A_p}\theta_{\mathtt{p}}^{\mathtt{n}+\frac{1}{3}} - \mathtt{A_w}\theta_{\mathtt{w}}^{\mathtt{n}+\frac{1}{3}} = \mathtt{Q}_{\theta\mathtt{p}}^{\mathtt{n}} + \mathtt{A_e}\mathtt{F_e}\mathbf{g}, & \mathtt{i} = \mathtt{n_x} - 1 \\[2mm]
\mathtt{A_p}\theta_{\mathtt{p}}^{\mathtt{n}+\frac{1}{3}} - \mathtt{A_e}\theta_{\mathtt{e}}^{\mathtt{n}+\frac{1}{3}} - \mathtt{A_w}\theta_{\mathtt{w}}^{\mathtt{n}+\frac{1}{3}} = \mathtt{Q}_{\theta\mathtt{p}}^{\mathtt{n}}, & \mathtt{i} = 3, \cdots, \mathtt{n_x} - 2 \\[2mm]
\mathtt{A_p}\theta_{\mathtt{p}}^{\mathtt{n}+\frac{1}{3}} - \mathtt{A_e}\theta_{\mathtt{e}}^{\mathtt{n}+\frac{1}{3}} = \mathtt{Q}_{\theta\mathtt{p}}^{\mathtt{n}} + \mathtt{A_w}\mathtt{F_w}\mathbf{g}, & \mathtt{i} = 2
\end{cases} \tag{A.30}$$

with the matrix coefficients defined as

$$\mathtt{A_e} = \frac{\mathrm{Ra}^{-0.5}}{\Delta\mathtt{x_p}\Delta\mathtt{x_p^+}}, \ \mathtt{A_w} = \frac{\mathrm{Ra}^{-0.5}}{\Delta\mathtt{x_p}\Delta\mathtt{x_p^-}}, \ \mathtt{A_p} = \begin{cases}
\Lambda + \mathtt{A_w} - \mathtt{A_e}(\mathtt{G_e} - 1), & \mathtt{i} = \mathtt{n_x} - 1 \\[2mm]
\Lambda + \mathtt{A_e} + \mathtt{A_w}, & \mathtt{i} = 3, \cdots, \mathtt{n_x} - 2 \\[2mm]
\Lambda + \mathtt{A_e} - \mathtt{A_w}(\mathtt{G_w} - 1), & \mathtt{i} = 2
\end{cases}$$

This algebraic equation system may be solved using the tridiagonal matrix algorithm to obtain $\theta^{\mathtt{n}+\frac{1}{3}}$.

This procedure is repeated for the second ADI sub-steps by replacing $\mathtt{Q}_{\theta\mathtt{p}}^{\mathtt{n}}$ by $\theta^{\mathtt{n}+\frac{1}{3}}$ and introducing the corresponding boundary conditions accordingly.

$$\begin{cases}
\mathtt{A_p}\theta_{\mathtt{p}}^{\mathtt{n}+\frac{2}{3}} - \mathtt{A_s}\theta_{\mathtt{s}}^{\mathtt{n}+\frac{2}{3}} = \theta_{\mathtt{p}}^{\mathtt{n}+\frac{1}{3}} + \mathtt{A_n}\mathtt{F_n}\mathbf{g}, & \mathtt{j} = \mathtt{n_y} - 1 \\[2mm]
\mathtt{A_p}\theta_{\mathtt{p}}^{\mathtt{n}+\frac{2}{3}} - \mathtt{A_n}\theta_{\mathtt{n}}^{\mathtt{n}+\frac{2}{3}} - \mathtt{A_s}\theta_{\mathtt{s}}^{\mathtt{n}+\frac{2}{3}} = \theta_{\mathtt{p}}^{\mathtt{n}+\frac{1}{3}}, & \mathtt{j} = 3, \cdots, \mathtt{n_y} - 2 \\[2mm]
\mathtt{A_p}\theta_{\mathtt{p}}^{\mathtt{n}+\frac{2}{3}} - \mathtt{A_n}\theta_{\mathtt{n}}^{\mathtt{n}+\frac{2}{3}} = \theta_{\mathtt{p}}^{\mathtt{n}+\frac{1}{3}} + \mathtt{A_s}\mathtt{F_s}\mathbf{g}, & \mathtt{j} = 2
\end{cases} \tag{A.31}$$

with the matrix coefficients defined as

$$\mathtt{A_n} = \frac{\mathrm{Ra}^{-0.5}}{\Delta\mathtt{y_p}\Delta\mathtt{y_p^+}}, \ \mathtt{A_s} = \frac{\mathrm{Ra}^{-0.5}}{\Delta\mathtt{y_p}\Delta\mathtt{y_p^-}}, \ \mathtt{A_p} = \begin{cases}
\Lambda + \mathtt{A_s} - \mathtt{A_n}(\mathtt{G_n} - 1), & \mathtt{j} = \mathtt{n_y} - 1 \\[2mm]
\Lambda + \mathtt{A_n} + \mathtt{A_s}, & \mathtt{j} = 3, \cdots, \mathtt{n_y} - 2 \\[2mm]
\Lambda + \mathtt{A_n} - \mathtt{A_s}(\mathtt{G_s} - 1), & \mathtt{j} = 2
\end{cases}$$

$$\mathtt{F_n} = \frac{2\Delta\mathtt{y_p^+}}{2\mathbf{c} + \mathbf{b}\Delta\mathtt{y_p^+}}, \quad \mathtt{F_s} = \frac{2\Delta\mathtt{y_p^-}}{2\mathbf{c} - \mathbf{b}\Delta\mathtt{y_p^-}}, \quad \mathtt{G_n} = \frac{2\mathbf{c} - \mathbf{b}\Delta\mathtt{y_p^+}}{2\mathbf{c} + \mathbf{b}\Delta\mathtt{y_p^+}}, \quad \mathtt{G_s} = \frac{2\mathbf{c} + \mathbf{b}\Delta\mathtt{y_p^-}}{2\mathbf{c} - \mathbf{b}\Delta\mathtt{y_p^-}}$$

and so on for the last ADI sub-step by replacing $\theta^{\mathtt{n}+\frac{1}{3}}$ with $\theta^{\mathtt{n}+\frac{2}{3}}$.

A.4   Solution for the provisional velocity

Solution of the provisional velocity field takes place on the staggered grid, one for each component of the velocity field. For the first two ADI sub-steps the procedure is the same as the one used in the temperature equation. For the last ADI sub-step, in which the velocity component is aligned to the direction of the ADI sweep.

Consider for instance, the first ADI sub-step from equation (A.11) along the x-direction. For the velocity components perpendicular to the ADI sweep, i.e. v (resp. w), one integrates over the control volume $\Omega_{\mathtt{p}} = \Delta\mathtt{x}_{\mathtt{p}}\Delta\mathtt{yv}_{\mathtt{p}}\Delta\mathtt{z}_{\mathtt{p}}$ (resp. control volume $\Omega_{\mathtt{p}} = \Delta\mathtt{x}_{\mathtt{p}}\Delta\mathtt{y}_{\mathtt{p}}\Delta\mathtt{zw}_{\mathtt{p}}$).

$$\int_{\Omega} v^{\mathtt{n}+\frac{1}{3}} \, \mathrm{d}\Omega - \frac{1}{\Lambda}\mathrm{PrRa}^{-0.5}\left[\int \partial_x v\Big|_{\mathtt{e}}^{\mathtt{n}+\frac{1}{3}}\mathrm{d}\mathtt{S}_{\mathtt{e}} - \int \partial_x v\Big|_{\mathtt{w}}^{\mathtt{n}+\frac{1}{3}}\mathrm{d}\mathtt{S}_{\mathtt{w}}\right] = \frac{1}{\Lambda}\int_{\Omega} \mathtt{Q_y}^{\mathtt{n}} \, \mathrm{d}\Omega \qquad (\mathrm{A}.32)$$

and the corresponding control surfaces.

Equations for the bulk nodes

Consider the interior points, or <u>bulk points</u>, which correspond to $\mathtt{i} = 3, \cdots, \mathtt{n_x} - 2$. Introducing the approximations to the volume and surface integrals one obtains

$$\mathtt{v_p}^{\mathtt{n}+\frac{1}{3}} - \frac{1}{\Lambda}\frac{\mathrm{PrRa}^{-0.5}}{\Delta\mathtt{x_p}}\left[\frac{(\mathtt{v_e}^{\mathtt{n}+\frac{1}{3}} - \mathtt{v_p}^{\mathtt{n}+\frac{1}{3}})}{\Delta\mathtt{x_p^+}} - \frac{(\mathtt{v_p}^{\mathtt{n}+\frac{1}{3}} - \mathtt{v_w}^{\mathtt{n}+\frac{1}{3}})}{\Delta\mathtt{x_p^-}}\right] = \frac{1}{\Lambda}\mathtt{Q_{y_p}}^{\mathtt{n}} \qquad (\mathrm{A}.33)$$

For convenience, the terms are rearranged as follows

$$\mathtt{A_p v_p}^{\mathtt{n}+\frac{1}{3}} - \mathtt{A_e v_e}^{\mathtt{n}+\frac{1}{3}} - \mathtt{A_w v_w}^{\mathtt{n}+\frac{1}{3}} = \mathtt{Q_{y_p}}^{\mathtt{n}}, \qquad \begin{cases} \mathtt{A_e} &= \frac{\mathrm{PrRa}^{-0.5}}{\Delta\mathtt{x_p}\Delta\mathtt{x_p^+}} \\[2mm] \mathtt{A_w} &= \frac{\mathrm{PrRa}^{-0.5}}{\Delta\mathtt{x_p}\Delta\mathtt{x_p^-}} \\[2mm] \mathtt{A_p} &= \Lambda + \mathtt{A_e} + \mathtt{A_w} \end{cases} \qquad (\mathrm{A}.34)$$

Equations for the boundary nodes

Two types of boundary conditions are imposed on the tangential velocity: either a Dirichlet or a Neumann condition. As in the previous case, the domain boundary overlaps the control surface of the boundary nodes. Let us consider a node $\mathtt{v_p}$ located on $\mathtt{x_{n_x-1}}$, such that the neighboring node $\mathtt{v_e}$ corresponds to a ghost point on $\mathtt{x_{n_x}}$ and the boundary is located on $\mathtt{xu_{n_x-1}}$.

For convenience, let us consider a general Robin boundary conditionon said boundary

$$\frac{(\mathtt{v_p} + \mathtt{v_e})}{2}\mathbf{b} + \frac{(\mathtt{v_e} - \mathtt{v_p})}{\Delta\mathtt{x_p^+}}\mathbf{c} = \mathbf{g} \qquad (\mathrm{A}.35)$$

where $\mathbf{b}$, $\mathbf{c}$, and $\mathbf{g}$ are the parameters of the boundary condition. Setting $\mathbf{b} = 1$ and $\mathbf{c} = 0$ (resp. $\mathbf{b} = 0$ and $\mathbf{c} = 1$) results in a Dirichlet (resp. Neumann) boundary condition. The

value required at the ghost node v_e would read as

$$v_e = F_e g + G_e v_p, \quad F_e = \frac{2\Delta x_p^+}{2c + b\Delta x_p^+}, \quad G_e = \frac{2c - b\Delta x_p^+}{2c + b\Delta x_p^+} \qquad (A.36)$$

If we introduce this expression into equation (A.34) one obtains

$$A_p v_p^{n+\frac{1}{3}} - A_w v_w^{n+\frac{1}{3}} = Q_{y_p}^n + A_e F_e g, \qquad \begin{cases} A_e &= \frac{\text{PrRa}^{-0.5}}{\Delta x_p \Delta x_p^+} \\ A_w &= \frac{\text{PrRa}^{-0.5}}{\Delta x_p \Delta x_p^-} \\ A_p &= \Lambda + A_w - A_e(G_p - 1) \end{cases} \qquad (A.37)$$

Conversely, if we consider a node v_p located on x_2, such that the neighboring node θ_w corresponds to a ghost point on x_1 and the boundary is located on xu_1, the value required at the ghost point would be

$$v_w = F_w g + G_w v_p, \quad F_w = \frac{2\Delta x_p^-}{2c - b\Delta x_p^-}, \quad G_w = \frac{2c + b\Delta x_p^-}{2c - b\Delta x_p^-} \qquad (A.38)$$

and the resulting equation

$$A_p v_p^{n+\frac{1}{3}} - A_e v_w^{n+\frac{1}{3}} = Q_{y_p}^n + A_w F_w g, \qquad \begin{cases} A_e &= \frac{\text{PrRa}^{-0.5}}{\Delta x_p \Delta x_p^+} \\ A_w &= \frac{\text{PrRa}^{-0.5}}{\Delta x_p \Delta x_p^-} \\ A_p &= \Lambda + A_e - A_w(G_w - 1) \end{cases} \qquad (A.39)$$

Resulting linear equation system

The resulting system is composed by equation (A.34) for the bulk nodes $i = 3, \cdots, n_x - 2$, equation (A.37) for boundary node $i = n_x - 1$ and equation (A.39) for boundary node $i = 2$. This algebraic equation system may be solved using the tridiagonal matrix algorithm to obtain $v^{n+\frac{1}{3}}$. This procedure is repeated for the second ADI sub-step sweeping along the z-direction by replacing $Q_{y_p}^n$ by $v^{n+\frac{1}{3}}$ and introducing the corresponding boundary conditions.

Last ADI sub-step

In last ADI-substep the velocity component is aligned to the direction on which the ADI sub-step is applied, i.e. for v when sweeping in the y-direction. In this case, the domain boundary overlaps with the center of the boundary nodes and we may only impose an homogeneous Dirichlet condition.

For the bulk nodes, $j = 2, \cdots, n_y - 2$ one has

$$A_p v_p^* - A_n v_n^* - A_s v_s^* = v_p^{n+\frac{2}{3}}, \qquad \begin{cases} A_n &= \frac{\text{PrRa}^{-0.5}}{\Delta yv_p \Delta yv_p^+} \\ A_s &= \frac{\text{PrRa}^{-0.5}}{\Delta yv_p \Delta yv_p^-} \\ A_p &= \Lambda + A_n + A_s \end{cases} \qquad (A.40)$$

The value $\mathtt{v_p^*} = 0$ is directly imposed on the boundary nodes $\mathtt{j} = 1$ and $\mathtt{j} = \mathtt{n_x} - 1$. The values imposed on the ghost nodes are $\mathtt{v_w^*} = -\mathtt{v_e^*}$ for $\mathtt{j} = 1$ and $\mathtt{j} = \mathtt{n_x} - 1$. Finally, since the grid overlaps the domain boundaries, our equation system is modifies to ensure that $\mathtt{v_p^*} = 0$. We do this by imposing a very large number on the matrix coefficients,

$$\mathtt{A_p v_p^*} - \mathtt{A_n v_n^*} - \mathtt{A_s v_s^*} = \mathtt{v_p^{n+\frac{2}{3}}}, \qquad \begin{cases} \mathtt{A_n} &= \dfrac{\mathrm{PrRa}^{-0.5}}{\Delta \mathtt{yv_p} \Delta \mathtt{yv_p^+}} \\[2mm] \mathtt{A_s} &= \dfrac{\mathrm{PrRa}^{-0.5}}{\Delta \mathtt{yv_p} \Delta \mathtt{yv_p^-}} \\[2mm] \mathtt{A_p} &= 10^{30} \end{cases} \tag{A.41}$$

The resulting system is composed by equation (A.40) for the bulk nodes $\mathtt{j} = 2, \cdots, \mathtt{n_y} - 2$, equation (A.41) and equation (A.39) for the boundary nodes $\mathtt{j} = 1$ and $\mathtt{j} = \mathtt{n_y} - 1$. This algebraic equation system may be solved using the tridiagonal matrix algorithm to obtain v^*.

A.5 Solution for the pressure potential

Integration of equation (A.13) over the scalar control volume gives

$$\int_\Omega \partial_i^2 \Pi^{\mathtt{n+1}} \, \mathrm{d}\Omega = \Lambda \oint u_n{}^* \, \mathrm{d}\mathtt{S} \tag{A.42}$$

Introducing the the approximations from the finite volume method one obtains

$$\mathrm{D}_{xyz}^2 \Pi^{\mathtt{n+1}} = \mathtt{RHS_p} \tag{A.43}$$

where D_{xyz}^2 represents the discrete Laplacian operator in 3D which can be written as a Kronecker sum of discrete Laplacians in each direction (see for instance Demmel, 1997)

$$\mathrm{D}_{xyz}^2 = (\mathrm{D}_x^2 \otimes \mathbf{I} \otimes \mathbf{I}) + (\mathbf{I} \otimes \mathrm{D}_y^2 \otimes \mathbf{I}) + (\mathbf{I} \otimes \mathbf{I} \otimes \mathrm{D}_z^2) \tag{A.44}$$

also written as

$$\mathrm{D}_{xyz}^2 = \mathrm{D}_x^2 \oplus \mathrm{D}_y^2 \oplus \mathrm{D}_z^2 \tag{A.45}$$

with D_x^2, D_y^2, and D_z^2 being the one-dimensional discrete Laplacian operators in the x, y and z-direction, respectively. Each discrete Laplacian must be consistent with the boundary conditions imposed on each direction.

The right-hand term $\mathtt{RHS_p}$ is evaluated as

$$\mathtt{RHS_p} = \Lambda \left[\frac{(\mathtt{u_p^*} - \mathtt{u_w^*})}{\Delta \mathtt{x_p}} + \frac{(\mathtt{v_p^*} - \mathtt{v_s^*})}{\Delta \mathtt{y_p}} + \frac{(\mathtt{w_p^*} - \mathtt{w_b^*})}{\Delta \mathtt{z_p}} \right] \tag{A.46}$$

In this section, we will present the bidiagonalization algorithm used for the Poisson problem, sometimes referred to as a fast Poisson solver, see for instance (Golub et al., 1998; Strang, 2007; Shishkina, Shishkin, et al., 2009).

Since this method is presented in terms of the Kronecker product, it is convenient to recall the definition of the Kronecker product and some of its most important properties.

Kronecker product

For any given matrix $\mathbf{A}$ of size $m \times n$ and matrix $\mathbf{B}$ of size $p \times q$, then $\mathbf{C} = \mathbf{A} \otimes \mathbf{B}$ is a matrix of size $(mp) \times (nq)$

$$\mathbf{C} = \mathbf{A} \otimes \mathbf{B} = \begin{bmatrix} a_{1,1}\mathbf{B} & \cdots & a_{1,n}\mathbf{B} \\ \vdots & \ddots & \vdots \\ a_{m,1}\mathbf{B} & \cdots & a_{m,n}\mathbf{B} \end{bmatrix} \tag{A.47}$$

or as expressed in index notation as

$$c_{\alpha,\beta} = a_{ij}b_{kl}, \qquad \begin{cases} \alpha = p(i-1) + k \\ \beta = q(j-1) + l \end{cases} \tag{A.48}$$

The Kronecker product verifies the following properties

$$(\mathbf{A} \otimes \mathbf{B})(\mathbf{C} \otimes \mathbf{D}) = (\mathbf{AC}) \otimes (\mathbf{BD}) \qquad \text{Mixed-product} \tag{A.49a}$$

$$(\mathbf{A} \otimes \mathbf{B})^{-1} = (\mathbf{A}^{-1} \otimes \mathbf{B}^{-1}) \qquad \text{Inversion} \tag{A.49b}$$

$$(\mathbf{A} \otimes \mathbf{B})^{T} = (\mathbf{A}^{T} \otimes \mathbf{B}^{T}) \qquad \text{Transposition} \tag{A.49c}$$

Bidiagonalization procedure

Let us consider $D_x = \mathbf{R}\,\boldsymbol{\Lambda}^x\,\mathbf{R}^{-1}$ (resp. $D_y = \mathbf{S}\,\boldsymbol{\Lambda}^y\,\mathbf{S}^{-1}$), as the eigendecomposition of D_x (resp. D_y). Here, the matrix $\mathbf{R}$ (resp. $\mathbf{S}$) is an orthogonal matrix whose columns are the eigenvectors of D_x (resp. D_y), whereas the matrix $\boldsymbol{\Lambda}^x$ (resp. $\boldsymbol{\Lambda}^y$) is a diagonal matrix composed with the eigenvalues of D_x (resp. D_y).

The first term of equation (A.44) becomes

$$(D_x^2 \otimes \mathbf{I} \otimes \mathbf{I}) = ((\mathbf{R}\,\boldsymbol{\Lambda}^x\,\mathbf{R}^{-1}) \otimes \mathbf{I} \otimes \mathbf{I}) \tag{A.50}$$

We multiply this expression by $\mathbf{SS}^{-1}$ and use the mixed-product property from equation (A.49a) and the inversion rule equation (A.49b)

$$\begin{aligned} (D_x^2 \otimes \mathbf{I} \otimes \mathbf{I}) &= ((\mathbf{R}\,\boldsymbol{\Lambda}^x\,\mathbf{R}^{-1}) \otimes (\mathbf{S}\,\mathbf{I}\,\mathbf{S}^{-1})) \otimes \mathbf{I} \\ &= (\mathbf{R} \otimes \mathbf{S})((\boldsymbol{\Lambda}^x \mathbf{R}^{-1}) \otimes (\mathbf{I}\,\mathbf{S}^{-1})) \otimes \mathbf{I} \\ &= (\mathbf{R} \otimes \mathbf{S})(\boldsymbol{\Lambda}^x \otimes \mathbf{I})(\mathbf{R}^{-1} \otimes \mathbf{S}^{-1}) \otimes \mathbf{I} \\ &= (\mathbf{R} \otimes \mathbf{S} \otimes \mathbf{I})(\boldsymbol{\Lambda}^x \otimes \mathbf{I} \otimes \mathbf{I})(\mathbf{R} \otimes \mathbf{S} \otimes \mathbf{I})^{-1} \end{aligned}$$

Supossing D_x^2 to be real an symmetric matrix we can write

$$(D_x^2 \otimes \mathbf{I} \otimes \mathbf{I}) = (\mathbf{R} \otimes \mathbf{S} \otimes \mathbf{I})(\boldsymbol{\Lambda}^x \otimes \mathbf{I} \otimes \mathbf{I})(\mathbf{R} \otimes \mathbf{S} \otimes \mathbf{I})^{T} \tag{A.51}$$

Similarly, we can write the second term of equation (A.44) as

$$(\mathbf{I} \otimes D_y^2 \otimes \mathbf{I}) = (\mathbf{R} \otimes \mathbf{S} \otimes \mathbf{I})(\mathbf{I} \otimes \boldsymbol{\Lambda}^y \otimes \mathbf{I})(\mathbf{R} \otimes \mathbf{S} \otimes \mathbf{I})^{T} \tag{A.52}$$

By multiplying both sides of equation (A.43) by a factor $(\mathbf{R} \otimes \mathbf{S} \otimes \mathbf{I})^T$ and using expressions (A.51) and (A.52) we obtain a tridiagonal system of the form

$$(\mathbf{\Lambda}^x \oplus \mathbf{\Lambda}^y \oplus \mathrm{D}_z^2)\mathrm{Vec}(\widetilde{\Pi}_{\mathtt{i,j,k}}^{\mathtt{n+1}}) = (\widetilde{\mathrm{RHS}}_{\mathtt{i,j,k}}) \tag{A.53}$$

with $\widetilde{\Pi}_{\mathtt{i,j,k}}^{\mathtt{n+1}}$ being the pressure potential projected on the eigenspace

$$\widetilde{\Pi}_{\mathtt{i,j,k}}^{\mathtt{n+1}} = (\mathbf{R} \otimes \mathbf{S} \otimes \mathbf{I})^T \Pi_{\mathtt{i,j,k}}^{\mathtt{n+1}} \tag{A.54}$$

$\widetilde{\mathrm{RHS}}_{\mathtt{i,j,k}}$ being the right-hand side of equation (A.43) projected on the same eigenspace, and $\mathrm{Vec}(\cdots)$ the column vector operator.

Solution of the potential pressure term

The bidiagonalization algorithm can be summarized as follows

i. Evaluate the one-dimensional discrete Laplacian D_x^2 and D_y^2 with a homogeneous Neumann boundary condition and evaluate the corresponding eigenvalues and eigenvectors only once.

ii. Evaluate the one-dimensional discrete Laplacian D_z^2 imposing a homogeneous Neumann boundary condition.

iii. Evaluate $\widetilde{\mathrm{RHS}}_{\mathtt{i,j,k}}$ by multiplying the right-hand side of equation (A.43) by the $(\mathbf{R} \otimes \mathbf{S} \otimes \mathbf{I})^T$

$$\widetilde{\mathrm{RHS}}_{\mathtt{l,m,q}} = \sum_{\mathtt{i=2}}^{\mathtt{n_x-1}} \sum_{\mathtt{j=2}}^{\mathtt{n_y-1}} \sum_{\mathtt{k=2}}^{\mathtt{n_z-1}} (\mathbf{r}^\mathsf{T}{}_{\mathtt{l,i}} \mathbf{s}^\mathsf{T}{}_{\mathtt{m,j}} \delta_{\mathtt{qk}}) \, \mathrm{RHS}_{\mathtt{i,j,k}} \tag{A.55}$$

iv. Evaluate $\widetilde{\Pi}_{\mathtt{i,j,k}}^{\mathtt{n+1}}$ from equation (A.53) using the tridiagonal matrix algorithm.

$$\widetilde{\mathrm{D}}_{\mathtt{l,m,q}}\widetilde{\Pi}_{\mathtt{l,m,q}}^{\mathtt{n+1}} - \widetilde{\mathrm{U}}_{\mathtt{l,m,q}}\widetilde{\Pi}_{\mathtt{l,m,q+1}}^{\mathtt{n+1}} - \widetilde{\mathrm{L}}_{\mathtt{l,m,q}}\widetilde{\Pi}_{\mathtt{l,m,q-1}}^{\mathtt{n+1}} = \widetilde{\mathrm{RHS}}_{\mathtt{l,m,q}} \tag{A.56}$$

with the corresponding coefficients defined as

$$\begin{cases} \widetilde{\mathrm{D}}_{\mathtt{l,m,q}} &= \frac{1}{\Delta \mathtt{z}_\mathtt{q}^+} + \frac{1}{\Delta \mathtt{z}_\mathtt{q}^-} + \Lambda^\mathtt{x}{}_{\mathtt{l,l}} + \Lambda^\mathtt{y}{}_{\mathtt{m,m}} \\ \widetilde{\mathrm{U}}_{\mathtt{l,m,q}} &= \frac{1}{\Delta \mathtt{z}_\mathtt{q}^+} \\ \widetilde{\mathrm{L}}_{\mathtt{l,m,q}} &= \frac{1}{\Delta \mathtt{z}_\mathtt{q}^-} \end{cases} \tag{A.57}$$

while $\widetilde{\mathrm{L}}_{\mathtt{l,m,q}} = 0$ for $\mathtt{q} = 2$ and $\widetilde{\mathrm{U}}_{\mathtt{l,m,q}} = 0$ for $\mathtt{q} = \mathtt{n_z} - 1$.

v. Finally, one multiplies $\widetilde{\Pi}_{\mathtt{l,m,q}}^{\mathtt{n+1}}$ by $(\mathbf{R} \otimes \mathbf{S} \otimes \mathbf{I})$ to obtain $\Pi_{\mathtt{i,j,k}}^{\mathtt{n+1}}$.

$$\Pi_{\mathtt{i,j,k}}^{\mathtt{n+1}} = \sum_{\mathtt{l=2}}^{\mathtt{n_x-1}} \sum_{\mathtt{m=2}}^{\mathtt{n_y-1}} (\mathbf{r}^\mathsf{T}{}_{\mathtt{l,i}} \mathbf{s}^\mathsf{T}{}_{\mathtt{m,j}} \delta_{\mathtt{nk}}) \, \widetilde{\Pi}_{\mathtt{l,m,k}}^{\mathtt{n+1}} \tag{A.58}$$

207

A.6 Corrected pressure and velocity fields

The correction for the velocity terms is obtained from equation (A.12)

$$u_p^{n+1} = u_p^* - \frac{(\Pi_e^{n+1} - \Pi_p^{n+1})}{\Delta x u_p} \tag{A.59a}$$

$$v_p^{n+1} = v_p^* - \frac{(\Pi_n^{n+1} - \Pi_p^{n+1})}{\Delta y v_p} \tag{A.59b}$$

$$w_p^{n+1} = w_p^* - \frac{(\Pi_f^{n+1} - \Pi_p^{n+1})}{\Delta z w_p} \tag{A.59c}$$

whereas the pressure field is obtained from equation (A.15)

$$p_p^{n+1} = p_p^n + \frac{1}{\Lambda}\Pi_p^{n+1} - \mathrm{PrRa}^{-0.5}\left[\frac{(u_p^* - u_w^*)}{\Delta x_p} + \frac{(v_p^* - v_s^*)}{\Delta y_p} + \frac{(w_p^* - w_b^*)}{\Delta z_p}\right] \tag{A.60}$$

Appendix B

Code BASILISK

Basilisk is an ensemble of solver-blocks written using an extension to the C programming language, called Basilisk C, useful to write discretization schemes in Cartesian grids (Stéphane Popinet, 2016). Instead of writing an entirely new code, existing blocks of code were combined to solve Boussinesq equations. Before presenting the numerical method used, it is convenient to mention some of the main features of this code.

B.1 Main features

B.1.1 Regular, Multi-grid or Adaptative grids
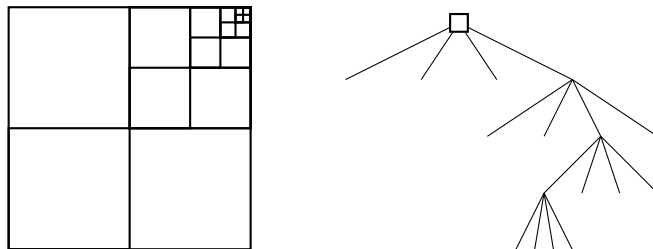
Figure B.1: Schematics of the spatial discretization and hierarchical structure for tree-based grids.

Three type of grids are available to us in Basilisk C: regular Cartesian grids (one level only), multi-level grids, and tree-based adaptative grids. Each discretized cell is a square in 2D and a cube in 3D. Code written in Basilisk C is meant to be the same for different types of grids. For tree-based grids, cells are organized hierarchically in levels, from a root cell placed at the lowest level to a leaf cell located at highest level. Each 'parent' cell may nest 4 'child' cells (resp. 8 cells) for 2D (resp. 3D) cells, see figure B.1. Each cell has at least one direct neighbour at the same level in each direction. Variables can be defined at the center of each cell (when declared using `scalar, vector, tensor`), on the center of the cell faces (using `face vector`), or at the vertex of the cell (using `vertex scalar`). In the present work, we limit ourselves to multi-level grids.

The use of pre-defined stencils simplifies the access to neighboring points. Assuming the shaded cell in figure B.2, corresponds to the current cell, the symbol × placed at the center

(a) `scalar, vector`

(b) `scalar vertex`

(c) `face vector`

x-component

y-component
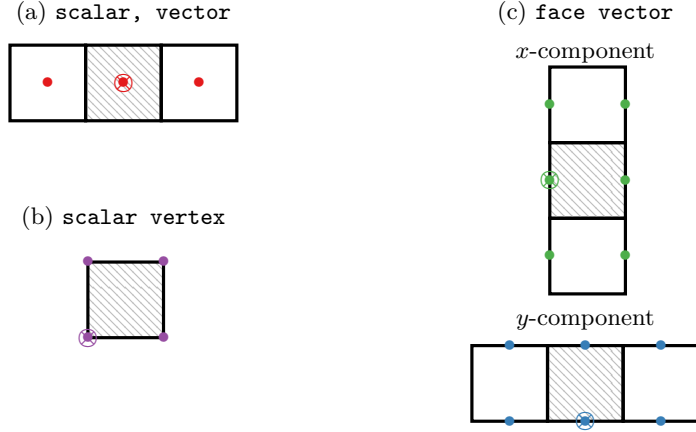
Figure B.2: Stencils for different scalar and vector fields used in Basilisk C. The hatched region indicates the current cell, while a $\otimes$ symbol marks the placement of the $[0, 0, 0]$ index relative to this cell.

of the cell, cell face, or cell vertex, accordingly, is associated to the index $[0, 0, 0]$ in the local stencil. Neighboring cells are referred to by their relative placement with respect to the current cell: The neighboring cell in the positive x-direction would correspond to index $[1, 0, 0]$, and so on. The stencils automatically define certain variables associated to the current grid, such as the position (x, y, z) of the current cell.

B.1.2 Fields and Iterators

The main difference with respect to other numerical codes, is the introduction of pre-defined types for scalar, vector, and tensor fields, and field iterators meant to reduce duplicate code. Consider for instance, the following scalar field $a(\mathbf{x})$ in $\mathbb{R}^2$, declared as follows

```
scalar a[];              // Declare field
foreach()                // Iterate over each cell
  a[] = (x + y)*Delta;   // Initialize values
```

A vector field $\mathbf{b}(\mathbf{x})$, defined as the discrete gradient of field $a(\mathbf{x})$ in $\mathbb{R}^2$, $\mathbf{b} = \nabla a$ evaluated at the center of the cell as

```
vector b[];              // Declare field
foreach(){               // Iterate over each cell
  b.x[] = (a[1,0] - a[-1,0])/sq(Delta); // Gradient in X
  b.y[] = (a[0,1] - a[0,-1])/sq(Delta); // Gradient in Y
}
```

210

B.1.3 Events and building blocks

The second main characteristic of <u>Basilisk C</u> is the use of *events*. An event allows to evaluate a code block or perform any given action at the specified interval, be it every n steps, or every fixed amount of time. The syntax to declare a new event `name`, every 1 time unit from t=1 to t=5, would read as follows

```
event name (t = 1; t <= 5; t += 1) {
  do_something();
}
```

Certain pre-defined solvers are available, with each one having events of their own. Consider for instance, the centered formulation of the incompressible Navier-Stokes equation included in `centered.h` (the numerical method will be introduced in the following section). For each time step, one evaluates the code contained inside the following events: `dtmax`, `stability`, `VOF`, `tracer_advection`, `properties`, `advection_term`, `viscosity`, `acceleration`, and `projection` events.

Instead of modifying these existing routines and trying to adapt them to a particular problem, we seek to re-use the existing code and use these events to make the required changes. Consider the event `properties` contained inside `centered.h`

```
event properties (i++,last) {
  boundary ({alpha, mu, rho});
}
```

Suppose that we define an event which is also named `properties` inside our main routine

```
#include "centered.h"
event properties (i++) {
  do_something(alpha, mu, rho);
}
```

The code contained inside the new event will be introduced just **before** the event of the same name inside the included file `centered.h`. If we include several files that contain an event with the same name, the code will be executed in the order of the inclusion. Instead of modifying the source code, we are piggybacking on the existing code. This building-block approach is specially well suited for split-step methods.

In the following section, we will provide a brief description of the numerical method used to solve the Bousinesq equation in Cartesian multi-level grids.

B.2   Overall temporal discretization scheme

A solution to the Boussinesq equation system is obtained by combining a centered formulation of the incompressible Navier-Stokes equations (see `centered.h`), a diffusion solver for the temperature field (see `diffusion.h`) and one tracer advection event (see `tracer.h`). The numerical scheme resulting from this combination has a global second-order accuracy, as shown in (Bell et al., 1989).

The formulation of the incompressible Navier-Stokes equations uses the fractional-step method using a staggered in time discretization of the velocity and the scalar fields (see Popinet, 2003; Popinet, 2009): one supposes the velocity field to be known at time n and the scalar fields (pressure, temperature, density) to be known at time $n - 1/2$, and one computes velocity at time $n + 1$ and scalars at time $n + 1/2$,

$$\partial_i u_i^{n+1} = 0 \tag{B.1a}$$

$$\frac{(u_i^{n+1} - u_i^{n})}{\Delta t} + \partial_j (u_j u_i)^{n+\frac{1}{2}} = -\partial_i \mathrm{p}^{n+\frac{1}{2}} + \frac{\nu \partial_j (\partial_j u_i^{n+1} + \partial_j u_i^{n})}{2} + a_i^{n+\frac{1}{2}} \tag{B.1b}$$

$$\frac{\theta^{n+\frac{1}{2}} - \theta^{n-\frac{1}{2}}}{\Delta t} + \partial_j (u_j \theta)^{n} = \partial_j (\kappa \partial_j \theta)^{n+\frac{1}{2}} \tag{B.1c}$$

where $\nu = \mathrm{Pr}\mathrm{Ra}^{-0.5}$ corresponds to the kinematic viscosity, $\kappa = \mathrm{Ra}^{-0.5}$ to the thermal diffusive coefficient. Since the external forcing term $a_i^{n+\frac{1}{2}}$ in our case corresponds to the buoyancy force $a_i^{n+\frac{1}{2}} = -\mathrm{Pr}\theta^{n+\frac{1}{2}} \delta_{i2}$, it is compulsory to start by solving the equation for temperature (B.1c), before the equations (B.1a) and (B.1b).

In the following, we use the lowercase (resp. uppercase) variables, for instance u_i and θ (resp. U_i and Θ) to identify the quantities evaluated at the cell center (resp. at the center of the cell face). The velocity component at the center of the face U_i^{n} is evaluated from the velocity u_i^{n} from both cells sharing this face through a simple interpolation. In addition, subscript (d) refers to the cell faces.

B.2.1   Solution of the energy equation

The solution of equation (B.1c) is obtained in two steps. First, the advection terms are evaluated using the Bell-Collela-Glaz (BCG) second-order un-split upwind scheme. Second, an Helmholtz-Poisson problem for the energy equation is solved using a multi-level Poisson solver to obtain $\theta^{n+\frac{1}{2}}$.

Approximation of the scalar advection term

Consider the advection term $\partial_j (u_j \theta)^{n}$ integrated over a control volume Ω, which is approximated as the sum of the fluxes in each control surface (4 in 2D or 6 in 3D).

$$\int_\Omega \partial_j (u_j \theta)^{n} \, \mathrm{d}\Omega = \oint_{\partial\Omega} (n_j u_j^{n}) \theta^{n} \, \mathrm{d}\mathtt{S} \approx \sum_{(d)} \mathtt{S}_{(d)} (n_j U_j^{n}) \Theta^{n} \tag{B.2}$$

where n_j corresponds to the (outward) normal unit vector at the face center.

Notation-wise, we refer to $\theta_{[0,0,0]}$ as the value of the temperature at the center of the current cell. The values $\theta_{[0,-1,0]}$, $\theta_{[0,0,0]}$, and $\theta_{[0,1,0]}$ correspond to the temperature evaluated at the center of three contiguous cells along the y-direction. Similarly, $\theta_{[0,0,-1]}$, $\theta_{[0,0,0]}$, and $\theta_{[0,0,1]}$ indicate the temperature evaluated at the center of three contiguous cells along the z-direction.

The process may be explained using the case of cell face that is perpendicular to the x-axis and located west of the current cell center [0,0,0]. Note that this process has to be repeated in each face, before proceeding to evaluate the total temperature flux using equation (B.2). Based on the face velocity $U_x{}^{\mathbf{n}}$, we identify the cell located upstream as $\mathcal{C}$ and located downstream as $\mathcal{N}_d$. We may define an index k, k $= -1$ for ($U_x{}^{\mathbf{n}-\frac{1}{2}} > 0$) and k $= 0$ otherwise, such that $\mathcal{C} = [\mathrm{k}, 0, 0]$.

Since the temperature field (and other scalar fields for that matter) $\Theta^{\mathbf{n}}$ is staggered in time and in space with respect to the centered field $\theta^{\mathbf{n}-\frac{1}{2}}$, the value $\Theta^{\mathbf{n}}$ has to be approximated. Two possible values of $\Theta^{\mathbf{n}}$ may be constructed (one from each cell sharing the same face). Since our main focus is the advection process, we consider the value obtained from the cell $\mathcal{C}$ located upstream using the BCG advection scheme.

We perform a Taylor series expansion around the upstream cell $\mathcal{C}$

$$\Theta^{\mathbf{n}} = \theta^{\mathbf{n}-\frac{1}{2}} + s\frac{\Delta \mathsf{x}}{2}(\partial_x\theta)^{\mathbf{n}-\frac{1}{2}} + \frac{\Delta \mathsf{t}}{2}(\partial_t\theta)^{\mathbf{n}-\frac{1}{2}} + \mathcal{O}(\Delta \mathsf{t}^2, \Delta \mathsf{x}^2) \tag{B.3a}$$

where $s = \mathrm{sign}(U_x{}^{\mathbf{n}})$. The temporal derivative is approximated in terms of spatial derivatives using the energy equation (discarding the diffusive terms) as

$$(\partial_t\theta)^{\mathbf{n}-\frac{1}{2}} = -(u_j\partial_j\theta)^{\mathbf{n}-\frac{1}{2}} \tag{B.3b}$$

Combining both expressions leads to

$$\Theta^{\mathbf{n}} = \theta^{\mathbf{n}-\frac{1}{2}} + s\frac{\Delta \mathsf{x}}{2}(\partial_x\theta)^{\mathbf{n}-\frac{1}{2}} - \frac{\Delta \mathsf{t}}{2}(u_j\widetilde{\partial}_j\theta)^{\mathbf{n}-\frac{1}{2}} \tag{B.3c}$$

where $\partial_x\theta$ is approximated by

$$(\partial_x\theta)^{\mathbf{n}-\frac{1}{2}}_{[\mathrm{k},0,0]} = (\theta^{\mathbf{n}-\frac{1}{2}}_{[\mathrm{k}+1,0,0]} - \theta^{\mathbf{n}-\frac{1}{2}}_{[\mathrm{k}-1,0,0]})/(2\Delta \mathsf{x}) \tag{B.4}$$

and $\widetilde{\partial}_j\theta$ denotes the spatial derivatives $\partial_j\theta$ evaluated numerically as follows. The gradient normal to the cell face, i.e. $u_x\widetilde{\partial}_x\theta$, is approximated by

$$(u_x\widetilde{\partial}_x\theta)^{\mathbf{n}-\frac{1}{2}}_{[\mathrm{k},0,0]} = U_x{}^{\mathbf{n}}_{[0,0,0]}(\theta^{\mathbf{n}-\frac{1}{2}}_{[\mathrm{k}+1,0,0]} - \theta^{\mathbf{n}-\frac{1}{2}}_{[\mathrm{k}-1,0,0]})/(2\Delta \mathsf{x}) \tag{B.5a}$$

For the other directions we do something different

$$(u_y\widetilde{\partial}_y\theta)^{\mathbf{n}-\frac{1}{2}} \approx \begin{cases} \widehat{u_y}^{\mathbf{n}}(\theta^{\mathbf{n}-\frac{1}{2}}_{[\mathrm{k},1,0]} - \theta^{\mathbf{n}-\frac{1}{2}}_{[\mathrm{k},0,0]})/\Delta \mathsf{y} & \text{if } \widehat{u_y}^{\mathbf{n}} < 0 \\ \widehat{u_y}^{\mathbf{n}}(\theta^{\mathbf{n}-\frac{1}{2}}_{[\mathrm{k},0,0]} - \theta^{\mathbf{n}-\frac{1}{2}}_{[\mathrm{k},-1,0]})/\Delta \mathsf{y} & \text{if } \widehat{u_y}^{\mathbf{n}} \geq 0 \end{cases} \tag{B.5b}$$

$$(u_z\widetilde{\partial}_z\theta)^{\mathbf{n}-\frac{1}{2}} \approx \begin{cases} \widehat{u_z}^{\mathbf{n}}(\theta^{\mathbf{n}-\frac{1}{2}}_{[\mathrm{k},0,1]} - \theta^{\mathbf{n}-\frac{1}{2}}_{[\mathrm{k},0,0]})/\Delta \mathsf{z} & \text{if } \widehat{u_z}^{\mathbf{n}} < 0 \\ \widehat{u_z}^{\mathbf{n}}(\theta^{\mathbf{n}-\frac{1}{2}}_{[\mathrm{k},0,0]} - \theta^{\mathbf{n}-\frac{1}{2}}_{[\mathrm{k},0,-1]})/\Delta \mathsf{z} & \text{if } \widehat{u_z}^{\mathbf{n}} \geq 0 \end{cases} \tag{B.5c}$$

where $\widehat{u_y}^{\mathbf{n}}$ and $\widehat{u_z}^{\mathbf{n}}$ are evaluated as follows

$$\widehat{u_y}^{\mathbf{n}} = \frac{1}{2}(U_{y[\mathbf{k},1,0]}^{\mathbf{n}} + U_{y[\mathbf{k},0,0]}^{\mathbf{n}}) \tag{B.6}$$

$$\widehat{u_z}^{\mathbf{n}} = \frac{1}{2}(U_{z[\mathbf{k},0,1]}^{\mathbf{n}} + U_{z[\mathbf{k},0,0]}^{\mathbf{n}}) \tag{B.7}$$

B.2.2 Solution of the velocity-pressure coupling

The velocity-pressure coupling is treated using a classical time-splitting projection method (see Chorin, 1969). First, the pressure term is ignored in order to obtain a provisional velocity field $\mathbf{u}^*$ which may not be divergence-free.

$$\frac{(u_i^* - u_i^{\mathbf{n}})}{\Delta \mathtt{t}} + \partial_j(u_j u_i)^{\mathbf{n}+\frac{1}{2}} = \partial_j(\nu(\partial_j u_i^* + \partial_j u_i^{\mathbf{n}})) + a_i^{\mathbf{n}+\frac{1}{2}} \tag{B.8a}$$

The momentum equation has the general form of an Helmholtz-type equation, which can be solved using a multi-level Poisson-Helmholtz solver if the advection term is provided, see below.

Second, a correction is sought by projecting the provisional velocity $\mathbf{u}^*$ into a divergence-free space, using a pressure such that

$$\frac{u_i^{\mathbf{n}+1} - u_i^*}{\Delta \mathtt{t}} = -\partial_i \mathtt{p}^{\mathbf{n}+\frac{1}{2}} \tag{B.8b}$$

Evaluated from the following Poisson problem

$$\partial_i\left(\Delta \mathtt{t}\partial_i \mathtt{p}^{\mathbf{n}+\frac{1}{2}}\right) = \partial_i u_i^* \tag{B.8c}$$

in order to verify the incompressibility

$$\partial_i u_i^{\mathbf{n}+1} = 0 \tag{B.8d}$$

This problem can be solved using the multi-level Poisson-Helmholtz solver (see `poisson.h`).

Approximation of the advection term

Consider the advection term integrated over a control volume Ω, which is approximated as the sum of the fluxes in each control surface (4 in 2D or 6 in 3D).

$$\int_\Omega \partial_j(u_j u_i)^{\mathbf{n}+\frac{1}{2}} \, \mathrm{d}\Omega = \oint_{\partial\Omega} ((n_j u_j)u_i)^{\mathbf{n}+\frac{1}{2}} \, \mathrm{d}\mathtt{S} \approx \sum_{(d)} \mathtt{S}_{(\mathbf{d})}(n_j U_j^{\mathbf{n}+\frac{1}{2}})\widehat{U_i}^{\mathbf{n}+\frac{1}{2}} \tag{B.9}$$

where n_j corresponds to the (outward) normal unit vector at the face center.

A priori, both $\widehat{U_i}^{\mathbf{n}+\frac{1}{2}}$ and $U_i^{\mathbf{n}+\frac{1}{2}}$ represent the same quantity, but are treated in a different way. In this context, $\widehat{U_i}^{\mathbf{n}+\frac{1}{2}}$ represents the "advectee" and $U_i^{\mathbf{n}+\frac{1}{2}}$ represents the "advector". The "advectee" is treated in the same way as any other advected field, whereas the "advector" receives an special treatment to ensure the conservation of mass. Both procedures will be detailed shortly.

In the following, we refer to $u_{i[0,0,0]}$ as the value of the ith-velocity component at the center of the current cell. The values $u_{i[0,-1,0]}$, $u_{i[0,0,0]}$, and $u_{i[0,1,0]}$ indicate the ith velocity component evaluated at the center of three contiguous cells along the y-direction. Similarly, we consider $u_{i[0,0,-1]}$, $u_{i[0,0,0]}$, and $u_{i[0,0,1]}$ indicate the velocity component evaluated at the center of three contiguous cells along the z-direction.

Consider the previous example with a control surface perpendicular to the x-direction located west of the current cell center $[0,0,0]$. Based on the face velocity $U_x{}^{\mathbf{n}}$, we identify the cell located upstream as $\mathcal{C}$ and located downstream as $\mathcal{N}_d$. We may define an index $\textcolor{red}{\mathrm{k}}$, $\textcolor{red}{\mathrm{k}} = -1$ for $(U_x{}^{\mathbf{n}} > 0)$ and $\textcolor{red}{\mathrm{k}} = 0$ otherwise, such that $\mathcal{C} = [\textcolor{red}{\mathrm{k}}, 0, 0]$.

Evaluation of the "advectee", i.e. $\widehat{U_i}^{\mathbf{n}+\frac{1}{2}}$

Since the required face velocity field $\widehat{U_i}^{\mathbf{n}+\frac{1}{2}}$ is staggered in time and in space with respect to the known velocity field $u_i{}^{\mathbf{n}}$, the value $\widehat{U_i}^{\mathbf{n}+\frac{1}{2}}$ has to be approximated. For given a cell face, two values of $\widehat{U_i}^{\mathbf{n}+\frac{1}{2}}$ may be constructed. Following a similar reasoning to the one used on the previous section, one selects the value obtained from the upstream cell $\mathcal{C}$ using a BCG advection scheme.

We perform a Taylor series expansion around the upstream cell $\mathcal{C}$

$$\widehat{U_i}^{\mathbf{n}+\frac{1}{2}} = u_i{}^{\mathbf{n}} + s\frac{\textcolor{red}{\Delta\mathbf{x}}}{2}(\partial_x u_i)^{\mathbf{n}} + \frac{\textcolor{red}{\Delta\mathbf{t}}}{2}(\partial_t u_i)^{\mathbf{n}} + \mathcal{O}(\textcolor{red}{\Delta\mathbf{t}}^2, \textcolor{red}{\Delta\mathbf{x}}^2) \tag{B.10a}$$

where $s = \text{sign}(U_x{}^{\mathbf{n}})$. The evolution of u_i is assumed to be governed by a non-conservative form of Euler equation in order to approximate the temporal derivative in terms of the spatial derivatives of u_i

$$(\partial_t u_i)^{\mathbf{n}} = -(u_j \partial_j u_i)^{\mathbf{n}} + g_i{}^{\mathbf{n}} \tag{B.10b}$$

where $g_i{}^{\mathbf{n}}$ contains both the pressure gradient and the external forcing term, $g_i{}^{\mathbf{n}} = -(\partial_i p)^{\mathbf{n}} + a_i{}^{\mathbf{n}}$ both evaluated at the cell face. Since scalar quantities may not be available at this instant, as a first approximation, we assume that

$$g_i{}^{\mathbf{n}} = -(\partial_i p)^{\mathbf{n}-\frac{1}{2}} + a_i{}^{\mathbf{n}-\frac{1}{2}} \tag{B.10c}$$

This leaves the following expression

$$\widehat{U_i}^{\mathbf{n}+\frac{1}{2}} = u_i{}^{\mathbf{n}} + s\frac{\textcolor{red}{\Delta\mathbf{x}}}{2}(\partial_x u_i)^{\mathbf{n}} - \frac{\textcolor{red}{\Delta\mathbf{t}}}{2}\left[(u_j \widetilde{\partial}_j u_i)^{\mathbf{n}} + g_i{}^{\mathbf{n}}\right] \tag{B.10d}$$

where $(\partial_x u_i)^{\mathbf{n}}$ is approximated by

$$(\partial_x u_i)^{\mathbf{n}}_{[\textcolor{red}{\mathrm{k}},0,0]} = (u_{i[\textcolor{red}{\mathrm{k}}+1,0,0]}^{\mathbf{n}} - u_{i[\textcolor{red}{\mathrm{k}}-1,0,0]}^{\mathbf{n}})/(2\textcolor{red}{\Delta\mathbf{x}}) \tag{B.11}$$

and $\widetilde{\partial}_j$ indicates the spatial derivatives ∂_j evaluated numerically as follows. The gradient normal to the cell face, i.e. $u_x \widetilde{\partial}_x u_i$, is approximated by

$$(u_x \widetilde{\partial}_x u_i)^{\mathbf{n}}_{[\textcolor{red}{\mathrm{k}},0,0]} = U_{x[0,0,0]}^{\mathbf{n}+\frac{1}{2}}(u_{i[\textcolor{red}{\mathrm{k}}+1,0,0]}^{\mathbf{n}} - u_{i[\textcolor{red}{\mathrm{k}}-1,0,0]}^{\mathbf{n}})/(2\textcolor{red}{\Delta\mathbf{x}}) \tag{B.12a}$$

For the other directions we do something different

$$(u_y \widetilde{\partial}_y u_i)^{\mathbf{n}} \approx \begin{cases} \widehat{u_y}^{\mathbf{n}+\frac{1}{2}}(u_{i[k,1,0]}^{\mathbf{n}} - u_{i[k,0,0]}^{\mathbf{n}})/\Delta\mathsf{y} & \text{if } \widehat{u_y}^{\mathbf{n}+\frac{1}{2}} < 0 \\ \widehat{u_y}^{\mathbf{n}+\frac{1}{2}}(u_{i[k,0,0]}^{\mathbf{n}} - u_{i[k,-1,0]}^{\mathbf{n}})/\Delta\mathsf{y} & \text{if } \widehat{u_y}^{\mathbf{n}+\frac{1}{2}} \geq 0 \end{cases} \qquad (\text{B.12b})$$

$$(u_z \widetilde{\partial}_z u_i)^{\mathbf{n}} \approx \begin{cases} \widehat{u_z}^{\mathbf{n}+\frac{1}{2}}(u_{i[k,0,1]}^{\mathbf{n}} - u_{i[k,0,0]}^{\mathbf{n}})/\Delta\mathsf{z} & \text{if } \widehat{u_z}^{\mathbf{n}+\frac{1}{2}} < 0 \\ \widehat{u_z}^{\mathbf{n}+\frac{1}{2}}(u_{i[k,0,0]}^{\mathbf{n}} - u_{i[k,0,-1]}^{\mathbf{n}})/\Delta\mathsf{z} & \text{if } \widehat{u_z}^{\mathbf{n}+\frac{1}{2}} \geq 0 \end{cases} \qquad (\text{B.12c})$$

where $\widehat{u_y}^{\mathbf{n}+\frac{1}{2}}$ and $\widehat{u_z}^{\mathbf{n}+\frac{1}{2}}$ are evaluated as follows

$$\widehat{u_y}^{\mathbf{n}+\frac{1}{2}} = \frac{1}{2}(U_{y[k,1,0]}^{\mathbf{n}+\frac{1}{2}} + U_{y[k,0,0]}^{\mathbf{n}+\frac{1}{2}}) \qquad (\text{B.13})$$

$$\widehat{u_z}^{\mathbf{n}+\frac{1}{2}} = \frac{1}{2}(U_{z[k,0,1]}^{\mathbf{n}+\frac{1}{2}} + U_{z[k,0,0]}^{\mathbf{n}+\frac{1}{2}}) \qquad (\text{B.14})$$

Evaluation of the "advector", i.e. $U_i^{\mathbf{n}+\frac{1}{2}}$

To obtain the field "advector" $U_i^{\mathbf{n}+\frac{1}{2}}$, we follow a very similar procedure up to equation (B.10d).

$$\widetilde{U_i}^{\mathbf{n}+\frac{1}{2}} = u_i^{\mathbf{n}} + s\frac{\Delta\mathsf{x}}{2}(\partial_x u_i)^{\mathbf{n}} - \frac{\Delta\mathsf{t}}{2}\left[(u_j\widetilde{\partial}_j u_i)^{\mathbf{n}} + g_i^{\mathbf{n}}\right]$$

However, the quantities in the expression above are evaluated in a different way.

For the gradient normal to the cell face one may use a CDS scheme,

$$(\partial_x u_i)_{[k,0,0]}^{\mathbf{n}} = (u_{i[k+1,0,0]}^{\mathbf{n}} - u_{i[k-1,0,0]}^{\mathbf{n}})/(2\Delta\mathsf{x}) \qquad (\text{B.15})$$

or the gradient may also be evaluated using a generalized minmod limiter (or any other kind of slope limiter for that matter), in which the gradient at the center of the neighboring cells in the x-direction may also be required. For our particular problem, we use CDS.

In contrast, the gradient normal to the cell face i.e. $u_x\widetilde{\partial}_x u_i$, is now approximated as follows

$$(u_x\widetilde{\partial}_x u_i)^{\mathbf{n}} = U_{x[0,0,0]}^{\mathbf{n}}(u_{i[k+1,0,0]}^{\mathbf{n}} - u_{i[k-1,0,0]}^{\mathbf{n}})/(2\Delta\mathsf{x}) \qquad (\text{B.16a})$$

which is slightly different from equation (B.12a).

For the other directions we do something different from equations (B.12c) and (B.12c) as well

$$(u_y\widetilde{\partial}_y u_i)^{\mathbf{n}} \approx \begin{cases} u_{y[k,0,0]}^{\mathbf{n}}(u_{i[k,1,0]}^{\mathbf{n}} - u_{i[k,0,0]}^{\mathbf{n}})/\Delta\mathsf{y} & \text{if } u_{y[k,0,0]}^{\mathbf{n}} < 0 \\ u_{y[k,0,0]}^{\mathbf{n}}(u_{i[k,0,0]}^{\mathbf{n}} - u_{i[k,-1,0]}^{\mathbf{n}})/\Delta\mathsf{y} & \text{if } u_{y[k,0,0]}^{\mathbf{n}} \geq 0 \end{cases} \qquad (\text{B.16b})$$

$$(u_z\widetilde{\partial}_z u_i)^{\mathbf{n}} \approx \begin{cases} u_{z[k,0,0]}^{\mathbf{n}}(u_{i[k,0,1]}^{\mathbf{n}} - u_{i[k,0,0]}^{\mathbf{n}})/\Delta\mathsf{z} & \text{if } u_{z[k,0,0]}^{\mathbf{n}} < 0 \\ u_{z[k,0,0]}^{\mathbf{n}}(u_{i[k,0,0]}^{\mathbf{n}} - u_{i[k,0,-1]}^{\mathbf{n}})/\Delta\mathsf{z} & \text{if } u_{z[k,0,0]}^{\mathbf{n}} \geq 0 \end{cases} \qquad (\text{B.16c})$$

The final step required to compute the advection term using equation (B.10d), is to ensure the "advector" to be divergence-free. This is done by projecting the provisional predicted

216

velocity into a divergence-free space which requires solving the following Poisson problem

$$D_{xyz}\phi = \frac{1}{\Delta x \Delta y \Delta z} \sum_d S_d \widetilde{U_{(d)}}^{n+\frac{1}{2}} \tag{B.17}$$

where D_{xyz} indicates a discrete Laplacian, then correcting the velocity field

$$U_i^{n+\frac{1}{2}} = \widetilde{U}_i^{n+\frac{1}{2}} - \partial_i \phi \tag{B.18}$$

We repeat this prediction-correction process for each component of the velocity field and for each face, in order to evaluate the non-linear term using equation (B.9).

The advection scheme implemented inside `tracer.h`, `gbc.h`, and `centered.h` follows closely the equivalent BCG scheme used in Gerris. The sequence of events required to solve one generic time step is represented in figure B.3. Additional details may be found in (Popinet, 2003).

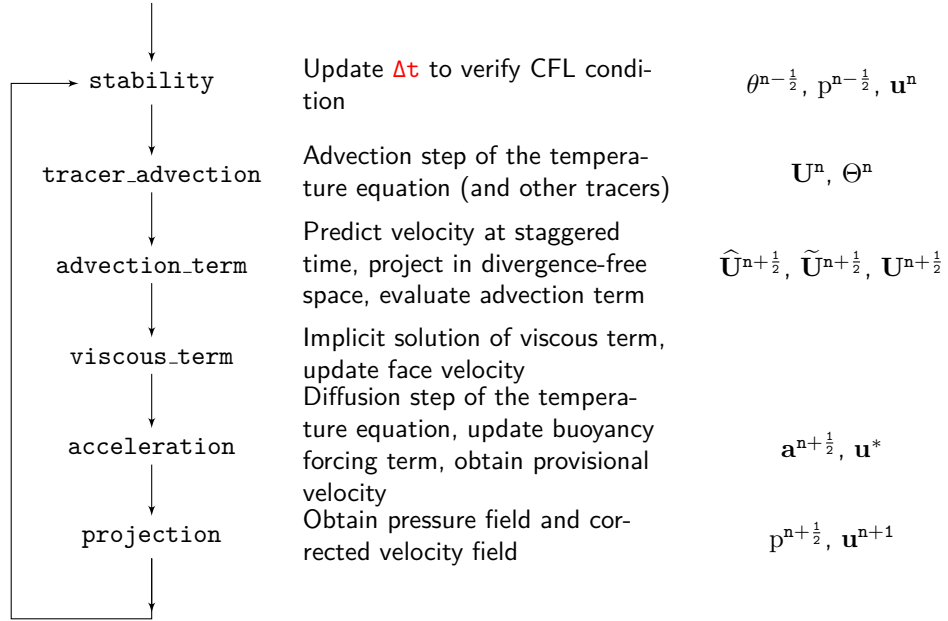|		
stability	Update Δt to verify CFL condition	$\theta^{n-\frac{1}{2}}$, $p^{n-\frac{1}{2}}$, $\mathbf{u^n}$
tracer_advection	Advection step of the temperature equation (and other tracers)	$\mathbf{U^n}$, Θ^n
advection_term	Predict velocity at staggered time, project in divergence-free space, evaluate advection term	$\widehat{\mathbf{U}}^{n+\frac{1}{2}}$, $\widetilde{\mathbf{U}}^{n+\frac{1}{2}}$, $\mathbf{U}^{n+\frac{1}{2}}$
viscous_term	Implicit solution of viscous term, update face velocity	
acceleration	Diffusion step of the temperature equation, update buoyancy forcing term, obtain provisional velocity	$\mathbf{a}^{n+\frac{1}{2}}$, $\mathbf{u^*}$
projection	Obtain pressure field and corrected velocity field	$p^{n+\frac{1}{2}}$, $\mathbf{u^{n+1}}$

Figure B.3: Flowchart to the generic time-step, providing a minimal description of the contents of each event.

Appendix C

Parallel I/O model using XDMF

C.1   Presentation of the XDMF Format

The *eXtensible Data Model and Format* (XDMF) was developed to exchange scientific data from different high performance computing (HPC) codes (see Clarke and Namburu, 2002; Clarke and Mark, 2007). XDMF data may be categorized by function: *format* data and *model* data. The format describes the rank and dimensions of arrays, while the model data describes what to use data for. Data may also be organized by size as *light* data and *heavy* data. Light data is stored using eXtensible Markup Language (XML) to describe the data model and the data format. Heavy data is composed of large datasets stored using the *Hierarchical Data Format* (HDF5).

Consider the following minimal example composed of one *Xdmf* element, one *Domain* element and one *Temporal collection* with one *Grid* element per time instant.

Example C.1: Temporal collections

```xml
<?xml version="1.0" ?>
<!DOCTYPE Xdmf SYSTEM "Xdmf.dtd" []>
<Xdmf Version="2.0">
  <Domain Name="Rayleigh-Benard Cell">
    <Grid Name="Snapshots" GridType="Collection" CollectionType="Temporal">
      <Grid Name="Time=0" GridType="Uniform">
        <Time Value="0.00"/>
        ...
      </Grid>
      <Grid Name="Time=5" GridType="Uniform">
        <Time Value="5.00"/>
        ...
      </Grid>
      ...
    </Grid>
  </Domain>
</Xdmf>
```

Each one of the *Grid* elements may contain one or more *Topology*, *Geometry*, and *Attribute* elements. Topology describes the general organization of the data, i.e. 2D or 3D, structured or unstructured, and so on. Geometry describes the mesh points. An Attribute element may define values associated with the mesh, such as a scalar, vector or tensor fields.

The following example, presents a domain with a structured mesh (3D) of size NX*NY*NZ. The mesh is defined by three arrays, one for each direction, all of them stored inside an external HDF5 file called "heavy_data.h5". Finally, one attribute defines a scalar field called "Temperature" for each grid point, stored in the same HDF5 file. Additional fields may be added by following this template.

Example C.2: A Cartesian grid containing one scalar field

```
...
<Grid Name="Time=0" GridType="Uniform">
  <Time Value="0.00"/>
  <Topology TopologyType="3DRectMesh" NumberOfElements="NZ NY NX"/>
  <Geometry GeometryType="VXVYVZ">
  <DataItem Dimensions=" NX " NumberType="Float" Precision="8" Format="HDF">
    heavy_data.h5:/grid/vertex/CoordinateX
  </DataItem>
  ...
  </Geometry>
  <Attribute Name="Temperature" AttributeType="Scalar" Center="Point">
    <DataItem Dimensions="NZ NY NX" NumberType="Float" Precision="8" Format="HDF">
      heavy_data.h5:/snapshot/time_0.0/Temperature
    </DataItem>
  </Attribute>
  ...
</Grid>
...
```

C.2   Presentation of the HDF5 format

The second half of the XDMF format, i.e. the heavy data, is composed of relatively large datasets stored using the *Hierarchical Data Format* (HDF5), see The HDF Group, 2016. As the name implies, data is organized following a hierarchical structure. HDF5 files can be read without any prior knowledge of the stored data. The list of software capable of reading HDF5 files includes *Visit*, *Paraview*, *Matlab*, and *Tecplot*, to name a few.

The type, rank, dimension and other properties of each array are stored inside the file in the form of meta-data. The following example uses a set of command-line tools to explore the contents of an existing file,

Example C.3: HDF5 file contents organized in groups and subgroups.

```
>> h5ls -r heavy_data.h5
  /                               Group
  /snapshot                       Group
  /snapshot/time_0.0              Group
  /snapshot/time_0.0/Temperature  Dataset {NZ, NY, NX}
  /snapshot/time_5.0              Group
  /snapshot/time_5.0/Temperature  Dataset {NZ, NY, NX}
  ...
  /grid                           Group
  /grid/vertex                    Group
  /grid/vertex/CoordinateX        Dataset {NX}
  ...
>> h5dump -d /grid/vertex/CoordinateX heavy_data.h5
HDF5 "output_basilisk.h5" {
  DATASET "/grid/vertex/CoordinateX" {
    DATATYPE  H5T_IEEE_F32LE
    DATASPACE  SIMPLE { ( NX ) / ( NX ) }
    DATA {
```

```
    (0): -0.5, -0.492188, -0.484375, -0.476562, -0.46875, -0.460938,
    ...
  }
 }
}
```

Additional features include support for a large number of objects, file compression, a parallel I/O implementation through the MPI-IO or MPI POSIX drivers. A software library that provides a high-level API with interfaces to both C and Fortran, can be usually found already installed in a large number of computing centers. If the library is available, one must add an include line in the program source code.

<div style="display: flex;">

Example C.4: Fusion

```fortran
program FUSION
  use declarations
  ...
  use hdf5

  implicit none

  ...

end program
```

Example C.5: Basilisk

```c
#include "grid/multigrid3D.h"
#include "navier-stokes/centered.h"
...
#include <hdf5.h>
...
int main() {
  ...
  run();
}
...
```

</div>

And then proceed to link the program with the library object file during compilation.

Appendix D

Demonstrations related to the available potential energy

D.1 Proof related to the change of the available potential energy

Consider the formal definition of $y_r(x, y, z, t)$ from Winters et al., 1995,

$$y_r(x, y, z, t) - y_{\text{bot}} = \frac{1}{V} \int \text{H}(\theta(x, y, z, t) - \theta(x', y', z', t)) \, \text{dV}' \qquad \text{(D.1a)}$$

where y_{bot} is the reference height at the bottom plate, $\text{H}(x)$ the Heaviside function, $\text{dV} = \text{dxdydz}$ and $\text{dV}' = \text{dx'dy'dz'}$. Now consider the following definitions

$$\delta(x) = \lim_{\varepsilon \to 0} \frac{1}{\varepsilon\sqrt{\pi}} \exp\left(-\frac{x^2}{\varepsilon^2}\right) \qquad\qquad \text{H}(x) = \frac{1}{2}\lim_{\varepsilon \to 0} \text{erfc}\left(-\frac{x}{\varepsilon}\right) \qquad \text{(D.1b)}$$

$$\text{erfc}(y) = 1 - \frac{2}{\sqrt{\pi}} \int_0^\infty \exp(-y^2) dt \qquad\qquad \frac{\text{d}}{\text{dt}}\text{erfc}(y) = -\frac{2}{\sqrt{\pi}} \exp(-y^2) \qquad \text{(D.1c)}$$

We define a variable $u = \theta(x, y, z, t) - \theta(x', y', z', t)$

$$\frac{\text{d}}{\text{dt}}\text{H}(u) = \lim_{\varepsilon \to 0} \frac{\partial}{\partial t} \left[\frac{1}{2}\text{erfc}\left(-\frac{u}{\varepsilon}\right)\right] = \lim_{\varepsilon \to 0} \frac{1}{\varepsilon\sqrt{\pi}} \exp\left(-\frac{u^2}{\varepsilon^2}\right) \partial_t u = \delta(u)\partial_t u \qquad \text{(D.1d)}$$

Finally, one combines this expression into the definition of $y_r(x, y, z, t)$

$$\int_V \theta\partial_t y_r \text{dV} = \frac{1}{V} \iint \theta\partial_r \text{H}(u) \, \text{dV}'\text{dV} = \frac{1}{V} \iint [\theta\delta(u)\partial_t u] \, \text{dV}'\text{dV} \qquad \text{(D.1e)}$$

which becomes zero if the temperature field is indeed univoque.

$$\int_V \theta\partial_t y_r \text{dV} = 0 \qquad \text{(D.1f)}$$

Appendix E

Demonstrations related to the vorticity functions

For a **two-dimensional** configuration $\mathbf{r} \in \mathbb{R}^2$, vorticity has only one component perpendicular to the plane (xy) $\boldsymbol{\omega} = \omega \mathbf{e}_z$. By taking the curl of the momentum equation one obtains the following dynamical equation for the vorticity ω,

$$\partial_t \omega + \partial_j (u_j \omega) = \mathrm{PrRa}^{-0.5} \partial_j \partial_j \omega + \mathrm{Pr} \partial_x \theta \tag{E.1}$$

The global angular impulse is defined as

$$\mathrm{L}_{\mathrm{2D}} \equiv -\frac{1}{2} \iiint r_k r_k \omega \ \mathrm{dxdy} \tag{E.2}$$

Such that

$$\frac{\mathrm{d}}{\mathrm{dt}} \mathrm{L}_{\mathrm{2D}} \equiv -\frac{1}{2} \iiint r_k r_k \partial_t \omega \ \mathrm{dxdy} \tag{E.3}$$

From the dynamical equation of the vorticity one has the following expression

$$\frac{\mathrm{d}}{\mathrm{dt}} \mathrm{L}_{\mathrm{2D}} = \mathrm{PrRa}^{-0.5} \mathrm{I} + \mathrm{II} + \mathrm{M} \tag{E.4}$$

with I, II, and M given as

$$\mathrm{I} = -\frac{1}{2} \iint (r_k r_k)(\partial_j \partial_j \omega) \ \mathrm{dxdy} \tag{E.5}$$

$$\mathrm{II} = \frac{1}{2} \iint (r_k r_k) \partial_j (u_j \omega) \ \mathrm{dxdy} \tag{E.6}$$

$$\mathrm{M} = -\frac{1}{2} \mathrm{Pr} \iint r_k r_k \partial_x \theta \ \mathrm{dxdy} \tag{E.7}$$

The first term I is transformed as follows

$$\mathrm{I} = -\frac{1}{2} \iint (r_k r_k)(\partial_j \partial_j \omega) \ \mathrm{dxdy} = -\frac{1}{2} \iint \left(\partial_j (r_k r_k \partial_j \omega) - \partial_j (r_k r_k) \ \partial_j \omega \right) \ \mathrm{dxdy} \tag{E.8}$$

where $\partial_j(r_k r_k)\, \partial_j \omega$ may be rewritten as follows

$$\partial_j(r_k r_k)\, \partial_j \omega = 2r_j \partial_j \omega = \partial_j(2r_j \omega) - \omega \partial_j(2r_j) = \partial_j(2r_j \omega) - 4\omega \tag{E.9}$$

Finally, we may write I as

$$\mathrm{I} = -\frac{1}{2} \oint r_k r_k \partial_n \omega \; \mathrm{ds} + \oint r_n \omega \; \mathrm{ds} - 2 \iint \omega \; \mathrm{dxdy} \tag{E.10}$$

where ds is an infinitesimal element of the boundary ∂A, dA = dxdy, and the loop integral is **counterclockwise**.

The second term II is transformed through the following relation

$$(r_k r_k)\partial_j(u_j \omega) = \partial_j(r_k r_k u_j \omega) - u_j \omega \partial_j(r_k r_k) = \partial_j(r_k r_k u_j \omega) - 2r_j u_j \omega \tag{E.11}$$

Leaving the following expression for II

$$\mathrm{II} = \frac{1}{2} \oint r_k r_k u_n \omega \; \mathrm{ds} - \iint r_j u_j \omega \; \mathrm{dxdy} \tag{E.12}$$

Since $\omega = \varepsilon_{li} \partial_l u_i$, one may write

$$r_j u_j \omega = \epsilon_{ji} r_j \partial_l \left[\frac{1}{2} u_m u_m \delta_{il} - u_l u_i \right] \tag{E.13}$$

$$= \epsilon_{ji} \partial_i \left[\frac{r_j}{2} u_m u_m \right] - \epsilon_{ji} \partial_l \left[r_j u_l u_i \right] \tag{E.14}$$

Applying the divergence theorem in two-dimensions

$$\mathrm{II} = \frac{1}{2} \oint r_k r_k u_n \omega \; \mathrm{ds} + \frac{1}{2} \oint u_k u_k \epsilon_{ji} n_j r_i \; \mathrm{ds} + \oint u_n \epsilon_{ji} n_j u_i \; \mathrm{ds} \tag{E.15}$$

Considering impermeable boundaries, i.e. $u_n = 0$, simplifies this expression to

$$\mathrm{II} = \frac{1}{2} \oint u_k u_k \epsilon_{ji} n_j r_i \; \mathrm{ds} \tag{E.16}$$

where ds is an infinitesimal element of the boundary ∂A, dA = dxdy, and the loop integral is **counterclockwise**. Furthermore, imposing **no-slip** boundary conditions results in the same expressions from Molenaar et al., 2004.

$$\mathrm{I} = -\frac{1}{2} \oint r_k r_k \partial_n \omega \; \mathrm{ds} + \oint r_n \omega \; \mathrm{ds} \tag{E.17}$$

$$\mathrm{II} = 0 \tag{E.18}$$

$$\mathrm{M} = -\frac{1}{2} \iint r_k r_k \partial_x \theta \; \mathrm{dxdy} \tag{E.19}$$

Appendix F

Derivation of a 2-D model with inertial corrections using the weighted residuals method

In this section we present a reduced model which takes into account inertial effects. This is done in the spirit of (Ruyer-Quil, 2001) that extended the work by (Gondret and Rabaud, 1997) using a weighted residuals method (WRM) (see for instance Finlayson, 2013).

F.1 Method of weighted residuals

Before presenting the model itself, let us present a general description of the weighted residuals method closely following (Kalliadasis et al., 2011). Consider a problem that can be formally written as $\mathcal{E}(\mathcal{U}) = 0$, for some set of variables $\mathcal{U}$. In our particular case, $\mathcal{U}$ corresponds to velocity and temperature fields and $\mathcal{E}$ to a simplified form of the non-dimensionalized Boussinesq equations (7.1a)-(7.1d). We proceed to search a solution of $\mathcal{U}$ in the form of a series expansion

$$\mathcal{U} = \sum_{n=0}^{N} \phi^{(n)}(x, y, t) f_n(z) \tag{F.1}$$

where $f_n(z)$ with $n = 0, 1, \cdots, N$ are called test functions. This set of functions forms a complete basis in the functional space $\mathcal{S}$ of functions of z inside the interval $[-\varepsilon, \varepsilon]$ and that satisfy the boundary conditions of the problem. It is reminded that in our case $\varepsilon = \Gamma_z/2$. In addition this space disposes of an inner product $\langle a|b \rangle = \int_{-\varepsilon}^{\varepsilon} (a\, b)\mathrm{d}z$.

The method of weighted residuals determines the amplitudes $\phi^{(n)}$ and is divided in three steps. First, one introduces a series of $N + 1$ weight functions $w_m(z)$, $m = 0, \cdots, N$. Second, one projects the original equation $\mathcal{E}(\mathcal{U}) = 0$ onto the $N + 1$ weight functions, leading to $N + 1$ residual problems

$$\mathcal{R}_m \equiv \langle w_m | \mathcal{E}(\mathcal{U}) \rangle = \langle w_m | \mathcal{E}(\sum_{n=0}^{N} \phi^{(n)} f_n) \rangle = 0 \qquad \text{for } m = 0, \cdots, N \tag{F.2}$$

Instead of solving the general problem $\mathcal{E}(\mathcal{U}) = 0$, the $N+1$ residuals yield a linear system of equations for the amplitudes $\phi^{(n)}$. The choice of the weight functions w_m determines the particular kind of weighted residual method being used. Note that a judicious choice of test functions simplifies the resulting equation system (Ruyer-Quil and Manneville, 2000). When the weight and test functions are identical, i.e. $w_m = f_m$, the WRM is the same as a Galerkin method.

F.2 Introduction to a reduced model with inertial corrections

In the following we introduce a rescaled space variable $\underline{z} \equiv \frac{z}{\varepsilon}$ defined in the interval $[-1, 1]$. The equation of continuity (7.1a) suggests the transversal velocity component w to be rescaled as

$$w = \varepsilon \tilde{w} \qquad \text{with } \tilde{w} \equiv -\int_{-1}^{z}(\partial_i u_i)\mathrm{d}\underline{z} \qquad \text{(F.3)}$$

The non-dimensionalization of velocity in system (7.1a)-(7.1d) is based on the free-fall velocity. For confined cells this characteristic velocity is no longer representative: velocities are smaller than one and the time scales are much longer. Indeed, the root mean squared velocity is such that (see table in figure F.1)

$$\alpha \equiv \sqrt{\langle \overline{\mathbf{u}^2} \rangle_{\mathrm{xz}}} \ll 1 \qquad \text{(F.4)}$$

One thus introduces a slow time scale $\underline{\tau}$ and rescaled velocities

$$\underline{\tau} = \alpha t \qquad \underline{u_i} = \frac{u_i}{\alpha} \qquad \underline{w} = \frac{\tilde{w}}{\alpha} \qquad \text{(F.5)}$$

Leading to the following system of equations

$$\partial_i \underline{u_i} + \partial_{\underline{z}} \underline{w} = 0 \qquad \text{(F.6a)}$$

$$\alpha^2 \left[\partial_{\underline{\tau}} \underline{u_i} + \partial_j(\underline{u_j} \underline{u_i}) + \partial_{\underline{z}}(\underline{w}\ \underline{u_i}) \right] = -\partial_i \mathrm{p} + \alpha \mathrm{Pr}\mathrm{Ra}^{-0.5}\left[\partial_j \partial_j \underline{u_i} + \varepsilon^{-2}\partial_{\underline{z}}^2 \underline{u_i} \right] + \mathrm{Pr}\theta\delta_{iy}$$
$$\text{(F.6b)}$$

$$\alpha^2 \left[\partial_{\underline{\tau}} \underline{w} + \partial_j(\underline{u_j} \underline{w}) + \partial_{\underline{z}}(\underline{w}\ \underline{w}) \right] = -\varepsilon^{-2}\partial_{\underline{z}}\mathrm{p} + \alpha \mathrm{Pr}\mathrm{Ra}^{-0.5}\left[\partial_j \partial_j \underline{w} + \varepsilon^{-2}\partial_{\underline{z}}^2 \underline{w} \right] \qquad \text{(F.6c)}$$

$$\alpha \left[\partial_{\underline{\tau}} \theta + \partial_j(\underline{u_j}\theta) + \partial_{\underline{z}}(\underline{w}\ \theta) \right] = \mathrm{Ra}^{-0.5}\left[\partial_j \partial_j \theta + \varepsilon^{-2}\partial_{\underline{z}}^2 \theta \right] \qquad \text{(F.6d)}$$

The characteristic temperature scale is still valid and the temperature field remains bounded in the interval $[-0.5, 0.5]$. However, outside the boundary layers the temperature is expected to be smaller than one. Since the pressure gradient and the thermal forcing are inextricably intertwined in the following we assume

$$\text{Far from the BL}: \qquad \begin{array}{rcl} \mathrm{p} & = & \alpha\underline{\mathrm{p}} \\ \theta & = & \alpha\underline{\theta} \end{array} \qquad \text{(F.7)}$$

where $\underline{\mathrm{p}}$ and $\underline{\theta}$ are terms of order one. Introducing these terms into equations (F.6a)-(F.6d) yields a system of equations where the orders of magnitude of each term is deduced in

terms of α, ε, Ra and Pr.

$$\partial_i \underline{u_i} + \partial_{\underline{z}} \underline{w} = 0 \tag{F.8a}$$

$$\alpha \left[\partial_{\underline{\tau}} \underline{u_i} + \partial_j (\underline{u_j}\underline{u_i}) + \partial_{\underline{z}} (\underline{w}\,\underline{u_i}) \right] = - \partial_i \underline{p} + \mathrm{PrRa}^{-0.5} \partial_j \partial_j \underline{u_i} \tag{F.8b}$$
$$+ \varepsilon^{-2} \mathrm{PrRa}^{-0.5} \partial_{\underline{z}}^2 \underline{u_i} + \mathrm{Pr}\underline{\theta}\delta_{iy}$$

$$\alpha \left[\partial_{\underline{\tau}} \underline{w} + \partial_j (\underline{u_j}\underline{w}) + \partial_{\underline{z}} (\underline{w}\,\underline{w}) \right] = - \varepsilon^{-2} \partial_{\underline{z}} \underline{p} + \mathrm{PrRa}^{-0.5} \partial_j \partial_j \underline{w} \tag{F.8c}$$
$$+ \varepsilon^{-2} \mathrm{PrRa}^{-0.5} \partial_{\underline{z}}^2 \underline{w}$$

$$\alpha \left[\partial_{\underline{\tau}} \underline{\theta} + \partial_j (\underline{u_j}\underline{\theta}) + \partial_{\underline{z}} (\underline{w}\,\underline{\theta}) \right] = \mathrm{Ra}^{-0.5} \partial_j \partial_j \underline{\theta} + \varepsilon^{-2} \mathrm{Ra}^{-0.5} \partial_{\underline{z}}^2 \underline{\theta} \tag{F.8d}$$

This is completed by the mechanical and thermal boundary conditions at the front and back walls

$$\underline{u_i} = \underline{w} = 0 \text{ at } \underline{z} = \pm 1 \tag{F.9a}$$
$$\partial_n \underline{\theta} = 0 \text{ at } \underline{z} = \pm 1 \tag{F.9b}$$

Inside Hele-Shaw cells, the terms highlighted in blue are expected to lead: the viscous and thermal diffusion operators in the transversal direction, i.e. $\partial_{\underline{z}}^2 \underline{u_i}$ and $\partial_{\underline{z}}^2 \underline{\theta}$, as well as the buoyancy force and the pressure gradient. This imposes the following constraints on the values of ε and Ra

$$\varepsilon^{-2} \mathrm{Ra}^{-0.5} \gg \alpha \quad \text{or equivalently} \quad \alpha \varepsilon^2 \mathrm{Ra}^{0.5} \ll 1 \tag{F.10}$$

Using the DNS results presented in chapter 7, we perform a data fit to obtain a very rough approximation for the velocity scale α in terms of Ra and ε, $\alpha \approx 0.083\varepsilon^{0.92}\mathrm{Ra}^{0.17}$ (see figure F.1). Introducing this expression into (F.10), one obtains an upper boundary in Ra and Γ_z for the range of validity of the Hele-Shaw approximation. Using this for a fixed value of Ra, the aspect ratio Γ_z must verify

$$\Gamma_z = 2\varepsilon \ll 4.689\mathrm{Ra}^{-0.2295} \tag{F.11}$$

This limit may be better represented on the phase diagram displayed on the bottom right part of figure F.1.

Ra	Γ_z	α	$\alpha\varepsilon^2\mathrm{Ra}^{0.5}$
$1\cdot10^6$	1/8.	0.069	0.271
$5\cdot10^6$	1/8.	0.091	0.798
$1\cdot10^7$	1/8.	0.107	1.324
$5\cdot10^7$	1/8.	0.132	3.646
$1\cdot10^8$	1/8.	0.137	5.362
$1\cdot10^6$	1/16.	0.033	0.033
$5\cdot10^6$	1/16.	0.045	0.098
$1\cdot10^7$	1/16.	0.068	0.209
$5\cdot10^7$	1/16.	0.077	0.533
$1\cdot10^8$	1/16.	0.086	0.836
$1\cdot10^6$	1/32.	0.011	0.003
$5\cdot10^6$	1/32.	0.020	0.011
$1\cdot10^7$	1/32.	0.023	0.018
$5\cdot10^7$	1/32.	0.035	0.060
$1\cdot10^8$	1/32.	0.041	0.099
$1\cdot10^9$	1/32.	0.069	0.534
$1\cdot10^7$	1/64.	0.008	0.002
$5\cdot10^7$	1/64.	0.013	0.006
$1\cdot10^8$	1/64.	0.017	0.010
$2\cdot10^8$	1/64.	0.021	0.018
$1\cdot10^9$	1/64.	0.032	0.063
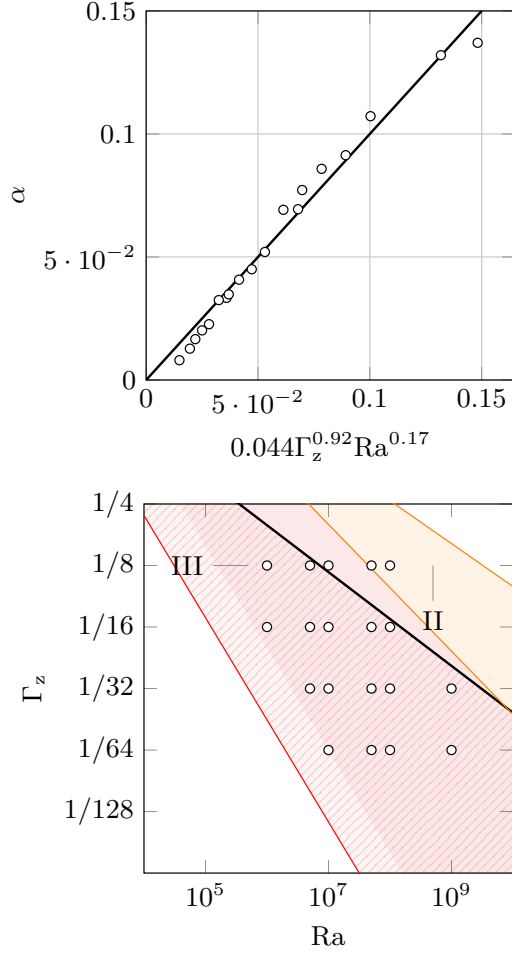
Figure F.1: (Left) Table providing the values of α and $\alpha\varepsilon^2\mathrm{Ra}^{0.5}$ obtained from DNS. The latter must remain small in order to satisfy the formulation proposed. Unwanted values are indicated in red. (Top right) Value of α compared to a data fit $\alpha = 0.083\varepsilon^{0.92}\mathrm{Ra}^{0.17}$ estimated using DNS data for different Ra and Γ_z. (Bottom right) Phase diagram reproduced from figure 7.1. Marks indicate the values of (Ra, Γ_z) considered and the thick line corresponds to the limit $\Gamma_z = 4.689\mathrm{Ra}^{-0.2295}$.

F.2.1 Solution to the zeroth-order formulation: recovering the profile of the simplified model

As a first approximation, consider removing the terms of order α from equations (F.8a) to (F.8d), and neglect the terms in $\mathrm{Ra}^{-0.5}$ with respect to $\varepsilon^{-2}\mathrm{Ra}^{-0.5}$. This zeroth-order approximation has the following form

$$\partial_{\underline{z}}\underline{w} = -\partial_i\underline{u}_i \tag{F.12a}$$

$$\partial_{\underline{z}}^2\underline{u}_i = \varepsilon^2\mathrm{Ra}^{0.5}\mathrm{Pr}^{-1}\left[\partial_i\underline{p} - \mathrm{Pr}\underline{\theta}\delta_{iy}\right] \tag{F.12b}$$

$$\partial_{\underline{z}}\underline{p} = 0 \tag{F.12c}$$

$$\partial_{\underline{z}}^2\underline{\theta} = 0 \tag{F.12d}$$

From equation (F.12d) and the adiabatic boundary conditions one deduces that the temperature profile must be constant along the transversal direction, i.e. $\underline{\theta}(x, y, \underline{z}, \underline{\tau}) = \underline{\theta}(x, y, \underline{\tau})$. Equation (F.12c) implies the pressure field to be independent of the transversal coordinate, i.e. $\underline{p}(x, y, \underline{z}, \underline{\tau}) = \underline{p}(x, y, \underline{\tau})$. Equation (F.12b) implies the velocity to have a parabolic profile in order to satisfy the no-slip boundary conditions on ($\underline{z} = \pm 1$). The solution at the zeroth-order has the following form

$$\underline{u}_i(x, y, \underline{z}, \underline{\tau}) = \varepsilon^2\frac{1}{3}\mathrm{Ra}^{0.5}\mathrm{Pr}^{-1}\left(-\partial_i\underline{p}(x, y, \underline{\tau}) + \mathrm{Pr}\underline{\theta}(x, y, \underline{\tau})\delta_{iy}\right)g_0(\underline{z}) \tag{F.13}$$

where

$$g_0(\underline{z}) \equiv \frac{3}{2}(1 - \underline{z}^2) \tag{F.14}$$

This parabolic profile (F.13) in addition to the continuity equation (F.12a) imposes

$$\underline{w} = 0 \quad \text{and} \quad \partial_i\underline{u}_i = 0 \tag{F.15}$$

This procedure leads to the same transversal profiles as in the simplified model 8.1, but does not lead to the same dynamical equations. In this case, this leads to a Poisson equation for the pressure field.

F.2.2 First-order formulation

We would like to go further than the zeroth-order approximation and compute the deviations from such profiles by taking into account the terms of order α from equations (F.8a)-(F.8b). Let us consider the temperature, pressure and velocity fields may be written in the following form

$$\underline{\theta} = \theta^{(0)} + \alpha\theta^{(1)} + \mathcal{O}(\alpha^2) \tag{F.16a}$$

$$\underline{p} = p^{(0)} + \alpha p^{(1)} + \mathcal{O}(\alpha^2) \tag{F.16b}$$

$$\underline{u}_i = u_i^{(0)} + \alpha u_i^{(1)} + \mathcal{O}(\alpha^2) \tag{F.16c}$$

The terms $\theta^{(0)}$, $p^{(0)}$, and $u_i{}^{(0)}$ have identical profiles as the zeroth-order solution

$$\theta^{(0)} = \vartheta^{(0)}(x, y, \underline{\tau}) f_0(\underline{z}) \quad \text{with} \quad f_0(\underline{z}) = 1 \tag{F.17a}$$

$$p^{(0)} = p^{(0)}(x, y, \underline{\tau}) \tag{F.17b}$$

$$u_i{}^{(0)} = a_i{}^{(0)}(x, y, \underline{\tau}) g_0(\underline{z}) \quad \text{with} \quad g_0(\underline{z}) = \frac{3}{2}(1 - \underline{z}^2) \tag{F.17c}$$

but their amplitudes may be different from the zeroth-order formulation.

To define precisely each term in equations (F.17a) and (F.17c), all contributions to the transversally averaged fields $\langle \mathbf{u} \rangle$, $\langle p \rangle$ and $\langle \theta \rangle$ are assumed to be concentrated in the zeroth-order terms,

$$\langle \theta \rangle = \theta^{(0)} \qquad\qquad \langle \mathbf{u} \rangle = a_i{}^{(0)} \qquad\qquad \langle p \rangle = p^{(0)} \tag{F.18}$$

In turn, this imposes gauge conditions for $\theta^{(1)}$, $u_i{}^{(1)}$, and $p^{(1)}$

$$\langle \theta^{(1)} \rangle = 0 \qquad\qquad \langle u_i{}^{(1)} \rangle = 0 \qquad\qquad \langle p^{(1)} \rangle = 0 \tag{F.19}$$

Introducing equation (F.17c) into the continuity equation (F.8a) and integrating over $\underline{z}$ from -1 to $\underline{z}$ gives the following expression for the transversal velocity $\underline{w}$

$$\underline{w} = -\int_{-1}^{\underline{z}} \partial_i u_i{}^{(0)} d\underline{z} - \alpha \int_{-1}^{\underline{z}} \partial_i u_i{}^{(1)} d\underline{z} = -\partial_i a_i{}^{(0)} G_0(\underline{z}) - \alpha \partial_i \left[\int_{-1}^{\underline{z}} u_i{}^{(1)} d\underline{z} \right] \tag{F.20}$$

where $G_0 = \frac{(2 + 3\underline{z} - \underline{z}^3)}{2}$. Since $\underline{w}$ verifies the no-slip boundary condition on $\underline{z} = 1$ and $u_i{}^{(1)}$ satisfies the gauge condition (F.19), the only non-trivial solution is

$$\partial_i a_i{}^{(0)} = 0 \tag{F.21}$$

which implies that $\underline{w}$ is at least of order α,

$$\underline{w} = \alpha w^{(1)} \tag{F.22}$$

Because of this, momentum equation along z (F.8c) is greatly simplified. Integrating the resulting equation between $-\varepsilon$ and z gives an expression for the pressure field

$$\underline{p} = p^{(0)} - \alpha \text{PrRa}^{-0.5} \partial_j u_j{}^{(1)} \tag{F.23}$$

where $\partial_j u_j|_{(\underline{z} = -1)} = 0$ due to the no-slip condition.

Because of all of the above, the expanded system reads at the first-order as

$$\alpha \partial_{\underline{\tau}} u_i{}^{(0)} + \alpha \partial_j (u_j{}^{(0)} u_i{}^{(0)}) = -\partial_i p^{(0)} + \text{PrRa}^{-0.5}(\partial_j \partial_j u_i{}^{(0)} + \alpha \partial_j(\partial_j u_i{}^{(1)} + \partial_i u_j{}^{(1)}))$$
$$+ \varepsilon^{-2} \text{PrRa}^{-0.5}(\partial_{\underline{z}}^2 u_i{}^{(0)} + \alpha \partial_{\underline{z}}^2 u_i{}^{(1)})$$
$$+ \text{Pr}(\theta^{(0)} + \alpha \theta^{(1)}) \delta_{iy} \tag{F.24a}$$

$$\alpha \partial_{\underline{\tau}} \theta^{(0)} + \alpha \partial_j (u_i{}^{(0)} \theta^{(0)}) = \text{Ra}^{-0.5}(\partial_j \partial_j \theta^{(0)} + \alpha \partial_j \partial_j \theta^{(1)} + \varepsilon^{-2} \alpha \partial_{\underline{z}}^2 \theta^{(1)}) \tag{F.24b}$$

We decide to keep the diffusion terms along x and y, $\text{PrRa}^{-0.5}\partial_j\partial_j u_i{}^{(0)}$ and $\text{PrRa}^{-0.5}\partial_j\partial_j\theta^{(0)}$,

as to preserve the boundary layers on the top and bottom plates, but we neglect the same terms associated to the first order, i.e. $\alpha \mathrm{PrRa}^{-0.5} \partial_j \partial_j u_i^{(1)}$ and $\alpha \mathrm{Ra}^{-0.5} \partial_j \partial_j \theta^{(1)}$. For the first order terms, we keep only the second derivatives along the transversal direction, which is ε^{-2} larger than the previous terms. In addition, we discarded the second term in equation (F.23) which generates in equation (F.24a) a term that is ε^2 smaller than the transversal diffusion. Since we neglect these terms, the model equation reads

$$\alpha \partial_{\underline{\tau}} a_i^{(0)} g_0 + \alpha \partial_j (a_j^{(0)} a_i^{(0)}) g_0^2 = -\partial_i \mathrm{p}^{(0)} + \mathrm{PrRa}^{-0.5} (\partial_j \partial_j a_i^{(0)} g_0 + \varepsilon^{-2} a_i^{(0)} g_0'' + \alpha \varepsilon^{-2} \partial_{\underline{z}}^2 u_i^{(1)})$$
$$+ \mathrm{Pr}(\vartheta^{(0)} + \alpha \theta^{(1)}) \delta_{iy} \qquad \text{(F.25a)}$$

$$\alpha \partial_{\underline{\tau}} \vartheta^{(0)} + \alpha \partial_j (a_i^{(0)} \vartheta^{(0)}) g_0 = \mathrm{Ra}^{-0.5} (\partial_j \partial_j \vartheta^{(0)} + \alpha \varepsilon^{-2} \partial_{\underline{z}}^2 \theta^{(1)}) \qquad \text{(F.25b)}$$

In the following section we present a solution to the first-order formulations from equations (F.25a) and (F.25b).

F.3 Solution of the first-order formulation by the WRM

The next step of the derivation of the reduced model consists in using the resulting equations to deduce an expression for $\theta^{(1)}(x, y, \underline{z}, \underline{\tau})$ and $u_i^{(1)}(x, y, \underline{z}, \underline{\tau})$ in terms of the zeroth-order terms $\vartheta^{(0)}(x, y, \underline{\tau})$, $\mathrm{p}^{(0)}(x, y, \underline{\tau})$ and $a_i^{(0)}(x, y, \underline{\tau})$, then to obtain a system of partial differential equations for the zeroth-order terms. This can be done using one of two different approaches: a gradient expansion method and weighted residuals. Both approaches are known to give the same system of equations.

The gradient expansion approach benefits from the fact that $\theta^{(1)}$ (resp. $u_i^{(1)}$) appears only once as $\partial_{\underline{z}}^2 \theta^{(1)}$ (resp. $\partial_{\underline{z}}^2 u_i^{(1)}$) in equation (F.25b) (resp. (F.25a)). Integrating both equations twice with respect to $\underline{z}$ and imposing the respective gauge condition yields directly the expressions for $\theta^{(1)}$ and $u_i^{(1)}$.

In the weighted residual approach we search a solution for $\theta^{(1)}$ and $u_i^{(1)}$ in the form of a series expansion

$$\theta^{(1)} = \sum_{n=1}^{N} \vartheta^{(1,n)}(x, y, \underline{\tau}) f_n(\underline{z}) \quad \text{with} \quad f_n'(\underline{z} = \pm 1) = 0 \qquad \text{(F.26a)}$$

$$u_i^{(1)} = \sum_{n=1}^{N} a_i^{(1,n)}(x, y, \underline{\tau}) g_n(\underline{z}) \quad \text{with} \quad g_n(\underline{z} = \pm 1) = 0 \qquad \text{(F.26b)}$$

where $\vartheta^{(1,n)}$ (resp. $a_i^{(1,n)}$) are amplitudes to determine and $f_n(\underline{z})$ (resp. $g_n(\underline{z})$) are called test functions which form a complete basis that satisfies the thermal (resp. mechanical) boundary conditions. The amplitudes are determined by introducing a series of weight functions w_m^θ (resp. w_m^u) and projecting the original equations onto the weight function in order to define a series of residual problems $\mathcal{R}_m = 0$. The last part consists in solving the vanishing residuals $\mathcal{R}_m = 0$ which yields a linear equation system for the amplitudes $\vartheta^{(1,n)}$ (resp. $a_i^{(1,n)}$).

At this point one is not required to make a specific choice of test functions, save for f_0 and g_0. Similarly, a specific choice of weight functions is not yet required.

We proceed to evaluate the inner product on (F.25b) by a series of $N+1$ weight functions w_m^u (to be specified later) leaving the following equation system for the velocity problem

$$\alpha \left[\partial_{\underline{\tau}} a_i^{(0)} \langle w_m^u | g_0 \rangle + \partial_j (a_j^{(0)} a_i^{(0)}) \langle w_m^u | g_0^2 \rangle \right] = - \partial_i \mathrm{p}^{(0)} \langle w_m^u | 1 \rangle \qquad (\text{F.27})$$

$$+ \mathrm{PrRa}^{-0.5} \partial_j^2 a_i^{(0)} \langle w_m^u | g_0 \rangle$$

$$+ \varepsilon^{-2} \mathrm{PrRa}^{-0.5} a_i^{(0)} \langle w_m^u | g_0'' \rangle + \mathrm{Pr} \vartheta^{(0)} \langle w_m^u | 1 \rangle \delta_{iy}$$

$$+ \alpha \varepsilon^{-2} \mathrm{PrRa}^{-0.5} \left[\sum_{n=1}^{N} a_i^{(1,n)} \langle w_m^u | g_n'' \rangle \right]$$

$$+ \alpha \mathrm{Pr} \left[\sum_{n=1}^{N} \vartheta^{(1,n)} \langle w_m^u | f_n \rangle \right] \delta_{iy}$$

with $m = 0, \cdots, N$. Notice how the only time derivatives present in (F.27) belong to the zeroth-order amplitude $a_i^{(0)}$. As such, the first-order amplitudes are pegged to the evolution and respond instantaneously to changes in these terms.

Likewise, we evaluate the inner product on equation (F.25b) by a series of $N+1$ weight functions w_m^θ and write the following equation system for the temperature amplitudes

$$\alpha \left[\partial_{\underline{\tau}} \vartheta^{(0)} \langle w_m^\theta | 1 \rangle + \partial_j (a_j^{(0)} \vartheta^{(0)}) \langle w_m^\theta | g_0 \rangle \right] = \mathrm{Ra}^{-0.5} \partial_j^2 \vartheta^{(0)} \langle w_m^\theta | 1 \rangle \qquad (\text{F.28})$$

$$+ \alpha \varepsilon^{-2} \mathrm{Ra}^{-0.5} \left[\sum_{n=1}^{N} \vartheta^{(1,n)} \langle w_m^\theta | f_n'' \rangle \right]$$

with $m = 0, \cdots, N$. In the two following sections we will select a set of test and weight functions, which reduces the complexity by removing the summations from equations (F.27) and (F.28).

F.3.1 Choice of test f_n functions and weight functions w_m^θ for the temperature

In order to simplify the summations from equation (F.28), test and weight functions are selected so that the following relation is satisfied

$$\sum_{n=1}^{N} \langle w_m^\theta | f_n'' \rangle = \langle w_m^\theta | f_m'' \rangle \quad \text{with} \quad m = 0, \cdots, N \qquad (\text{F.29})$$

It is reminded that $f_0 = 1$ and each test function f_n satisfies $f_n'(\pm 1) = 0$ to ensure the adiabatic boundary conditions and a gauge condition $\langle 1 | f_n \rangle = 0$ for $n \geq 1$.

One alternative is to use test functions f_m that satisfy $\langle f_m'' | f_n'' \rangle = c_n \delta_{mn}$ and to use as weight functions $w_0^\theta = 1$ and $w_m^\theta = f_m''$ for $m \geq 1$. In order to find such a basis, let us consider a set F_n of linearly independent functions that verify $\mathrm{F}_n'(\pm 1) = 0$. For instance, let us consider a basis F_n such that $\mathrm{F}_n' = \underline{z}^n(\underline{z}^2 - 1)$. The second derivate of F_n reads as $\mathrm{F}_n'' = \underline{z}^{n-1}((n+2)\underline{z}^2 - n)$ for $n \geq 1$. One then proceeds to apply a Gram-Schmidt orthogonalization procedure to F_n'' to obtain an orthogonal basis over the interval $[-1, 1]$ for $n \geq 1$. The first orthogonalized function reads as

$$f_1'' = \mathrm{F}_1'' = 2\underline{z}$$

and the n-th orthogonalized function reads as

$$f_n'' = F_n'' - \sum_{j=1}^{n-1} \mathrm{proj}_{f_j''}(F_n'') \quad \text{for} \quad n > 1 \tag{F.30}$$

with $\mathrm{proj}_a(b) = \frac{\langle b|a \rangle}{\langle a|a \rangle} a$ being the projection of b on a. The resulting orthogonal basis $f_n''(\underline{z})$ is integrated twice taking care to ensure that both $f_n'(\pm 1) = 0$ and $\langle 1|f_n \rangle = 0$ for $n \geq 1$ are verified to obtain the following set of optimal test functions $f_n(\underline{z})$

$$
\begin{aligned}
f_0(\underline{z}) &= 1, \\
f_1(\underline{z}) &= -\frac{1}{3}\underline{z}(3 - \underline{z}^2), \\
f_2(\underline{z}) &= \frac{1}{60}(7 - 30\underline{z}^2 + 15\underline{z}^4) \\
f_3(\underline{z}) &= \frac{1}{5}\underline{z}(1 - 2\underline{z}^2 + \underline{z}^4) \\
f_4(\underline{z}) &= -\frac{1}{42}(1 - 9\underline{z}^2 + 15\underline{z}^4 - 7\underline{z}^6)
\end{aligned}
$$

so on and so forth.

F.3.2 Choice of test g_n functions and weight functions w_m^u for the velocity

Similarly, one way to remove the summations from equation (F.27) is to select test and weight functions that satisfy the following

$$\sum_{n=1}^{N} \langle w_m^u | g_n'' \rangle = \langle w_m^u | g_m'' \rangle \tag{F.31}$$

In this case, each test function must satisfy $g_n(\pm 1) = 0$ so that expression (F.26b) verifies the no-slip boundary condition. We also require to verify the gauge condition $\langle 1|g_n \rangle = 0$ for $n \geq 1$. One alternative is to choose the weight functions as $w_m^u = g_m$ (Galerkin method) and seek to define a complete basis that verifies $\langle g_m|g_n'' \rangle = d_l \delta_{mn}$ and $g_n(\pm 1) = 0$. This is obtained as linear combination of Legendre polynomials in the following form (Luke, 1969; Livermore, 2010)

$$g_n(\underline{z}) = \frac{1}{4} \sum_{i=1}^{3} c_i(n) P_{n+2-i}^{(0,0)}(\underline{z}) \tag{F.32}$$

where $P_n^{(0,0)}(\underline{z})$ denotes the n-th degree Legendre polynomial

$$P_n^{(0,0)}(\underline{z}) = \frac{1}{2^n n!} \frac{d^n}{d\underline{z}^n}(\underline{z}^2 - 1)^n \tag{F.33}$$

and the three values of c_i are independent of n and are determined by the boundary condition as $c_1 = -4$, $c_2 = 0$, and $c_3 = 4$.

The resulting series has the following form

$$g_0(\underline{z}) = \frac{3}{2}(1 - \underline{z}^2),$$

$$g_1(\underline{z}) = \frac{5}{2}\underline{z}(1 - \underline{z}^2),$$

$$g_2(\underline{z}) = -\frac{1}{8}(7 - 21\underline{z}^2 + 35\underline{z}^4)$$

$$g_3(\underline{z}) = -\frac{1}{8}\underline{z}(27 - 90\underline{z}^2 + 63\underline{z}^4)$$

$$g_4(\underline{z}) = \frac{1}{16}(11 - 165\underline{z}^2 + 385\underline{z}^4 - 231\underline{z}^6)$$

Having selected the weight and test functions for each problem, we may proceed to solve for the amplitudes.

F.3.3 Amplitudes for the temperature field

Thanks to the choice of test and weight functions, equations (F.27) is simplified reducing the summation to one term.

- For $m = 0$ one obtains an equation for $\vartheta^{(0)}$

$$\alpha\left[\partial_{\underline{\tau}}\vartheta^{(0)}\langle 1|1\rangle + \partial_j(a_j{}^{(0)}\vartheta^{(0)})\langle 1|g_0\rangle\right] = \mathrm{Ra}^{-0.5}\partial_j^2\vartheta^{(0)}\langle 1|1\rangle \qquad \text{(F.34a)}$$

- For $m = 2$, one obtains an expression for $\vartheta^{(1,2)}$ as function of $a_i{}^{(0)}$ and $\vartheta^{(0)}$

$$\vartheta^{(1,2)}\langle f_2''|f_2''\rangle = \varepsilon^2\mathrm{Ra}^{0.5}\partial_j(a_j{}^{(0)}\vartheta^{(0)})\langle f_2''|g_0\rangle \qquad \text{(F.34b)}$$

- The remaining amplitudes are zero.

$$\vartheta^{(1,m)} = 0 \quad \text{for} \quad m \neq 0, 2 \qquad \text{(F.34c)}$$

The temperature field takes the form

$$\theta(x, y, \underline{z}, \underline{\tau}) = \alpha\underline{\theta}(x, y, \underline{z}, \underline{\tau}) = \alpha\vartheta^{(0)} + \alpha^2\vartheta^{(1,2)}f_2 \qquad \text{(F.35)}$$

or alternatively as

$$\theta(x, y, \underline{z}, \underline{\tau}) = \langle\underline{\theta}\rangle(x, y, \underline{\tau}) + \alpha^2\vartheta^{(1,2)}(x, y, \underline{\tau})f_2(\underline{z}) \qquad \text{(F.36)}$$

F.3.4 Amplitudes for the velocity field

Thanks to the choice of test and weight functions (F.27) is also simplified but a summation remains. However, because of (F.35), this summation reduces to one term.

- For $m = 0$ one obtains an equation for $a_i{}^{(0)}$

$$\alpha\left[\partial_{\underline{\tau}}a_i{}^{(0)}\langle g_0|g_0\rangle + \partial_j(a_j{}^{(0)}a_i{}^{(0)})\langle g_0|g_0^2\rangle\right] = -\partial_i\mathrm{p}^{(0)}\langle g_0|1\rangle \tag{F.37a}$$
$$+ \mathrm{PrRa}^{-0.5}\partial_j^2 a_i{}^{(0)}\langle g_0|g_0\rangle$$
$$+ \varepsilon^{-2}\mathrm{PrRa}^{-0.5}a_i{}^{(0)}\langle g_0|g_0''\rangle + \mathrm{Pr}\vartheta^{(0)}\langle g_0|1\rangle\delta_{iy}$$
$$+ \alpha\mathrm{Pr}\vartheta^{(1,2)}\langle g_0|f_2\rangle\delta_{iy}$$

- For $m = 2$ one obtains an expression for $a_i{}^{(1,2)}$

$$\alpha\left[\partial_{\underline{\tau}}a_i{}^{(0)}\langle g_2|g_0\rangle + \partial_j(a_j{}^{(0)}a_i{}^{(0)})\langle g_2|g_0^2\rangle\right] = \mathrm{PrRa}^{-0.5}\partial_j^2 a_i{}^{(0)}\langle g_2|g_0\rangle \tag{F.37b}$$
$$+ \alpha\varepsilon^{-2}\mathrm{PrRa}^{-0.5}a_i{}^{(1,2)}\langle g_2|g_2''\rangle$$
$$+ \alpha\mathrm{Pr}\vartheta^{(1,2)}\langle g_2|f_2\rangle\delta_{iy}$$

- For $m = 4$ one obtains an expression for $a_i{}^{(1,4)}$

$$\varepsilon^{-2}\mathrm{PrRa}^{-0.5}a_i{}^{(1,4)}\langle g_4|g_4''\rangle = \partial_j(a_j{}^{(0)}a_i{}^{(0)})\langle g_4|g_0^2\rangle - \mathrm{Pr}\vartheta^{(1,2)}\langle g_4|f_2\rangle\delta_{iy} \tag{F.37c}$$

- The remaining amplitudes are zero

$$a_i{}^{(1,m)} = 0 \quad \text{for} \quad m \neq 0, 2, 4 \tag{F.37d}$$

The velocity field has the following form

$$u_i(x, y, \underline{z}, \underline{\tau}) = \alpha\underline{u}_i(x, y, \underline{z}, \underline{\tau}) = \alpha a_i{}^{(0)}g_0 + \alpha^2 a_i{}^{(1,2)}g_2 + \alpha^2 a_i{}^{(1,4)}g_4 \tag{F.38}$$

or alternatively

$$u_i(x, y, \underline{z}, \underline{\tau}) = \langle u_i\rangle(x, y, \underline{\tau})g_0(\underline{z}) + \alpha^2 a_i{}^{(1,2)}(x, y, \underline{\tau})g_2(\underline{z}) + \alpha^2 a_i{}^{(1,4)}(x, y, \underline{\tau})g_4(\underline{z}) \tag{F.39}$$

F.4 Resulting equation system

All of the above leads to a dynamical equation for the average fields: $\mathbf{a}^{(0)}$, $\vartheta^{(0)}$ and $\mathrm{p}^{(0)}$, and to an expression for the inertial correction terms: $\vartheta^{(1,2)}$, $a_i{}^{(1,2)}$, and $a_i{}^{(1,4)}$.

F.4.1 Equation system for the transversally averaged fields

Using (F.34b) and equations (F.21), (F.34a) and (F.37a) gives a dynamical equation for $\mathbf{a}^{(0)}$, $\vartheta^{(0)}$ and $\mathrm{p}^{(0)}$. However, it is much more convenient to write these expressions in terms of more physical quantities such as the mean temperature $\langle\theta\rangle = \alpha\langle\vartheta^{(0)}\rangle$, velocity $\langle\mathbf{u}\rangle = \alpha\langle\mathbf{a}^{(0)}\rangle$, and pressure $\langle\mathrm{p}\rangle = \alpha\langle\underline{\mathrm{p}}\rangle$

- Continuity equation: from equation (F.21)

$$\nabla_{\mathrm{xy}} \cdot \langle\mathbf{u}\rangle = 0 \tag{F.40a}$$

237

- Momentum equation: from equation (F.37a) and (F.34b)

$$\frac{6}{5}\partial_t\langle\mathbf{u}\rangle + \frac{54}{35}\langle\mathbf{u}\rangle\cdot\nabla_{\mathrm{xy}}\langle\mathbf{u}\rangle = -\nabla_{\mathrm{xy}}\langle\mathrm{p}\rangle + \frac{6}{5}\mathrm{Pr}\mathrm{Ra}^{-0.5}\nabla^2_{\mathrm{xy}}\langle\mathbf{u}\rangle - \lambda_1\langle\mathbf{u}\rangle$$

$$+ \ \mathrm{Pr}\left[\langle\theta\rangle - \frac{1}{\lambda_2}\langle\mathbf{u}\rangle\cdot\nabla_{\mathrm{xy}}\langle\theta\rangle\right]\mathbf{e}_y \qquad (\mathrm{F.40b})$$

- Temperature equation: from equation (F.34a)

$$\partial_t\langle\theta\rangle + \langle\mathbf{u}\rangle\cdot\nabla_{\mathrm{xy}}\langle\theta\rangle = \mathrm{Ra}^{-0.5}\nabla^2_{\mathrm{xy}}\langle\theta\rangle \qquad (\mathrm{F.40c})$$

with $\nabla_{\mathrm{xy}} = \mathbf{e}_x\partial_x + \mathbf{e}_y\partial_y$, a friction coefficient λ_1 and a correction coefficient λ_2

$$\lambda_1 = \frac{3}{\varepsilon^2}\mathrm{Pr}\mathrm{Ra}^{-0.5} \quad \text{and} \quad \lambda_2 = \frac{105}{2\varepsilon^2}\mathrm{Ra}^{-0.5} \qquad (\mathrm{F.41})$$

F.4.2 Equations for the inertial correction terms

For the evolution of the mean fields $\langle\theta\rangle$ and $\langle\mathbf{u}\rangle$, the equations (F.40a) to (F.40c) are sufficient. However, one may be interested on computing the inertial corrections in order to perform a a reconstruction of the temperature and velocity fields (F.36) and (F.39), or to compute different global quantities.

$$\theta(x,y,\underline{z},t) = \langle\theta\rangle + \alpha^2\vartheta^{(1,2)}f_2 \qquad (\mathrm{F.42a})$$

$$\mathbf{u}(x,y,\underline{z},t) = \langle\mathbf{u}\rangle g_0 + \alpha^2\mathbf{a}^{(1,2)}g_2 + \alpha^2\mathbf{a}^{(1,4)}g_4 \qquad (\mathrm{F.42b})$$

where the correction terms are given by the following expressions:

- One correction for the temperature field evaluated from (F.34b)

$$\alpha^2\vartheta^{(1,2)} = -\frac{\varepsilon^2\mathrm{Ra}^{0.5}}{2}\left[\langle\mathbf{u}\rangle\cdot\nabla_{\mathrm{xy}}\langle\theta\rangle\right] \qquad (\mathrm{F.43a})$$

- One correction for the velocity field is obtained from (F.37b)

$$\frac{1}{35}\partial_t\langle\mathbf{u}\rangle + \frac{2}{35}\left[\langle\mathbf{u}\rangle\cdot\nabla_{\mathrm{xy}}\langle\mathbf{u}\rangle\right] = \frac{1}{35}\mathrm{Pr}\mathrm{Ra}^{-0.5}\nabla^2_{\mathrm{xy}}\langle\mathbf{u}\rangle + \alpha^2\mathrm{Pr}\varepsilon^{-2}\mathrm{Ra}^{-0.5}\mathbf{a}^{(1,2)}$$

$$+ \alpha^2\frac{2}{315}\mathrm{Pr}\vartheta^{(1,2)}\mathbf{e}_y \qquad (\mathrm{F.43b})$$

which is combined to (F.40b) and (F.43a) to get rid of the time derivative and gives the following expression in terms of $\langle\mathbf{u}\rangle$, $\langle\mathrm{p}\rangle$, and $\langle\theta\rangle$

$$\alpha^2\mathbf{a}^{(1,2)} = -\frac{\varepsilon^2\mathrm{Ra}^{0.5}}{42\mathrm{Pr}}\left[\nabla_{\mathrm{xy}}\langle\mathrm{p}\rangle + \lambda_1\langle\mathbf{u}\rangle - \mathrm{Pr}\langle\theta\rangle\mathbf{e}_y\right] \qquad (\mathrm{F.43c})$$

$$+ \frac{\varepsilon^2\mathrm{Ra}^{0.5}}{49\mathrm{Pr}}\left[\langle\mathbf{u}\rangle\cdot\nabla_{\mathrm{xy}}\langle\mathbf{u}\rangle\right] + \frac{2\varepsilon^4\mathrm{Ra}}{735}\left[\langle\mathbf{u}\rangle\cdot\nabla_{\mathrm{xy}}\langle\theta\rangle\right]\mathbf{e}_y$$

- An additional correction for the velocity field evaluated from (F.37c)

$$\alpha^2 \mathbf{a}^{(1,4)} = -\frac{2\varepsilon^2 \mathrm{Ra}^{0.5}}{385 \mathrm{Pr}} \left[\langle \mathbf{u} \rangle \cdot \nabla_{\mathrm{xy}} \langle \mathbf{u} \rangle \right] + \frac{\varepsilon^4 \mathrm{Ra}}{3465} \left[\langle \mathbf{u} \rangle \cdot \nabla_{\mathrm{xy}} \langle \theta \rangle \right] \mathbf{e}_y \qquad (\text{F.43d})$$

F.5 Mechanical energy budget for the model with inertial corrections

We are interested in describing the evolution of different global quantities in terms of the amplitudes to the velocity field $\mathbf{a}^{(n)}$ and the amplitudes of the temperature field $\vartheta^{(n)}$.

F.5.1 Global kinetic energy and transfer rates

Using (F.42b) we may approximate the kinetic energy as

$$\mathrm{e}_{\mathrm{k}} = \frac{1}{2} \left[\langle \mathbf{u} \rangle g_0 + \alpha^2 \mathbf{a}_i^{(1,2)} g_2 + \alpha^2 \mathbf{a}_i^{(1,4)} g_4 \right]^2$$

Integrating over the fluid volume leaves the following expression

$$\mathrm{E}_{\mathrm{k}}(t) = \frac{3}{5} \langle \langle \mathbf{u} \rangle \cdot \langle \mathbf{u} \rangle \rangle_{\mathrm{xy}} - \frac{\alpha^2}{5} \langle \langle \mathbf{u} \rangle \cdot \mathbf{a}^{(1,2)} \rangle_{\mathrm{xy}} + \qquad\qquad (\text{F.44})$$
$$\alpha^4 \left[\frac{7}{45} \langle \mathbf{a}^{(1,2)} \cdot \mathbf{a}^{(1,2)} \rangle_{\mathrm{xy}} - \frac{1}{9} \langle \mathbf{a}^{(1,2)} \cdot \mathbf{a}^{(1,4)} \rangle_{\mathrm{xy}} + \frac{11}{117} \langle \mathbf{a}^{(1,4)} \cdot \mathbf{a}^{(1,4)} \rangle_{\mathrm{xy}} \right]$$

In practice, the terms of order α^4 in equation (F.44) may be safely neglected. A Reynolds number based on the root mean squared velocity, $\mathrm{Re} \equiv \mathrm{Ra}^{0.5} \mathrm{Pr}^{-1} \sqrt{2 \mathrm{E}_{\mathrm{k}}}$ may be evaluated using equation (F.44).

Now consider the rate-of-change for the kinetic energy as $\frac{\mathrm{d}}{\mathrm{dt}} \mathrm{E}_{\mathrm{k}}(t) = \mathrm{Pr} \mathrm{Ra}^{-0.5} (\Phi_{\mathrm{y}} - \epsilon)$. Each term can be subsequently written in terms of the amplitudes $\mathbf{a}^{(n)}$ and $\vartheta^{(n)}$.

Vertical heat-flux

Using (F.42a) and (F.42b) we may approximate the vertical heat flux as

$$v\theta = \left[\langle u_y \rangle g_0 + \alpha^2 a_y^{(1,2)} g_2 + \alpha^2 a_y^{(1,4)} g_4 \right] \left[\langle \theta \rangle f_0 + \alpha^2 \vartheta^{(1,2)} f_2 \right]$$

Integrating over the fluid volume, gives an expression for Φ_{y}

$$\Phi_{\mathrm{y}} = \mathrm{Ra}^{0.5} \langle \langle u_y \rangle \langle \theta \rangle \rangle_{\mathrm{xy}} + \alpha^2 \mathrm{Ra}^{0.5} \frac{4}{105} \langle \langle u_y \rangle \vartheta^{(1,2)} \rangle_{\mathrm{xy}} \qquad\qquad (\text{F.45})$$
$$- \alpha^4 \mathrm{Ra}^{0.5} \left[\frac{2}{45} \langle a_y^{(1,2)} \vartheta^{(1,2)} \rangle_{\mathrm{xy}} - \frac{2}{315} \langle a_y^{(1,4)} \vartheta^{(1,2)} \rangle_{\mathrm{xy}} \right]$$

where terms of order α^4 may be neglected.

Viscous dissipation rate

Consider the following expression

$$(\nabla \mathbf{u})^2 = (\nabla_{\text{xy}} \mathbf{u})^2 + (\partial_z \mathbf{u})^2$$

where each part can be written in terms of the amplitudes $\mathbf{a}^{(n)}$ and $\vartheta^{(n)}$.

$$(\nabla_{\text{xy}} \mathbf{u})^2 = \left[\nabla_{\text{xy}} \langle \mathbf{u} \rangle g_0 + \alpha^2 \nabla_{\text{xy}} \mathbf{a}^{(1,2)} g_2 + \alpha^2 \nabla_{\text{xy}} \mathbf{a}^{(1,4)} g_4 \right]^2$$

$$(\partial_z \mathbf{u})^2 = \left[\langle \mathbf{u} \rangle g_0' + \alpha^2 \mathbf{a}^{(1,2)} g_2' + \alpha^2 \mathbf{a}^{(1,4)} g_4' \right]^2$$

Expanding and integrating both expressions over the volume gives

$$\epsilon^{(xy)} = \frac{6}{5} \langle \nabla_{\text{xy}} \langle \mathbf{u} \rangle : \nabla_{\text{xy}} \langle \mathbf{u} \rangle \rangle_{\text{xy}} - \alpha^2 \frac{2}{5} \langle \nabla_{\text{xy}} \langle \mathbf{u} \rangle : \nabla_{\text{xy}} \mathbf{a}^{(1,2)} \rangle_{\text{xy}} \tag{F.46}$$

$$+ \alpha^4 \left[\frac{14}{45} \langle \nabla_{\text{xy}} \mathbf{a}^{(1,2)} : \nabla_{\text{xy}} \mathbf{a}^{(1,2)} \rangle_{\text{xy}} - \frac{2}{9} \langle \nabla_{\text{xy}} \mathbf{a}^{(1,2)} : \nabla_{\text{xy}} \mathbf{a}^{(1,4)} \rangle_{\text{xy}} \right.$$

$$\left. + \frac{22}{117} \langle \nabla_{\text{xy}} \mathbf{a}^{(1,4)} : \nabla_{\text{xy}} \mathbf{a}^{(1,4)} \rangle_{\text{xy}} \right]$$

$$\epsilon^{(z)} = \frac{3}{\varepsilon^2} \langle \langle \mathbf{u} \rangle \cdot \langle \mathbf{u} \rangle \rangle_{\text{xy}} + \alpha^4 \frac{7}{\varepsilon^2} \langle \mathbf{a}^{(1,2)} \cdot \mathbf{a}^{(1,2)} \rangle_{\text{xy}} + \alpha^4 \frac{11}{\varepsilon^2} \langle \mathbf{a}^{(1,4)} \cdot \mathbf{a}^{(1,4)} \rangle_{\text{xy}} \tag{F.47}$$

where terms of order α^4 may be neglected. Combining these expressions gives the total viscous dissipation $\epsilon = \epsilon^{(xy)} + \epsilon^{(z)}$.

F.5.2 Total potential energy and transfer rates

The total potential energy $\mathrm{E_p} = -\mathrm{Pr} \langle y\theta \rangle_{\text{vol}}$ may be rewritten as

$$\mathrm{E_p} = -\mathrm{Pr} \langle y \langle \theta \rangle \rangle_{\text{xy}} \tag{F.48}$$

Now consider the rate-of-change $\frac{\mathrm{d}}{\mathrm{dt}} \mathrm{E_p}(t) = \mathrm{Pr}\mathrm{Ra}^{-0.5}(\Phi_{\text{y}} - \Phi_{\text{i}} - \Phi_{\text{b1}})$. Similarly to Φ_{y}, the terms Φ_{i} and Φ_{b1} can be written as function of the amplitudes $\mathbf{a}^{(n)}$ and $\vartheta^{(n)}$.

$$\Phi_{\text{i}} = \langle \partial_y \langle \theta \rangle \rangle_{\text{xy}} \tag{F.49}$$

$$\Phi_{\text{b1}} = -\frac{1}{\Gamma_{\text{x}}} \oint y \partial_n \langle \theta \rangle \mathrm{ds} \tag{F.50}$$

with ds being an infinitesimal element of the boundary ∂A, where $\mathrm{dA} = \mathrm{dxdy}$ and the loop integral is **counterclockwise**.

F.5.3 Global thermal fluctuations and transfer rate

Using the equation (F.42a) we may approximate the temperature fluctuations

$$\theta^2 = \left[\langle \theta \rangle f_0 + \alpha^2 \vartheta^{(1,2)} f_2 \right]^2 \tag{F.51}$$

Integrating over the fluid volume, we can approximate $E_\theta \equiv \frac{1}{2}\langle\theta^2\rangle_{xyz}$ as

$$E_\theta(t) = \frac{1}{2}\langle\langle\theta\rangle\langle\theta\rangle\rangle_{xy} + \frac{2\alpha^4}{525}\langle\vartheta^{(1,2)}\vartheta^{(1,2)}\rangle_{xy} \tag{F.52}$$

where terms of order α^4 may be neglected. Now consider the rate-of-change $\frac{d}{dt}E_\theta(t) = -\text{Ra}^{-0.5}(\epsilon_\theta - \Phi_{b3})$. Each term can be written as function of the amplitudes $\vartheta^{(n)}$.

Thermal dissipation rate

Consider the following expression

$$(\nabla\theta)^2 = (\nabla_{xy}\theta)^2 + (\partial_z\theta)^2$$

Each part can be written in terms of the amplitudes $\vartheta^{(n)}$.

$$(\nabla_{xy}\theta)^2 = \left[\nabla_{xy}\langle\theta\rangle f_0 + \nabla_{xy}\vartheta^{(1,2)} f_2\right]^2$$
$$(\partial_z\theta)^2 = \left[\langle\theta\rangle f_0' + \vartheta^{(1,2)} f_2'\right]^2$$

Expanding and integrating both expressions over the volume gives

$$\epsilon_\theta = \langle\nabla_{xy}\langle\theta\rangle \cdot \nabla_{xy}\langle\theta\rangle\rangle_{xy} + \frac{4\alpha^4}{525}\langle\nabla_{xy}\vartheta^{(1,2)} \cdot \nabla_{xy}\vartheta^{(1,2)}\rangle_{xy} + \frac{8\alpha^4}{105}\langle\vartheta^{(1,2)}\vartheta^{(1,2)}\rangle_{xy} \tag{F.53}$$

where terms of order α^4 may be neglected.

Boundary flux

A similar procedure is used to evaluate Φ_{b3}

$$\Phi_{b3} = \frac{1}{\Gamma_x}\oint\langle\theta\rangle\partial_n\langle\theta\rangle ds + \frac{1}{\Gamma_x}\frac{4\alpha^4}{525}\oint\vartheta^{(1,2)}\partial_n\vartheta^{(1,2)}ds$$

with ds being an infinitesimal element of the boundary ∂A, where $dA = dxdy$ and the loop integral is **counterclockwise**. A closer inspection of equation (F.43a) reveals that $\vartheta^{(1,2)} = 0$ on the boundaries such that

$$\Phi_{b3} = \frac{1}{\Gamma_x}\oint\vartheta^{(0)}\partial_n\vartheta^{(0)}ds \tag{F.54}$$